Dimensionality-Driven Graphene Nanomaterials for Optical Identity Encoding and Lithium Battery Interfaces

Fangling Wu

Department of Physics

Lancaster University

June 2025

This thesis is submitted in partial fulfilment of the requirements for the degree of Doctor of Philosophy

Preface

This thesis is submitted in fulfilment of the requirements for the degree at Lancaster University and presents original research conducted between January 2020 and August 2023. Except where otherwise indicated, the work is entirely my own and has not been submitted, nor is it currently being submitted, for a degree at any other university or institution. Contributions from others have been appropriately acknowledged within the text. The total word count of this thesis does not exceed the maximum permitted limit of 80,000 words.

Fangling Wu

Lancaster University

June 2025

List of Publications

- Chen, Yue, et al. ‘Nanoarchitecture factors of solid electrolyte interphase formation via 3D nano-rheology microscopy and surface force-distance spectroscopy.’ Nature Communications 14.1(2023): 1321.
- F Wu, et al. ‘Graphene quantum dots from biowaste for anti-counterfeiting.’ Under preparation.
- F Wu, et al. ‘MoS_2 / Graphene Heterostructure for anti-counterfeiting.’ Under preparation.

Conference presentation

- Contribution to conference: presenting poster ‘Graphene quantum dots derived from biowaste for anti-counterfeiting.’ Bristol Integrated Photonic summer school 2023.
- Contribution to conference: presenting poster ‘Graphene-MoS_2 van der Waal heterostructure for optical physical unclonable functions.’ National Physical Laboratory Scale-Up and Standardization for Photonic Quantum Technologies 2023.
- Contribution to conference: presenting poster ‘Graphene-MoS_2 van der Waal heterostructure for optical physical unclonable functions.’ Graphene week 2024.

Contribution

The preparation and fabrication of Highly Oriented Pyrolytic Graphite (HOPG) electrodes, their assembly in EL-CELL electrochemical cells, and the formulation of the electrolyte solutions described in Chapter 3 were carried out by my colleague Yue Chen. Jake Manning performed the UV–Vis's measurements of the graphene quantum dot (GQDs) reported in Chapter 3. Dr Angelo Lamantia provided training and assisted in optimising the electrospray setup. Dr James Fong and Dr Richa Soni provided key support in the experimental design of the GQD study. The manual for binary map generation was developed based on Dr Elliot Ball's manual. Jay Little contributed substantially to the generation of the photoluminescence (PL) maps, and the corresponding manual was developed based on his initial plotting workflow described in Chapter 5.6.

Abstract

This thesis investigates how dimensionality in graphene-based nanomaterials—from zero-dimensional graphene quantum dots (GQDs) to two-dimensional graphene–MoS_2 heterostructures and bulk highly oriented pyrolytic graphite (HOPG)—influences their optical and interfacial properties. The research follows two main directions: the development of optical physically unclonable functions (PUFs) for secure identity encoding, and the study of solid–electrolyte interphase (SEI) formation in lithium-ion batteries.

For optical security, electrospray-deposited, biomass-derived GQDs produced high-entropy, excitation-dependent fluorescence patterns. These were digitally encoded using local binary pattern algorithms, demonstrating strong randomness and reproducibility for stochastic PUFs. In contrast, deterministic optical fingerprints were achieved in graphene–MoS_2 heterostructures, where photoluminescence (PL) variations across the flake were driven by stacking order and interlayer strain. Low-temperature PL confirmed the spatial and thermal stability of these emission patterns.

In the energy storage study, operando Raman spectroscopy was used to examine SEI formation on surface-treated HOPG in EC/DMC- and DX-based electrolytes with varying salt concentrations. The results revealed that SEI formation precedes lithium intercalation and is strongly influenced by solvation structure, which shifts with solvent type and salt concentration. Edge-plane reactivity, solvation-driven decomposition, and SEI growth mechanisms were systematically analysed. By linking dimensionality to optical entropy and interfacial chemistry, this work provides a unified framework for engineering graphene-based nanomaterials across domains. The findings offer new strategies for secure device authentication and stable battery interface design.

Table of Contents

Chapter 1: Introduction

1.1 Background and Motivation

Advancements in nanomaterials have opened new possibilities in both secure hardware authentication and electrochemical energy storage. Among these, carbon-based materials—particularly graphene and its dimensional variants—have emerged as versatile platforms due to their tuneable electronic, optical, and interfacial properties. Graphene quantum dots (GQDs), two-dimensional (2D) heterostructures, and bulk graphite offer unique functionalities depending on their dimensionality, which controls quantum confinement, surface chemistry, and electron–phonon interactions [1-3].

Two critical challenges motivate this thesis. First, in the context of hardware security, there is an urgent need for physically unclonable functions (PUFs)—devices that derive security from physical randomness and are extremely difficult to duplicate [4]. Optical PUFs are attractive due to their non-invasive readout and high parallelism, but require stable, unique, and high-entropy optical features [5]. Second, in lithium-ion battery (LIB) technology, improving the stability and efficiency of electrode–electrolyte interfaces remain a major barrier to long-term performance. The solid–electrolyte interphase (SEI), formed during early cycling on graphite anodes, plays a critical role in determining interfacial stability and lithium-ion transport [6-8].

This thesis bridges these two domains by using a dimensionality-driven framework to explore how graphene-based materials—from 0D to 2D to bulk—can be engineered for high-entropy optical encoding and interfacial control in LIBs. Each system offers a unique platform for probing structure–function relationships across photonic and electrochemical applications.

1.2 Research Objectives and Questions

The central objective of this research is to investigate how the dimensionality of graphene-based nanomaterials governs their optical behaviour and interfacial chemistry. Specifically, the thesis aims to answer the following questions:

- Can biomass-derived GQDs generate high-entropy, stable photoluminescence patterns suitable for stochastic optical PUF applications?
- How does stacking geometry in graphene–MoS_2 heterostructures influence deterministic photoluminescence patterns for secure identity encoding?
- How do solvation structures and surface morphology affect SEI formation and lithium-ion intercalation on graphite electrodes?

By addressing these questions, this thesis develops a structure–function framework for designing multifunctional graphene-based systems that span both secure electronics and energy storage.

1.3 Scope and Approach

This work investigates three classes of carbon-based materials across increasing dimensionality:

- Zero-dimensional GQDs, synthesized from waste tea leaves and deposited using electrospray techniques to create high-entropy emission maps.
- Two-dimensional graphene–MoS_2 heterostructures, fabricated via dry transfer and characterized using spatially resolved and low-temperature photoluminescence mapping.
- Bulk highly oriented pyrolytic graphite (HOPG), treated via mechanical and thermal methods to expose edge and basal planes and probed via operando Raman spectroscopy under electrochemical cycling.

GQDs were characterised by AFM, PL, Raman, fluorescence microscopy, and UV–Vis's absorption spectroscopy. Graphene–MoS_2 heterostructures were characterised by AFM, PL, and Raman. Electrochemical interfacial processes on HOPG were monitored by *in situ/operando* Raman in EC/DMC and DX-based electrolytes with varied LiFSI concentration.

1.4 Key Contributions

This thesis makes the following original contributions to the fields of nanomaterials, optical security, and energy storage:

- Demonstrates a scalable, green method for producing stochastic optical PUFs using electrospray-deposited biomass-derived GQDs, achieving near-ideal entropy and reproducibility.
- Introduces deterministic optical fingerprinting based on interlayer exciton modulation in 2D graphene–MoS_2 heterostructures, with spatially stable, reproducible patterns verified across excitation powers and temperatures.
- Provides operando Raman evidence that SEI formation on graphite initiates at edge sites prior to lithium intercalation, and that solvation structure—modulated by electrolyte composition and salt concentration—critically governs interfacial chemistry.

Together, these contributions highlight the role of dimensionality as a design axis for multifunctional graphene systems.

1.5 Thesis Structure

This thesis is organized as follows:

- Chapter 2 reviews the literature on graphene nanomaterials, dimensionality-governed structure–function relationships, optical PUFs, and SEI formation in lithium-ion batteries.
- Chapter 3 describes the fabrication and characterization techniques used across all three material systems.
- Chapter 4 presents the design and evaluation of stochastic optical fingerprints using GQDs.
- Chapter 5 focuses on deterministic photoluminescence encoding in graphene–MoS_2 heterostructures.
- Chapter 6 explores solvation and SEI formation on graphite via operando Raman spectroscopy under varying electrolyte environments.
- Chapter 7 concludes with a synthesis of findings, limitations, and future directions.

Chapter 2 Theoretical Background

This chapter provides the theoretical background for this thesis. It begins by discussing graphene-based nanomaterials with varying dimensionalities—ranging from quantum dots to 2D heterostructures and bulk graphite—and how these structural forms influence their physical and chemical behaviour. Based on this framework, the chapter then explores its implications for two distinct fields: optical security and battery chemistry.

Section 2.2 introduces the concept of optical physically unclonable functions (PUFs), outlining their fundamental principles and the role of dimensionality-driven optical properties in secure identity encoding. Section 2.3 focuses on interfacial chemistry in lithium-ion batteries, with an emphasis on solid–electrolyte interphase (SEI) formation and solvation structures at the electrode–electrolyte interface. This chapter bridges the fundamental properties of graphene nanomaterials to their applications in optical security and battery chemistry.

2.1 Graphene-Based Nanomaterials: Structure and Dimensionality

Carbon forms a wide range of allotropes, including 3D diamond and graphite, 2D graphene, 1D carbon nanotubes, 0D fullerenes, and disordered amorphous carbons, each defined by distinct atomic coordination and bonding topology [9,10]. This diversity arises from carbon's ability to adopt sp^3, sp^2, or mixed hybridisation, which fixes local bond geometry (tetrahedral versus trigonal-planar) and controls the extent of π electron delocalisation, thereby governing the electronic structure and optical response [10].

Figure 2.1-1 summarises the key bonding motifs in graphitic materials. In sp^3 hybridization, one 2s and three 2p orbitals mix to form four equivalent sp^3 orbitals with tetrahedral geometry (109.5° bond angles). Each carbon atom forms four strong σ bonds, creating a three-dimensional network of largely localized electrons. In the sp^2 hybridization, carbon mixes one 2s and two 2p orbitals to produce three trigonal planar sp^2 orbitals (120° bond angles), while the unhybridized p_z orbital remains perpendicular to the plane, enabling the formation of three in-plane σ bonds constitute a hexagonal lattice, along with out-of-plane π bonding via lateral p_z orbital overlap.

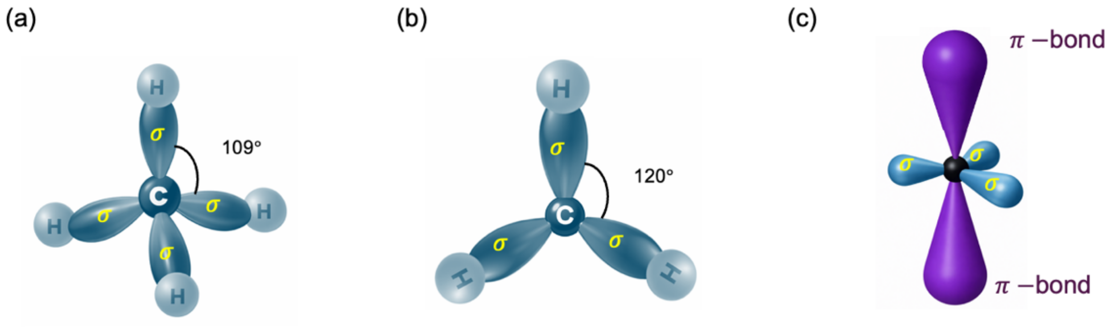

Figure 2.1-1. Schematic illustration of carbon orbital hybridisation and bonding geometries: (a) sp^3 hybridisation in a tetrahedral configuration with σ bonds (bond angle ≈ 109°); (b) sp^2 hybridisation in a trigonal planar configuration with σ bonds (bond angle ≈ 120°); (c) sp^2 bonding showing three in-plane σ bonds and the out-of-plane π bond formed by overlap of the remaining p orbitals above and below the plane.

While graphene-derived materials are primarily composed of an sp^2-bonded lattice, edges, defects, and surface functional groups introduce a controllable sp^2/sp^3 distribution that enables tuneable electronic structure and optical emission [11,12]. The delocalized π-electron network inherent to sp^2 bonding underpins the electronic and optical properties of these materials. For example, in graphene, the π and π* (antibonding) bands meet at the Dirac point, creating a zero-bandgap semimetal, while disruption of the π network through defects, edges, or functionalization introduces localized states within the bandgap [11]. In GQDs, where quantum confinement effects become significant, optical transitions are dominated by π–π* and n–π* excitations. When carbon bonds to heteroatoms—notably oxygen or nitrogen—non-bonding (n) electronic states associated with lone-pair orbitals can appear, enabling n–π* transitions that are often linked to functional groups like C=O, C–OH, and C–O–C [12]. The relative contributions of π–π* and n–π* pathways therefore depend on crystallinity, edge density, and surface chemistry—parameters that become increasingly significant as dimensionality is reduced and the surface-to-volume ratio increases [9,12].

2.1.1 Dimensionality, Density of States, and Quantum Confinement (3D → 2D → 0D)

The physical, optical, and electrical properties of graphene-based materials evolve systematically with dimensionality. As illustrated in Figure 2.1.1-1, HOPG represents a 3D stack of graphene layers, where strong in-plane covalent bonding is coupled with weak interlayer Van der Waals interactions; exfoliation yields 2D graphene, which can also be combined with MoS_2 to form a graphene–MoS_2 van der Waals heterostructure, introducing additional interfacial coupling. Further lateral size reduction produces 0D graphene quantum dots (≈1–10 nm), where edge termination and dangling bonds become dominant and the bonding environment evolves from predominantly sp^2 basal-plane carbon to a higher proportion of sp^3 hybridization at the edges.

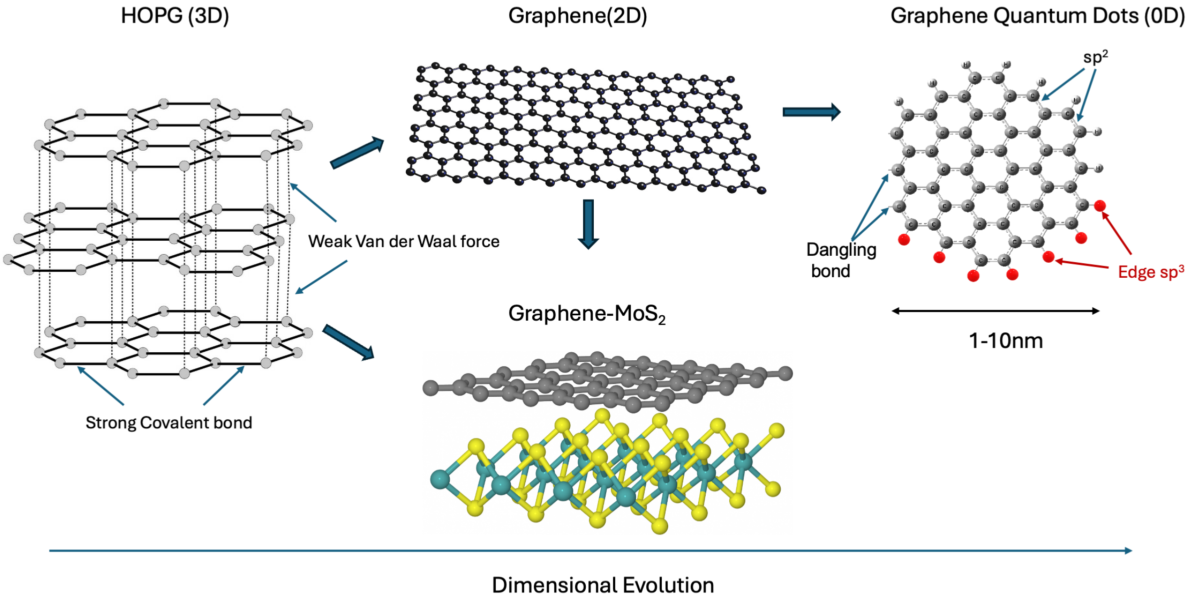

Figure 2.1.1-1. Dimensional evolution of graphitic materials used in this thesis: HOPG (3D), graphene (2D), graphene–MoS_2 van der Waals heterostructures, and graphene quantum dots (0D; ~1–10 nm)—highlighting the dominant bonding interactions (in-plane covalent vs interlayer van der Waals) and the emergence of edge features in 0D structures (dangling bonds and increased edge sp^3 character relative to basal-plane sp^2 carbon).

When the material dimensions approach the de Broglie wavelength of charge carriers, spatial confinement imposes boundary conditions on the carrier wavefunctions and drives the quantization of electronic states. As a result, bulk-like continuous energy bands progressively transform into discrete levels as the system transitions from 3D to 2D, 1D, and ultimately 0D confinement. A standard way to formalize this transition is via the density of states, $g(E)$, defined as the number of electronic states per unit energy interval per unit system size (volume in 3D, area in 2D, length in 1D). Equivalently, $g(E)\,\mathrm{d}E$ counts the states between E and $E + \mathrm{d}E$. For parabolic bands, $g(E)$ exhibits characteristic dimensional scaling:

- 3D (bulk): $g_{3D}(E) \propto \surd(E - E_c)$
- 2D (quantum well / monolayer limit): $g_{2D}(E)$ is step-like (constant within each sub band)
- 1D (quantum wire): $g_{1D}(E) \propto 1 / \surd(E - En)$ (diverges at sub band edges)
- 0D (quantum dot): $g_{0D}(E)$ becomes discrete (set of delta-like levels), broadened in practice by disorder and size dispersion.

These density of states (DOS) differences strongly influence optical absorption and emission: reduced dimensionality concentrates oscillator strength into fewer states and enhance spectral selectivity, while 0D confinement yields discrete transitions and size-tuneable effective gaps. A simple conceptual model for confinement is the particle-in-a-box approximation. For a carrier confined in a cubic region of side length L, allowed energies scale as:

$$E(nx, ny, nz) = \left(\frac{h^2}{8m} * L^2\right) \cdot (nx^2 + ny^2 + nz^2), \text{(Equation 2.1.1-1)}$$

where h is Planck's constant, m^* is the effective mass, and nx, ny, nz are positive integers. The inverse-square dependence on L highlights why optical gaps in quantum dots strongly blue-shift as size decreases. Although graphene is not a conventional parabolic semiconductor, confinement in graphene quantum dots still imposes quantisation and edge boundary conditions that convert quasi-continuous bands into discrete levels and enable optical emission via confined and defect-associated states.

2.1.2 3D: Highly Oriented Pyrolytic Graphite (HOPG) Structure

Graphite is a stacked layered allotrope composed of graphene sheets separated by an interlayer spacing of approximately 0.335 nm and held together primarily by van der Waals interactions, most commonly in the Bernal (AB) stacking arrangement. Within each layer, sp²-hybridized carbon atoms form a two-dimensional hexagonal lattice with strong in-plane covalent σ-bonds and a delocalized π-electron system. This bulk structure features strong dielectric screening—arising from the polarizability of the stacked π-electron systems—which effectively reduces long-range Coulomb interactions compared to isolated 2D systems [13,14]. The stacking also introduces pronounced anisotropy: robust σ bonding and π-electron delocalization within basal planes enable high in-plane conductivity, while interlayer coupling remains comparatively weak [15].

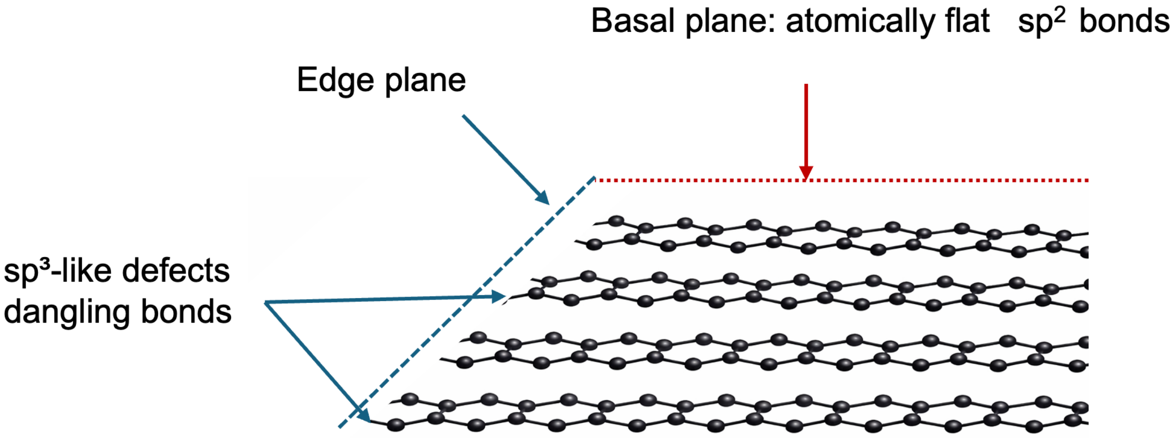

Figure 2.1.2-1. Schematic illustration of a HOPG structure highlighting the distinction between the basal plane and edge plane. The basal plane consists of atomically flat, sp^2 bonded graphene layers, whereas the edge plane terminates the stacked layers and exposes under-coordinated carbon sites that can host sp^3-like defects and dangling bonds, providing higher chemical reactivity compared with the basal surface.

In quasi-3D graphitic systems such as HOPG, this anisotropy and the distinction between basal-plane and edge-plane terminations are central for interfacial chemistry and electrochemical reactivity (Figure 2.1.2-1). Basal planes are atomically flat, chemically inert surfaces with low defect density and minimal dangling bonds; their dense, sp^2-bonded structure provides a smooth pathway for lithium-ion intercalation with minimal volume expansion.

In contrast, edge planes represent lattice termination sites with rough, reactive surfaces containing sp^3-like defects, dangling bonds, and functional groups, serving as active sites for electrochemical reactions including electrolyte decomposition and lithium-ion intercalation [16,17]. This surface anisotropy directly influences solid-electrolyte interphase (SEI) formation in lithium-ion batteries: basal planes promote thin, organic-rich SEI layers through solvent reduction, whereas edge planes facilitate thicker, inorganic-rich SEI formation via salt decomposition [18,19]. Understanding this distinction is essential for stable battery interface design, further details are presented in Section 2.3.

2.1.3 2D: Graphene-Based Van der Waals Heterostructure

Two-dimensional materials, epitomized by graphene and monolayer MoS_2, exhibit unique electronic and optical behaviours that arise from quantum confinement in one dimension. Their properties are highly sensitive to thickness, stacking order, and interfacial coupling when combined into van der Waals heterostructures. The following sections outline the individual characteristics of graphene and MoS_2, then introduce the coupled behaviour that emerges in their van der Waals heterostructures—a system central to the optical physically unclonable functions discussed in Chapter 5.

2.1.3.1 Monolayer Graphene

Graphene is a single atomic layer of sp^2-bonded carbon arranged in a hexagonal lattice with two atoms per unit cell. As shown in Figure 2.1.3.1-1, its low-energy electronic structure is characterised by linear dispersion near the Brillouin-zone corners—the K and K′ points (high-symmetry points in reciprocal space)—where the conduction band (lowest unoccupied electronic states) and valence band (highest occupied states) meet at the Dirac point, resulting in an effectively zero bandgap (the energy separation between maximum of valence and minimum of conduction bands) and a vanishing density of states at charge neutrality.

In pristine, undoped monolayer graphene, the Fermi level E_F (the equilibrium chemical potential, which sets electronic state occupancy through the Fermi–Dirac distribution) lies at the Dirac point. Here, the density of states (DOS) approaches zero linearly with energy:

$$E = \pm\hbar v_F \mid k \mid, \text{ (Equation 2.1.3.1-1)}$$

Where E is the charge carrier energy (electron or hole) relative to the Dirac point (in *J* or *eV*); $\hbar$ is the reduced Planck constant ($\hbar = h/2\pi \approx 1.055 \times 10^{-34}$ J · s), relating energy to wavevector; v_F represents the Fermi velocity of graphene ($\approx 1 \times 10^6$ m/s); k is the magnitude of the crystal wavevector measured relative to the K or K' point in the Brillouin zone(m^{-1}).

This relation describes massless Dirac fermions—charge carriers that obey a relativistic-like dispersion and exhibit zero effective mass—with a characteristic Fermi velocity $v_F \approx 10^6$ m/s. Such linear, gapless band dispersion underpins graphene's exceptionally high carrier mobility, semi metallic electronic structure, and broadband optical absorption. The vanishing DOS near the Dirac point makes graphene highly sensitive to external perturbations: small changes in carrier density—the concentration of free electrons or holes per unit volume—induced by electrostatic gating, adsorption, or substrate charge traps can significantly shift the Fermi level, thereby modifying both transport and optical response.

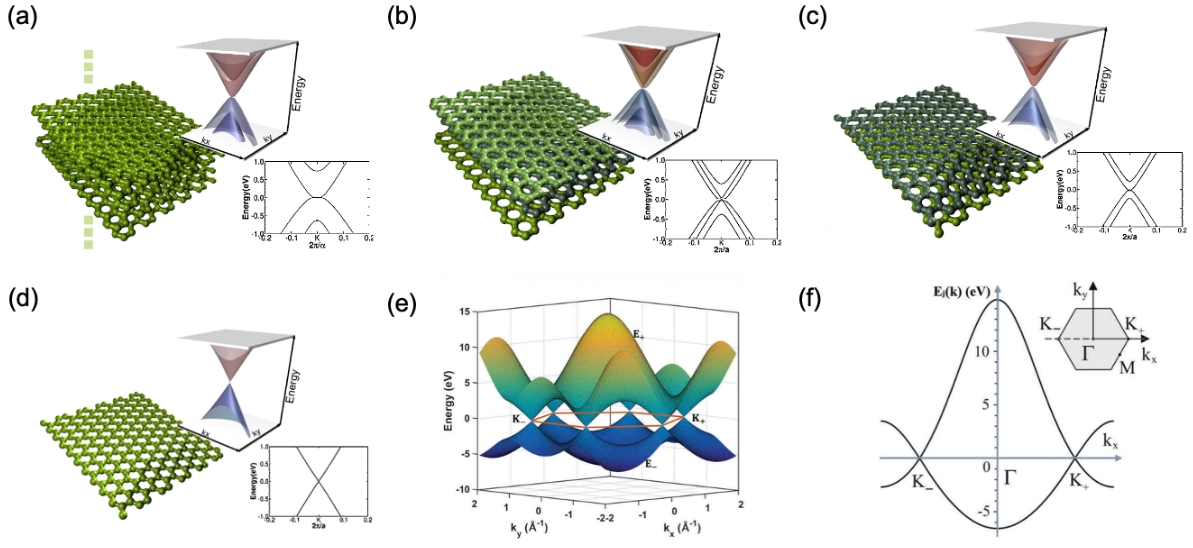

Figure 2.1.3.1-1. Evolution of the low-energy electronic band structure from graphite to graphene. (a–d) Low-energy DFT band structures and near-K projections for bulk graphite, ABA-stacked tri-layer graphene, AB-stacked bilayer graphene, and monolayer graphene (Fermi level set to 0). (e–f) Tight-binding band structure of monolayer graphene and a representative line cut along k_x ($k_y = 0$), showing the Dirac-point crossing near K/K′. Panels (a–d) are adapted from Terrones *et al.*, *Nano Today* 5(4), 351–372 (2010) and are reproduced with permission from Elsevier [20]. Panels (e–f) are adapted from Yang *et al.*, *Sci. Technol. Adv. Mater.* 19(1), 613–648 (2018), under Creative Commons CC BY 4.0 license [21].

Unlike conventional semiconductors, graphene's gapless electronic structure suppresses intrinsic light emission, rendering it more suitable as a conductive, tuneable electrode material. Its Fermi level can be modulated via electrostatic gating, chemical doping, or interfacial charge transfer, enabling fine control over carrier density and optical properties. When integrated into heterostructures, graphene primarily serves as a charge reservoir and screening layer.

2.1.3.2 Monolayer MoS_2

In contrast, molybdenum disulfide (MoS_2) is a layered transition-metal dichalcogenide (TMD) with a sandwich-like S–Mo–S structure held together by strong in-plane covalent bonds and weak interlayer van der Waals forces. Its electronic band structure depends strongly on thickness (Fig. 2.1.3.2-1). In bulk and few-layer MoS_2, the valence-band maximum (VBM) and conduction-band minimum (CBM) reside at different crystal momenta, requiring phonon assistance for radiative recombination and resulting in inherently weak photoluminescence (PL). When thinned to a monolayer, reduced interlayer coupling and quantum confinement shift the band-edge energies, rendering the lowest-energy transition direct at the K/K′ valley (direct bandgap ≈1.8 eV)[22]. This indirect-to-direct crossover arises because the VBM moves from the Γ-point to the K-point, eliminating the need for momentum-conserving phonons and leading to a pronounced increase in PL quantum efficiency.

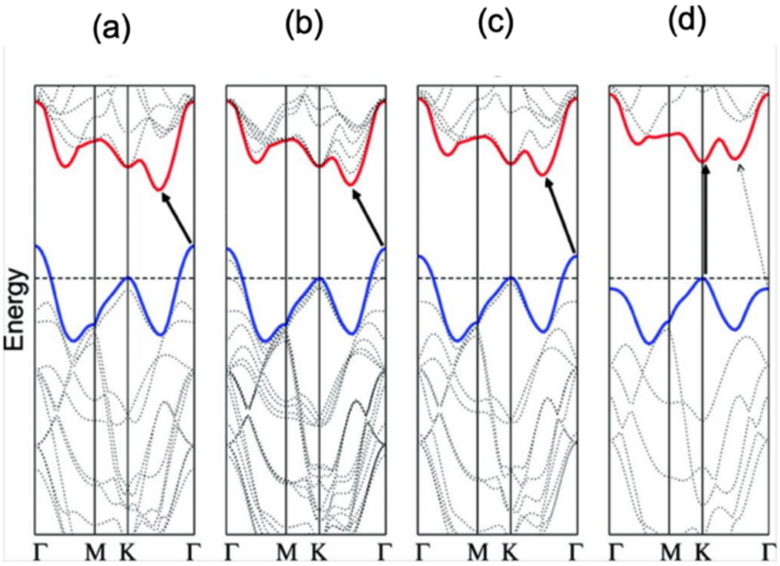

Figure 2.1.3.2-1. Band structure of MoS_2, with a solid arrow showing the lowest energy transition in: (a) Bulk, (b) 4 layers, (c) Bilayer and (d) Monolayer. Adapted from Splendiani et al., *Nano Letters* 10(4), 1271–1275 (2010)[22], with permission from the American Chemical Society.

When monolayer MoS_2 is photoexcited, electron-hole pairs form and bind via Coulomb attraction into neutral quasiparticles called excitons. Their binding energy E_b—the energy required to separate them into free carriers—is significantly enhanced in two dimensions due to reduced dielectric screening. The binding energy follows a 2D hydrogenic scaling inversely with the effective dielectric constant κ_{eff}:

$$E_b \propto \frac{1}{\kappa_{\text{eff}}^2}(\mathrm{Eg} - \mathrm{Ex}),$$ (Equation 2.1.3.2-1)

where E_X is the exciton emission energy, $\kappa_{\text{eff}} = (\kappa_{\text{substrate}} + \kappa_{\text{environment}})/2$ averages the dielectric screening from the substrate and environment, resulting exciton energies are highly sensitive to encapsulation and substrate. The large binding energy of monolayer MoS_2 (≈500 meV) stabilizes excitons at room temperature, thereby enhancing radiative recombination and photoluminescence efficiency.

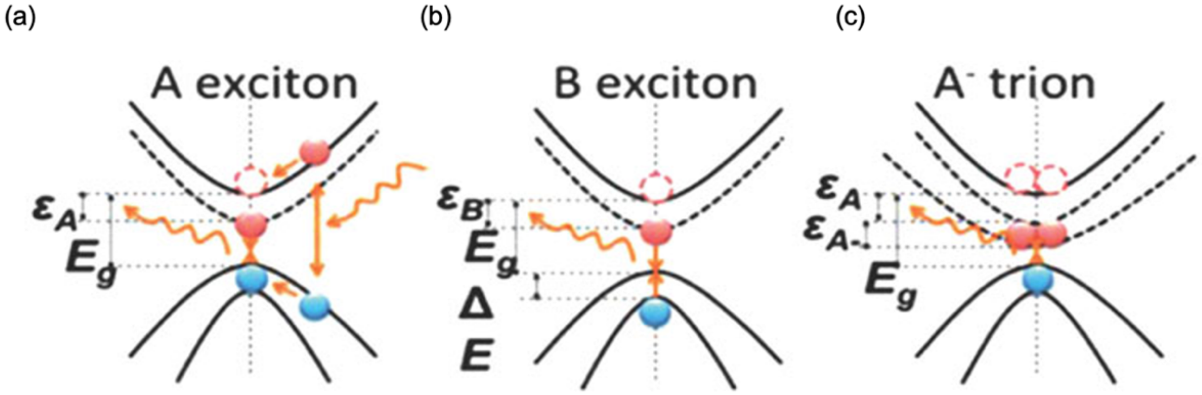

Figure 2.1.3.2-2. Schematic of exciton-related radiative transitions at the K valley in monolayer MoS_2, illustrating (a) the A exciton, (b) the B exciton, and (c) the negative trion (A^-). E_g denotes the quasiparticle band gap. Δ denotes the spin–orbit splitting of the valence band, which gives rise to the A and B excitonic transitions. ε_A and ε_B denote the binding energies of the A and B excitons, respectively, while ε_{A^-} denotes the binding energy of the A^- trion (relative to the free-carrier continuum). Adapted from Lin *et al.*, *Nano Letters* 14(10), 5569–5576 (2014)[23], with permission from the American Chemical Society.

Several distinct excitonic resonances are observed in monolayer MoS_2. A and B excitons arise from transitions between spin–orbit split valence bands (K_v1 and K_v2) and the conduction band at the K-point, with an energy splitting ($\Delta_{SO} \approx 150–200$ meV) reflecting strong spin–orbit coupling (Figure 2.1.3.2-2)[23]. The A-exciton corresponds to the lower-energy transition and yields strong photoluminescence (PL), whereas the B-exciton contributes a comparatively weaker pl signal. Trions (charged excitons, X^-

or X^+) form when excess carriers are present; their relative intensity to neutral excitons follows a mass-action relation,

$$\frac{I_{X^-}}{I_X} \propto n_e \exp\left(\frac{E_b^{X^-}}{k_B T}\right), \text{ (Equation 2.1.3.2-2)}$$

Where with n_e the electron density and $E_b^{X^-}$ the trion binding energy. The exciton–trion balance is highly sensitive to local doping, defects, strain, and dielectric environment, making photoluminescence (PL) a powerful probe for mapping spatial and spectral heterogeneity in 2D semiconductors. Additionally, localized excitons can bind to defects, impurities, or strain potentials, giving rise to distinct defect-related PL peaks that further encode local structural and electronic variations.

The PL spectrum is characterized by the quasiparticle gap E_g, the spin–orbit valence band splitting Δ, and the binding energies $\varepsilon_A, \varepsilon_B, \varepsilon_{A^-}$ of the A/B excitons and the negatively charged A^- trion. The electron–hole interaction is commonly described by a dielectric-screened 2D Coulomb potential,

$$V_{2D}(L) = \frac{e^2}{2\varepsilon_0 \kappa_{\text{eff}} L_0} \cdot f\left(\frac{L}{L_0}\right), \text{ (Equation 2.1.3.2-3)}$$

where κ_{eff} is the effective dielectric constant and L_0 is a characteristic length scale, so changes in the dielectric environment can directly shift the PL peak energy and linewidth. Together, these relationships quantify how changes in the dielectric environment and doping level cooperatively modulate the spectral balance between neutral excitons and charged trions.

Photoluminescence efficiency is governed by competition between radiative recombination and non-radiative decay pathways. The internal quantum yield is

$$\eta_{\text{PL}} = \frac{\Gamma_r}{\Gamma_r + \Gamma_{\text{nr}}}, \text{ (Equation 2.1.3.2-4)}$$

where Γ_r and Γ_{nr} are the radiative and non-radiative rates, respectively. In low-dimensional systems, non-radiative recombination mechanisms become especially pronounced. Surface recombination dominates in nanomaterials with high surface-to-volume ratios; Auger recombination transfers energy to a third carrier at high excitation densities; and energy transfer to adjacent materials (e.g., graphene quenching MoS_2 PL) together with defect-induced trapping further reduce efficiency. These recombination pathways exhibit strong dimensionality dependence: 2D systems display pronounced excitonic effects accompanied by interfacial losses, while

0D systems are governed by surface- and edge-dominated recombination, with possible suppression of Auger processes due to discretized energy levels.

2.1.3.3 Interfacial Coupling in the Graphene-MoS_2 Van der Waals Heterostructure

When graphene is stacked with MoS_2 to form a van der Waals heterostructure (vdWH), the resulting system inherits complementary properties: graphene contributes tuneable Fermi level and charge transport pathways, while MoS_2 provides strong light–matter interaction and excitonic emission(24,25). The electronic, optical, and dynamic properties of the composite system are governed by interlayer coupling, a collective term describing the non-covalent interactions modulated by several interdependent physical parameters at a given spatial coordinate r:

$$\mathrm{C}(\mathrm{r}) = \{d(\mathrm{r}), \varepsilon(\mathrm{r}), \sigma(\mathrm{r}), E_{\text{int}}(\mathrm{r}), \theta(\mathrm{r})\}, \text{ (Equation 2.1.3.3-1)}$$

where $d(\mathrm{r})$ is the local interlayer spacing (Å), $\varepsilon(\mathrm{r})$ is the local in-plane strain, $\sigma(\mathrm{r})$ is the interfacial charge transfer density (C m^{-2}), $E_{\text{int}}(\mathrm{r})$ is the built-in interfacial electric field (V m^{-1}), and $\theta(\mathrm{r})$ is the local twist angle, controlling momentum-space overlap between the two layers (as shown in Figure 2.1.3.3-1).

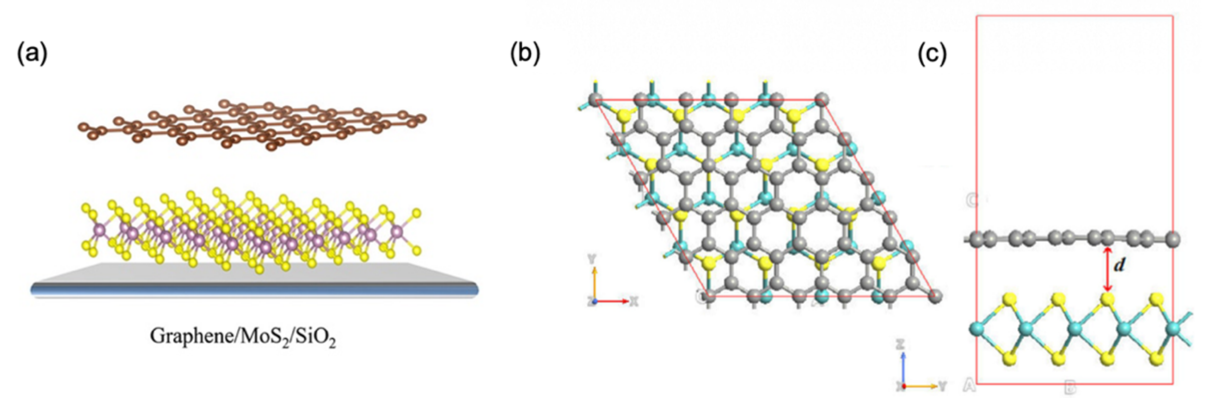

Figure 2.1.3.3-1. The atomic structure of the G/MoS_2 interface. The top and side views show the relaxed configuration with an interlayer distance d. The blue, violet, and yellow spheres represent Mo, S, and C atoms, respectively This structural motif is the foundation for all proximity effects. Adapted from (a) Zou et al., *J. Phys. Chem. Lett.* 13(23), 5123–5130 (2022) [26], with permission from the the American Chemical Society; (b–c) Phuc et al., *Surf. Sci.* 668, 23–28 (2018) [27], with permission from Elsevier.

The interlayer spacing d directly modulates the charge transfer σ and the interfacial field E_{int}:

$$\sigma(\mathrm{r}) \propto f_1(d(\mathrm{r}), \Delta\Phi(\mathrm{r})), E_{\text{int}}(\mathrm{r}) \approx \frac{\Delta V(\mathrm{r})}{d_{\text{eff}}(\mathrm{r})}, \text{(Equation 2.1.3.3-2)}$$

where $\Delta\Phi(\mathrm{r}) = \Phi_{\text{Gr}} - \Phi_{\text{MoS}_2} + \delta\Phi(\varepsilon)$ is the local work function difference, which can be modified by strain.

In graphene/MoS$_2$ van der Waals heterostructures, electronic coupling involves charge transfer and tunnelling, where at equilibrium, charge transfer occurs until the Fermi levels align: $\mu_{\text{Gr}} = \mu_{\text{MoS}_2}$ [26]. This process creates an interfacial dipole, a built-in potential step ΔV, and a Schottky barrier. The barrier heights for electrons and holes are defined as

$$\Phi_{B,n} = E_C - E_F, \Phi_{B,p} = E_F - E_V, \text{(Equation 2.1.3.3-3)}$$

For the equilibrium spacing $d_0 \approx 3.34$ Å, DFT calculations predict an n-type Schottky barrier of $\Phi_{B,n} \approx 0.49$ eV[26,27]. Compressing the interlayer distance can induce a transition from n-type to p-type Schottky contact. This electronic coupling underpins the doping of MoS$_2$ and the modification of its exciton/trion balance.

Excitonic coupling refers to energy transfer, where photoexcited excitons in MoS$_2$ can non-radiatively transfer energy to graphene via Förster-like processes, characterized by a rate k_{ET}. This process depends strongly on the interlayer distance and leads to photoluminescence (PL) quenching. Dielectric coupling, or screening, occurs as graphene modifies the dielectric environment of MoS$_2$, screening the Coulomb interaction and renormalizing the exciton binding energy. The effective dielectric constant ϵ_{eff} influences the radiative recombination rate:

$$k_r(\mathrm{r}) = k_{r,0} \cdot \frac{1}{\epsilon_{\text{eff}}^2(\mathrm{r})} \cdot F_{\text{osc}}(\mathrm{r}), \text{(Equation 2.1.3.3-4)}$$

Thus, the overall coupling is a multifaceted interplay of distance, strain, charge, field, and twist angle. Upon contact, Fermi level alignment drives a net charge transfer σ, forming an interfacial dipole. The built-in field E_{int} arises from the potential step ΔV across the interface. DFT studies show that the intrinsic band structures of graphene and MoS$_2$ are largely preserved in the heterostructure, but their relative alignment is shifted by charge redistribution (as shown in Figure 2.1.3.3-2). Changing the interlayer distance d tunes the amount of charge transfer and the Schottky barrier height while leaving the intrinsic band shapes largely intact [26,27]. This tunability is central to engineering the interfacial properties.

The central optical consequence of coupling is the modification of MoS_2's recombination dynamics. The local PL intensity $I_{\text{PL}}(\mathrm{r})$ is governed by the competition between radiative and non-radiative pathways:

$$I_{\text{PL}}(\mathrm{r}) = I_0 \cdot \frac{k_r(\mathrm{r})}{k_r(\mathrm{r})+k_{\text{nr}}(\mathrm{r})+k_{\text{CT}}(\mathrm{r})+k_{\text{ET}}(\mathrm{r})}, \text{ (Equation 2.1.3.3-5)}$$

where: k_r is the radiative recombination rate of MoS_2 excitons, k_{nr} is the intrinsic non-radiative rate in MoS_2, k_{CT} is the interlayer charge-transfer rate to graphene, and k_{ET} is the interlayer energy-transfer rate to graphene.

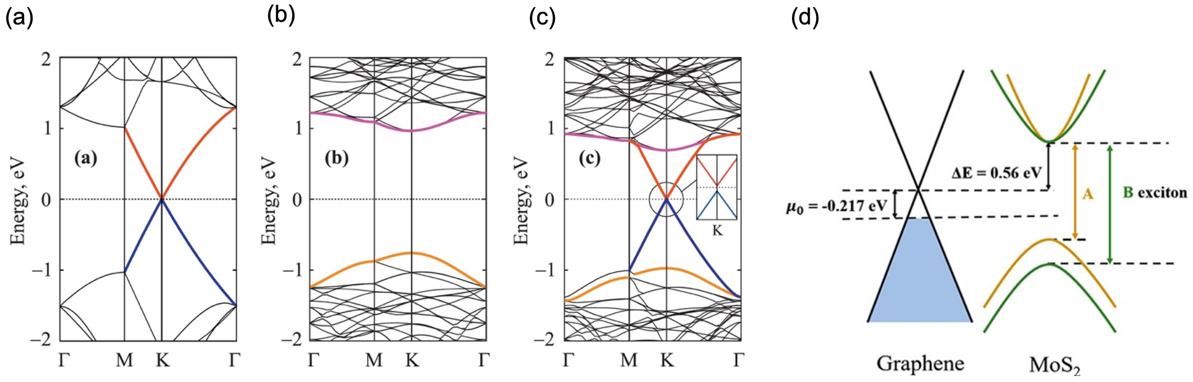

Figure 2.1.3.3-2 Presents the electronic structure evolution. Panel (a) shows the linear Dirac cone of freestanding graphene, (b) shows the direct bandgap of isolated MoS_2, and (c) shows the coupled Gr/MoS_2 heterostructure., where the Dirac cone of graphene appears within the bandgap of MoS_2. The bands are color-coded: blue/red for graphene's π/π^* bands, and purple/orange for MoS_2's CBM/VBM. Panel (d) provides a schematic band diagram, highlighting the band alignment, Fermi level E_F, and the Schottky barrier $\Phi_{B,n}$. Adapted from (a–c) Phuc et al., *Surface Science* 668, 23–28 (2018) [27], with permission from Elsevier; and (d) Zou et al., *J. Phys. Chem. Lett.* 13(23), 5123–5130 (2022) [26], with permission from the American Chemical Society.

Non-radiative quenching via charge transfer occurs as graphene provides a continuum of states accepting carriers from MoS_2. The charge-transfer rate depends on the interlayer tunnelling matrix element M_{CT} and the density of states in graphene $D_{\text{Gr}}(E_F)$:

$$k_{\text{CT}}(\mathrm{r}) \propto | M_{\text{CT}}(\theta, d) |^2 \cdot D_{\text{Gr}}(E_F), \text{ (Equation 2.1.3.3-6)}$$

Ultrafast studies shows that the charge-transfer time constant $\tau_{\mathrm{CT}} = 1/k_{\mathrm{CT}}$ is on the order of sub-ps to ps and depends strongly on the twist angle θ. Smaller twist angles lead to faster charge transfer due to increased momentum-space overlap. Exciton–trion rebalancing via interfacial doping results from equilibrium charge transfer $\sigma(\mathrm{r})$ doping the MoS_2 layer, shifting the local electron density $n_e(\mathrm{r})$. This can be probed optically by the trion-to-exciton intensity ratio:

$$R_{\mathrm{TX}}(\mathrm{r}) = \frac{I_T(\mathrm{r})}{I_X(\mathrm{r})} = A \cdot \frac{n_e(\mathrm{r})}{1+B\cdot n_e(\mathrm{r})}, \text{ (Equation 2.1.3.3-7)}$$

$$\text{where } n_e(\mathrm{r}) = \frac{\sigma(\mathrm{r})}{e} + n_0 \text{ , (Equation 2.1.3.3-8)}$$

This doping effect can locally enhance or suppress trion emission, creating spatial contrast in PL maps. Additionally, dielectric screening and interfacial states renormalize the exciton binding energy and radiative rate, while strong interfacial coupling can lead to the formation of interfacial excitons with distinct emission characteristics[26].

The parameters in $\mathrm{C}(\mathrm{r})$ are intrinsically heterogeneous due to trapped adsorbates, nanobubbles, wrinkles, and strain gradients from the transfer process. This causes spatial modulation of the rate coefficients k_{CT}, k_{ET}, and k_r. Consequently, the observable PL intensity, peak energy, and linewidth become functions of the local coupling variation:

$$I_{\mathrm{PL}}(\mathrm{r}), E_{\mathrm{peak}}(\mathrm{r}), \Gamma(\mathrm{r}) = \mathcal{F}[d(\mathrm{r}), \varepsilon(\mathrm{r}), \sigma(\mathrm{r}), \theta(\mathrm{r})], \text{ (Equation 2.1.3.3-9)}$$

This results in a stable, device-specific optical texture in PL maps. The texture is "frozen-in" by the irreversible interfacial morphology, making it repeatable for a given device but irreproducible across different fabrications. This provides the physical foundation for engineered entropy, where controlled assembly yields unique, spatially complex optical signatures. Collectively, key causes of spatial variation include: interlayer separation variations such as bubbles and residues, which exhibit a strong distance dependence of k_{CT} and k_{ET} [28]; local strain, which shifts band edges and modifies exciton energy; local electrostatics from trapped charges, which modulates doping and the trion/exciton ratio; and local twist angle / stacking registry, which modifies electronic overlap and charge transfer efficiency[29-31].

2.1.4 0D: Graphene Quantum Dots – Structure, Confinement, and Photoluminescence

Graphene quantum dots (GQDs) represent the zero-dimensional form of graphene-based nanomaterials, defined as nanoscale fragments of graphene with lateral dimensions below 10 nm and thicknesses of one to a few atomic layers. When confined to nanoscale dimensions, the extended, semi-metallic π-electron system of graphene undergoes quantum confinement, yielding a set of discrete electronic states, opening a finite, size-tuneable optical bandgap and enabling strong photoluminescence (PL). This section outlines the structure, electronic properties, and photoluminescence mechanisms of GQDs, providing the theoretical foundation for their application as optical emitters in physically unclonable functions (Section 2.2).

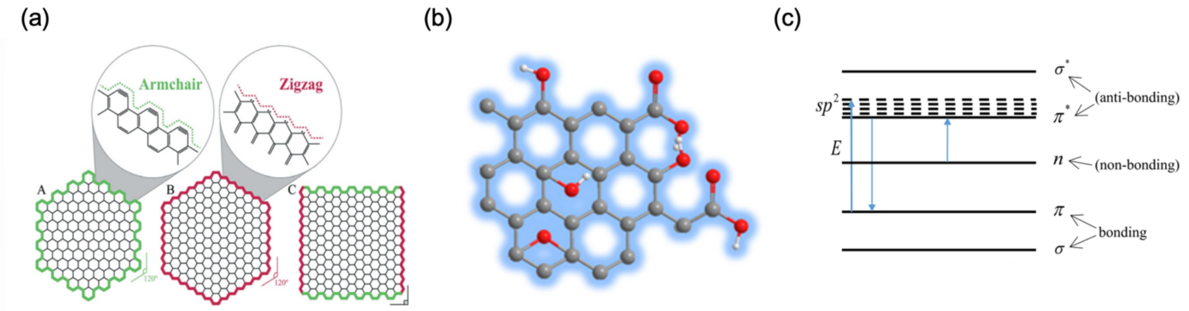

Figure 2.1.4-1. Structural and electronic schematic of graphene quantum dots (GQDs). (a) Representative GQD geometries highlighting the two crystallographic edge terminations—armchair and zigzag—and their influence on dot shape. (b) Example of an oxygen-functionalised GQD, illustrating edge chemical groups (red) that introduce localised electronic states. (c) Simplified molecular-orbital energy diagram showing bonding (σ, π), non-bonding (n), and antibonding (π*, σ*) levels associated with an sp^2 carbon framework, indicating optical transitions that contribute to GQD photoluminescence. (a) Adapted from Facure *et al.*, *Environ. Sci.: Nano* 7, 3710–3734 (2020) [32], with permission from the Royal Society of Chemistry (RSC). (b) Adapted from Suvarnaphaet and Pechprasarn, *Sensors* 17, 2161 (2017) [33], under CC BY 4.0 licence. (c) Adapted from Uran *et al.*, *AIP Advances* 7(3), (2017) [34], under CC BY 4.0 license.

The hybrid sp^2–sp^3 structure of GQDs comprises a crystalline sp^2-bonded graphene core, which sustains delocalized π-electron states, surrounded by edge and defect sites that introduce localized sp^3-like electronic states. The edge termination geometry—armchair or zigzag—strongly influences electronic and magnetic properties, and together with edge functionalisation determines the overall shape and chemical reactivity of the dot (Figure 2.1.4-1(a, b)). Delocalized π and π* orbitals in the sp²-hybridized graphene core enable intrinsic optical transitions and support charge transport, while edge and defect sites containing sp³-hybridized carbon, functional groups (e.g., C=O, C–OH, C–O–C), heteroatom dopants, and lattice vacancies break π-conjugation, localize carriers, and introduce additional electronic states within the bandgap[32,33]. This structural duality gives rise to an optical response comprising both intrinsic (core-related) and extrinsic (surface and edge related) emissive contributions.

GQDs exhibit complete three-dimensional confinement, which leads to a fully discrete density of states (DOS) as described in Section 2.1.2. The resulting quantized energy levels can be understood within the particle-in-a-box framework, where energy scales inversely with the square of the confinement length L:

$$E_n \propto \frac{1}{L^2}, \text{ (Equation 2.1.4-1)}$$

Here, L corresponds to the lateral size of the sp² domain in GQDs. This inverse-square relationship underlies the pronounced size dependence of the optical bandgap: smaller dots possess larger effective bandgaps, leading to blue-shifted photoluminescence, while larger dots display red-shifted emission due to reduced quantum confinement. Experimentally, the observed emission spectra are further broadened by the size distribution of sp² domains and the heterogeneous contribution of surface states.

The photoluminescence of GQDs is commonly described by two radiative pathways. Intrinsic (core) emission arises from π→π* transitions within quantum-confined sp² domains, where the transition energy increases as the domain size decreases following the confinement scaling of Eq. (2.1.4-1). Extrinsic (surface/edge) emission involves localized electronic states introduced by functional groups, dopants, or defects. For oxygen-containing surface groups, these often exhibit n→π transitions, where non-bonding (n) electrons associated with lone pairs (e.g., on C=O) are excited into the π system (Fig. 2.1.4-1(c)). In GQDs derived from spent tea—which are typically nitrogen-doped—both radiative pathways coexist, and their relative contributions depend on the degree of oxidation/reduction and the local chemical environment, such as pH, ionic strength, and solvent polarity[33,34]. This coexistence of emissive pathways gives rise to excitation-dependent photoluminescence, wherein different excitation wavelengths selectively populate distinct emissive states, and leads to sensitivity to solvent interactions and aggregation effects.

In summary, graphene quantum dots are the zero-dimensional form in the graphene material family, where quantum confinement and a high edge-to-area ratio produce discrete electronic states and a tuneable optical gap. Their photoluminescence emerges from a combination of size-dependent core transitions and surface-state-mediated recombination, resulting in concentration and excitation-dependent emission. The structural and chemical heterogeneity of GQD ensembles—variations in sp^2 domain size, edge termination, functional-group density, and inter-dot interactions—generates a broad distribution of emission. This intrinsic randomness enables the unique, irreproducible fluorescence “fingerprint” of each GQD deposition to be encoded into a secure binary identifier, as detailed in Section 2.2.

2.1.5 Dimensionality as a Design Framework

By combining GQDs (0D), vdWHs (2D), and HOPG (bulk), this thesis constructs a dimensionality-driven framework for understanding structure–function relationships across optical and electrochemical systems. The ability to tune emission randomness in GQDs, deterministic exciton dynamics in vdWHs, and interfacial reactions in graphite electrodes through structural control provides a unified strategy for device development in both security and energy domains. This foundation supports the following sections, which explore how these materials are applied in optical PUFs and lithium battery interfaces.

2.2 Optical Physical Unclonable Functions (PUFs)

As digital technologies advance, hardware security faces growing threats from counterfeiting, cloning, and unauthorized access. Conventional cryptographic techniques, while powerful, often rely on stored keys that can be intercepted or reverse engineered. Physical Unclonable Functions (PUFs) offer an alternative approach by exploiting the inherent randomness of physical systems to generate unique, irreproducible identifiers. These systems harness material-level disorder, fabrication imperfections, or quantum-level fluctuations to produce device-specific “fingerprints” without requiring embedded keys[35-37].

2.2.1 Fundamentals of Optical PUFs

PUF architectures are categorized by their entropy source and readout, encompassing electronic, coating, resistive, and optical variants (Table 2.2.1-1). While electronic PUF devices enable lightweight authentication without stored secrets, prominent designs are vulnerable to modelling attacks given sufficient challenge-response pairs. Similarly, material-based PUFs enhance entropy density via micro- or nano-scale disorder but must contend with stability issues such as aging and drift. In contrast, optical PUFs provide a distinct, non-contact, and high-throughput method to interrogate complex disorder, traditionally using laser speckle patterns and more recently via guided-mode mixing or other photonic mechanisms[38,39].

PUF architecture	Physical entropy source	Typical CRP mechanism	Readout modality	Example implementations
Delay-based electronic PUFs	delay variation in paths/oscillators	Apply challenge → compare delays/frequencies	Digital timing/logic	Silicon PUF / PRF; RO/arbiter-style PUF [40,41].
Memory-based PUFs	start-up states / cell mismatch	Power-up/read → derive response	Digital memory readout	FPGA intrinsic SRAM PUFs[42].
Coating / capacitive PUFs	dielectric particle distribution	Probe local capacitance pattern	Electrical sensing	Capacitive/coating PUF analysis [43].
Resistive PUFs	Stochastic filament formation / device variability	Bias/set-reset → conductance states	I–V / resistance	Memristive PUF primitive[44].
Optical scattering PUFs	Multiple scattering in disordered media	Illuminate (angle/wavelength) → speckle response	Camera / photodetector	Physical one-way functions / speckle PUFs[38].

Table 2.2.1-1. Comparison of representative PUF architectures and typical implementations.

Optical Physical Unclonable Functions (PUFs) generate unique challenge-response pairs (CRPs) by interrogating the inherent, irreproducible nanoscale disorder of a material through light–matter interactions such as scattering, fluorescence, or reflection. This disorder arises from structural irregularities that are physically unclonable—even with full knowledge of the fabrication process—and must remain stable over time and under varying environmental conditions [45]. A practical PUF must also demonstrate robustness against benign perturbations such as illumination variation or temperature drift and must offer scalability and a large CRP capacity to enable secure authentication and consistent key extraction.

The cryptographic strength of a PUF is determined by its secrecy capacity, which quantifies the maximum number of independent, unpredictable bits extractable from the physical system, govern by the entropy density and spatial correlations of the underlying disorder[40, 46]. Strong PUFs must possess an exceptionally large CRP space to enable many unique exchanges without key storage and must resist machine-learning modelling attacks, even when an adversary has access to a subset of CRPs[41,47].

The entropy sources in optical PUFs can be categorized as implicit or explicit [48]. Implicit randomness arises from uncontrollable fabrication variability, such as defects, thickness fluctuations, trapped adsorbates, or interfacial residues. Explicit randomness is introduced through designed processing steps or engineered degrees of freedom—such as controlled assembly parameters, stacking sequences, or excitation conditions—that amplify entropy or enhance optical contrast while preserving un-clonability. In practice, many platforms combine both: implicit disorder provides an irreproducible microscopic seed, while explicit design enhances usable entropy, improves readout robustness, and expands the challenge space[49].

This thesis investigates implicit and explicit entropy sources to enhance usable randomness in optical security systems. Two graphene-based material platforms are developed to increase challenge-response pair (CRP) capacity. The first platform leverages Graphene Quantum Dots (GQDs), which harness implicit randomness from their inherent nanoscale heterogeneity in size, edge structure, and surface chemistry. This is augmented by explicit randomness introduced through electrospray deposition, generating complex, spatially variable fluorescence patterns. These analogue patterns are then digitized into robust cryptographic keys using local binary pattern (LBP) feature extraction. The system's performance is rigorously evaluated through uniformity (bias) and Hamming distance metrics.

The second platform is based on graphene–MoS_2 van der Waals heterostructures, where optical entropy arises from stacking disorder and spatially non-uniform interfacial coupling. During transfer and alignment, the interface develops heterogeneous morphology—wrinkles, bubbles, residue pockets, and associated strain gradients—that becomes effectively fixed after assembly and modulates excitonic emission across the device. Spatial variations in twist angle and local interlayer separation further perturb charge transfer efficiency and dielectric screening, thereby reshaping the exciton–trion balance and recombination dynamics in MoS_2. The resulting photoluminescence (PL) distribution is spatially complex and reproducible for a given sample, providing a basis for optical identity encoding.

2.2.2 Graphene-Based Nanomaterials for Optical PUFs

This section outlines how the structural and electronic principles from Section 2.1 are leveraged for O-PUF operation. It focuses on the physical origin of optical entropy in each platform, the mechanism of challenge–response pair (CRP) generation, and how explicit design choices expand the usable entropy. The dimensionality-dependent properties of graphene-derived materials, detailed in Section 2.1, establish a powerful materials platform for optical physically unclonable functions (O-PUFs). Their optical response is intrinsically sensitive to nanoscale structure, disorder, and interfacial electrostatics, converting subtle physical variations into measurable optical signals. As dimensionality is reduced, the increasing surface-to-volume ratio and the transition from continuous to discrete electronic states amplify the optical impact of variations in size, edge structure, and local environment.

The photoluminescence (PL) of quantum dots (QDs) illustrates the variation of the optical response in 0D systems. Conventional semiconductor QDs (e.g., CdSe, InP, perovskites) exhibit size-tuneable optical gaps via quantum confinement. When monodisperse and well-passivated, their PL is dominated by band-edge excitonic recombination, resulting in largely excitation-independent emission where the peak position is fixed and only the intensity varies with excitation conditions [50,51]. In contrast, excitation-dependent PL is common in the presence of ensemble heterogeneity—from size/shape dispersion or multiple emissive channels like surface or defect states—a characteristic feature of carbon-based dots and graphene quantum dots (GQDs)[52,53].

For GQDs (~1–10 nm), this excitation dependence arises from the emission is an ensemble average over distinct sub-populations, which vary in sp^2-conjugated domain size, edge structure, and surface functional groups [52,54]. Mechanistically, shorter wavelength excitation preferentially activates higher-energy states (often linked to smaller sp^2 domains), while longer wavelengths selectively address lower-energy states (associated with larger domains or surface/edge sites). This leads to an apparent red shift and spectral broadening with increasing excitation wavelength, a behaviour frequently discussed in terms of selective excitation and “red edge” effects in carbon nanomaterials[52,53]. The local environment and inter-dot spacing further modulate PL by altering surface passivation and non-radiative pathways. At higher concentrations or reduced spacing, aggregation and π–π stacking can introduce lower-energy emissive channels and enhance reabsorption or energy transfer, often resulting in red-shifted, broadened, and sometimes quenched emission[52].

The optical entropy of GQDs derived from *spent tea* in this work stems from multiple sources of implicit randomness. The size distribution of lateral sp^2 domains (L) yields a broad, inhomogeneous emission spectrum, as dictated by the particle-in-a-box model ($E \propto 1/L^2$, Eq. 2.1.4-1). Variability in edge termination (armchair vs. zigzag) and the distribution of oxygen- or nitrogen-based functional groups (e.g., C=O, C–OH) introduce a diversity of localized electronic states, enabling multiple radiative pathways that include π–π^* transitions from the core and n–π^* transitions from surface groups (Figure 2.1.4-1(c)). Furthermore, deposition methods such as electrospray produce a non-uniform spatial distribution characterized by complex clustering and local density fluctuations. These fluctuations modulate the local photoluminescence via excitation coupling, thereby mapping the ensemble's intrinsic spectral heterogeneity onto a corresponding spatial distribution of photoluminescence intensity.

For O-PUF, this combination of structural and depositional entropy provides a stable, physical "fingerprint." An optical challenge, such as a specific excitation wavelength or power, selectively excites a sub-population of GQDs. The response is the resulting fluorescence image—a two-dimensional map where each pixel's intensity integrates the contribution from a local, unique ensemble of GQDs. To convert this analogue pattern into a robust digital key, feature extraction methods like Local Binary Patterns (LBP) are employed. This method derive stability by encoding contrasts in local intensity variation, which are inherently resistant to global illumination drift compared to absolute intensity values, thereby ensuring reliable key generation.

Graphene–MoS_2 van der Waals heterostructure represents a 2D platform where entropy arises from fabrication induced variation of interfacial coupling. The system uses excitons in monolayer MoS_2, which is then spatially modulated by uncontrollable nanoscale variations "locked in" during heterostructure assembly. The fundamental mechanism is the perturbation of MoS_2's excitonic photoluminescence by proximal graphene through several coupling channels:

- Charge Transfer: Fermi-level alignment induces interfacial doping, altering the local carrier density in MoS_2 and shifting the balance between neutral exciton (X) and charged trion (X^{-}) emission.
- Dielectric Screening: Graphene modifies the local dielectric environment, renormalizing exciton binding energies and radiative recombination rates.
- Non-Radiative Quenching: Graphene provides efficient pathways for energy and charge transfer, locally quenching the PL intensity.

The critical entropy source is the spatial heterogeneity of the coupling strength, governed by the parameter set $C(r) = \{d(r), \varepsilon(r), \sigma(r), \theta(r)\}$, which includes local interlayer spacing d, strain ε, charge transfer density σ, and twist angle θ. During dry-transfer assembly, nanoscale disorder—such as trapped adsorbates, wrinkles, and nanobubbles—creates a spatially varying map of these parameters. Consequently, each device exhibits a stable heterogeneous PL pattern, characterized by pixel-to-pixel variations in intensity, peak energy, and exciton/trion ratio. This platform enables a rich challenge space, where a challenge can be defined not only by spatial coordinates (r) but also by an external parameter: stacking order. Intentionally varying the sequence of layers (e.g., graphene-on-MoS_2 vs. MoS_2-on-graphene) alters the dielectric environment and interfacial interactions, thereby generating a suite of distinct optical responses from the same graphene-MoS_2 heterostructure. Thus, this positions vdWHs as a new class of “engineered entropy” platforms for secure optical encoding. In summary, the 0D and 2D platforms demonstrate complementary entropy-generation strategies rooted in their dimensionality. GQDs (0D) exploit intrinsic compositional and morphological randomness within an ensemble. The primary design lever is controlling the deposition process to maximize the density of independent stochastic features. Conversely, the Graphene–MoS_2 heterostructure (2D) exploits interfacial coupling that is spatially modulated by assembly disorder, stacking configuration and multi-parameter readout to extract maximal independent information from a single, structured interface.

2.2.3 Stability and Encoding Strategies

For an optical PUF to be practically viable, it must generate stable digital keys—binary responses that remain consistent across repeated measurements despite environmental fluctuations and measurement noise. Stability, which enables reliable enrolment and verification, is achieved through a combination of controlled protocols, noise-tolerant encoding, and robust feature extraction.

For Graphene Quantum Dots (GQDs), stability is addressed through optimized fluorescence imaging. The encoding workflow begins with image pre-processing to select a stable region of interest and normalize global intensity gradients. The core step applies a Reduced Modal Local Binary Pattern (RMLBP) algorithm. This method encodes local texture contrasts rather than absolute brightness, making the resulting binary fingerprint inherently robust to illumination drift and minor rotational misalignment—key requirements for maintaining consistency. The final bitstring is derived from thresholded, rotation-invariant local patterns.

For Graphene–MoS_2 heterostructures, stability is engineered via temperature and power-resilient spectral mapping protocols. The process starts with pixel-wise fitting of hyperspectral photoluminescence (PL) data to extract stable peak intensity features. Trusted-pixel selection is then applied to exclude regions with poor fit quality or low signal-to-noise, ensuring only reliable data contributes to the key. The emission intensity maps are adaptively binarized and interleaved. Finally, cryptographic hashing (e.g., SHA-256) is optionally applied to the concatenated bitstring, which expands entropy and strengthens resistance to modelling attacks. These tailored strategies—RMLBP for GQDs and multi-feature binarization for heterostructures—form the core of the O-PUF workflow: extract stable features, apply adaptive thresholding, and generate a compact cryptographic key.

The quality of the generated PUF keys is quantified using standard statistical metrics that assess cryptographic suitability. Bias (or Uniformity) measures the randomness and balance of the binary key, calculated as the average value of its bits:

$$\text{Bias} = \frac{1}{n}\sum_{i=1}^{n} b_i, \text{ (Equation 2.2.3-1)}$$

where b_i is the i-th bit (0 or 1) and n is the total bit length. An ideal value of 0.5 indicates an equal probability of '0's and '1's, maximizing per-bit entropy. A significant deviation signals a systematic skew, which reduces randomness and increases vulnerability to statistical attacks.

Hamming Distance (HD) is the principal metric for evaluating uniqueness (inter-device variation). The HD between two n-bit strings A and B is defined as:

$$\text{HD}(A, B) = \frac{1}{n}\sum_{i=1}^{n} | A_i - B_i |, \text{ (Equation 2.2.3-2)}$$

For uniqueness, the mean inter-HD is calculated between keys from different PUF tokens. An ideal value approaching 0.5 signifies that devices are statistically independent and maximally distinguishable.

The use of graphene-based nanomaterials for optical PUFs not only offers a scalable and sustainable platform but also highlights the role of material dimensionality in controlling optical disorder and encoding complexity. GQDs primarily leverage inherent stochasticity, whereas van der Waals heterostructures motivate an alternative route in which deterministic nanoscale design variables and interfacial coupling can expand the challenge–response space and support unclonable identities.

2.3 Interfacial Chemistry in Lithium-Ion Batterie

Rechargeable battery chemistries span from lead–acid and nickel–metal hydride (NiMH) to sodium-ion, lithium–sulfur, metal–air, and emerging all-solid-state systems. Among these, lithium-ion batteries (LIBs) are particularly compelling and are widely used in portable electronics, electric vehicles, and grid storage because of their high energy density, long cycle life, low self-discharge, and design flexibility[55]. The long-term performance and safety of LIBs are critically governed by the stability of the electrode–electrolyte interface, particularly on the anode side, where a large potential drop drives electrolyte reduction and the formation of a nanoscale passivation layer called the solid–electrolyte interphase (SEI) during initial charging cycles[56].

A well-formed SEI functions as a selective ionic conductor and electronic insulator. This dual role enables efficient Li^+ transport while passivating the electrode surface to suppress continuous electrolyte decomposition and undesirable side reactions[57]. By regulating ion transport and mitigating degradation, it preserves active lithium and electrolyte, maintains high charge–discharge efficiency, and ensures consistent energy delivery over extended cycling. Mechanically, a robust interphase prevents anode dissolution, mitigates structural degradation, and promotes uniform current distribution. Conversely, an unstable, porous, or excessively growing SEI consumes cyclable lithium and electrolyte, hinders ion transport, and increases internal resistance, ultimately leading to capacity fade, power loss, shortened battery lifetime, and heightened safety risks[58]. This section provides an overview of the mechanisms underlying SEI formation, the influence of anode surface structure, and the critical role of solvation structures—both in the bulk electrolyte and at the interface.

2.3.1 SEI Formation and Anode Surface Effects

The SEI is a passivating layer that forms when electrolyte components—typically solvent molecules and lithium salts—undergo reductive decomposition on the anode surface during the first few charging cycles. This interphase serves a dual purpose: it allows lithium-ion transport while blocking electrons, thereby preventing further electrolyte degradation. However, the chemical composition, morphology, and mechanical integrity of the SEI vary widely depending on the electrode material and electrolyte environment [59].

Highly Oriented Pyrolytic Graphite (HOPG) serves as a foundational model system for studying SEI formation, primarily due to its distinct and well-defined basal and edge planes, which exhibit vastly different interfacial reactivities[60]. The basal planes, characterized by a densely packed, low-defect structure and high chemical inertness, enable smooth lithium-ion intercalation with minimal volume change. This inherent low reactivity results in minimal SEI formation, typically yielding thin, organic-rich layers. Minimizing SEI growth on these planes is crucial to preserving cyclable lithium, as direct intercalation does not occur across them.

In contrast, the edge planes present a highly reactive surface due to lattice termination, which generates sp^3 sites, dangling bonds, and functional groups. These features serve as active sites for lithium-ion intercalation and induce strong electrolyte interactions, leading to preferential and substantial SEI formation [61]. The resulting interphase is thicker and more homogeneous, dominated by inorganic species such as LiF and lithium carbonates derived from salt reduction. For example, in a 1 M $LiPF_6$ EC: DMC electrolyte, the SEI on edge planes can be several nanometres thicker than on basal planes. This SEI often exhibits a multi-layer structure, with loosely packed organic and inorganic carbonates near the electrolyte interface transitioning to a denser inner layer of LiF, Li_2O, and Li_2CO_3 closer to the graphite surface[62]. The mechanical stress from lithium insertion at these rough edges can also induce local structural distortions, contributing to mechanical degradation over time[63].

Consequently, while the basal-plane SEI consists mainly of lithium carbonates with minor inorganic compounds, the edge-plane SEI is defined by its thickness, inorganic richness, and complex layered morphology. These structural and compositional differences directly impact overall interfacial stability, lithium intercalation kinetics, and the long-term cycling performance of graphite electrodes[64,65].

2.3.2 Bulk and Interfacial Solvation Structures

Beyond surface morphology of HOPG, the electrolyte’s bulk and interfacial solvation structures critically influence SEI chemistry. In the bulk electrolyte, lithium ions are solvated by a sheath of solvent molecules and occasionally anions, forming solvent-separated ion pairs (SSIPs), contact ion pairs (CIPs), or ion aggregates (AGGs)-

structural motifs defined by whether anions are absent from (SSIPs), directly contact (CIPs), or bridge between (AGGs) the solvated cations. The preferential solvation of Li^+ in the bulk solvation structures plays a crucial role in governing ion migration and de-solvation at the electrode-electrolyte interface. For instance, ethylene carbonate (EC) exhibits strong coordination with Li^+, which impedes de-solvation and increases interfacial resistance. In contrast, the dominant Li-ion-anion aggregation (AGG) structure in electrolytes containing solvents like 1,3-dioxolane (DOL) yields excellent ionic conductivity, low activation energy, and minimal charge transfer resistance by facilitating a hopping-assisted de-solvation process.

The bulk solvation structure of electrolytes governs not only transport properties but also mechanical (compressibility, viscosity), thermal (heat conductivity, capacity), chemical (solubility, reactivity), and interfacial electrochemical behaviour. For example, chemical compatibility between solvation sheath components and electrode materials determines SEI stability. Incompatible species can lead to excessive electrolyte decomposition and higher interfacial resistance, reducing battery lifespan. Furthermore, the size and stability of the solvation sheath impact lithium-ion intercalation: a bulky or overly stable sheath can hinder direct Li^+-electrode interactions, leading to an irregular and less compact SEI.

While the bulk solvation structure mainly governs transport, mechanical and thermal properties in the electrolyte, the interfacial solvation structure mediate supramolecular interactions—including metal coordination, van der Waals forces, and electrostatic effects—which dynamically influence charge transport, ion mobility, and interfacial capacitance. At the core of these processes lies the electric double layer (EDL), which formed when an applied potential induces excess charge on the electrode surface that is compensated by the accumulation of counter-ions and depletion of co-ions in the adjacent electrolyte, creating a region of charge separation that controls both capacitive behaviour and interfacial electron transfer[66].

The Stern model divides the EDL into two distinct regions (shown in Fig. 2.3.2-1): the Inner Stern Layer (or Inner Helmholtz Layer, IHL), where ions and solvent molecules are directly adsorbed onto the electrode surface, forming a tightly bound interfacial layer, and the Diffuse Layer, where mobile ions move freely due to thermal fluctuations, resulting in a charge density gradient that extends into the bulk electrolyte. The layered structure of the Electric Double Layer (EDL) governs all electrochemical reactions at the electrode-electrolyte interface, defining key properties such as charge-potential relationships, ion transport, and interfacial capacitance. A well-structured EDL not only facilitates efficient lithium-ion transport across the interface but also reduces interfacial resistance, thereby enhancing charge-discharge efficiency. Beyond its role in charge distribution, the EDL plays a crucial role in SEI formation, shaping its composition, structure, and mechanical stability. By regulating the initial reduction reactions of electrolyte components, the EDL controls charge transport and ion mobility, passivating the anode and preventing further electrolyte decomposition. Ultimately, the synergistic interplay between bulk solvation structures and EDL characteristics dictates lithium-ion transport efficiency, SEI stability, and overall battery performance.

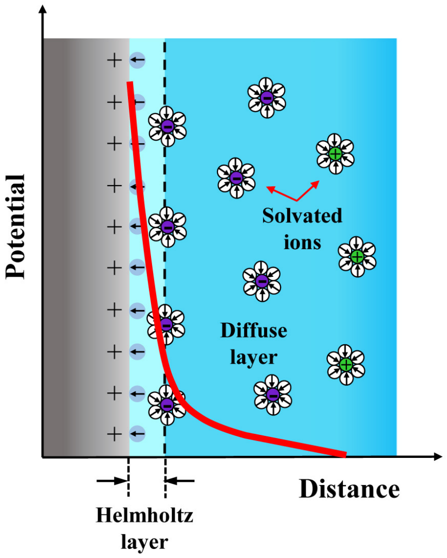

Figure 2.3.2-1. Electric double layer (EDL) structure at an electrified Pt (111)/water interface. Reproduced from Le et al., Current Opinion in Electrochemistry 27, 100693 (2021) [66], under the CC BY-NC 4.0 license.

Operando spectroscopic techniques, particularly Raman spectroscopy, have enabled the dynamic, real-time probing of solvation structures and SEI formation. The technique is based on inelastic light scattering, where incident photons interact with molecular vibrations, resulting in characteristic energy shifts of the scattered light that are exquisitely sensitive to the local chemical environment. This principle allows

Raman spectroscopy to provide molecular-level insights into lithium-ion intercalation pathways, solvation-shell evolution, and decomposition reactions at the graphite surface. Specifically, the coordination of Li^+ to the carbonyl oxygen of ethylene carbonate (EC) shifts the C=O stretching frequency, enabling the quantification of Li^+–EC solvation via the intensity ratio of coordinated-to-free solvent bands. Similarly, for FSI^--based salts, systematic shifts in the S–N–S bending and stretching vibrations allow direct discrimination between free anions, contact ion pairs (CIPs), and ion aggregates (AGGs). By deconvoluting these spectral bands—especially in ethereal solvents like 1,3-dioxolane (DX)—the relative populations of solvent-separated ion pairs (SSIPs), CIPs, and AGGs can be extracted, providing a spectroscopic basis for understanding and quantifying the solvation structures that govern SEI formation and stability.

2.3.3 Electrolyte Engineering and SEI Modulation

Electrolyte design plays a key role in tailoring both bulk and interfacial solvation environments. High-concentration electrolytes (HCEs) and localized high-concentration electrolytes (LHCEs) promote anion-driven SEI formation, enhancing interfacial stability through dense, inorganic-rich layers. Weakly solvating electrolytes (WSEs), such as DX-based systems, further support this approach by minimizing solvent decomposition and promoting Li–F-rich SEI chemistry. Ultimately, salt type and concentration directly modulate the Li^+ solvation environment by collectively governing ion pairing, dissociation behaviour, and solvation strength from the bulk electrolyte to the electrode interface[67].

Salt type alters the solvation environment by governing ion dissociation, which in turn dictates interfacial kinetics and deposition morphology: highly dissociative salts (e.g., $LiPF_6$, LiFSI) favor solvent-separated ion pairs (SSIPs) that enhance ionic mobility moderately dissociative salts (e.g., LiTFSI) promote contact ion pairs (CIPs), modifying viscosity and transport [68], and weakly dissociative salts (e.g., LiCl, $LiBF_4$) lead to ion aggregates (AGGs) that deplete free ions and hinder diffusion[69,70]. Beyond dissociation, anion coordination strength directly controls charge transfer, where weakly coordinating anions (e.g., PF_6^-) facilitate rapid de-solvation, while strongly coordinating ones (e.g., $TFSI^-$) increase de-solvation barriers and impedance.

Consequently, electrolytes with anions like FSI^- and $TFSI^-$ often enable uniform lithium deposition, whereas AGG-prone salts like $LiBF_4$ promote inhomogeneous ion transport and dendritic growth.

Salt concentration further reshapes the solvation structure and interfacial behaviour. In dilute systems, Li^+ coordination is dominated by ion-dipole interactions with approximately four solvent molecules, forming SSIPs where anions are largely excluded from the primary solvation sheath[71]. As concentration increases, the reduced free solvent availability disrupts the secondary solvation sheath and draws anions into the primary coordination sphere, increasing ion pairing and leading to a more compact electric double layer that alters lithium-ion mobility, charge transfer kinetics, and viscosity. In highly concentrated electrolytes (HCEs, ~3-6 M), extreme solvent scarcity forces anions into the primary sheath, forming CIPs and AGGs[72,73]. This restructuring, while potentially reducing bulk ionic conductivity introduces key interfacial advantages: it facilitates Li^+ de-solvation enhances oxidative/reductive stability [72,74], and promotes the formation of a robust, anion-derived SEI. This anion-rich interphase improves interfacial stability, suppresses dendrite formation, and supports high-rate, long-term cycling in graphite and lithium metal electrodes [72,75,76]. Thus, strategic manipulation of salt identity and concentration provides a direct pathway to tailor solvation structures, transport properties, and interfacial chemistry for advanced battery performance.

This thesis employs Raman spectroscopy to investigate how electrolyte composition, solvent environment (EC/DMC and DX), and salt concentration (0.1M–6M LiFSI) modulate solvation structure and SEI behavior on graphite electrodes. By combining operando techniques with surface-treated HOPG, the work aims to establish a molecular-level understanding of the coupled roles of dimensionality, solvation, and interfacial chemistry in guiding SEI formation.

Chapter 3 Fabrication and Characterisation

This chapter presents the synthesis, fabrication, and characterisation methodologies employed across the three material systems investigated in this thesis: graphene quantum dots (GQDs), graphene–MoS_2 van der Waals heterostructures (vdWHs), and highly oriented pyrolytic graphite (HOPG) electrodes. These systems were chosen to explore how material dimensionality — from zero-dimensional (0D) to two-dimensional (2D) structures — governs structure–function relationships. In particular, the study examines how dimensionality influences optical responses critical for optical physical unclonable functions (O-PUFs), as well as interfacial phenomena in lithium-ion batteries, including solid electrolyte interphase (SEI) formation and solvation-structure-driven electrolyte decomposition.

Section 3.1 details the fabrication of GQD-based optical PUF devices using biomass-derived carbon precursors. GQDs were synthesized from tea leaves and deposited via electrospray techniques to form randomly distributed optically active patterns on target silicon substrates. The section then describes the exfoliation, transfer, and deterministic stacking of graphene and MoS_2 monolayers for constructing vdWH devices. The section concludes with the preparation of HOPG substrates for operando electrochemical studies, including mechanical polishing and thermal annealing, and the formulation of two electrolyte systems—polar EC/DMC and non-polar DX—each with lithium salts ($LiPF_6$ or LiFSI) to probe solvation-dependent SEI formation.

Section 3.2 introduces the suite of characterisation tools used throughout this work. Optical microscopy was used to identify graphene and MoS_2 monolayers via contrast differences, while fluorescence imaging assessed the spatial distribution and brightness of GQDs, enabling visualisation of optical fingerprints central to PUF applications.

Spectroscopic methods formed the core of structural and optical analysis. Raman spectroscopy was used to evaluate GQD crystallinity, interlayer coupling in vdWHs, and SEI evolution on graphite during lithiation. Photoluminescence (PL) spectroscopy probed interlayer exciton behaviour in vdWHs, with temperature-dependent measurements from 10 K to 300 K revealing energy shifts and emission dynamics. UV–Vis's absorption spectroscopy provided insight into the optical bandgap and absorption features of GQDs, supporting synthesis optimisation and emission tuning. Finally, atomic force microscopy (AFM) offered nanoscale topographical characterisation of GQDs, capturing their lateral dimensions, height distribution, and surface uniformity. Together, these integrated fabrication and characterisation strategies form a comprehensive platform for uncovering the dimensionality-dependent optical and interfacial properties of graphene-based nanomaterials.

3.1 Fabrication of Graphene-Based Nanomaterials

This section describes the sample preparation procedures for the graphene-based nanomaterials investigated in this thesis, including graphene quantum dots (GQDs), graphene–MoS_2 heterostructures, and graphite electrodes for lithium-ion battery applications.

3.1.1 Fabrication of Graphene Quantum Dots Optical PUFs Devices

This section outlines the complete fabrication process of the GQD-based optical physical unclonable function (O-PUF) device, from GQDs synthesis to deposition on silicon substrate. Among reported synthesis of biomass-derived GQD—such as orange peel/juice, grape and banana juices, honey, durian, and cabbage[77-79]—spent oolong tea leaves were selected because they have been shown to yield GQDs with high quantum yield and robust optical properties[79,80]. During hydrothermal treatment, the lignocellulosic matrix and associated biomolecules undergo dehydration and aromatisation, forming nanoscale sp^2-carbon cores decorated with oxygen- and nitrogen-containing functional groups[81,82]. These functionalities promote water dispersibility and provide accessible surface sites without the need for strong oxidants or extensive post-synthetic modification. Critically, oolong tea is partially oxidized, containing both catechin-rich components (as in green tea) and oxidation/polymerization products (as in black tea), which provides a chemically diverse, oxygen-rich feedstock. In parallel, the oolong tea leaves supply nitrogen-bearing biomolecules such as amino acids and proteins, facilitating nitrogen doping during synthesis.

The process begins with the hydrothermal synthesis of GQDs derived from spent tea leaves, selected as an abundant and sustainable carbon precursor. After purification and redispersion, the GQDs were deposited onto silicon substrates by simple drop casting or electrospray deposition using a custom-built electrospray ionisation (ESI) system, yielding nanoscale deposits after drying as confirmed by AFM (see Section 4.2.2). The resulting GQD samples were then imaged by fluorescence microscopy and converted into binary maps for key generation and PUF analysis.

3.1.1.1 Hydrothermal Synthesis of GQDs from Spent Tea Leaves

Graphene quantum dots (GQDs) were synthesised via hydrothermal carbonisation using spent oolong tea leaves as biomass precursor. The tea leaves were sourced from Solaris Botanicals Ltd. (via Amazon), and all aqueous solutions were prepared using distilled deionised (DDI) water with a resistivity greater than 18 MΩ·cm, obtained from a Millipore Milli-Q-RO4 system. Dialysis membranes with a molecular weight cut-off (MWCO) of 500–1000 Da were supplied by Carl Roth & Co.

Figure 3.1.1.1-1. Schematic workflow for green synthesis of Graphene quantum dots (GQDs) from spent tea bags. The tea precursor was ground to a fine powder, dispersed in deionised water to form a uniform solution, and transferred to a hydrothermal reactor. The resulting GQD dispersion was purified by centrifugation and dialysis. Photographs show the GQD solution under ambient illumination and under 450 nm excitation, demonstrating green photoluminescence.

In the hydrothermal synthesis procedure (Figure 3.1.1.1-1), spent tea leaves were thoroughly rinsed, oven-dried at 80 °C for 12 hours, and ground to a particle size below 90 µm. A 0.2 g portion of the dried powder was dispersed in 10 mL of DDI water and ultrasonicated at 40 °C for 20 minutes to promote homogeneous dispersion. The resulting mixture was transferred into a 45 mL Teflon-lined stainless-steel autoclave and heated at 220 °C for 3 hours. After naturally cooling to room temperature, the reaction product was centrifuged at 4000 rpm for 20 minutes to remove large carbonaceous residues. The supernatant containing the GQDs was then purified via dialysis using a 500–1000 Da MWCO membrane for 48 hours under continuous magnetic stirring. Following purification, the GQD solution was dried in a vacuum oven at 80 °C. The dried GQDs were subsequently redispersed in DDI water at varying concentrations to investigate how dispersion concentration affected their photoluminescence properties.

3.1.1.2 Deposition of GQDs on Silicon substrate

In this section, the deposition of graphene quantum dots (GQDs) onto silicon substrates is described using both drop casting and electrospray ionisation (ESI). Drop casting was initially explored because it is simple and rapid; however, film formation is often dominated by the coffee-ring effect, which leads to edge accumulation and non-uniform coverage across large areas. While such drying-induced inhomogeneity can introduce randomness, the resulting patterns are difficult to tune and are poorly reproducible from sample to sample, which can compromise within-device uniformity and long-term readout stability. By contrast, ESI enables deposition over larger areas or multiple samples in a scalable manner with improved control over areal coverage and thickness, while still producing spatially random photoluminescent micro-patterns suitable for optical physical unclonable function (O-PUF) operation.

To deposit GQDs by drop casting, the purified GQD dispersion was diluted with deionised water to a working concentration of 1.0 mg mL^{-1} and briefly sonicated to ensure a homogeneous suspension. Si/SiO_2 wafers (Si with a thermally grown SiO_2 overlayer) were cleaned sequentially in acetone and isopropyl alcohol (IPA) to remove organic contaminants and surface residues (Figure 3.1.1.2-1). Each wafer was immersed in acetone and sonicated for 5 min, followed by sonication in IPA for 5 min.

The chips were then rinsed with deionised water and dried under a nitrogen stream. Finally, oxygen plasma treatment was applied for 2 min to enhance surface cleanliness and hydrophilicity prior to deposition.

The cleaned wafer was placed on a hot plate at 60 °C to accelerate evaporation of the aqueous solvent during deposition. Droplets of GQD solution (≈10 µL) were dispensed sequentially across the surface using a micropipette, allowing each droplet to dry completely before subsequent droplets were applied. After drying, each droplet formed a visible circular coffee-ring deposit on the Si/SiO_2 surface. To mitigate coffee-ring–induced edge accumulation and improve areal coverage, subsequent droplets were placed with a small lateral offset such that their coffee-ring patterns partially overlapped, helping to fill the central low-coverage regions of preceding deposits. In total, approximately 0.5 mL of GQD solution (≈50 droplets) was deposited per wafer. After deposition, each wafer was cooled down to room temperature before further characterisation.

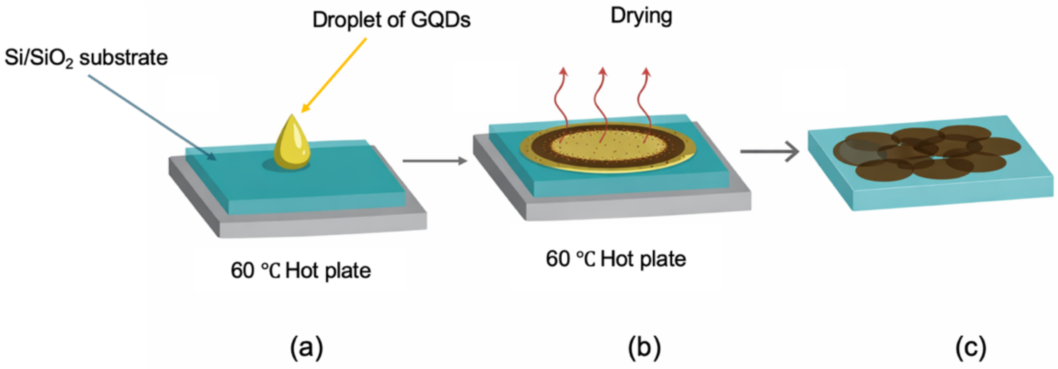

Figure 3.1.1.2-1. Schematic illustration of the drop-casting process for depositing graphene quantum dots (GQDs) on a Si/SiO_2 substrate. (a) Drop deposition: a droplet of GQD dispersion is placed on the Si/SiO_2 surface supported on a 60 °C hot plate. (b) Drying and coffee-ring formation: solvent evaporation under mild heating leads to a characteristic coffee-ring deposit with edge-enriched GQD accumulation. (c) Offset droplet coverage (partial overlap): sequential, slightly offset droplet placement produces partially overlapping deposits, improving areal coverage while retaining a spatially random distribution of GQD clusters.

The second deposition method employed was electro spraying (Figure 3.1.1.2-2). In this process, graphene quantum dots were dispersed in a diluted ethanol-based solution and deposited onto the substrate using a custom-built electrospray ionisation

(ESI) setup. A 30-gauge needle was used to atomise the solution into fine droplets. The ESI system was powered by a high-voltage DC generator (0.1–5 kV), which applied potential between the needle tip and a grounded copper plate positioned beneath a thin water layer. This configuration produced micron-sized aerosol droplets that were significantly smaller and more uniform than those generated by conventional syringe-based deposition [83,84].

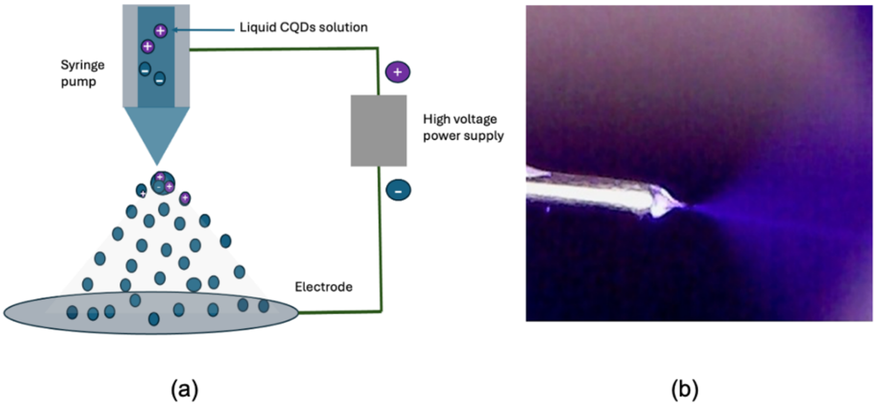

Figure 3.1.1.2-2. Electrospray ionisation (ESI) setup and spray regime used for depositing graphene quantum dots (GQDs) onto Si/SiO_2 substrates. (a) Schematic of the electrospraying mechanism: a high voltage applied between the syringe needle and the grounded collector induces charge accumulation at the liquid meniscus, forming a Taylor cone and emitting a fine jet of charged microdroplets. As the droplets travel toward the substrate, solvent evaporation and Coulombic repulsion disperse the droplets into a stable aerosol, enabling deposition of a thin GQD coating over the collector surface. (b) Representative ESI spray image for an ethanol-based GQD dispersion captured using a USB endoscope, showing the stable single-jet (cone–jet) mode obtained at an applied potential in the range of 2.5–3.0 kV between the needle and copper plate.

The working principle of electrospray deposition (Figure 3.1.1.2-2(a)) relies on the balance between electrostatic and surface tension forces on the liquid meniscus at the needle tip. When a high voltage is applied between the positively charged needle and the grounded electrode, charge accumulation at the liquid surface induces electrostatic stress that overcomes surface tension, forming a conical meniscus known as a Taylor cone. From the apex of this cone, a fine jet of charged droplets is emitted and subsequently breaks into smaller aerosol droplets through Coulombic repulsion. As these charged droplets travel toward the grounded electrode, solvent evaporation progressively reduces their size while maintaining surface charge density. The combined effects of evaporation, charge redistribution, and Coulomb fission (droplet splitting due to charge overaccumulation) result in uniform submicron droplets. Upon reaching the substrate, these droplets spread and coalesce to form a thin, randomly distributed GQD film.

A syringe pump maintained a constant flow rate of the GQD solution to ensure stable jet formation, while the applied voltage controlled the spray mode. At an optimal voltage (typically 2.5–3.0 kV), a steady single-jet or cone-jet mode was achieved, characterised by minimal oscillation and uniform deposition. Excessive voltage led to multi-jet or pulsating modes, resulting in droplet instability and aggregation. The liquid's conductivity, viscosity, and surface tension, along with the working distance and solvent polarity, collectively influenced spray stability and the final film morphology. This controlled electro spraying mechanism enabled precise tuning of droplet size and deposition density, allowing the creation of homogeneous, optically active GQD layers essential for reproducible O-PUF device fabrication.

The ESI apparatus comprised a 5 mL plastic syringe (HSW Norm-Ject) equipped with a 30-gauge precision needle (Adhesive Dispensing Ltd.). To ensure electrical continuity, a silver electroconductive coating connected the syringe body to the needle, providing electrical contact through a metal screw mounted inside the syringe holder. A 5 × 5 cm^2 copper plate was grounded and positioned under a shallow water layer to prevent direct contact with the substrate boundaries and to minimise electrical noise. This configuration ensured stable spraying with reduced large-droplet formation.

A critical parameter for achieving uniform deposition was the spreading coefficient, which governs droplet behaviour on the water surface. A positive coefficient promotes spreading, whereas a negative one favours aggregation. By tuning the needle gauge and solution polarity (through concentration or solvent composition), the spray characteristics were optimised: a finer gauge produced smaller initial droplets, while a more polar solution enhanced charge distribution and droplet breakup under the electric field—both contributing to a stable and uniform aerosol.

As shown in Figure 3.1.1.2-2 (b), applying 2.5–3.0 kV produced a stable, narrow spray that widened into a cone at greater distances. Higher voltages introduced instability, causing spray oscillations. The aerosol plume was monitored in real time using an endoscope under UV illumination. Under optimal conditions, depositing 0.5 mL of GQD solution required approximately 30 minutes and produced a uniform thin film. Although minor aggregation remained, the electrospray method significantly improved film homogeneity compared with drop-casting, making it the preferred approach for O-PUF device fabrication.

3.1.2 Graphene-MoS_2 Van der Waal Heterostructure OPUF Device Fabrication

This section outlines the step-by-step fabrication protocol for constructing Graphene–MoS_2 van der Waals heterostructures (vdWHs), which form the foundational platform for investigating interlayer exciton dynamics and optical PUF behaviour. The fabrication process (See Figure 3.1.2-1) begins with the mechanical exfoliation of high-quality graphene and MoS_2 crystals to isolate monolayer flakes. These exfoliated layers are initially deposited onto a polydimethylsiloxane (PDMS) stamp, which allows for flexible manipulation and visual identification under optical microscopy.

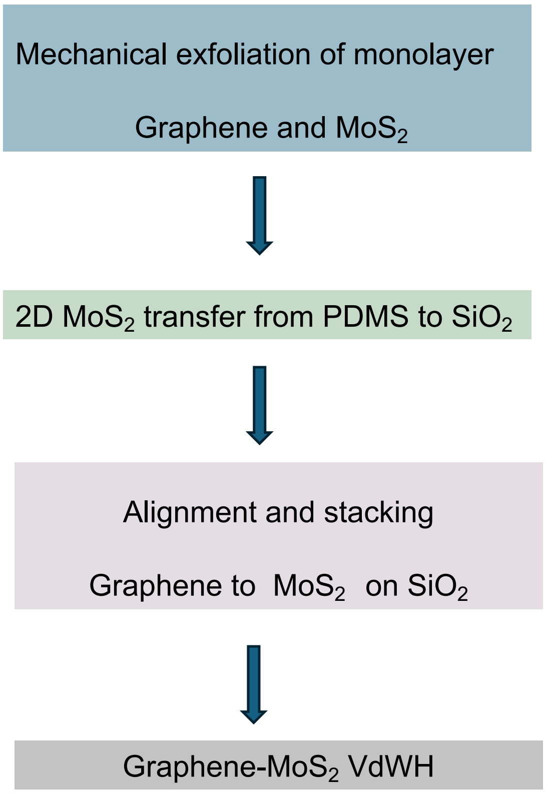

Figure 3.1.2 -1 Workflow for the Fabrication of Graphene–MoS_2 van der Waals Heterostructures (vdWHs)

The selected flakes are then transferred from the PDMS onto a clean Si/SiO_2 substrate using a dry transfer technique that combines precise mechanical alignment, optical verification, pressure control, and controlled heating. Finally, the stacked heterostructure is formed by carefully aligning a second 2D material—typically graphene—on top of the pre-transferred MoS_2 layer, followed by annealing to enhance interfacial contact and reduce trapped residues or air pockets. Each step in this fabrication sequence is designed to ensure high fidelity in layer positioning, clean interfaces, and minimal damage to the delicate monolayers. The assembled vdWHs are subsequently characterised by Raman and photoluminescence spectroscopy to confirm their quality and structural integrity.

3.1.2.1 Mechanical Exfoliation of 2D Materials

To fabricate graphene–MoS_2 van der Waals heterostructures (vdWHs), high-purity graphite and MoS_2 crystals were sourced from HQ Graphene. A polydimethylsiloxane (PDMS) stamp (Gel-Film PF-40-X4, Gel-Pak) and blue tape (BT-150E-KL) were used to mechanically exfoliate thin flakes from the bulk crystals.

The exfoliation process relies on the contrast between strong intralayer and weak interlayer forces in van der Waals materials. Graphene and MoS_2 flakes were isolated using Nitto tape, selected for its low adhesion to reduce organic contamination. The process began by cleaning a glass substrate with isopropyl alcohol (IPA). A Gel-Pak film was then trimmed to size, and its protective layer was removed to expose the PDMS surface (Figure 3.1.2.1-1(a-c)). The PDMS stamp was mounted onto the glass substrate while avoiding air bubbles, and only the edges were handled to minimise contamination.

The exfoliation step was performed by bringing Nitto (blue) tape pre-coated with the bulk 2D crystal into conformal contact with the PDMS stamp (Figure 3.1.2.1-1d–e), applying uniform pressure across the contact area. After 10–15 minutes to allow conformal contact and interfacial adhesion to stabilise, the tape was removed in a single rapid motion while one edge of the PDMS/glass support was held with tweezers to prevent stamp lift-off.

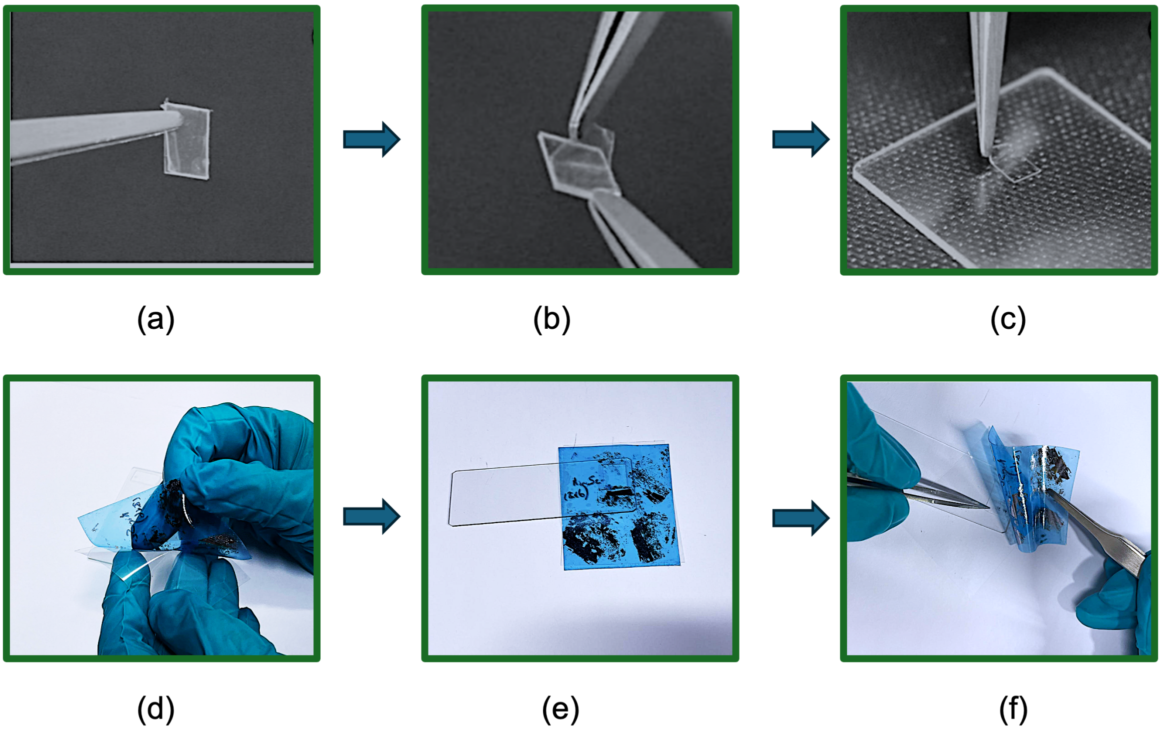

Figure 3.1.2.1-1. Mechanical exfoliation workflow for graphene and MoS_2. (a) Gel-Pak film trimmed to size. (b) Protective layer removed to expose the PDMS surface. (c) PDMS stamp mounted onto a clean glass slide, avoiding air bubbles. (d) 2D material crystal prepared on Nitto tape. (e) Tape pressed onto the PDMS surface to transfer and thin flakes. (f) Tape rapidly peeled back (≈60–90°) while the PDMS/glass is held in place, leaving exfoliated flakes on PDMS for subsequent transfer/inspection. Panels (a–c) are reproduced with permission from the Royal Society of Chemistry from Wang et al., Nanoscale 7, 877–884 (2015) [85].

The tape was peeled back at a 60–90° angle to promote efficient layer separation (Figure 3.1.2.1-1(f)). This rapid-peel step is critical because the peel rate governs the interfacial stress at the peel front. Previous research shows that increasing peel speed introduces a kinetic stress contribution ($\propto v^2$) to the static adhesion term, increasing the effective mechanical driving force for crack propagation and favouring detachment of thinner layers rather than bulk removal [86]. Fast removal also minimises adhesive relaxation and interlayer sliding that can occur during slow peeling, which would otherwise promote re-adhesion of thicker regions and reduce the probability of ultrathin flake formation[87]. The peel angle further tunes the shear-to-normal stress ratio at the interface, with larger angles (~60–90°) enhancing lateral shear and interlayer slip, thereby the yield of mono- and few-layer flakes [88]. Under these conditions, rapid peeling at ~60–90° generates a sharp shear front and fracture edge within the crystal, leaving flakes of varying thickness—often including monolayers—on the PDMS surface. This controlled rapid-peel step therefore significantly improves the probability of obtaining large-area, high-quality thin flakes on the PDMS surface. As a result, flakes of various thicknesses, including monolayers, were left behind on the PDMS and subsequently identified by optical microscopy.

Flakes were identified and characterised by optical microscopy and Raman spectroscopy. Under optical microscopy, potential monolayer regions were first distinguished by their characteristic semi-transparent colour contrast on PDMS—graphene appeared as a faint, transparent grey, whereas monolayer MoS_2 exhibited a slightly transparent dark blue (see details in Chapter 3.2.1). Raman spectroscopy was subsequently used to confirm flake thickness and crystalline quality. For graphene, monolayer regions were primarily from the characteristic single, symmetric 2D band shape, with a high intensity ratio (typically $I_{2D}/I_G > 2$ for lightly doped by silicon substrate) used as supporting evidence. While for MoS_2, monolayer was assigning from the frequency separation between the in-plane E_{2g} and out-of-plane A_{1g} modes ($\Delta \approx 19–20$ cm^{-1}) taken as indicative of monolayer MoS_2. The detailed optical and spectroscopic procedures are described in Sections 3.2.1 and 3.2.4. All steps were conducted under clean conditions to ensure reproducibility and flake quality.

3.1.2.2 Monolayer MoS_2 and Graphene transfer from PDMS to Silicon Substrate

The transfer of exfoliated 2D MoS_2 from PDMS to a Si/SiO_2 substrate requires a meticulously clean environment and precise mechanical alignment. Substrate cleaning began with sequential ultrasonic baths—first in acetone, then in isopropyl alcohol (IPA)—each lasting 5 minutes. After nitrogen drying, the substrate was treated with oxygen plasma to remove organic residues and render the surface hydrophilic.

The transfer system consisted of a custom-built stage equipped with a vacuum chuck, closed-loop heating element, pressure sensor and three-axis micromanipulators. The PDMS-containing glass slide was mounted inverted onto a slide holder, and the silicon substrate was fixed on the substrate holder by vacuum chuck and viewed through the optical microscope. As shown in the schematics diagram of PDMS dry transfer method in Figure 3.1.2.2-1 (steps 3–4), alignment began by centring a corner of the Si/SiO_2 substrate in the microscope's field of view—a position near the substrate edge closest to the stamp holder chosen to minimize the initial area of contact. The microscope focus was then shifted to the PDMS stamp surface to locate the flake intended for transfer. The substrate position was subsequently adjusted to align the target flake. Following alignment, the stamp was lowered toward the substrate using a z-axis controller, with the approach speed reduced as the stamp neared the surface. Continuous optical monitoring was maintained while lowering the stamp until it was close to contact. At this stage, the approach speed was further decreased to prevent unintended contact between the flake and the substrate. The stamp was then lowered incrementally until a portion of the PDMS made initial contact with the substrate.

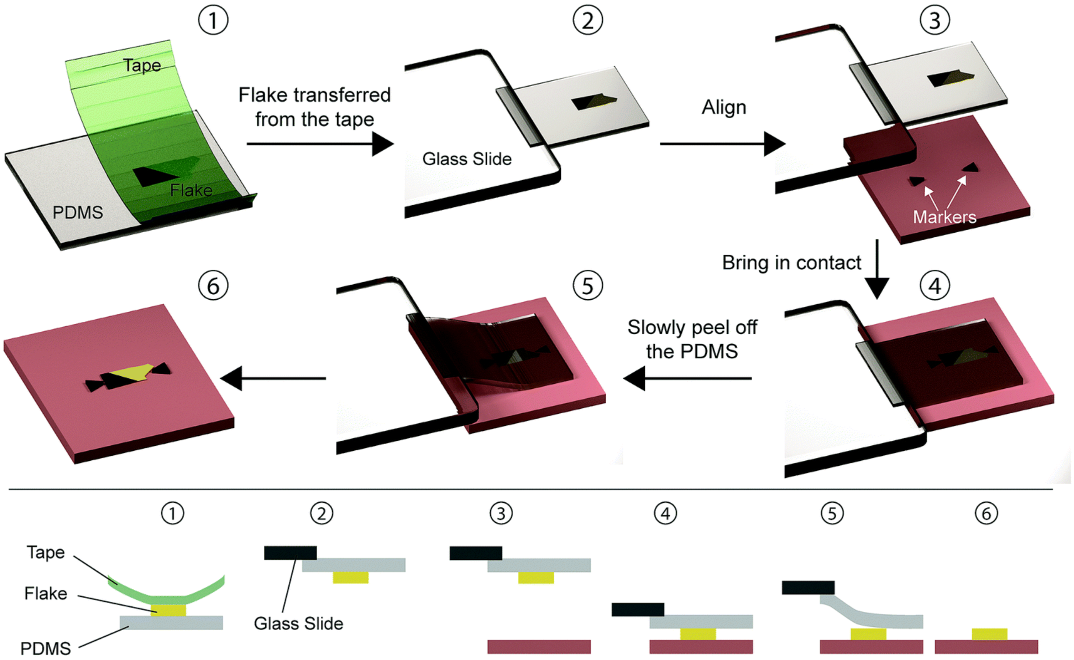

Figure 3.1.2.2-1. Schematics of the PDMS dry transfer method. The flake to be transferred is exfoliated onto a PDMS stamp (1) and the stamp is then attached to a glass slide connected to a micromanipulator (2). Using a microscope the flake can be aligned with the final substrate (3) and brought in contact (4). By slowly peeling of the PDMS stamp (5) the flake can be deposited on the substrate (6). Reproduced with permission from the Royal Society of Chemistry from Frisenda et al., Chemical Society Reviews 47, 53–68 (2018) [89].

The moment of PDMS stamp–substrate contact was identified optically by monitoring changes in colour/contrast and the evolution of interference fringes at the interface. Prior to contact, a thin interfacial gap generated bright fringe patterns (Newton's rings) due to optical interference. Upon initial adhesion, Newton's rings locally disappeared as a darker region spread laterally from the first point of contact, indicating conformal stamp–substrate contact (Figure 3.1.2.2-2). The progression of this dark front confirms that intimate, conformal contact has been achieved across the target region—a critical step in deterministic transfer prior to heating and release [90,91].

When the PDMS made contact across the flake, bonding was aided by heating the substrate to 65 °C for approximately 2 minutes. Adhesion time varied from 10 to 60 minutes depending on flake size and substrate condition. After cooling, the stage was slowly lowered to peel back the PDMS. The peeling speed was carefully controlled—slow enough to avoid delamination, but efficient enough to prevent bubble formation. A successful transfer was indicated by the flake disappearing from the PDMS and appearing on the substrate.

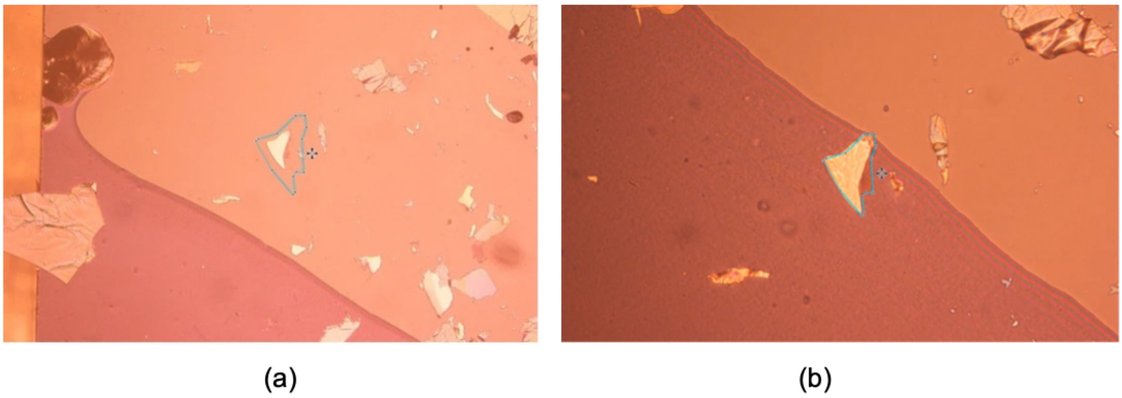
(a) (b)

Figure 3.1.2.2-2. Optical observation of PDMS stamp–SiO_2/Si substrate contact during viscoelastic transfer. Optical micrographs acquired during approach of a PDMS stamp onto the SiO_2/Si substrate. The darker region corresponds to conformal stamp–substrate contact, while the brighter region corresponds to the non-contact area, where a thin interfacial gap remains between the PDMS and the substrate. (a) Initial contact formed before the advancing dark contact front reaches the target flake (highlighted by a blue outline); (b) Increased contact area such that the region around the target flake is fully within the contact zone. Image remains the copyright of Ossila. Taken with permission from Ossila.

Post-transfer inspection was first performed under optical microscopy to verify flake position, continuity, and edge integrity. Visual confirmation of a successful transfer was indicated by the disappearance of the flake from the PDMS and its presence on the Si/SiO_2 substrate without visible tears or residues. Raman and photoluminescence

(PL) spectroscopy were subsequently employed to assess structural quality and determine layer number. Raman analysis focused on the E_2g^1 and A_1g vibrational modes of MoS_2 and the G and 2D bands of graphene, where peak positions, widths, and intensity ratios served as indicators of monolayer character and strain. Complementary PL spectra were used to confirm monolayer MoS_2 through its characteristic direct-gap emission around 1.85 eV and to identify interlayer excitonic features in stacked heterostructures. Detailed measurement procedures are described in Sections 3.2.1 and 3.2.2.

3.1.2.3 Assembly of Graphene–MoS_2 Van der Waals Heterostructures

Following the successful transfer of MoS_2 onto a silicon substrate, the next step involved stacking and aligning a graphene monolayer atop the MoS_2 to construct the heterostructure (Figure 3.1.2.3-1). Using a high-resolution optical microscope (typically 10× or 100× objective), the region of interest on the MoS_2 was identified and centred within the field of view. The substrate stage was then adjusted to ensure optimal overlap with the graphene flake on the PDMS stamp.

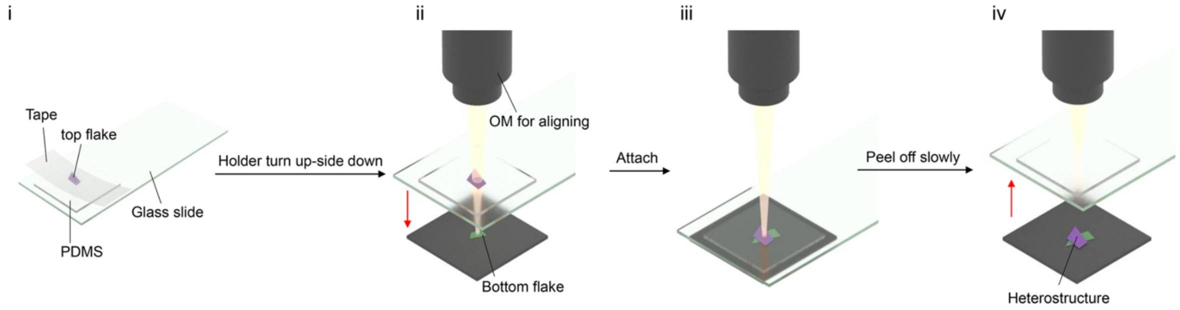

Figure 3.1.2.3-1. Schematic illustration of van der Waals heterostructure assembly using a PDMS-based dry transfer method. (i) The top-layer flake is mechanically exfoliated onto a PDMS stamp mounted on a glass slide. (ii) The stamp holder is inverted and mounted on the transfer station; the top flake is aligned to a target bottom flake pre-prepared on a 300 nm SiO_2/Si substrate under an optical microscope. (iii) The PDMS stamp is lowered to bring the flakes into contact. (iv) The stamp is slowly retracted, releasing the top flake onto the substrate and forming the stacked heterostructure. Reproduced with permission from IOP Publishing from Fan et al., 2D Materials 7, 022005 (2020) [92].

Precise manipulation was achieved using a micro-manipulator system capable of nanometre-scale resolution and angular adjustments up to 30°. The graphene/PDMS stamp was gradually lowered until its edge made initial contact with the edge of the Si/SiO_2 substrate; the motion was paused to prevent unintended flake pickup. Next, the stamp was slightly retracted and realigned so that the targeted monolayer MoS_2 flake was precisely centred beneath the graphene. Following confirmation of this alignment, the PDMS stamp was gently lowered further until the contact front covered the MoS_2 region.

Upon achieving full contact, the interface was heated to 65 °C and maintained for approximately 10 minutes to initiate van der Waals bonding. Mild heating softens the viscoelastic PDMS and increases the mobility of interfacial adsorbates, enabling conformal adhesion between the graphene and MoS_2 layers while displacing trapped air and moisture. This temperature is sufficient to promote uniform bonding without inducing thermal strain or damage to the monolayers[90,93]. The sample was subsequently allowed to cool naturally for ~30 minutes. During this phase, the stage was carefully lowered in a controlled manner while observing the interface under the microscope. Upward adjustments were applied as needed to slow the retreat of the PDMS and minimise the risk of delamination or bubble formation.

Once the PDMS had cleared the area of the graphene flake, the remainder of the detachment was carried out more swiftly, though still under controlled conditions. Automated stage control software was used to fine-tune the vertical movement and ensure stable peeling without abrupt mechanical disturbance.

To further enhance interfacial contact and eliminate trapped bubbles, the stacked heterostructure was subjected to vacuum annealing at 200 °C for 3 hours. This post-transfer treatment was critical to improving the overall uniformity and mechanical stability of the interface[94]. The success of the stacking process was confirmed through post-transfer optical imaging, Raman spectroscopy, and photoluminescence (PL) measurements (see Sections 3.2.1–3.2.4), which validated both the presence and quality of interlayer coupling in the assembled Graphene–MoS_2 van der Waals heterostructure.

3.1.3 Graphite Electrode and Solvent-Electrolyte Systems Preparation

In this section, sample preparation for Raman spectroscopic analysis is presented with detailed protocols that are critical for understanding the solid-electrolyte interphase (SEI) formation in battery systems. Preparation encompassed crafting of Highly Ordered Pyrolytic Graphite (HOPG) electrodes, assembly of these electrodes within an electrochemical cell (EL-CELL), and the precise formulation of various electrolyte solutions. Each procedure was optimised to create a laboratory setting that mirrors the internal conditions of lithium-ion batteries during operation. This alignment was essential to gather data that accurately represents SEI development and properties, contributing to a deeper insight into the electrochemical behaviours. HOPG/electrolyte/EL-CELL preparation was performed by Yue Chen; Raman measurements and analysis were performed by the author.

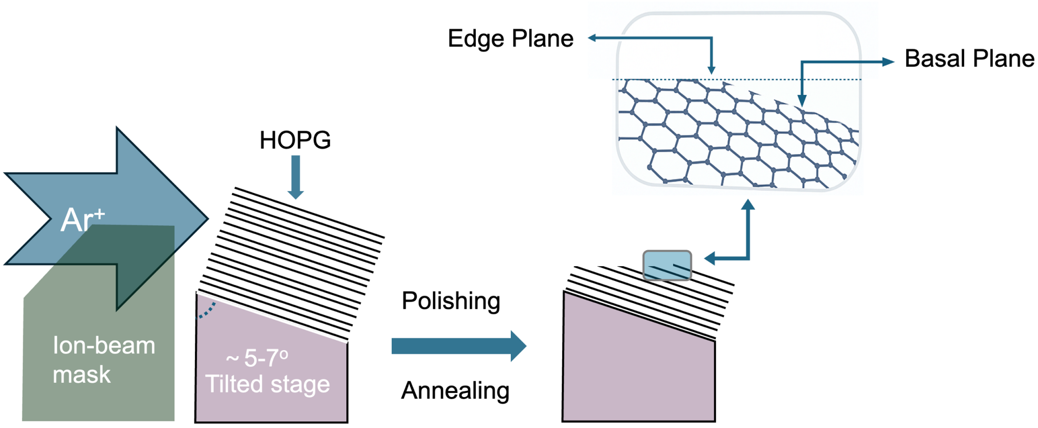

Figure 3.1.3-1. Schematic of the HOPG polishing and annealing procedure, illustrating how surface treatment exposes distinct basal- and edge-plane regions. HOPG is mounted on a tilted stage (~5–7°) and patterned by Ar^+ ion-beam exposure through a mask, followed by polishing and thermal annealing to define terraces and step edges. The resulting surface comprises graphene basal planes (terrace regions) and edge planes (step-edge sites), which provide chemically distinct locations for interfacial reactions.

Preparation of the Highly Ordered Pyrolytic Graphite (HOPG) electrode involved a carefully controlled procedure (Figure 3.1.3-1). HOPG samples were purchased from SPI (438HP-AB, SPI-1 Grade). A micro-section was created on the HOPG sample using a Leica TIC-3X cross-section polisher (from Leica, Germany) to yield two distinct areas: the section area with a mix of graphite edge and basal planes, and the terrace area with predominantly basal planes. The polished HOPG was then cleaned with

Scotch tape to remove impurities and annealed at 500 °C for one hour in both air and argon atmospheres. The air annealing step oxidises and removes surface contaminants, amorphous carbon residues, and organic impurities generated during polishing, thereby exposing a cleaner graphite surface. However, extended exposure to oxygen can also introduce defects or partial surface oxidation. To mitigate this, a subsequent anneal in argon was performed to restore surface order, desorb oxygenated species, and stabilise the graphite structure under an inert atmosphere. This two-step treatment ensures both chemical cleanliness and structural integrity of the basal and edge planes prior to Raman analysis, providing a reproducible and well-defined surface for interfacial electrochemical studies[95-97].

The annealing process was pivotal for removing any amorphous carbon and ensuring the section is electrically and ionically conductive. The final section angle is maintained at approximately 6–7 degrees, ideal for the Raman spectroscopic analysis.

The EL-CELL configuration (ECC-Opto Std, Germany) plays a crucial role in the operando Raman measurements. After the BEXP polishing process, the approximately 0.5 mm thick HOPG sample is mounted horizontally within the cell. This setup includes an electrolyte composed of 1 M $LiPF_6$ dissolved in a solvent mixture of ethylene carbonate (EC) and dimethyl carbonate (DMC) in equal volume parts. The secure and precise placement of the HOPG sample within the EL-CELL is critical for capturing high-quality Raman spectroscopy data during the lithiation process.

Regarding electrolyte preparation, this study employs a regular electrolyte solution of 1M $LiPF_6$ in EC: DMC (1:1 v/v) and a series of solutions with LiFSI salt dissolved in the same solvents at varying concentrations (0.1 M, 0.5 M, 1.0 M, 1.5 M, 3.0 M, and 6.0 M). A weakly solvating electrolyte using 1M LiFSI in 1,4-dioxane is also prepared. These solutions are meticulously formulated to observe the impact of concentration on solvation structures and subsequent SEI formation. The diverse concentration spectrum of the electrolytes is designed to systematically study how changes in solvation structure influence the nature and properties of the SEI, providing insights that could lead to the development of more robust battery systems.

3.2 Characterisation of Graphene-Based Nanomaterials

This section outlines the characterization methods used for graphene-based nanomaterials, focusing on optical microscopy, photoluminescence (PL), fluorescence spectroscopy, Raman spectroscopy, UV–visible (UV–vis) spectroscopy, and atomic force microscopy (AFM). Each technique serves a distinct purpose and provides complementary information that is crucial for understanding the properties and behaviour of graphene-based nanomaterials. The section first summarises the advantages and specific insights offered by each method, and then describes the experimental procedures employed for the corresponding measurements. The combination of these characterization techniques provides a robust framework for understanding graphene-based nanomaterials. Each method uniquely contributes to the overall characterization, offering detailed insights into their structural, optical, and electronic properties.

3.2.1 Optical Microscope

Bright-field optical microscopy was used as an initial non-destructive characterisation method to rapidly locate exfoliated flakes, estimate thickness from optical contrast, and screen sample quality and uniformity (lateral size, shape, and the presence of wrinkles, cracks, or contamination) on SiO_2/Si and PDMS substrate. This technique employs broadband white-light illumination and objective lenses to form magnified images of a sample, with contrast arising from absorption, reflection and thin-film interference between the 2D material and the underlying substrate. In graphene-based systems, these contrast variations are highly sensitive to layer thickness and local morphology, allowing rapid discrimination between monolayer and few-layer flakes and the identification of wrinkles, cracks and contamination.

The optical contrast C is commonly quantified by comparing the reflected intensity from the bare substrate (I_1) with that from the flake-covered region (I_2), defining the optical contrast C as

$$C = \frac{I_1 - I_2}{I_1} \qquad \text{(Equation 3.2.1-1)}$$

As thickness increases, changes in absorption and the phase accumulated upon reflection modify the interference condition, leading to systematic shifts in the colour and intensity observed under the microscope.

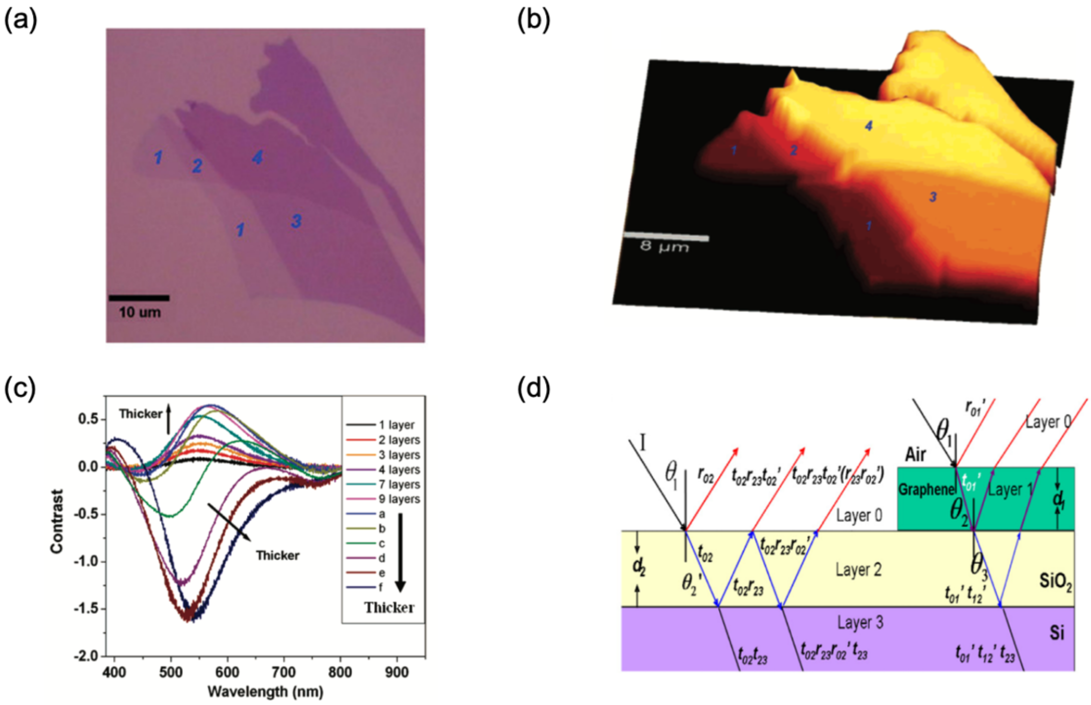

Figure 3.2.1-1. Optical-contrast method for identifying graphene thickness on Si/SiO$_2$. (a) Bright-field optical micrograph of exfoliated graphene exhibiting regions of different layer number on a ~285 nm SiO$_2$/Si substrate. (b) Corresponding 3D optical-contrast map highlighting thickness-dependent contrast across the flake. (c) Measured contrast spectra as a function of wavelength for graphene with different thicknesses, showing systematic contrast evolution with increasing layer number. Panels (a–c) are reproduced with permission from the American Chemical Society from Ni et al., Nano Letters 7, 2758–2763 (2007) [98]. (d) Schematic illustrating multiple reflections and thin-film interference in the air/graphene/SiO$_2$/Si stack underlying the optical-contrast mechanism, adapted with permission from Elsevier from Bing et al., Optics Communications 406, 128–138 (2018) [99].

This principle is illustrated for graphene on Si/SiO$_2$ in Figure 3.2.1-1, distinct optical contrasts arise for different layer numbers (Figure 3.2.1-1a) because the reflected spectrum from the material differs from the bare substrate. This wavelength dependent difference is quantified in a contrast spectrum (Figure 3.2.1-1c), providing a reliable method to distinguish layer numbers when the SiO$_2$ thickness (optimally ~90 nm or ~285 nm for graphene) is chosen to maximize visibility. Governed by the refractive indices of the material and substrate, this interference mechanism also enables identification of MoS_2 and other TMDCs, which often show sufficient contrast on PDMS. With proper calibration, this non-destructive approach can determine thickness with uncertainties down to ±2 nm, facilitating the reliable selection of flakes for fabrication and measurement [100].

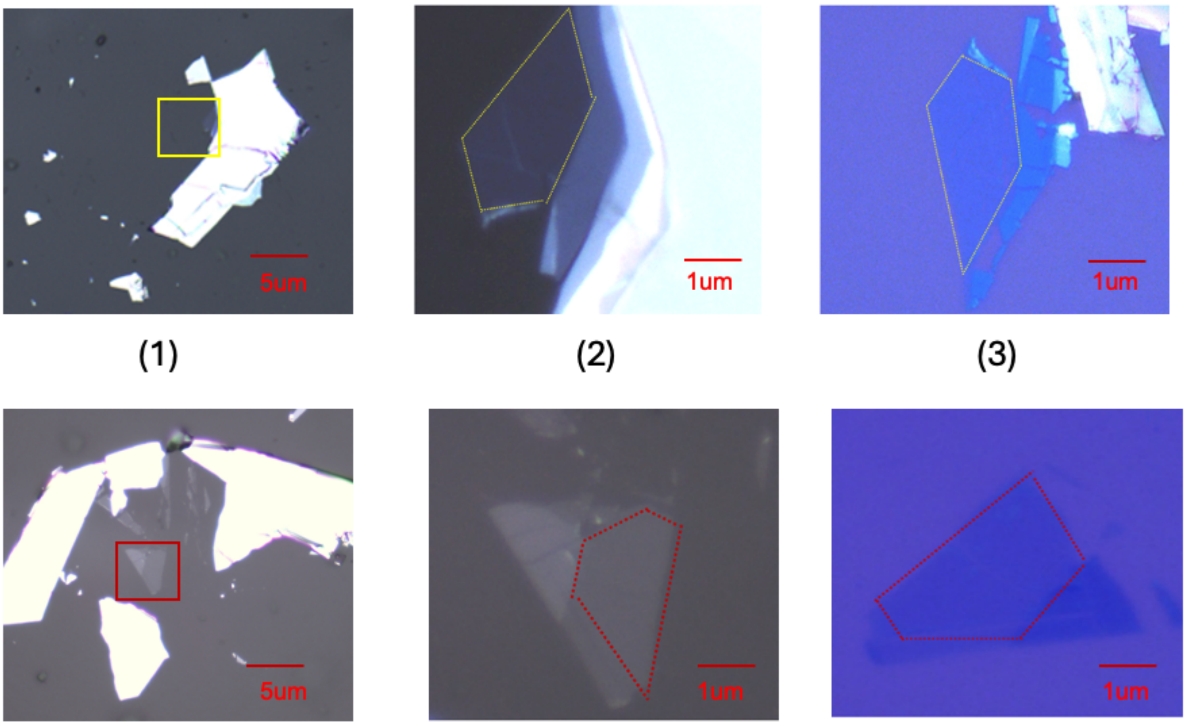

(1) (2) (3)

(4) (5) (6)

Figure 3.2.1-2. Bright-field optical microscopy images used to identify monolayer MoS_2 and graphene for vdWH fabrication. Flakes are shown on PDMS (transfer stamp) and on Si/SiO_2 (target substrate), imaged at 10× (overview) and 50× (zoom). (1–3) MoS_2: (1) 10× on PDMS; (2) 50× on PDMS (yellow dashed outline indicates the selected monolayer region); (3) 50× on Si/SiO_2 (yellow dashed outline). (4–6) Graphene: (4) 10× on PDMS; (5) 50× on PDMS (red dashed outline); (6) 50× on Si/SiO_2 (red dashed outline). Scale bars: 5 μm in (1) and (4), and 1 μm in (2), (3), (5), and (6).

A Zeiss optical microscope equipped with Zeiss Motic Image Plus 3.1 software was used to identify monolayer MoS_2 and graphene flakes. The procedure began with calibration using a grid or known scale to ensure accurate dimensional measurements. Live video mode in the software enabled central positioning of the glass slide containing exfoliated flakes, followed by focusing on 5× or 10× magnification. Once suitable candidate flakes were located, the magnification was increased to 50×, with careful refocusing to avoid damage to both sample and objective. Images were acquired at 10× and 50× magnifications (Figure 3.2.1-2) to document flake positions and were saved for subsequent analysis. Illumination was optimised by adjusting the diaphragm and light source to achieve uniform brightness and contrast, and multiple images were collected at different focal planes to fully capture the region of interest. During analysis, the images were examined for layer number estimation and for morphological features such as wrinkles, tears, or surface contamination, with detailed records kept of layer thickness, defects, and specific areas of interest.

3.2.2 Photoluminescence Microscopy

Photoluminescence (PL) techniques—macro-PL, micro-PL, room-temperature PL, and low-temperature PL—were employed to investigate the emission characteristics and interlayer interactions in graphene–MoS_2 van der Waals heterostructures (vdWHs). Room-temperature PL revealed unique emission patterns associated with heterostructure formation, while low-temperature PL (10–300 K) provided deeper insights into excitonic dynamics and interfacial coupling. These techniques, detailed in the following subsections (3.2.2.1–3.2.2.3), were essential for verifying structural quality and generating the spectral fingerprints used in optical physical unclonable functions (O-PUFs).

3.2.2.1 Macro-PL for Monolayer Identification

Macro-photoluminescence (macro-PL) was employed to verify the successful stacking of graphene–MoS_2 van der Waals heterostructures (vdWHs) and to screen for monolayer MoS_2. The custom epi-illumination setup (Fig. 3.2.2.1-1) comprises a SOLIS 3C white LED source (5700 K) coupled into a 3 mm liquid light guide, with output attenuated to ~0.1–0.5 mW at the sample after spectral filtering. In this technique, white light is filtered by a 500 nm short-pass filter and delivered to the sample via a beamsplitter and 50x, 0.75 numerical aperture (NA) lens. The emitted light is collected through the same objective, then filtered by a 550nm long pass filter to ensure only sample luminescence reaches to the CCD camera. This enables rapid, large area (>100 µm²) spatial mapping in a single exposure, facilitating identification of heterostructure regions.

Strong photoluminescence in MoS_2 occurs only in the monolayer due to its direct bandgap (~1.8 eV); consequently, bright zones in the macro-PL image correspond to monolayer flakes, while bilayer and thicker regions remain dark. When a monolayer is stacked onto graphene, interlayer charge transfer quenches the MoS_2 exciton emission. As a result, the heterostructure overlap appears as a local suppression of PL intensity relative to the surrounding monolayer MoS_2, while graphene alone remains dark. By comparing the macro-PL map with the corresponding optical microscopy images, the heterostructure region can be precisely identified, and features such as folds or cracks are revealed as local intensity variations.

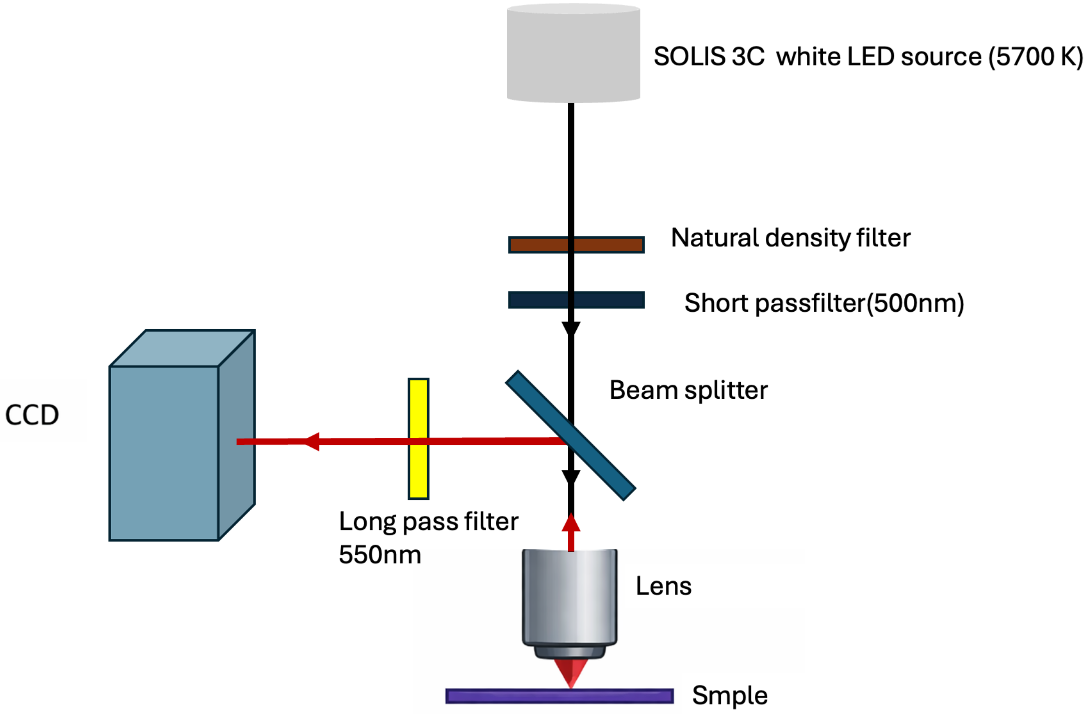

Figure 3.2.2.1-1. Schematic of the epi-illumination optical path for Macro-PL setup. White light is attenuated by a neutral-density filter, spectrally shaped by a 500 nm short-pass filter, and directed by a beamsplitter through the lens onto the sample. The reflected light returns through the same lens, passes through a 550 nm long-pass filter, and is recorded by the CCD.

The procedure begins by identifying graphene–MoS_2 vdWH with the 10× lens, and then a 50× objective was used for higher-magnification imaging, and images were acquired with Image Focus Alpha software using 240 s integration and 10% gain to compensate for the low quantum yield of MoS_2 and graphene–MoS_2.

3.2.2.2 Room-Temperature Micro-PL and Spatial Mapping

Room-temperature micro-photoluminescence (PL) characterization was conducted using a Horiba LabRAM Odyssey confocal microscope operated in PL mode. Micro-PL spectra were collected for isolated monolayer MoS_2, MoS_2–graphene, and graphene–MoS_2 heterostructures. Full spatial photoluminescence maps were also acquired to probe spatial inhomogeneity across the graphene-MoS_2 heterostructure interface. As illustrated in the optical path schematic (Figure 3.2.2.2-1), a continuous-wave 532 nm laser was used for excitation and passed through a clean-up interference filter and neutral-density filters to remove off-centre sideband and adjust the incident power. The beam was directed into the microscope by steering mirrors and focused onto the sample through a high-NA objective(100x), producing an excitation spot of approximately 1 μm. Emission from the sample was collected in a backscattering geometry by the same objective. The signal was first passed through a confocal pinhole to filter the out of focus light, thus enhancing spatial resolution and reduce background noise. It was then routed to the detection path, where a long-pass edge filter suppressed the Rayleigh-scattered laser line while transmitting the PL signal. Finally, the filtered emission was coupled into the spectrograph through the entrance slit, dispersed by a diffraction grating, and detected using a thermoelectrically cooled CCD.

The procedure for micro-photoluminescence (PL) measurements on MoS_2 and MoS_2–graphene heterostructures involved several key steps. First, the Raman spectrometer was auto-calibrated using a clean silicon wafer as a reference. Under 532 nm excitation and with 600 grooves/mm grating, the system was aligned to the first-order Si Raman peak at 520.7 cm^{-1} using the built-in LabSpec 6 auto-calibration function. This calibration was verified before each measurement by confirming that the peak position remained within ± 1 cm^{-1} of the reference value. To obtain the PL spectra, samples were first positioned on the microscope stage, and the flakes of interest were located using a 10× objective before focusing with a 100×, high-numerical-aperture objective. To avoid heating, the laser power was maintained at 0.01% (~5 μW). Spectra were acquired over 550–750 nm with a 30 s integration time, after ensuring the room lights were off, the laser shutter was open, and the beamsplitter was placed in the upright position.

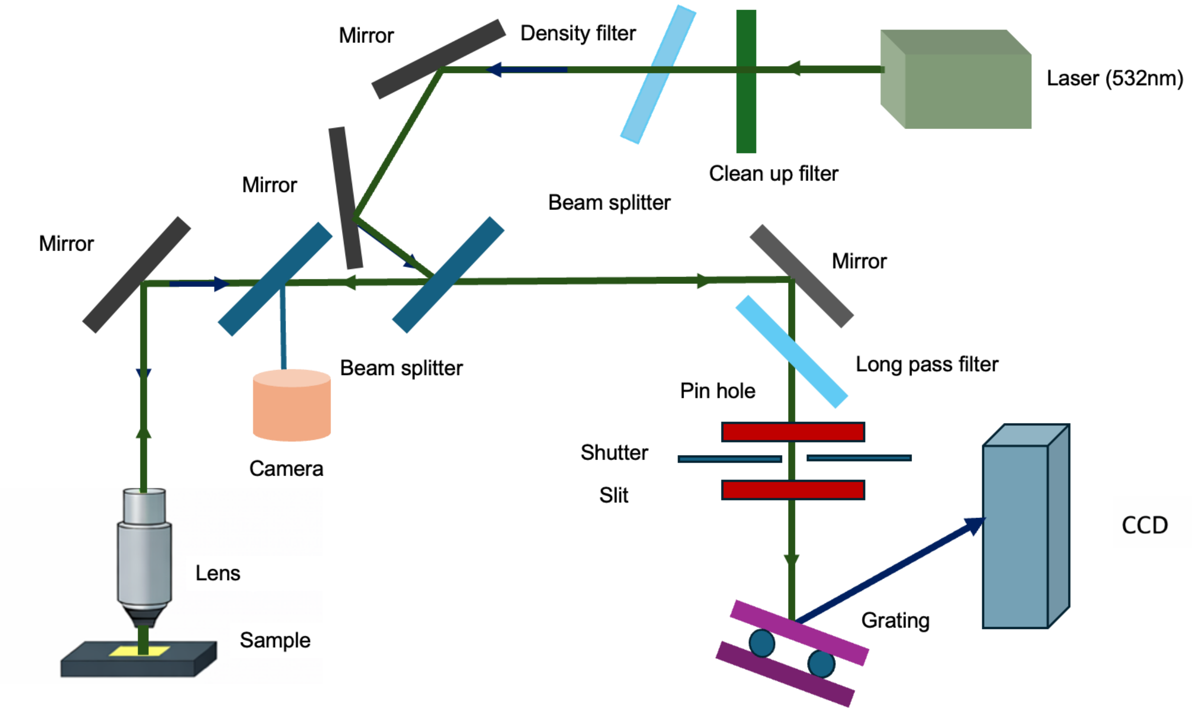

Figure 3.2.2.2-1. Schematic diagram of the photoluminescence (PL) spectroscopy setup (Horiba LabRAM Odyssey); A 532 nm laser is spetcral refined by a clean-up filter and attenuated by a neutral-density filter, then focused onto the sample by an objective. The emission is collected in epi-configuration, first was suppressed Rayleigh scatering by a long-pass edge filter, and spatially filtered by a confocal pinhole. It is then dispersed by a diffraction grating (600 grooves mm^{-1}) and detected by a CCD. A camera port enables sample alignment.

For high-resolution spatial mapping of the graphene–MoS$_2$ heterostructure, a 48 × 14 grid spanning 48 μm × 28 μm (step sizes of 1.0 μm in x and 2.0 μm in y) was employed to cover both monolayer MoS$_2$ and heterostructure regions. At each point of the map, a full PL spectrum was recorded using the same acquisition parameters (0.01% laser power and a 30 s integration time). The acquired spectral data were processed to generate spatially resolved heatmaps of the integrated PL intensity and the peak emission energy. These complementary metrics provide a quantitative, micrometre-scale visualization of interfacial heterogeneity by exploiting the sensitivity of the MoS$_2$

excitonic emission to local variations in interlayer coupling, doping, and defects. The integrated PL intensity, reflecting the total radiative efficiency, reveals variations in contact quality and local non-radiative recombination. Quenching of the PL intensity relative to bare MoS_2 (though subtle at room temperature) indicates activated non-radiative pathways, while spatial fluctuations pinpoint defects such as contaminants, wrinkles, or regions of incomplete interlayer contact. The emission peak energy captures shifts in the excitonic emission, reporting on local changes in the dielectric environment, carrier density, and strain induced by the graphene interface. Collectively, these spatially resolved photoluminescence maps provide a comprehensive visualization of the structural and electronic heterogeneity across the graphene–MoS_2 heterostructure interface.

3.2.2.3 Low-Temperature PL Measurements

Low-temperature photoluminescence (*u*-PL) measurements were employed to investigate temperature and excitation-power-dependent excitonic emission in Graphene–MoS_2 van der Waals heterostructures. Cryogenic cooling alters the PL response through renormalization of the electronic band structure, the suppression of dephasing and scattering processes, and the rebalancing of radiative versus non-radiative recombination dynamics. The resulting reduction in phonon scattering lowers non-radiative recombination, leading to narrower and more intense excitonic peaks while unveiling fine spectral features—such as neutral excitons, trions, and defect-bound states that are thermally obscured at room temperature. Conversely, variations in excitation power primarily tune the photogenerated carrier density and induce localized heating. As the power increases, laser-induced local heating lowers the excitonic optical transition energy through lattice expansion and enhanced electron–phonon coupling.

The experimental setup is shown in Figure 3.2.2.3-1. Samples were mounted under vacuum within an ICE Oxford optical cryostat, cooled by a closed-cycle Sumitomo GM cryocooler. Vibrational isolation was provided by a He-4 exchange-gas bellows connecting the cold head, enabling stable sample temperatures approaching 10 K with root-mean-square (RMS) vibrations of approximately 50 nm. A continuous-wave, frequency-double 532nm laser was selected as laser source; and the laser intensity was regulated by two neutral-density filter wheels and monitored via a calibrated power meter sampling 10% of the beam. A beam splitter (BS2) with an 8:92 reflection-to-transmission ratio directed the beam toward the cryostat, maximizing output signal to the spectrometer. The laser beam was then focused to an approximately 1 um^2 spot by a 50× Olympus LCPLN-IR objective (numerical aperture = 0.65), which was mounted on a three-axis piezo stage with 25 nm step resolution and 20 μm travel range.

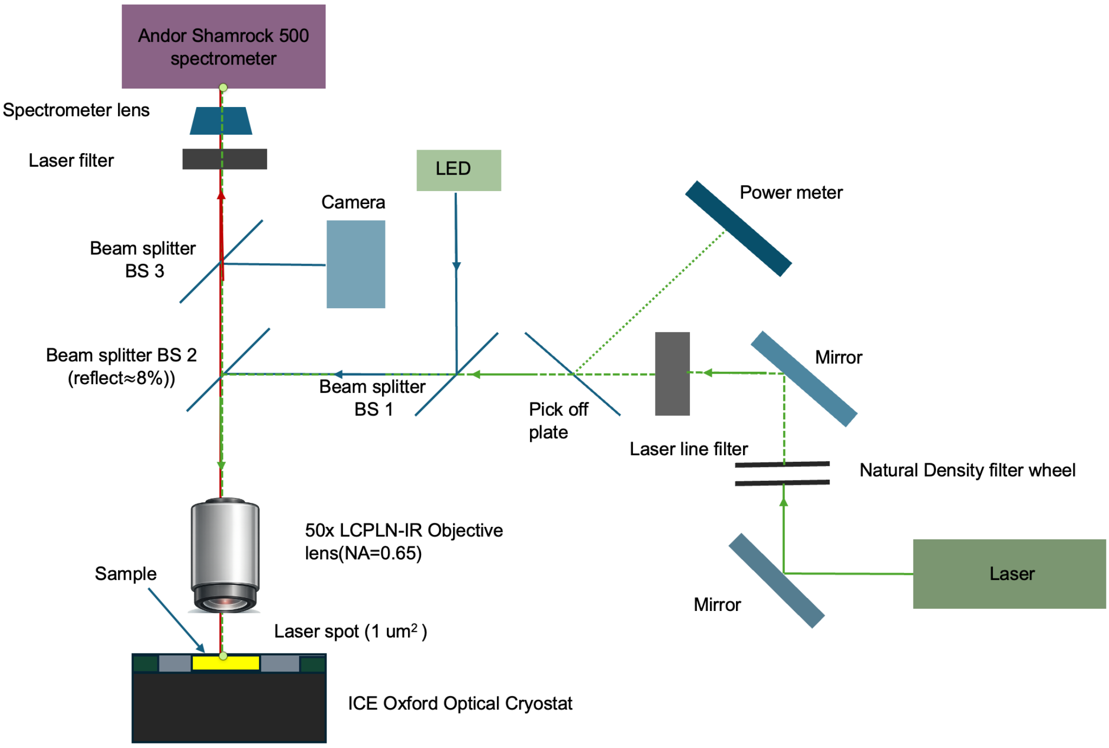

Figure 3.2.2.3-1 shows the schematic of the low-temperature micro-PL setup. A 532 nm continuous-wave laser was used to excite the sample mounted inside a closed-cycle optical cryostat. The laser beam was guided through a series of mirrors and beam splitters (BS1–BS3) before being focused onto the sample by a 50× Olympus LCPLN-IR objective lens (NA = 0.65). BS1 reflected approximately 8 % of the incoming light into the cryostat to enhance emission collection efficiency while slightly reducing the maximum excitation power.

The photoluminescence (PL) was collected through the same optical path, filtered by a long pass filter to remove reflected laser light. The signal was then focused through a variable-width entrance slit into an Andor Shamrock 500 spectrometer and detected by an EMCCD camera. For initial sample alignment, a white-light LED was coupled into the optical path via a second beam splitter (BS2) and was directed to the camera by the third bean splitter (BS3). Following alignment, BS3 was removed and the LED was switched off to optimize PL collection efficiency during the measurement.

During the *u*-PL measurements, samples were cooled to 10K and gradually warmed to 300 K, with spectra acquired every 10 K. Temperature was stabilised within ±0.1 K and was monitored by an AttoCube controller. Power-dependent measurements were performed by varying the excitation power incident on the sample between 1.1 and 13.1 uW. The excitation power at the sample surface was adjusted using two neutral-density (ND) filter wheels and quantified with a beam-sampling power meter and monitored in real time using the QEO LabView VI software. The Daisy Positioning managed the piezo stage and ThorCam provided real-time visualisation of the laser spot for precise focusing. The procedure began with venting the chamber, mounting the sample using electro-conductive adhesive, and re-establishing vacuum. After optical alignment, PL spectra were first recorded at 300 K, repeated at 10 K, and subsequently during controlled warming from 10 K to 300 K. This systematic procedure ensured reproducible data across temperature and power ranges, enabling quantitative analysis of exciton peak shifts and intensity variations associated with interfacial coupling in the heterostructure.

3.2.3 Fluorescence Imaging of GQDs

Fluorescence imaging was employed to characterize the photoluminescence properties of graphene quantum dots (GQDs), following initial UV-Vis and spectrofluorometric analyses to confirm excitation/emission profiles. These techniques enabled the analysis of optical band gaps, excitation-dependent emission, and spatial emission patterns—critical for both fundamental understanding and potential fingerprinting applications.

3.2.3.1 Fluorescence Spectroscopy Setup and Procedure

Fluorescence spectroscopy (Pico Quant FT300; schematic in Figure 3.2.3.1-1) was used to investigate the excitation-dependent optical response of GQD dispersions. The system uses a high-intensity Xe lamp (300 W) as the excitation source, the laser light is wavelength-selected by the excitation monochromator and directed onto the GQD solution, the resulting fluorescence are collected and spectrally filtered by the emission monochromator and detected by the photomultiplier tubes (PMTs) coupled to a computer for signal acquisition and processing. The resulting fluorescence spectrum providing information on the electronic structure, defect states and aggregation behaviour of the GQDs, thereby guiding the filter selection for subsequent fluorescence microscopy imaging.

GQD fluorescence measurements were performed on aqueous dispersions prepared by first dispersing the GQDs in deionised water, sonicating at 40 °C for 10 minutes, and then diluting to appropriate concentrations to avoid saturation. The spectrometer was operated in scan mode with excitation wavelengths between 320 nm and 570 nm, and the photomultiplier tube (PMT) voltage set between 650 and 800 V. For each measurement, a quartz cuvette filled with deionised water was first used as a blank; it was placed in the spectrofluorometer, and a baseline scan was acquired to account for background fluorescence. A clean quartz cuvette was then filled with the GQD solution, placed in the same position, and fluorescence scans were recorded over the defined excitation wavelength range, collecting the emission spectrum for each excitation wavelength.

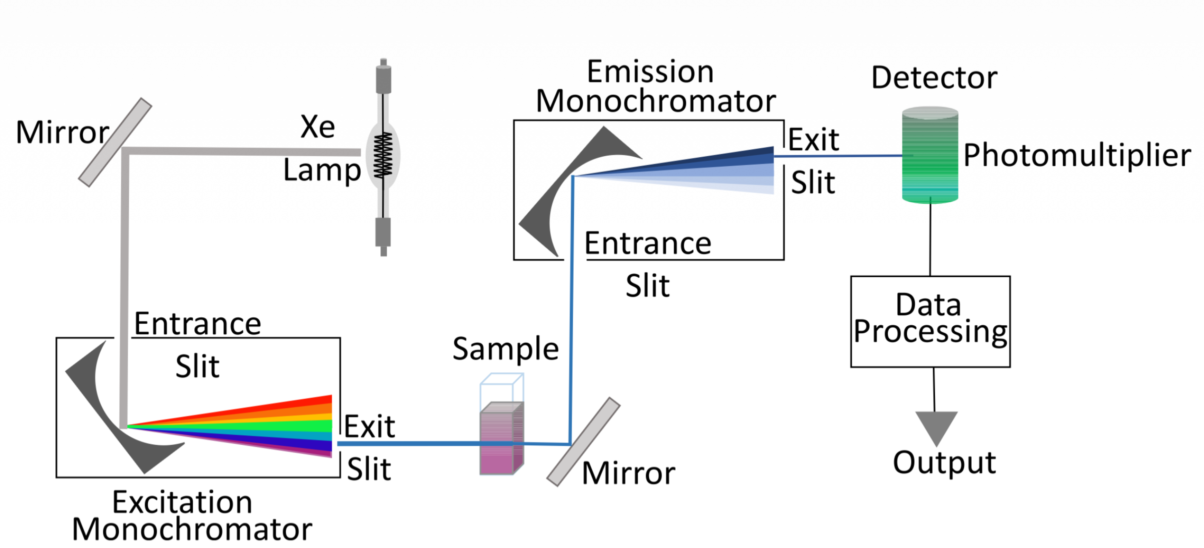

Figure 3.2.3.1-1 Schematic of the fluorescence spectroscopy. Excitation from a Xe lamp is directed via mirror into the excitation monochromator and delivered to the GQDs sample; the emitted fluorescence is collected, filtered through an emission monochromator, and detected by a photomultiplier tube, with the signal processed to generate the fluorescence spectrum. Reproduced with permission from John Wiley & Sons from Gomes et al., The Canadian Journal of Chemical Engineering 97, 2168–2175 (2019) [101].

The baseline fluorescence was subtracted from the sample signal to obtain corrected emission spectra, which were analysed to identify the characteristic excitation-dependent emission peaks of the GQDs. All measurements were performed in triplicate to ensure reproducibility and accuracy. The resulting spectra revealed excitation-dependent emission peaks from 460 to 600 nm (under 320–570 nm excitation; see details in section 4.4.2-4.4.3). Based on these results, filter sets were chosen for subsequent fluorescence microscopy to target these spectral ranges, specifically long-pass filters (550, 600, 650 nm) and short-pass filters (500, 550 nm).

3.2.3.2 Fluorescence Microscopy for Optical Fingerprinting

Following fluorescence spectroscopy, filter sets were selected for fluorescence microscopy imaging (long-pass: 550, 600, and 650 nm; short-pass: 500 and 550 nm). GQD samples were deposited on Si/SiO_2 substrates and imaged using the same custom epi-illumination microscope described in Section 3.2.2.1 (Fig. 3.2.2.1-1). To capture the full sample area, a 10× objective was used. The selected filters were installed in a kinematic fluorescence filter cube (DFM1, Thorlabs) for fluorescence image acquisition.

Imaging was performed with a gain of 200% and a 30-second exposure. To reduce noise, the lab environment was darkened, screen brightness lowered, and external light sources blocked. At each position, 10 images were captured to ensure consistency. Multiple fields of view were recorded for statistical comparison.

Fluorescence images were analysed using Motic Images Plus 3.1, which extracted intensity profiles, spatial distribution, and emission uniformity. These high-resolution fluorescence maps revealed characteristic emission patterns of the GQD aggregates, enabling their use as secure, tamper-proof optical fingerprints for future PUF (physically unclonable function) applications.

3.2.4 Raman Spectroscopy

Raman spectroscopy was employed as a central characterisation technique across all three graphene-based systems investigated in this study—graphene quantum dots (GQDs), graphene–MoS_2 van der Waals heterostructures (vdWHs), and highly oriented pyrolytic graphite (HOPG). Its application enabled the extraction of detailed structural, interfacial, and electrochemical information relevant to the design of optical physical unclonable functions (O-PUFs) and interfacial processes in lithium-ion batteries.

Raman spectroscopy measurements were conducted using a Horiba LabRAM Odyssey spectrometer in Raman mode (see the setup in Figure 3.2.2.2-1), which detects Stokes-shifted inelastically scattered light rather than the direct emission recorded in photoluminescence (PL) mode. As illustrated in Figure 3.2.4-1(a), Raman spectroscopy probes the atomic structure, defect density, and lattice vibrations of graphene-based nanomaterials through detecting inelastically scattered light arising from photon–phonon interactions: when a monochromatic laser illuminates the sample, most photons are elastically scattered (Rayleigh scattering) and retain the incident energy, while a small fraction undergoes inelastic Stokes Raman scattering and lose energy by generating a vibrational excitation (phonons).In this setup, scattered light is collected in a backscattering geometry. A notch filter suppresses the intense Rayleigh line, transmitting only the Stokes-shifted Raman signal, which is then dispersed by a diffraction grating and focused onto a charge-coupled device (CCD) detector. The resulting Raman shifts correspond to distinct phonon modes and are highly sensitive to bonding symmetry, crystallinity, strain, and electronic structure of the sample.

All Raman measurements began with automatic calibration using the characteristic silicon reference peak at ~520 cm^{-1}. Initial sample positioning was carried out using a 10× objective lens, followed by fine focusing under a 100× lens. Accurate sample alignment was confirmed through vertical alignment of the laser spot on the sample surface. Acquisition parameters—including grating, neutral density (ND) filter, laser power and spectral range—were configured using the Horiba control interface. To minimize local heating and photodegradation, low laser powers and long acquisition times were used consistently for all samples. For graphene, MoS_2, and graphene–MoS_2 heterostructures, as well as for HOPG crystals (including operando measurements), the 532 nm laser (50 mW output) was attenuated to 0.01% (~5 μW at the sample) with a 30 s integration time per spectrum. For graphene quantum dots

(GQDs), the laser power was raised to 0.1% (~50 μW) and the acquisition time extended to 120 s per spectrum to compensate for their strong fluorescence background.

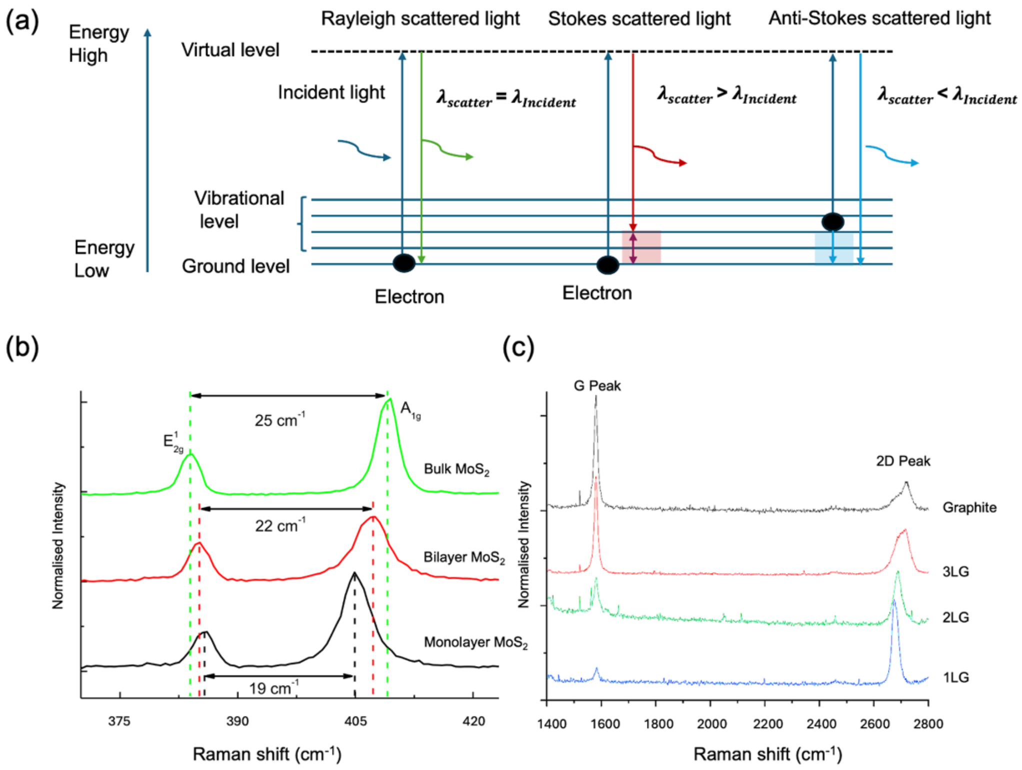

Figure 3.2.4-1. (a) Schematic energy-level diagram illustrating elastic Rayleigh scattering and inelastic Raman scattering via Stokes and anti-Stokes processes, where the scattered photon energy is unchanged, decreased, or increased, respectively. (b) Representative Raman spectra of MoS$_2$ showing the layer-dependent $E_{2g}{}^1$(in-plane) and A_{1g} (out-of-plane) phonon modes and the increasing peak separation with thickness from monolayer to bulk. (c) Representative Raman spectra of graphene/graphite highlighting the G and 2D bands, with systematic evolution in 2D intensity and spectral shape from monolayer graphene to multilayer graphene and graphite.

Raman spectra were initially acquired from two graphene–MoS$_2$ heterostructures to evaluate layer quality, interfacial coupling, and strain effects. Measurements were conducted on individual monolayers of graphene and MoS$_2$, both on PDMS and SiO$_2$ substrates, followed by their corresponding stacked van der Waals heterostructures. Monolayer MoS$_2$ was identified by the characteristic frequency separation between its $E_{2g}{}^1$ and A_{1g} modes (Fig. 3.2.4-1(b)). The $E_{2g}{}^1$ mode corresponds to in-plane vibrations of Mo and S atoms, while the A_{1g} mode arises from out-of-plane vibrations of S atoms. Enhanced interlayer Van der Waals coupling with increasing layer number stiffens the

A_{1g} mode and softens the E_{2g}^1 mode, causing the frequency separation $\Delta = A_{1g} - E_{2g}^1$ to increase from ~19 cm^{-1} in monolayers to ~25 cm^{-1} in bulk crystals.

Monolayer graphene was confirmed using the G and 2D bands (Fig. 3.2.4-1(c)). The G band results from in-plane C–C bond stretching, whereas the 2D band is a second-order two-phonon process highly sensitive to the electronic band structure. As layer thickness increases, interlayer coupling modifies the electronic dispersion, resulting in a broadening of the 2D band and a decrease in the intensity ratio I_{2D}/I_G from >2 in monolayer graphene to <1 in multilayer graphene or graphite. Upon the formation of van der Waals heterostructures (vdWHs), interfacial interactions can induce strain and charge transfer (interfacial doping), which result in spectral shifts or linewidth changes in the characteristic modes of both monolayers. Consequently, the peak positions and spectral shapes of the MoS_2 E_{2g}^1 and A_{1g} peaks and the graphene G and 2D bands were monitored to quantify interlayer interactions and doping effects within the heterostructures.

For GQDs, Raman spectroscopy was used to evaluate the degree of graphitisation and quantify structural disorder. The D and G bands were monitored because these features provide complementary information on defect/edge density and overall crystalline quality: the D band (~1350 cm^{-1}) is activated by symmetry-breaking defects and edge sites (breathing modes of sp^2 carbon rings), and its intensity relative to the G band(I_D/I_G) is commonly used to estimate defect concentration and average sp^2 domain size, whereas the G band arises from in-plane stretching of sp^2-hybridised carbon and reflects the degree of graphitic ordering. For sample preparation, 1 mL of the GQD dispersion was drop-cast onto a clean silicon substrate and dried under ambient conditions for 2 h, producing a characteristic coffee-ring deposition pattern. Raman spectra were collected at the ring edge using a 100× objective with the 532nm excitation laser attenuated to 0.1% (≈50 μW at the sample), an integration time of 120 s per spectrum, and a spectral window of 1000–2000 cm^{-1}.

Raman spectroscopy also played a crucial role in characterising HOPG electrodes, both before and after surface treatment. Measurements following polishing and annealing at 500 °C revealed distinct structural contrasts between basal and edge planes, highlighting the impact of these treatments on surface crystallinity and defect states. Furthermore, operando Raman spectroscopy was employed to monitor real-time SEI formation and lithium intercalation during the first lithiation cycle. An electrochemical workstation was used to control the voltage between 0 V and 1.4 V vs. Li/Li^+. A long-working-distance 50× objective was employed for these measurements, using the 532 nm laser attenuated to 0.01% (≈5 µW at the sample) with an integration time of 30 s per spectrum across a 500–3500 cm^{-1} window. Solvent-dependent SEI formation was further investigated by analysing electrolytes with varying LiFSI concentrations in EC: DMC and DX solvents, with particular focus on the 700–900 cm^{-1} region to monitor solvation-related vibrational signatures.

Altogether, Raman spectroscopy enabled a multidimensional understanding of graphene-based nanomaterials—probing not only structural order and defects but also dynamic interfacial processes such as doping, strain, solvation, and SEI formation, which are critical to both O-PUF device performance and lithium-ion battery stability.

3.2.5 UV-Vis's Spectroscopy

A Cary 60 UV–Vis's spectrophotometer (Agilent) was used to determine the optical absorption features of GQDs synthesised under different conditions. The schematics of the UV-Vis spectroscopy is shown in Figure 3.2.5-1, a xenon flash lamp provided broadband illumination across the UV–visible range (190–1100 nm). Incident wavelengths were selected by a diffraction grating monochromator and directed through a quartz cuvette containing the GQD dispersion. Photon absorption at wavelengths corresponding to electronic transitions in the GQDs attenuated the transmitted beam intensity, which was detected by a silicon photodiode. This yielded the absorption spectrum, typically recorded over the 200–560 nm range.

To measure the absorption of graphene quantum dots (GQDs), stock dispersions were first prepared in deionised water and sonicated at 40 °C for 10 min to ensure a homogeneous suspension. The resulting dispersion was then diluted to an appropriate concentration (typically yielding absorbance values between 0.1 and 1) so that measurements lay within the linear response range of the spectrophotometer and avoided saturation. For baseline correction, a quartz cuvette filled with pure deionised water was placed in the UV–Vis's spectrophotometer and a reference scan was acquired, accounting for the absorbance of the solvent and cuvette; cuvettes were handled carefully to avoid scratches and fingerprints. A clean quartz cuvette was then filled with the diluted GQD dispersion and placed in the same position, and absorbance spectra were recorded over the 200–800 nm wavelength range. Each sample was measured in triplicate to ensure reproducibility and accuracy. The solvent baseline was subtracted from the sample spectra to obtain corrected absorbance curves, from which characteristic electronic transitions of GQDs were identified.

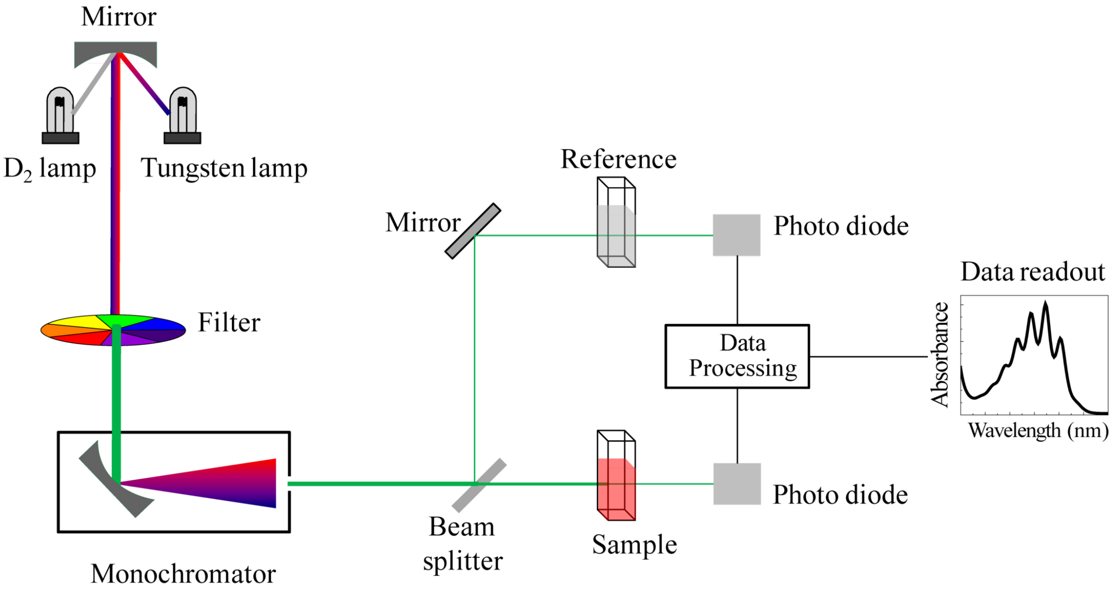

Figure 3.2.5-1. Schematic representation of a UV–Vis's absorption spectroscopy setup. Broadband UV–visible light is wavelength-selected and passed through a quartz cuvette containing the GQD dispersion; the transmitted intensity is recorded by a detector to obtain the absorbance spectrum. A cuvette filled with deionised water is used as the baseline reference for background correction. Image from Wikimedia Commons (Public Domain).

In the absorbance spectra of GQDs, absorption bands associated with π–π* and n–π* transitions are attribute to the formation of conjugated carbon nanostructures with oxygen/nitrogen surface functional groups. The π–π* transition arises from excitation of electrons between π bonding and π* antibonding orbitals within sp^2-hybridised carbon domains, typically appearing around 230–270 nm and indicating the presence of conjugated aromatic C=C bonds in the graphitic core. The n–π* transition originates from non-bonding (n) electrons on oxygen-containing groups (e.g. C=O or C–O) that are promoted to π* antibonding orbitals and is generally observed around 300–350 nm. The coexistence of these two features shows that the GQDs possess both sp^2

carbon frameworks and oxygen-functionalised edge states, providing spectroscopic evidence for successful dot formation and chemical modification.

3.2.6 Atomic Force Microscopy

Atomic force microscopy (AFM) analyses of GQDs were performed on a Bruker MultiMode 8 AFM equipped with a NanoScope V controller and a commercial silicon tip (SCOUT 70, silicon AFM probe with Al-coated reflective backside; spring constant ≈ 2 N/m; resonant frequency ≈ 70 kHz) operated in ScanAsyst™-in-air mode.

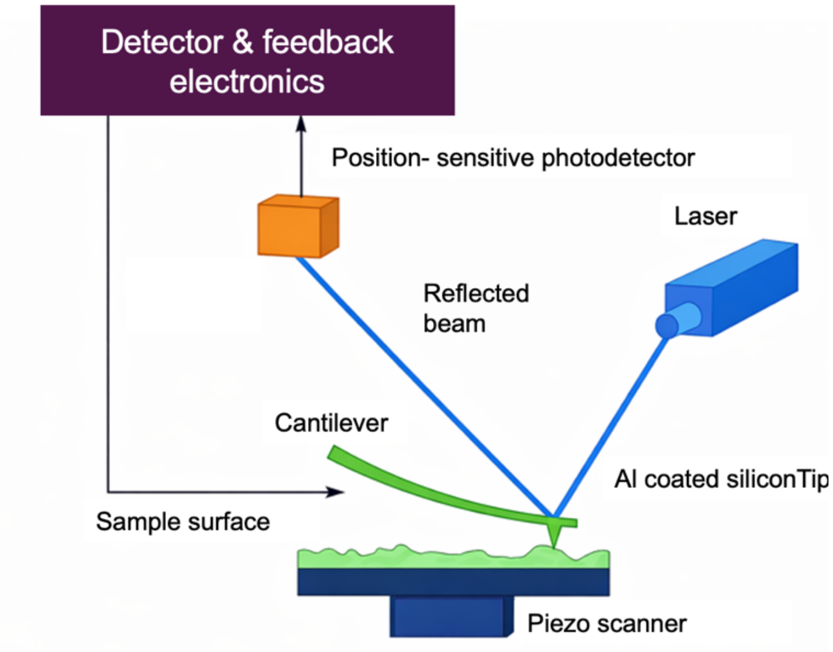

Figure 3.2.6-1. Schematic of an atomic force microscope (AFM). An Al-coated silicon tip mounted on a cantilever is raster-scanned across the sample surface. Tip–sample interaction forces deflect the cantilever; this deflection is measured by the optical lever method, in which a laser beam reflected from the cantilever is directed onto a position-sensitive photodiode. A feedback controller adjusts the z-position to maintain a constant deflection (setpoint), and the required vertical motion is recorded to reconstruct the surface topography. *Redrawn from Wikimedia Commons (public domain).*

In the AFM setup (Figure 3.2.6-1), a silicon tip mounted on a cantilever interacts with the sample surface while a piezoelectric scanner raster the sample in the x–y plane. The tip–sample separation is controlled by a feedback loop in the NanoScope V controller, which adjusts the scanner's z-displacement to maintain a constant interaction force (setpoint). Cantilever deflection is monitored using an optical lever system, where a laser beam reflected from the Al-coated cantilever strikes a position-sensitive photodetector, enabling the optical amplification of sub-nanometre deflections into a measurable displacement signal. As the tip scans, changes in surface topography cause deflections of the cantilever, which are amplified by the photodetector and recorded as a displacement signal. ScanAsyst™ automatically optimises imaging parameters (including setpoint, feedback gains, and scan rate) in real time, minimising tip–sample forces and improving image quality, thereby enabling high-resolution surface topography mapping of both GQDs and MoS_2.

GQDs samples were prepared by drop casting 20 µL of the GQD dispersion onto a silicon wafer, followed by drying in an oven at 40 °C. AFM measurements were preceded by calibration using a silicon reference sample prior to each session. Large-area scans (10 µm × 10 µm) were first acquired at a scan rate of 2 Hz to locate clean and representative regions. The scan size was then progressively reduced from 5 µm, to 3 µm, 1 µm, and finally 500 nm, while the scan rate was lowered to 0.5 Hz to obtain high-resolution images of the graphene quantum dots. Particle height, lateral dimensions, and surface roughness were extracted from the topography data, and statistical analysis across multiple regions was used to obtain particle size distributions and related metrics.

Monolayer MoS_2 sample was exfoliated from bulk crystal onto a PDMS stamp and transferred onto Si/SiO_2 substrates. Large-area AFM scans (12 µm × 12 µm) were first acquired at a scan rate of 2 Hz to locate the flake and identify uniform regions. The scan size was then sequentially reduced to 5 µm, 3 µm, 1 µm, and finally 500 nm, while the scan rate was lowered to 0.5 Hz for high-resolution imaging. These scans were used to examine nanoscale topography and assess surface cleanliness and continuity, including the identification of wrinkles, folds, particulates, and transfer residues, providing complementary structural information to optical microscopy and Raman/PL characterisation.

Chapter 4: Graphene Quantum Dots for Optical Physical Unclonable Functions

Physically unclonable functions (PUFs) are systems that harness inherent physical randomness to generate unique and irreproducible identifiers, offering a promising route toward secure, tamper-evident authentication. This chapter presents an experimental investigation into the use of biomass-derived graphene quantum dots (GQDs) as a stochastic optical platform for PUF applications. As zero-dimensional carbon-based nanomaterials, GQDs exhibit tuneable, excitation-dependent fluorescence that is highly sensitive to variations in size, surface chemistry, and environmental conditions [102-104]. These photoluminescent properties make them strong candidates for generating non-reproducible optical fingerprints suitable for low-cost, scalable security solutions [105].

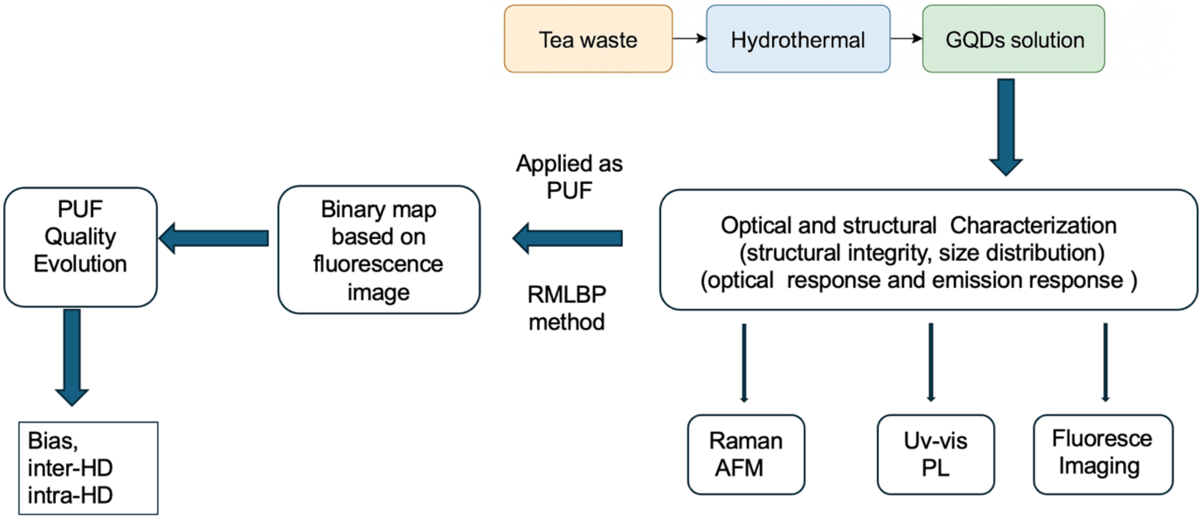

Figure 4-1. Schematic workflow for the synthesis, characterization, and application of tea waste-derived graphene quantum dots (GQDs) as Physical Unclonable Functions (PUFs).

In this study, GQDs were synthesised using a green, hydrothermal carbonisation process from spent oolong tea leaves (Figure 4-1). Their structural and optical characteristics were evaluated using Raman spectroscopy, atomic force microscopy (AFM), UV-Vi’s absorption, photoluminescence (PL) spectroscopy, and fluorescence imaging. A particular focus was placed on assessing the influence of deposition technique on fluorescence pattern quality, comparing conventional drop-casting with electrospray deposition. The electrospray method was found to produce more spatially uniform and entropy-rich emission patterns by reducing aggregation and minimising coffee-ring effects.

To convert the fluorescence emission patterns into digital identifiers, a binary encoding method based on the Rotationally Invariant Modified Local Binary Pattern (RMLBP) algorithm was applied. The RMLBP technique encodes the local textural features of an image by comparing the intensity of each pixel with those of its neighbouring pixels arranged in a circular pattern. Each neighbourhood is converted into a binary sequence representing local contrast and structural variation, which is then reduced to a single modal bit to enhance noise tolerance and rotation invariance. This process transforms continuous fluorescence intensity distributions into discrete, reproducible binary maps that preserve the spatial characteristics of each GQD emission pattern.

The resulting binary maps were quantitatively evaluated using standard physically unclonable function (PUF) performance metrics. Bias measures the proportion of binary 1s and 0s within a map; a value of 0.5 indicates perfect balance and high entropy with no bit-value preference. Inter-Hamming distance (inter-HD) quantifies the bitwise distinctness between maps derived from different samples, providing a measure of uniqueness; an ideal value of 0.5 corresponds to complete independence between encoded identifiers. Together, these metrics provide a quantitative assessment of the uniqueness, stability, and reproducibility of the encoded optical fingerprints.

The objectives of this chapter are twofold: (1) to characterise the fluorescence and structural properties of GQDs under different deposition and imaging conditions; and (2) to evaluate the performance of GQD-based O-PUFs through image-based binary encoding and statistical analysis. Together, these efforts demonstrate the potential of GQDs as environmentally friendly, tuneable, and physically unclonable photonic materials.

4.1 Introduction: Green-Synthesized Graphene Quantum Dots for Optical PUFs

Optical physical unclonable functions (O-PUFs) exploit inherent material disorder to generate unique optical responses that are physically unclonable and digitally verifiable[106,107]. Quantum dot (QD)-based systems have gained prominence due to their bright, tuneable photoluminescence and compatibility with scalable fabrication methods[108]. Current QD-O-PUF approaches typically rely on either spatial randomness (QD distributions) or multi-dimensional optical encoding (spectral, temporal, or polarization characteristics) to enhance security[108,109]. However, practical implementation faces challenges including environmental instability (particularly for perovskite QDs), toxicity concerns with heavy-metal QDs, and complex readout requirements that limit real-world deployment[110,111].

Graphene quantum dots (GQDs) present a promising alternative, combining zero-dimensional quantum confinement effects with the chemical robustness, low toxicity, and biocompatibility of carbon-based materials[112,113]. Unlike conventional semiconductor QDs, GQDs exhibit photoluminescence arising from both quantum-confined sp^2 domains and surface/edge functional groups, leading to excitation-dependent emission and environmental sensitivity that provide multiple intrinsic entropy source" for security applications[114,115]. This intrinsic heterogeneity enables the creation of complex optical fingerprints without requiring toxic precursors or complex lithography [116].

Recent advances in GQD-based anti-counterfeiting demonstrate their potential for security applications. GQDs have been developed as tuneable fluorescent inks[117], lifetime-encoded tags[118], and time-multiplexed systems[119] that introduce additional security dimensions. However, most studies remain focused on encryption rather than formal PUF implementation, with limited evaluation of standard PUF metrics such as inter-device uniqueness, intra-device reproducibility, and entropy density under realistic conditions [120].

The synthesis approach plays a crucial role in determining GQD properties and applicability. Green synthesis routes, particularly hydrothermal processing of biomass waste like spent tea leaves, offer sustainable, low-cost production while naturally introducing oxygen-containing surface groups that enhance dispersion and optical tunability[121,122]. This method inherently produces variability in size, edge chemistry, and functionalization—features that contribute to the physical randomness essential for PUF operation [123]. When combined with scalable deposition techniques such as electrospray, biomass-derived GQDs can generate spatially complex, irreproducible emission patterns suitable for high-entropy optical encoding [124].

Despite these advances, a significant research gap exists in the development of formally evaluated, green-synthesized GQD O-PUFs that integrate sustainable material design with rigorous security performance assessment[120,125]. Specifically, there is a need to translate biomass-derived GQDs into a comprehensive PUF pipeline encompassing defined challenge-response protocols, reliable binary key extraction, and systematic evaluation under practical operating conditions[126].

This study addresses this gap through the development of an O-PUF platform based on hydrothermally synthesized GQDs derived from spent oolong tea waste. The research objectives include establishing a green, scalable synthesis route for GQDs from biomass waste, followed by comprehensive characterization of the structural and optical properties of GQDs. Building on this foundation, the work aims to optimize deposition methods to maximize spatial entropy and pattern uniformity, implement a reproducible encoding strategy using local binary pattern algorithms, and finally evaluate PUF performance using standard metrics including bias, inter-Hamming distance.

The experimental approach encompasses material synthesis, structural characterization (Raman, AFM), optical analysis (UV-Vis, PL spectroscopy), deposition optimization (drop-casting vs. electrospray), and security performance evaluation. By bridging sustainable nanomaterial synthesis with hardware security engineering, this work aims to deliver an eco-friendly, high-entropy O-PUF platform suitable for next-generation authentication and anti-counterfeiting applications.

4.2 Visual Evolution of Graphene Quantum Dots (GQDs) derived from Spent Oolong Tea

The synthesis of graphene quantum dots (GQDs) from spent oolong tea follows a multistep purification process to isolate fluorescent nanomaterials from organic biowaste. Figure 4.2-1 presents a visual summary of each synthesis stage, highlighting distinct changes in colour and clarity that reflect underlying physical and chemical transformations. These observable shifts serve as real-time indicators of synthesis progression and the emergence of photoluminescent graphene quantum dots (GQDs).

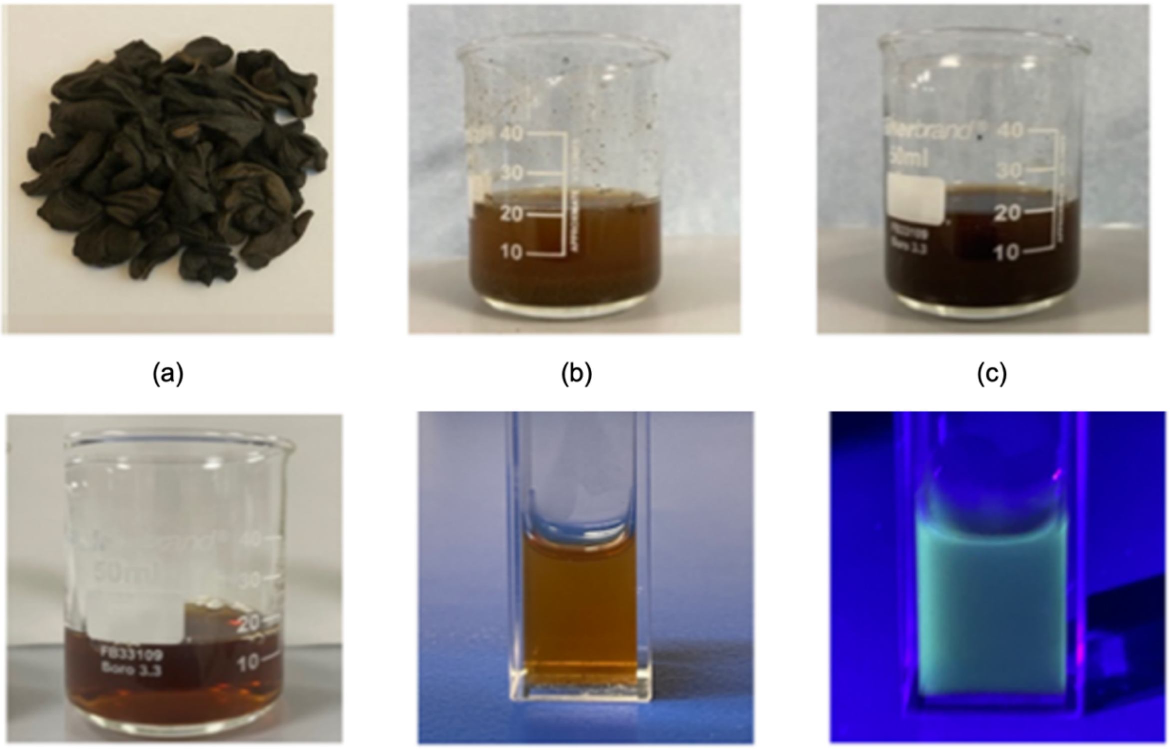

(a) (b) (c)

(d) (e) (f)

Figure 4.2-1 Visual evolution of graphene quantum dots derived from spent oolong tea at key synthesis stages: (a) Dried spent oolong tea leaves(b) 20ml initial raw tea–water precursor solution exhibits a deep brown colour, reflecting its rich organic content; (c) 20ml post-hydrothermal treatment; (d) 18ml post-centrifugation; (e) 1ml GQDs after dialysis purification; (f) 1ml final fluorescent GQDs under 450 nm UV light.

Each purification step is accompanied by noticeable colour shifts. The initial precursor solution (B), formed by dispersing raw tea powder in water, appears as a dense, dark-brown slurry rich in organic compounds but does not exhibit any visible photoluminescence. After hydrothermal treatment (C), the solution darkens further, suggesting the formation of polyaromatic domains through dehydration and aromatization—hallmarks of early-stage carbonization[127,128]. Although this stage signals the onset of graphene nanodot formation, the solution remains heterogeneous and contains residual organic matter.

Centrifugation eliminates coarse particulates and unreacted matter, producing a more homogeneous, clarified brown solution (D) enriched with smaller carbon nanodots. Subsequent dialysis removes low-molecular-weight by-products and ionic impurities, yielding a light-yellow transparent solution (E). The increasing clarity of the solution throughout purification signifies the effective removal of unreacted organics and impurities, reducing optical background noise and enhancing luminescence quality. Notably, the transition from a dark, opaque precursor to a transparent yellow solution indicates improved optical purity.

Under 450 nm excitation, the purified GQD dispersion exhibits a bright green photoluminescence readily visible to the naked eye (Figure 4.2.1(f)). The origin of this green emission arises from electronic transitions in π-conjugated sp^2 carbon domains formed during carbonisation of the tea-derived precursors. As the precursor aromatises into small sp^2 clusters, delocalised π electrons undergo π–π^* transitions upon absorption of UV photons, and radiative relaxation from these excited states produces the observed visible photoluminescence [129]. In parallel, oxygen-containing surface groups (e.g. carbonyl and carboxyl species) introduce additional surface-localised states within the bandgap, so that recombination via these surface states broadens and modulates the green emission band [130]. These mechanistic assignments are examined quantitatively in the subsequent UV–Vis and excitation-dependent PL analyses (Sections 4.5.1–4.5.2), which confirm both the photoluminescent origin and excitation-dependent tunability of the synthesised GQDs. This characteristic emission provides clear visual evidence of the formation of fluorescent carbon nanodomains associated with graphene quantum dots. The spatially homogeneous intensity of the fluorescence indicates that non-emissive organic residues have been effectively removed during purification, allowing the intrinsic photoluminescence of the nanodots to dominate.

Together with the transformation from a dense brown precursor to a fluorescent yellow solution, this behaviour reflects increasing structural order and optical purity in the synthesised GQDs and provides a visual indication of the conversion of biowaste into a photoluminescent nanomaterial. The observed luminescence characteristics are consistent with previous reports on biomass-derived GQDs, reinforcing the effectiveness of tea waste as a low-cost and sustainable carbon source[131-133].

4.3 Structural Characterisation of GQDs

To understand the internal structure and surface morphology of the graphene quantum dots (GQDs), Raman spectroscopy and atomic force microscopy (AFM) were employed. These complementary techniques provide insights into graphitic domain formation, defect density, particle dimensions, and nanoscale distribution—key structural factors that influence photoluminescence performance and the viability of GQDs in physically unclonable function (PUF) applications.

4.3.1 Raman spectroscopy analysis

Raman spectroscopy was used to investigate the carbon structure of the synthesised GQDs. As shown in Figure 4.3.1-1, the blue curve corresponds to the experimental Raman spectrum in the 1200–1700 cm^{-1} region, while the green and orange dashed curve represents the fitted spectrum used to extract the positions and intensities of the G and D bands. Prior to fitting, the raw experimental spectrum was baseline-corrected to remove the broad background signal, and each peak (D and G) was modelled using a Lorentzian function:

$$I(\omega) = \frac{A}{\pi} \frac{(0.5\Gamma)}{(\omega-\omega_0)^2+(0.5\Gamma)^2} \text{ (Equation 4.3.1-1)}$$

Where A is the peak area, Γ is the FWHM, and ω_0 is the peak centre. The fitting was performed by nonlinear least-squares optimisation (Levenberg-Marquardt) algorithm to minimal residual error ($R^2 > 0.99$, R^2 is the coefficient of determination). The fitted spectrum exhibits two prominent features: the D band at ~1369.3 cm^{-1}, associated with disorder and sp^3-hybridised carbon such as edge defects, vacancies and oxygenated functional groups, and the G band at ~1585.1 cm^{-1}, arising from the in plane E_{2g} stretching mode of sp^2-bonded carbon atoms within graphitic domains [134,135].

The D band originates from the A_1g breathing mode of aromatic sp^2 rings and is active by translational symmetry is broken by defects, edges or sp^3 sites, whereas the G band reports on the extent of ordered sp^2 domains [136-140]. Consequently, the intensity ratio I_D/I_G serves as a sensitive probe of defect density, domain size and overall graphitic ordering [132-135,141-142]. Reported values typically range from 0.2–0.5 for highly ordered graphite, 0.8–1.0 for moderately disordered or oxidised graphene quantum dots, and >1.2 for amorphous carbon[136,140]. In this work, the intensity ratio $I_D/I_G \approx 0.89$ reflect a moderate level of structural disorder. This is consistent with GQDs comprising well-developed sp^2-hybridized cores that are peripherally decorated with defect-rich, oxygenated edges, a morphology introduced by the hydrothermal carbonization process.

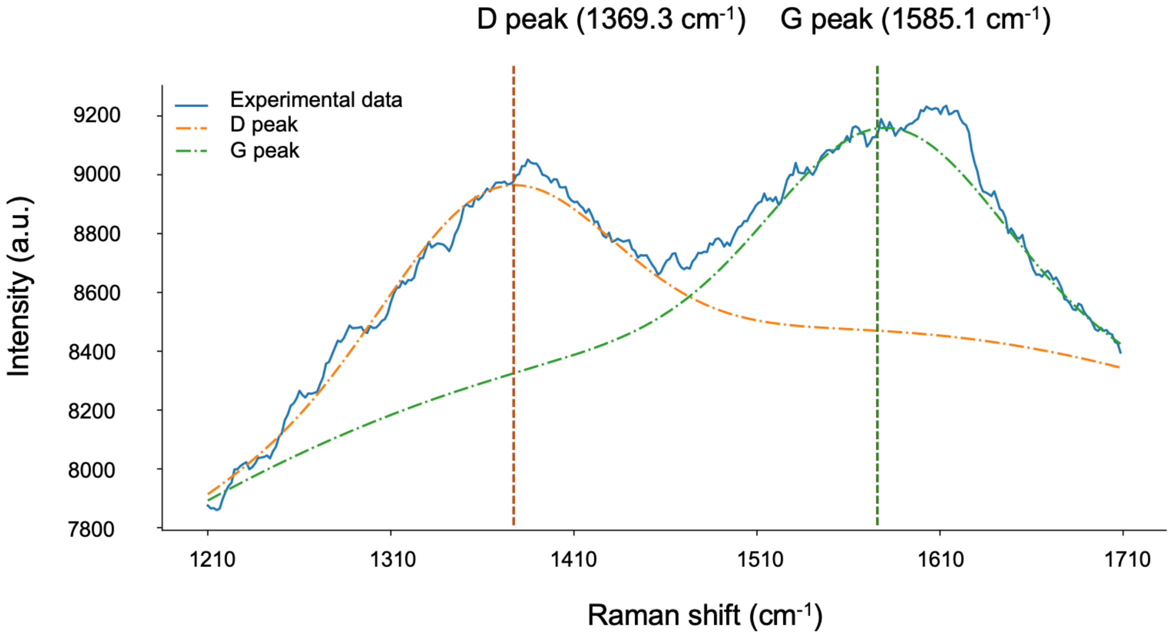

Figure 4.3.1-1 Raman spectrum of the synthesised graphene quantum dots (GQDs) in the 1200–1700 cm^{-1} region. The blue curve shows the experimental spectrum, while the yellow dashed curve represents the Lorentzian fit obtained by modelling the D and G bands with two Lorentzian functions and a linear background after baseline correction.

This intermediate disorder level is characteristic of few-nanometre GQDs, where edge-related defects dominate over in-plane lattice damage. Previous studies have shown that introducing oxygen-containing groups (C–O, C=O, COOH) and reducing the lateral size of graphene domains both drive I_D/I_G into the 0.8–1.0 range, corresponding to an optimally controlled structural disorder that balances crystalline π-conjugated regions and defect-activated sites[143]. Thus, the Raman results indicate that the GQDs produced by hydrothermal synthesis from spent tea leaves form a nanocrystalline, defect-engineered graphitic structure in which sp^2 cores preserve electronic delocalisation, while oxidised edge states provide radiative recombination centres that enhance photoluminescence without fully disrupting graphitic ordering. Such controlled structural disorder is advantageous for optical physically unclonable functions (PUFs), as it increases spatial entropy and yields distinct fluorescence signatures required for unclonable optical encodings.

4.3.2 AFM Morphology and Size Distribution

AFM was used to assess the morphology and size distribution of the GQDs on silicon substrate. The 12 µm × 12 µm scan (Figure 4.3.2-2) shows a well-dispersed nanodots across the surface without large-scale aggregation, while the higher-resolution scan 0.7 µm × 0.7 µm (Figure 4.3.2-1) resolves discrete particles with uniform lateral separation.

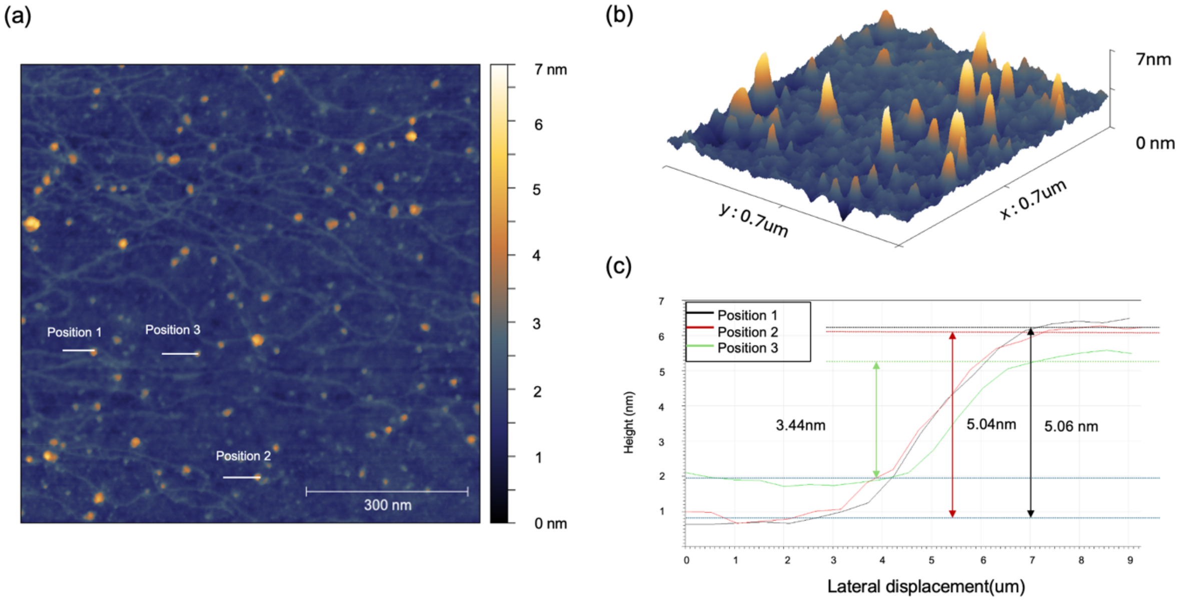

Figure 4.3.2-1: AFM characterisation of the GQD sample on Si/SiO_2. (a) AFM height (topography) map showing dispersed nanoscale features across the surface; the colour scale indicates a height range of 0–7 nm. Three representative line-scan locations are marked (Positions 1–3). Scale bar: 300 nm. (b) Corresponding 3D rendering of the same area (0.7 µm × 0.7 µm), highlighting the surface height variation. (c) Height profiles extracted from the line scans at Positions 1–3.

Figure 4.3.2-1 shows a uniform distribution of GQD nanodots across the silicon substrate, without large-scale clustering or continuous film formation. The AFM topography (a) and 3D rendering (b) indicate that the GQDs are deposited predominantly as isolated, laterally separated particles rather than forming extended agglomerated islands. Consistent with this morphology, the representative height profiles (c) show modest heights for individual GQDs of ~5.04 nm (Position 1), ~5.06nm (Position 2), and ~3.44 nm (Position 3), consistent with a few-layer thickness regime and suggesting that most deposited dots are thin rather than tall, stacked aggregates. Occasional brighter features approaching the upper colour-scale limit are more likely due to local overlap/stacking of multiple dots than pervasive aggregation.

Size analysis of >100 particles (Figure 4.3.2-2) was performed by measuring the lateral dimensions of individual GQDs from tapping-mode AFM height images acquired over a 12 μm × 12 μm area, ensuring sufficient particle coverage and statistical reliability.

Topographic analysis was carried out in Gwyddion: images were flattened to remove background slope, and a threshold-based particle detection was used to identify individual dots, with overlapping or poorly resolved features excluded. The size and thickness of the graphene quantum dot (GQDs) were quantified from AFM topography images using a standard grain analysis workflow in Gwyddion. The procedure involved: (i) plane levelling to correct for background tilt, (ii) feature segmentation via the Mark by Threshold tool to isolate individual protrusions, (iii) manual mask cleaning to remove small artefacts and separate aggregated features, and (iv) extraction of statistical parameters for each grain. The particle height was defined as the grain maximum height (z_{max}), and the apparent lateral diameter was calculated as the equivalent diameter $d = 2r_{\mathrm{eq}}$, where r_{eq} is the equivalent radius derived from the projected grain area.

The lateral size distribution (Figure 4.3.2-2(c)) was fitted with a lognormal model, which is appropriate for describing the right-skewed size distributions typical of nanoparticle populations arising from multiplicative growth or fragmentation processes[144-147]. The fit yielded a mean apparent lateral size of ~3.69 nm with a standard deviation of

~1.94 nm, indicating a moderately polydisperse population centred in the few nanometre range. It is important to note that these are apparent lateral dimensions, as AFM measurements are broadened by tip–sample convolution and pixel discretisation, leading to systematic overestimation compared to transmission electron microscopy (TEM) [146-147].

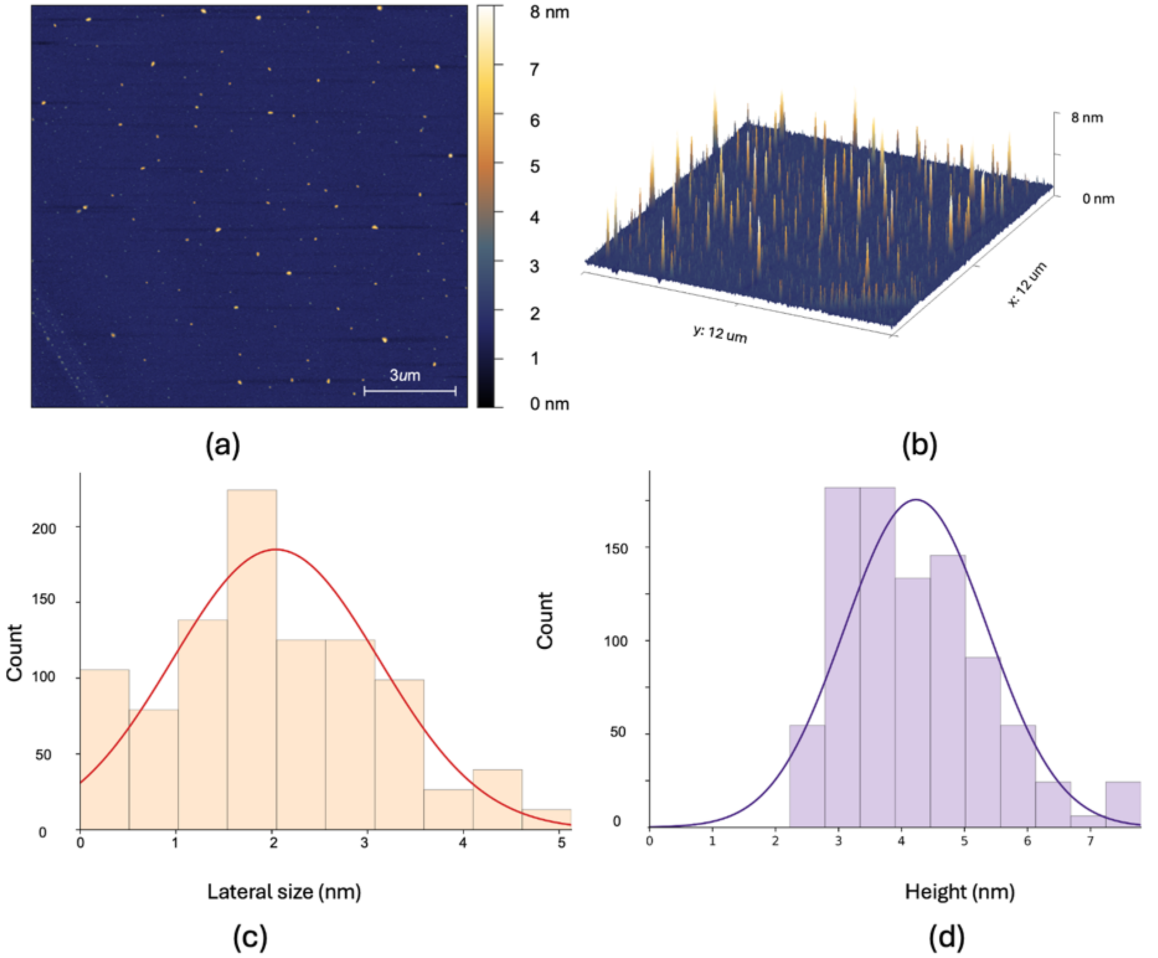

Figure 4.3.2-2. AFM topography and statistical size analysis of GQDs on silicon. (a) tapping-mode AFM height image acquired over a 12 µm × 12 µm area; colour scale: 0–16.4 nm. (b) Corresponding 3D surface rendering highlighting the spatial distribution of discrete GQDs. (c) Histogram of lateral particle size (diameter) measured from the same AFM images, showing the overall size distribution of the GQD. (d) Histogram of particle height extracted from >100 individual GQDs after image flattening, threshold-based particle detection, and exclusion of overlapped/poorly resolved features.

Conversely, the height distribution (Figure 4.3.2-2(c)) was plotted by using a Lorentz fit, as height measurements are less susceptible to tip-radius effects and their distribution is often dominated by symmetric instrumental noise, local substrate variability, and finite sampling, rather than the skewed tails characteristic of lateral size distributions. The Lorentz fit gives an average particle height of 3.84 nm (σ ≈ 1.29 nm). However, AFM-measured thicknesses for graphene-based materials on oxide substrates are frequently overestimated due to interfacial water layers, adsorbates, and imaging-mode artefacts—a well-documented phenomenon contributing to reported variations in monolayer graphene step heights. Considering the typical graphite interlayer spacing of 0.34 nm and the additional ~0.4–1.0 nm contribution from surface adsorbates and substrate interactions in AFM measurements, the observed height corresponds to approximately 3–5 layers [148,149]. Although precise layer counting via AFM is constrained by tip–sample convolution, this thickness range aligns with few-layer GQD structures.

The extracted dimensions are consistent with those reported for solution-processed GQDs. For instance, hydrothermal or biomass-derived GQDs are frequently in the sub-5 nm lateral size regime, with AFM height profiles of ~1–2 nm commonly interpreted as few-layer structures after accounting for systematic offsets[150-153]. The results therefore indicate that the synthesis produces predominantly few-nanometre, few-layer GQDs. This size and thickness regime is highly relevant for exploiting size-dependent and quantum-confined optical and electronic properties in subsequent applications.

Overall, the relatively narrow distributions in both lateral size and height imply good uniformity and minimal aggregation during deposition, which is important for reproducible photoluminescence and robust binary encoding in optical PUF applications. Uniform dispersion also promotes spatially unpredictable nanoscale features, supporting high-entropy, tamper-resistant optical identifiers. Together with the Raman results, the AFM data confirm the formation of well-dispersed, few-layer GQDs with controlled morphology and spatial distribution suitable for secure optical fingerprinting[104,141].

4.4. UV–Vis and Steady-State Photoluminescence of GQDs

Before integrating graphene quantum dots (GQDs) into an optical PUF system, their fundamental photophysical properties must be characterised. This section presents a systematic analysis of the optical behaviour of oolong tea–derived GQDs, beginning with their intrinsic absorption and steady-state emission (4.4.1). It then investigates their excitation-dependent photoluminescence (4.4.2), a hallmark of heterogeneous carbon nanomaterials, and concludes by examining how GQD concentration can be used as a tuning parameter to modulate spectral output (4.4.3). This foundational characterisation establishes the link between the GQDs optical properties and the functional requirements for entropy-rich, unclonable encoding.

4.4.1 UV–Vis Absorption and Photoluminescence of GQDs

The UV–visible absorption spectrum of the graphene quantum dots (GQDs), synthesized via a hydrothermal route from spent oolong tea leaves, is shown in Figure 4.4.1-1(a). A strong absorption band centred at 269 nm observed, assigned to π–π* transitions within conjugated aromatic C=C domains of the sp^2 carbon core. According to molecular-orbital theory, these transitions correspond to promotion of π electrons from the highest occupied to the lowest unoccupied molecular orbitals in fused ring systems, which typically results in absorption in the UVC–UVB region((≈200–315 nm, spanning high- to medium-energy ultraviolet radiation) and shifts to longer wavelength as the effective π-conjugation length increases. A weaker shoulder at ~316 nm is attributed to n–π* transitions involving lone-pair electrons on carbonyl- and amide-type surface groups (C═O/C–N), which require lower excitation energy and therefore appear at longer wavelength in the Ultraviolet A region[154].

In the oolong tea–derived GQDs, these electronic transitions are consistent with the expected chemical structure of hydrothermally carbonised oolong tea, where polyphenols and catechin-based aromatics generate graphitic sp^2 domains, while oxidised carbohydrates, proteins and amino-acid–derived species provide abundant surface carbonyl, amide and other heteroatom-containing functionalities that give rise to the observed n–π* band.

Complementary photoluminescence (PL) measurements under 450 nm excitation revealed a strong green emission peak at ~512.7 nm (Figure 4.4.1-1(b)). Comparing this emission maximum with the primary absorption band at 269 nm (Figure 4.4.1-1a) yields a Stokes shift of ~243.7 nm ($\Delta\lambda = \lambda_{em} - \lambda_{abs}$), indicating substantial non-radiative relaxation between the initial electronic excitation and photon emission. Such a large Stokes shift is characteristic of surface-functionalised graphene quantum dots, where excitation of π–π* transitions in the sp^2 domains is followed by energy dissipation (vibrational relaxation and internal conversion) and subsequent radiative recombination via lower-energy surface or defect states.

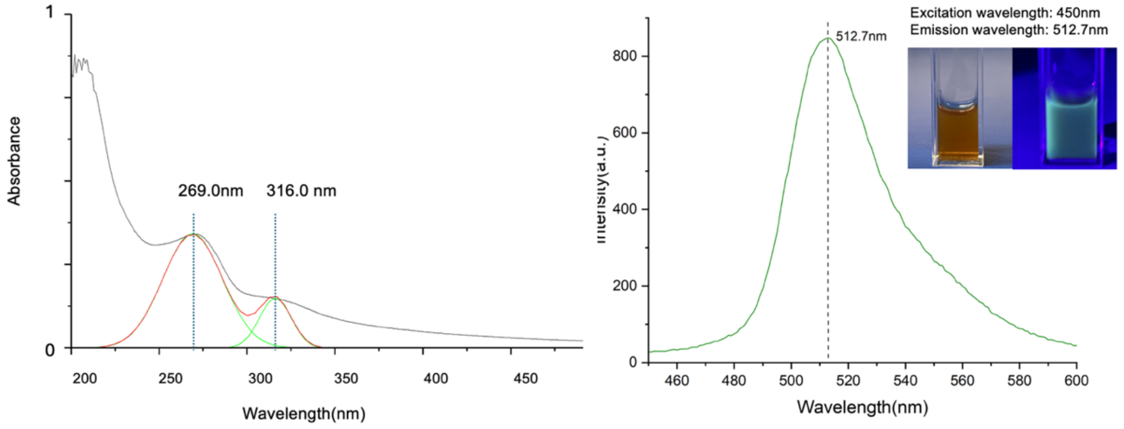

(a) (b)

Figure 4.4.1-1. Optical absorption and photoluminescence of tea-derived GQDs. (a) UV–vis absorption spectrum of the aqueous GQD dispersion (black curve) with multi-peak Larentz fitting (coloured curves), revealing two main bands centred at 269.0 nm and 316.0 nm. (b) Steady-state photoluminescence spectrum recorded under 450 nm excitation, showing a strong green emission maximum at 512.7 nm, inset: photographs of the GQD solution in ambient light (left, brown) and under 450 nm UV illumination (right), displaying bright green fluorescence visible to the naked eye.

The bright green fluorescence is clearly visible to the naked eye under UV illumination(450nm), with the GQD solution appearing brown in ambient light and emitting green under 450 nm excitation, as shown in the inset. This pronounced Stokes shift, together with the bright visible fluorescence and the presence of both π–π* and n–π* transitions, confirms the formation of optically active, surface-functionalised GQDs and is consistent with previously reported optical behaviour of biomass-derived GQDs synthesised from tea and other plant precursors [155,156]. These combined spectral features point to a hybrid core–shell architecture, comprising a conjugated graphitic carbon core surrounded by an oxygen-rich surface layer. The resulting surface states play a central role in governing the excitation-dependent photoluminescence and provide oxidation-induced emissive sites that underpin the tuneable fluorescence response[157,158].

4.4.2 Excitation-Dependent Photoluminescence of GQDs

To assess the emission tunability of the synthesized graphene quantum dots (GQDs), a series of photoluminescence (PL) spectra were recorded under excitation wavelengths ranging from 320 nm to 490 nm (Figure 4.4.2-1). The emission peak shifts gradually from 403.1 nm to 511.9 nm, indicating a pronounced excitation-dependent fluorescence—a hallmark feature of carbon-based nanodots with heterogeneous surface states and varied emissive sites[159,160].

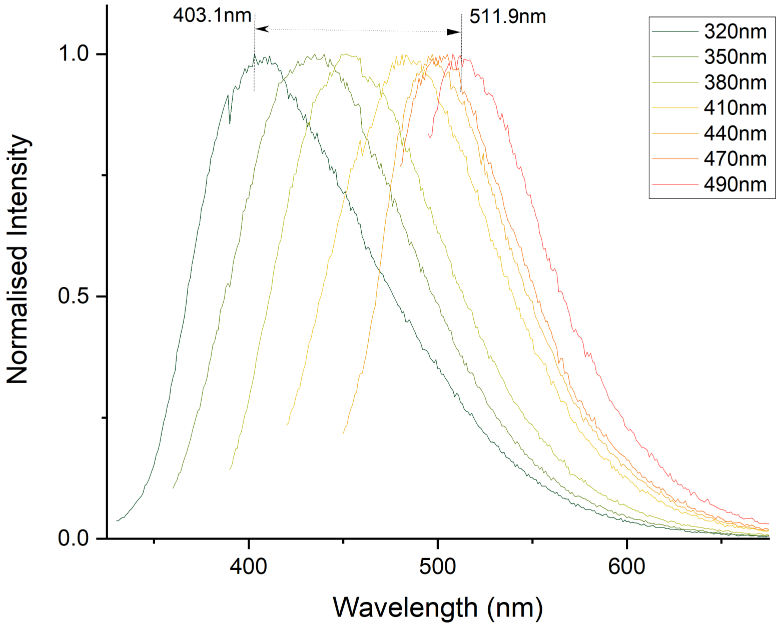

Figure 4.4.2-1 Normalized photoluminescence spectra of GQDs under excitation wavelengths from 320 nm to 490 nm. A red-shift in the emission peak from 403.1 nm to 511.9 nm confirms excitation-dependent fluorescence, attributed to surface state diversity and quantum confinement effects.

In graphene quantum dots (GQDs), the red shift of the PL with increasing excitation wavelength is often attributed to a heterogeneous distribution of emissive centres. The tea-derived GQDs contain size-distributed sp^2 carbon domains (core states) and oxygen-related surface/defect sites, resulting in a distribution of electronic states across multiple energy levels [161]. Under higher-energy excitation, emission is dominated by higher-energy transitions associated with smaller sp^2 domains and π–π* excitation within the carbon core, resulting in blue-shifted PL [162]. As the excitation wavelength increases, photoexcitation increasingly populates lower-energy emissive centres, including larger sp^2 domains (reduced quantum confinement → smaller effective bandgap) and surface/defect-related states introduced by oxygen-containing groups (e.g., C=O, COOH, OH)[163]. Following excitation, charge carriers can undergo rapid non-radiative relaxation into these lower-energy trap states before radiative recombination, which shifts the PL to longer wavelength[164].

Thus, the excitation-dependent red shift can be rationalised in terms of (i) quantum confinement across a distribution of sp^2 domain sizes and (ii) relaxation via defect or functional-group-derived surface states. From a quantum-confinement perspective, the electronic bandgap increases as the lateral size of the sp^2-hybridised domain decreases[165]. When the size of the sp^2-hybridised domain becomes comparable to the exciton Bohr radius (~2–5 nm), carrier motion is spatially confined, leading to discrete energy levels and higher transition energies, which leading to blue-shifted emission. Conversely, larger domains exhibit reduced confinement and narrower bandgaps, resulting in lower-energy (red-shifted) emission. In addition, structural disorder and oxygen-containing functional groups (e.g., C=O, COOH, OH) introduce surface trap states within the bandgap, which facilitate radiative recombination at lower energies[166,167].

To quantify changes in emission bandwidth, the full width at half maximum (FWHM) was extracted from the normalised PL spectra. The FWHM decreases from ~110 nm (Ex 330–360 nm) to ~79–80 nm (Ex 450–470 nm), indicating a modest narrowing of the emission band at longer excitation wavelengths. This behaviour can be rationalised by spectral selection within an in-homogeneously broadened population of emissive centres: because the GQDs comprise a distribution of emissive sub-states (core-, surface/defect-, and/or molecular-like centres), varying excitation energy modulates the relative contribution of these sub-populations to the measured PL [168,169]. At longer excitation wavelengths, photoexcitation increasingly populates a narrower set of lower-energy emissive centres, thereby reducing contributions from higher-energy emissive pathways and minimising spectral superposition between multiple components [170]. Consequently, the PL peaks red shifts while the emission profile becomes less dispersed.

The observed excitation-dependent PL is consistent with previous reports on GQDs synthesised from green and sustainable precursors. For example, Li et al. (2016) observed comparable excitation-dependent red-shifting in biomass-derived GQDs [171,172]. Notably, Yogesh et al. (2017) further reported an excitation-dependent decrease in the PL linewidth (FWHM) for carbon nanoparticles, indicating that spectral narrowing with increasing excitation wavelength can also occur in heterogeneous carbon-dot systems [173]. Overall, the excitation-dependent PL confirms that the tea-derived GQDs possess a heterogeneously functionalised core–shell structure with multiple emissive sites, underscoring their potential for tuneable optical security and fluorescence-based applications.

4.4.3 Concentration-Dependent Photoluminescence and Optimisation for O-PUF Applications

In the development of optical physical unclonable functions (O-PUFs), a central objective is to maximise entropy density—the extractable, unpredictable information per unit area. This is evaluated alongside critical performance parameters such as bit uniformity, uniqueness, and reliability[174]. Information-theoretic analyses show that effective entropy is constrained by spatial correlations and readout noise, making it essential to maximise the number of statistically independent features [175]. In practice, this is pursued through two primary methods: (i) increasing the density of resolvable independent sites, and (ii) increasing the number of independent response states per site—such as by using multi-channel spectral data—while ensuring stable readout [174,176]. For quantum dot-based O-PUFs, stochastic deposition methods produce random fluorescence patterns whose encoding capacity can scale with the number of particles [176,177]. Entropy density can be further enhanced by introducing additional optical degrees of freedom; for example, multi-colour quantum dots expand the symbol states per pixel and enable robust key extraction[177].

In this GQD-based O-PUF system, tuning the concentration serves as a scalable method to concurrently regulate photoluminescence (PL) characteristics and deposition quality. This dual control is critical because concentration simultaneously governs (a) fluorescence brightness and contrast, which impact readout robustness, and (b) surface coverage and feature density, which determine the number of independent sites—both fundamental to achieving high entropy density [174,176]. To investigate this concentration-dependent photoluminescence, GQD suspensions were prepared at three concentrations: 0.5 mg/mL, 1.0 mg/mL, and 1.5 mg/mL. Excitation-dependent PL spectra were recorded across the 320–570 nm range.

At the lowest concentration (0.5 mg/mL; Figure 4.4.3-1), the emission peak ranged from 403.1 nm to 508.5 nm under 320–470 nm excitation, consistent with predominantly surface-state (R1) recombination and minimal inter-dot interaction [178,179]. Emission was not detectable for excitations above 470 nm. While the spectrum remained excitation-tuneable, this sample exhibited weak intensity at longer wavelengths and a narrow overall emission bandwidth. This spectral limitation constrains the information content available for multi-channel spectral encoding, leading to low entropy capacity for binary key generation.

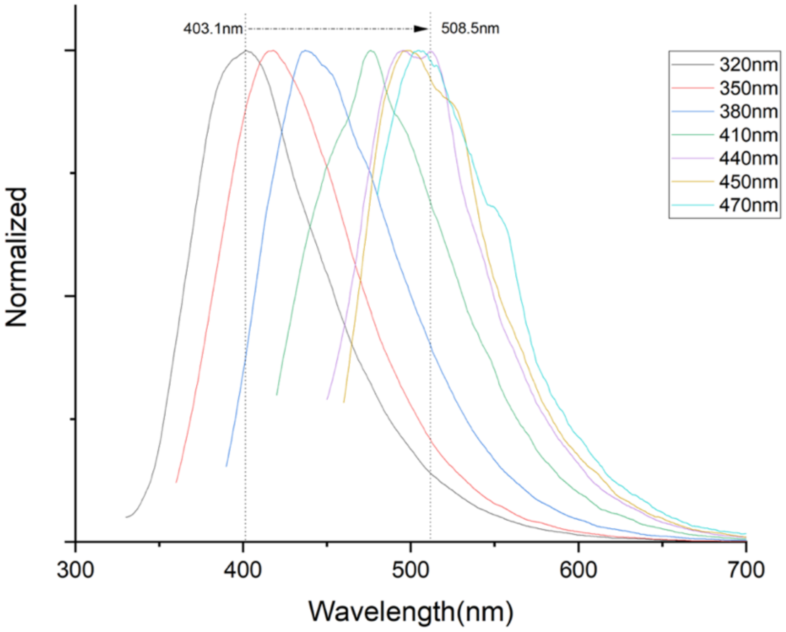

Figure 4.4.3-1. Excitation dependent photoluminescence (PL) spectra of 0.5 mg/mL GQDs recorded under 320–470 nm excitation.

In contrast, the medium concentration (1.0 mg/mL; Figure 4.4.3-2) exhibited emission from 515.07 nm to 567.05 nm under 470–530 nm excitation. Compared to the

0.5 mg/mL sample, this represents a significant red shift and an expansion of the total emission range: the emission maximum shifted from 508.5 nm to 567.05 nm, and the spectral window widened from 403.1–508.5 nm to 403.01–567.05 nm. This indicates the activation of additional emissive centres and a clear enhancement of longer-wavelength contributions. This behaviour can be attributed to two primary physicochemical mechanisms. First, the increased concentration enhances self-absorption, where emitted photons are reabsorbed by neighbouring dots, resulting in a red shift of the emission spectrum[180]. Second, stronger inter-dot interactions reduce the surface electric potential, which shifts the dominant radiative pathway from surface-state recombination (R1) to defect-level recombination (R2)[180,181].

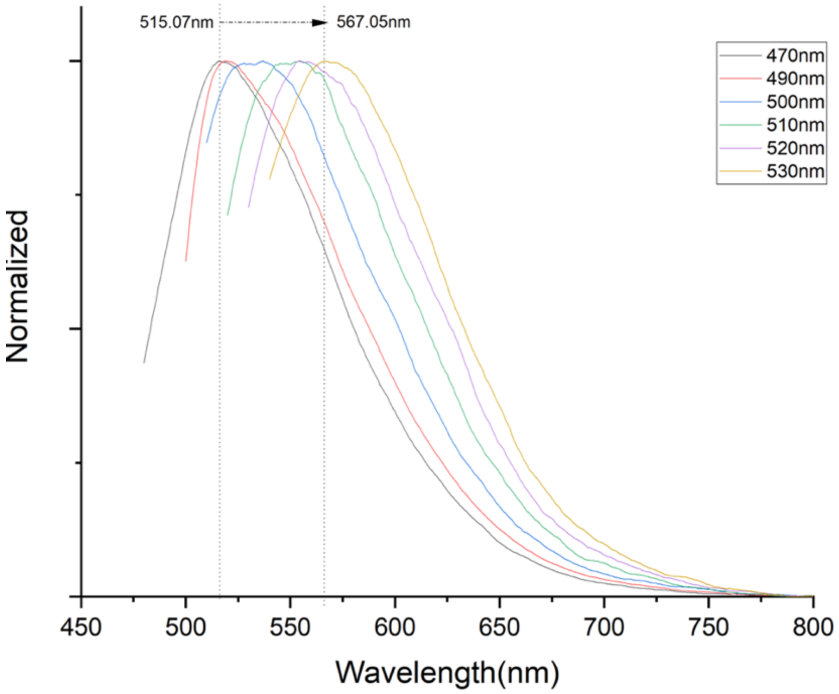

Figure 4.4.3-2. Excitation-tuneable photoluminescence of GQDs (1.0 mg mL⁻¹) under 470–530 nm excitation.

At the highest concentration (1.5 mg/mL; Figure 4.4.3-3), emission extended across a broad multi-colour range (~466–600 nm) under the 320–570 nm excitation range. This significant broadening and further red-shifting result from aggregation-induced effects. First, aggregation alters the local dielectric environment and introduces new surface states, leading to a broader distribution of energy levels [180]. The reduced inter-dot spacing creates a more carbon-rich, less solvent-dominated local optical environment, modifying the dielectric constant experienced by emitting domains[179]. This proximity promotes inter-dot electronic coupling (partial overlap of neighbouring sp²/π domains). Combined with the inherent heterogeneity in spacings, oxidation levels, and interface chemistries within aggregated clusters, this creates a wide spread of emissive energy levels[182]. Consequently, emission occurs from multiple, non-identical sites, collectively manifesting as a broadened and red-shifted PL spectrum[181].

Thus, GQD concentration is a critical parameter for tuning the photoluminescence (PL) properties that are essential to O-PUF performance. Among the tested concentrations, both 1.0 mg/mL and 1.5 mg/mL induce significant spectral broadening, which enhances the potential for multi-channel encoding and increases the theoretical entropy density per site. However, while a higher concentration favourably modulates the spectral emission range, excessive aggregation at 1.5 mg/mL may compromise the spatial randomness of the deposited features—a fundamental requirement for un-clonability. To identify the optimal trade-off between emission complexity (for entropy-rich encoding) and deposition quality (for spatial randomness), the concentration will be further optimized via fluorescence imaging in the following section (4.5.3). The objective is to identify an optimal concentration that delivers sufficient spectral breadth, stable deposition without detrimental aggregation, and the spatial randomness required to generate robust, unclonable optical fingerprints.

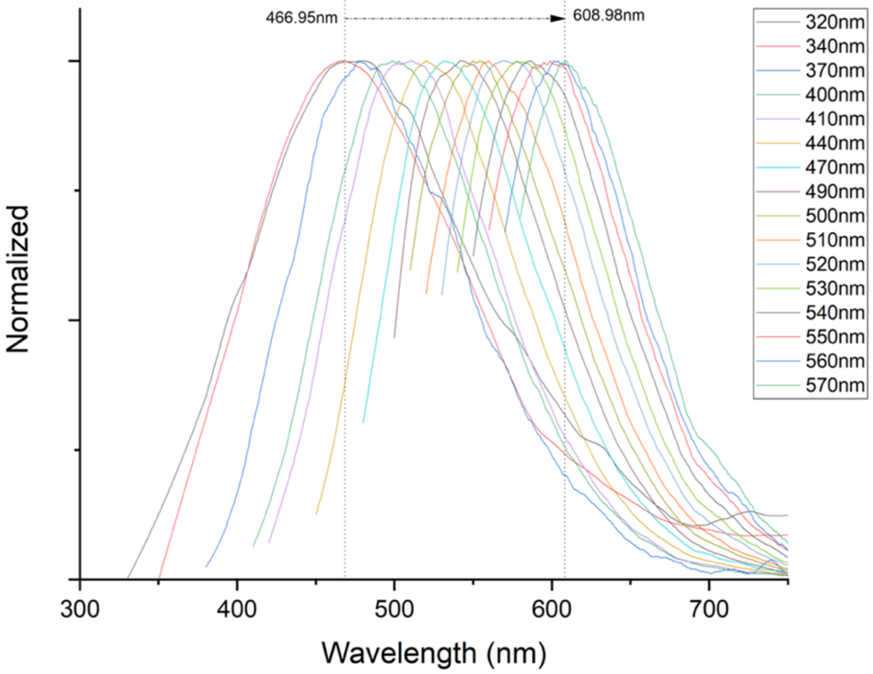

Figure 4.4.3-3. Excitation-tuneable photoluminescence of GQDs (1.5 mg mL⁻¹) recorded under 320–570 nm excitation.

4.5 Fluorescence Imaging of GQDs

Fluorescence imaging plays a vital role in the development of optical physical unclonable functions (O-PUFs), serving as the visual and quantifiable expression of GQD-based emission randomness. This section establishes the foundation for using fluorescence intensity maps to generate binary patterns. Achieving high entropy and device uniqueness requires imaging conditions that promote reproducibility, avoid overexposure, and capture fine spatial detail. As discussed in Section 4.4.3, GQDs demonstrated excitation-dependent multicolour emission. Among the RGB filters, the green channel (450–500 nm) consistently provided optimal image contrast and fidelity, making it ideal for entropy analysis. The broad visible emission of GQDs allows for multi-channel imaging using red, green, and orange filters. These filters act as emission channels, enabling spectral multiplexing and enhancing encoding versatility. To fine-tune imaging quality, a systematic evaluation of camera gain and exposure time was conducted using drop-cast samples. The results guided the standard imaging protocol used in subsequent electrospray-based O-PUF fabrication.

4.5.1 Fluorescence Imaging Parameter Optimization (Drop-Casting)

Drop-cast GQDs were imaged under three gain/exposure settings: gain 200–20 s, gain 200–30 s, and gain 300–30 s. Each sample was observed under green, orange, and red emission filters to evaluate contrast, signal saturation, and noise. Figure 4.5.1-1 compares the effect of acquisition settings on fluorescence image quality. At gain 200 and 20 s, signals were weak across all channels. Increasing to gain 300 and 30 s enhanced intensity but also introduced noticeable noise and partial saturation, particularly in the brightest regions. The best overall performance was obtained at gain 200 and 30 s, which provided strong, well-resolved fluorescence while avoiding oversaturation.

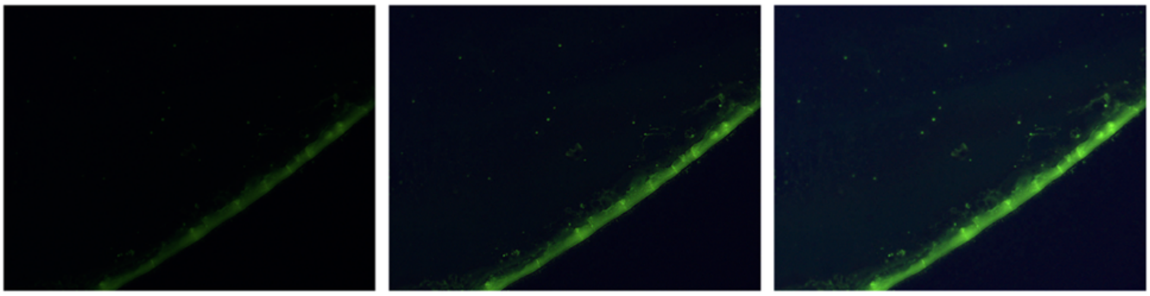

(a) (b) (c)

Green emission: Short Pass: 450nm; Long Pass: 500nm

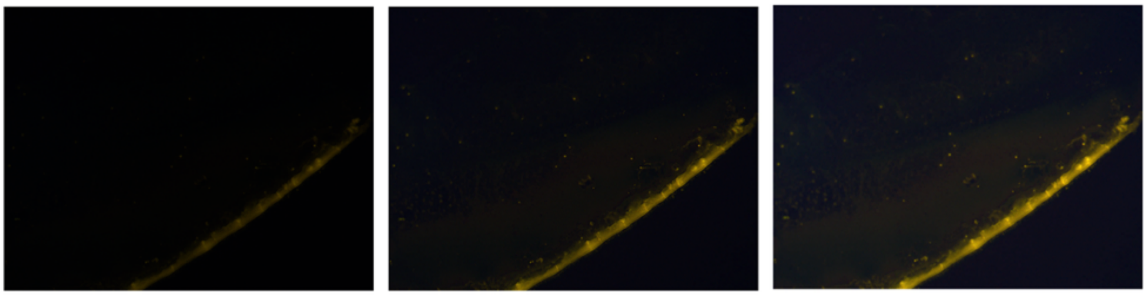

(d) (e) (f)

Yellow emission:Short Pass: 500nm; Long Pass: 550nm

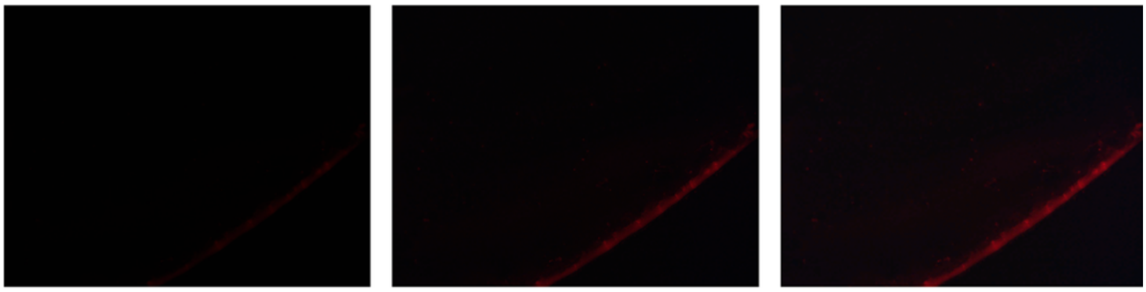

(g) (h) (i)

Red emission: Short Pass: 500nm; Long Pass: 550nm

Figure 4.5.1-1. Fluorescence images of GQDs under three emission filter settings: (a–c) Green emission (SP: 450 nm, LP: 500 nm); (d–f) Yellow emission (SP: 500 nm, LP: 550 nm); (g–i) Red emission (SP: 550 nm, LP: 600 nm). Each set corresponds to three imaging conditions: (a, d, g) Gain = 200, Exposure = 20 s; (b, e, h) Gain = 200, Exposure = 30 s; (c, f, i) Gain = 300, Exposure = 30 s. These images demonstrate the effect of gain and exposure time on fluorescence intensity and clarity across multiple emission channels.

Multicolour emission was visible under all three channels—green (~500 nm), orange (~550 nm), and red (~600 nm)—confirming the broad photoluminescence bandwidth of the GQDs. These observations validate the flexibility of GQD imaging and reinforce the choice of the green filter for quantitative fluorescence analysis and binary map generation. The final selected imaging setting is illustrated in Figure 4.5.1-2. This setting was validated through both drop-cast and electrospray imaging.

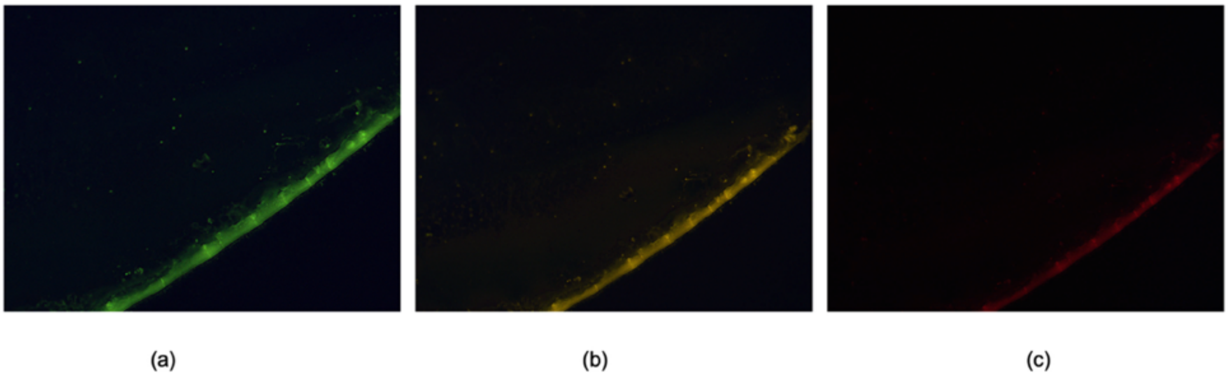

Figure 4.5.1-2. Fluorescence images of GQDs acquired under the optimized imaging condition: Gain = 200, Exposure = 30s; Emission filters used were:(a) Green (SP: 450 nm, LP: 500 nm), (b) Yellow (SP: 500 nm, LP: 550 nm), and (c) Red (SP: 550 nm, LP: 600 nm). This setting was selected for its optimal balance of signal intensity, spatial resolution, and reproducibility across multiple channels, and was used for all subsequent electrospray-based fluorescence imaging.

4.5.2 Deposition Method Comparison: Drop-Casting vs. Electrospray

Deposition method strongly affects the spatial distribution and randomness of fluorescence signals. To evaluate how deposition influences fluorescence pattern uniformity and randomness—critical factors for optical PUF generation—GQDs were deposited onto Si substrates using drop-casting and electrospray techniques, and the resulting emission patterns were imaged by fluorescence microscopy.

Under the optimised imaging setting (gain = 200, exposure = 30 s; SP 450 nm, LP 500 nm), the drop-cast films (Fig. 4.5.2-1a–c) exhibit pronounced non-uniformity characteristic of the coffee-ring effect. Panel (a) captures a section of the coffee-ring perimeter, visible as a bright curved fluorescent band at the pinned droplet edge, while the surrounding region is comparatively depleted. This behaviour arises from evaporation-driven capillary flow: solvent evaporates faster at the droplet edge, liquid from the centre flows outward to replenish the perimeter, transporting suspended GQDs toward the contact line. With the contact line remaining pinned during drying, particles accumulate at the edge while the central region becomes depleted, producing a ring-shaped fluorescence profile and spatially uneven emission[183]. Panels (b) and (c) show sparse, widely separated fluorescent dots with relatively little aggregation; however, the low emitter density leaves large background regions and limits the number of statistically independent features per unit area. As a result, although clustering is less pronounced away from the perimeter, the effective encoding area and entropy density remain restricted, and binary extraction becomes more sensitive to noise and threshold selection.

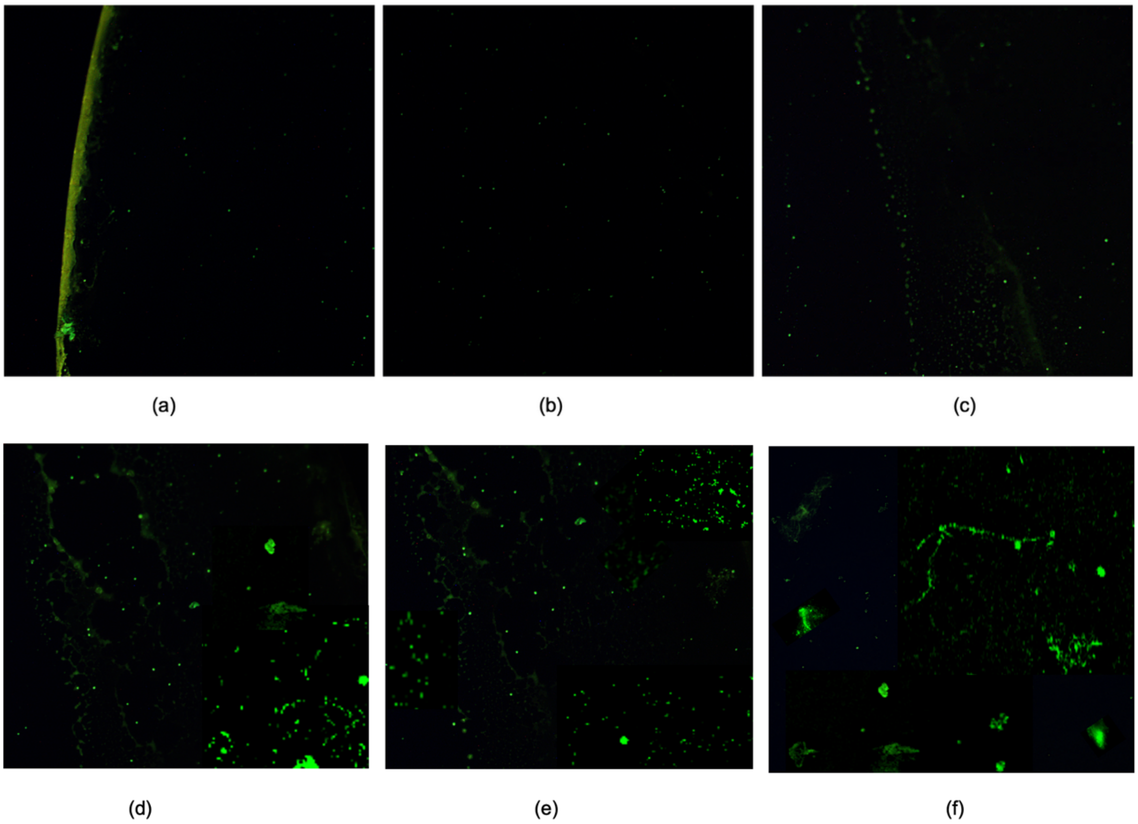

Figure 4.5.2-1. Comparison of fluorescence images of GQDs deposited by drop-casting and electrospray under identical imaging conditions (gain = 200, exposure = 30 s; green filter: SP 450 nm, LP 500 nm). (a–c) Drop-cast GQDs fluorescence images, showing typical coffee-ring artifacts, edge aggregation, and low spatial randomness. (d–f) Electrospray-deposited GQDs fluorescence images, showing uniform dot dispersion and enhanced spatial randomness—key features for high-entropy O-PUF encoding.

In contrast, electrospray deposition (Fig. 4.5.2-1d–f) produces a more uniform, stochastic dot pattern with well-distributed intensity fluctuations. Across panels (d)–(f), the GQD feature density remains broadly consistent, and the fluorescence intensity varies locally, generating a rich micro-texture without large-area intensity inhomogeneities, which associated with evaporation-driven capillary flow. Although occasional brighter clusters or elongated features are present, these remain isolated and localised, rather than forming continuous edge-enriched structures or generating a large-scale spatial pattern.

To quantify spatial randomness, each RGB fluorescence micrograph was converted into a background corrected green emission intensity map using an excess green transformation (Lorentz blur background subtraction, blur radius = 10 px),

$$Ig = \max(G - \max(R, B)\,, 0),\text{(Equation 4.5.2-1)}$$

which reduces low frequency shading and background bias prior to quantitative comparison [184-186]. Spatial inhomogeneity was assessed using four statistic metrics: (i) intensity inhomogeneity via the coefficient of variation ($CV=\sigma/\mu$); (ii) macroscopic deposition bias through an edge to centre intensity ratio, defined as the mean intensity in a 10 % border band divided by that in the central 50 % region; (iii) spatial correlation length, taken as the first radius at which the radially averaged 2D autocorrelation function decays below 1/e; and (iv) feature density and spacing, obtained by Otsu thresholding followed by connected component analysis (spots MPx^{-1}) and calculation of the median nearest neighbour distance—standard descriptors for point pattern dispersion [187,188].

Drop-cast GQD films exhibited pronounced spatial heterogeneity. This was characterized by significant nanoparticle aggregation at the edges (edge-to-centre intensity ratio up to 1.188), a wide range of electrical responses (CV range: 4.34–47.21), and a low density of emissive sites (0–179 spots MPx^{-1}; median: 23.7 spots MPx^{-1}). In sparse regions, the median distance between sites was large (~101.8 px). This non-uniform distribution is consistent with coffee-ring effects, which drive nanoparticle migration and reduce the number of independent emissive sites[189]. In contrast, electrospray-deposited GQD films showed consistently higher and more uniform feature densities (~198–508 spots MPx^{-1}), moderate nearest neighbour spacing (~14–19 px), short autocorrelation lengths (~4–6 px), and a narrow CV range (~4.54–5.74). This indicates a dense, spatially stochastic distribution of emitters with correlation lengths confined to a few pixels and no emergent macroscopic patterning. Collectively, these quantitative metrics indicates that electrospray deposition produces spatial fluorescence emission patterns with higher effective entropy, characterised by a greater density of statistically independent emissive sites and reduced macroscopic artefacts.

Overall, the drop-cast images exhibited a distinct ring-like deposition morphology due to capillary flow, leading to a depleted and homogeneous interior, which compromises spatial randomness and introduces redundancy that can reduce the uniqueness and reproducibility of the extracted binary fingerprints. In contrast, electrospray deposition suppresses edge-enrichment and limits the formation of large aggregates, producing stochastic dot-like patterns with spatially distributed intensity fluctuations. This increases feature density while reducing long-range correlations, leading to higher pixel-level unpredictability and a more stable intensity distribution for thresholding—thereby supporting more robust binarization and higher-entropy O-PUF encoding. Accordingly, electrospray deposition was selected for all subsequent fluorescence imaging and binary map generation.

4.5.3 Electrospray Concentration Optimization

Building on the results from PL spectroscopy and fluorescence imaging of electrospray-deposited GQDs, this section finalizes the concentration to meet core O-PUF requirements. The analysis focuses on the critical interplay between fluorescence brightness, spatial randomness, and spectral output to identify the concentration that offers the optimal balance for entropy-rich encoding. Fluorescence images of electro sprayed GQDs at low (0.5 mg/mL), medium (1.0 mg/mL), and high (1.5 mg/mL) concentrations were compared (Figure 4.5.3-1). All images were acquired under the optimized settings (gain = 200, exposure = 30 s) using a green emission filter (SP 450nm, LP 500 nm) to assess pattern quality and brightness.

Low concentration (0.5 mg/mL) resulted in sparse dot coverage with weak fluorescence. The image shows discrete, bright features distributed across a largely dark background, indicating a low areal density of emissive sites. This sparsity decreases the number of statistically independent features per unit area and increases sensitivity to readout noise, as minor intensity fluctuations disproportionately affect thresholding and pattern assignment.

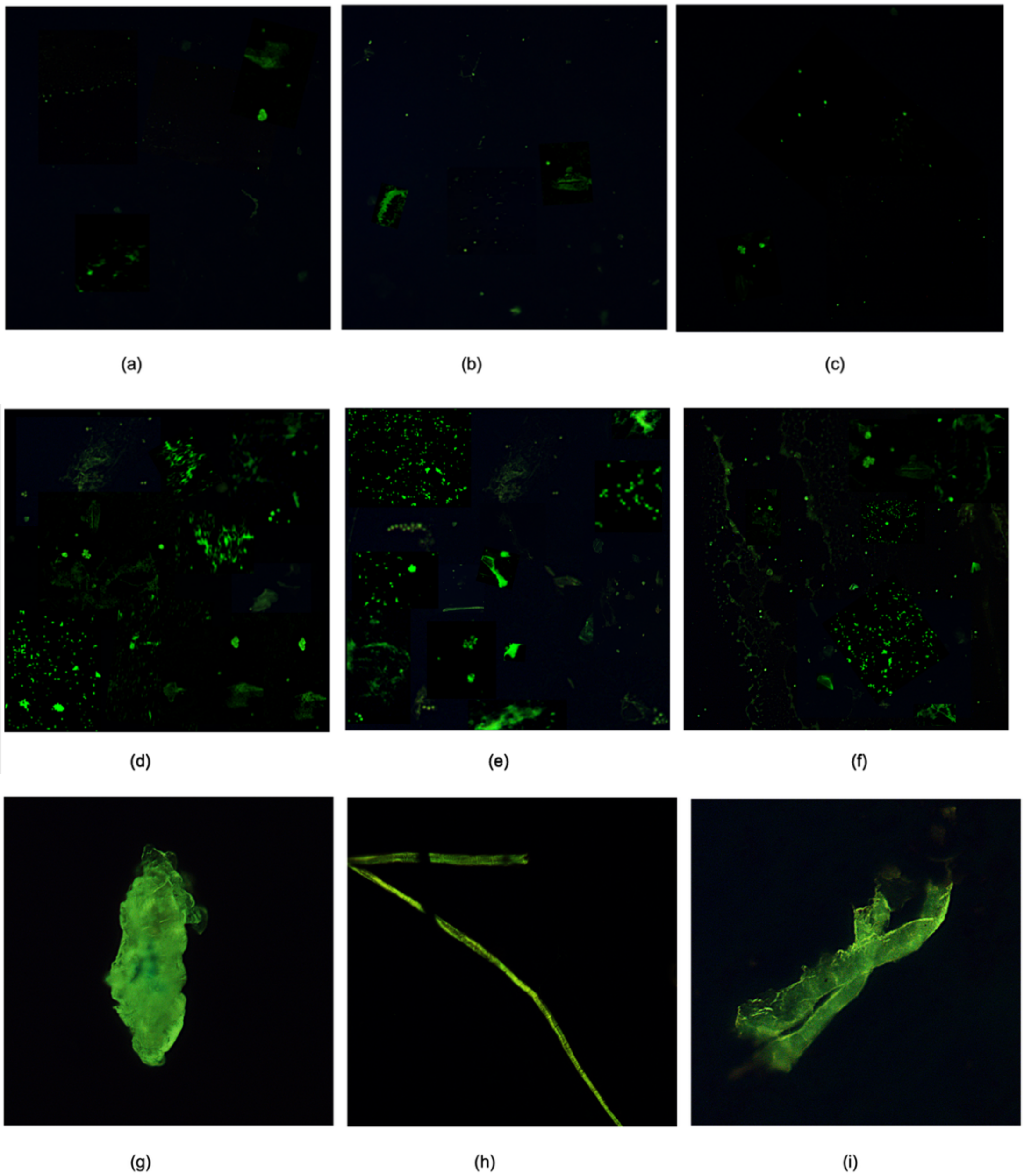
(a) (b) (c)

(d) (e) (f)

(g) (h) (i)

Figure 4.5.3-1. Fluorescence images of electro sprayed GQDs under green emission filter (SP: 450 nm, LP: 500 nm), Gain = 200, Exposure = 30 s, at different concentrations: (a–c) 0.5 mg/mL (low concentration) – sparse fluorescence signals and poor pattern uniformity; (d–f) 1.0 mg mL^{-1} (medium concentration): GQDs are well dispersed with spatially heterogeneous intensity; occasional localised clusters/bright agglomerates are present, but no dominant large-scale aggregation is observed; (g–i) 1.5 mg/mL (high concentration) – oversaturated features and aggregation-induced film-like structures.

Medium concentration (1.0 mg/mL) produced an ideal deposition profile, characterized by well-dispersed, bright dots without clustering. The corresponding fluorescence image exhibits high contrast, a high density of resolvable features, and strong, uniform emission. This morphology supports a high number of independent spatial sites and provides a strong, information-rich optical readout with excellent inter-channel separability, which is crucial for robust multi-bit key extraction.

High concentration (1.5 mg/mL), while yielding very high brightness, introduced significant aggregation artifacts. The emission was dominated by large, non-uniform clumps and streak-like features. These macroscopic structures reduce local micro-scale contrast and increase spatial correlation between pixels, thereby diminishing the number of statistically independent features despite the high signal intensity. PL spectra corroborated these imaging observations: low concentration exhibited a narrow green emission window, medium concentration produced broader green-to-yellow emission, and high concentration yielded multicolour emission extending into the red. Thus, while spectral complexity was highest at 1.5 mg/mL, this advantage is outweighed by the degraded spatial pattern quality for O-PUF applications. Consequently, the optimal balance of imaging quality and spatial entropy was achieved at 1.0 mg/mL.

In summary, GQD concentration directly governs both optical readout quality (brightness, spectral range) and spatial statistics (feature density, correlation), which jointly determine O-PUF entropy density. The 0.5 mg/mL condition offers spectral cleanliness but suffers from low feature density and weak signal. The 1.5 mg/mL regime demonstrates that maximizing spectral breadth and brightness is insufficient if aggregation compromises spatial randomness. In contrast, the 1.0 mg/mL concentration provides the optimal trade-off: a high signal-to-noise ratio, clear two-channel (green/yellow) spectral output, and uniform deposition necessary for generating entropy-rich, reproducible binary fingerprints. This section establishes the optimized fluorescence imaging framework for GQD-based O-PUFs. Electrospray deposition was selected over drop-casting for its superior spatial uniformity. The parameters of gain 200, 30s exposure, and a green emission filter were found to provide optimal contrast. The medium concentration of 1.0 mg/mL was identified as optimal through integrated fluorescence and PL analysis. These parameters form the foundation for generating unclonable binary maps, detailed in Section 4.6.

4.6 Binary Map Generation and Optical PUF Evaluation

Building upon the optimized fluorescence imaging conditions established in Section 4.5, this section introduces the methodology for generating binary maps from GQD-based emission patterns. These binary maps represent the digitized version of spatial fluorescence signals and serve as the foundation for optical physically unclonable function (O-PUF) encoding. To ensure uniqueness, reproducibility, and entropy, a Reduced Modal Local Binary pattern (RMLBP) algorithm was employed. The following subsections outline the binary encoding workflow, present representative binary maps, and provide a statistical evaluation of their suitability for secure optical authentication.

4.6.1 Binary Map Generation Method

To extract device-specific optical fingerprints from electro sprayed GQD fluorescence images, a standardized binary encoding workflow based on the Reduced-Modal Local Binary Pattern (RMLBP) method was employed. The goal of this approach is to transform stochastic photoluminescence (PL) patterns into reproducible, high-entropy binary maps suitable for secure authentication and optical physical unclonable function (O-PUF) applications.

The optical PUF workflow follows a four-stage pipeline: data capture → pre-processing → fingerprint generation → binary output. First, raw fluorescence images were converted to 8-bit grayscale and cropped to a central 284×284 px region of interest (ROI). Global histogram equalisation was then applied to enhance contrast, followed by Lorentz smoothing and down-sampling to a fixed 100×100 px resolution to standardise input size and suppress high-frequency noise.

Binary fingerprints were subsequently extracted using a Rotation-Invariant Modified Local Binary Pattern (R-MLBP) encoder. For each pixel, intensities were sampled on a circular neighbourhood (radius *r*, $N = 16$ points), and a reduced feature vector—comprising diametric gradient bits and a centre-to-mean contrast bit—was computed. The final per-pixel bit was obtained via modal reduction to improve noise robustness. A detailed, step-by-step implementation of the pre-processing and encoding algorithms is provided in Appendix 1.1.

Applying R-MLBP procedure to every pixel in the pre-processed 100×100 ROI yields a binary fingerprint map—a logical matrix that can be flattened to a fixed-length binary string for key-based analysis. This approach offers three key advantages for device identification. First, it relies on local, relative intensity comparisons within a circular neighbourhood. This makes the encoding dependent on intrinsic texture and contrast structure rather than absolute brightness, conferring robustness against global illumination shifts, intensity drift, and rotation while ensuring reproducible cross-sample comparison. Second, R-MLBP reduces the MLBP feature vector to a single modal (majority) bit per pixel. This suppresses isolated bit flips caused by centre-pixel noise or single-neighbour outliers, thereby enhancing fingerprint repeatability. Third, the circular neighbourhood supports rotation-invariant encoding, ensuring consistent codes for the same local microstructure regardless of orientation. Together, these properties provide a consistent, noise-resilient, and comparable method for converting GQD fluorescence textures into binary maps that capture device-specific spatial emission signatures.

The quality of the generated binary maps was evaluated using two fundamental PUF performance metrics: bit bias and the inter-Hamming distance (inter-HD) to probe statistical balance/entropy and inter-sample uniqueness. Bit bias measures the proportion of binary '1's in a fingerprint and serves as an indicator of statistical balance. An ideal bias of 0.5 corresponds to an equal likelihood of both bit states, ensuring maximal Shannon entropy and reducing statistical predictability, whereas large deviations imply a systematically easier-to-guess response distribution. In optical PUFs, a bias of 0.5 represents uniform optical complexity and high entropy density—key attributes for security and reproducibility. The inter-Hamming distance (inter-HD) is the average bitwise difference between fingerprints generated from different GQD samples. It is defined as the fraction of bits that differ between two binary maps of equal size. An ideal mean inter-HD of 0.5 indicates that any two PUF responses are statistically independent and unique. Values significantly lower than 0.5 suggest redundancy and correlation between samples, while higher values may signal instability or excessive noise. Together, these metrics provide a foundational assessment of the entropy, uniqueness, and independence of the encoded optical fingerprints.

These metrics are calculated as follows. For a binary map α of dimensions $n \times m$ and for comparisons between maps A and B, each containing $N = n \times m$ bits. Bias is computed as

$$bias(\alpha) = \frac{\sum_{i=1}^{m} \sum_{j=1}^{n} \alpha_{i,j}}{n \times m}, \text{(Equation 4.6.1-1)}$$

A bias of 0.5 represents perfect balance, implying maximum randomness. Deviations indicate a systematic skew: bias < 0.5 denotes a dominance of '0's (dark pixels), while bias > 0.5 indicates a dominance of '1's (bright pixels).

Hamming Distance (HD) between two maps is the normalized count of differing bits:

$$\mathrm{HD}(A, B) = \frac{1}{N} \sum_{i=1}^{N} | A_i - B_i |, \text{ (Equation 4.6.1-2)}$$

The inter-HD is the mean HD calculated across all unique pairs of fingerprints from different PUF instances:

$$inter - HD = < HD_{A,B} >_{all\ pairs}, \text{ (Equation 4.6.1-3)}$$

In an ideal PUF system, the inter-HD distribution (comparisons between different instances) should centre at 0.5, indicating that each optical fingerprint is unique and uncorrelated. Therefore, achieving a mean inter-HD close to 0.5 and a bias near 0.5 are essential for the optimal randomness and uniqueness required for secure, unclonable optical identifiers.

Figure 4.6.1-1. shows the resulting fingerprints across the range of radius values. As the radius r increases, the neighbourhood used for local comparisons expands from fine, pixel-scale structure to more mesoscopic texture. Consequently, the binary patterns become progressively smoother and more spatially coherent, reflecting reduced sensitivity to high-frequency fluctuations (e.g., isolated noisy pixels) while attenuating small-scale spatial detail. This behaviour illustrates the expected trade-off in neighbourhood-based encoders: small r retains more local detail but is more susceptible to capture noise, whereas larger r improves robustness by integrating information over a wider spatial support.

Quantitatively, at the selected operating radius $r = 3$, the bit bias (fraction of ‘1’s) measured from the 100×100 binary maps were 0.4892 for Sample 1. Including three additional samples (Samples 2-4) from Appendix 1.2 gave biases of 0.5012, 0.4931, and 0.5032, respectively, which yielding a mean ± SD of 0.4967 ± 0.0066 (n = 4), corresponding to a 0.67% deviation from the ideal unbiased value of 0.5. The corresponding inter-Hamming distance, reported as the per-sample average inter-HD values for Samples 1–4, was 0.4838 ± 0.0063 (mean ± SD, n = 4), deviating from the ideal uncorrelated value of 0.5 by 0.0163 (≈3.25%), indicating slightly lower inter-sample uniqueness than the perfectly uncorrelated limit (see Appendix 1.2). Together, these results indicate that $r = 3$ provides a favourable operating point: the fingerprints remain statistically balanced (high entropy) while maintaining strong inter-sample uniqueness, satisfying core requirements for robust O-PUF encoding [190].

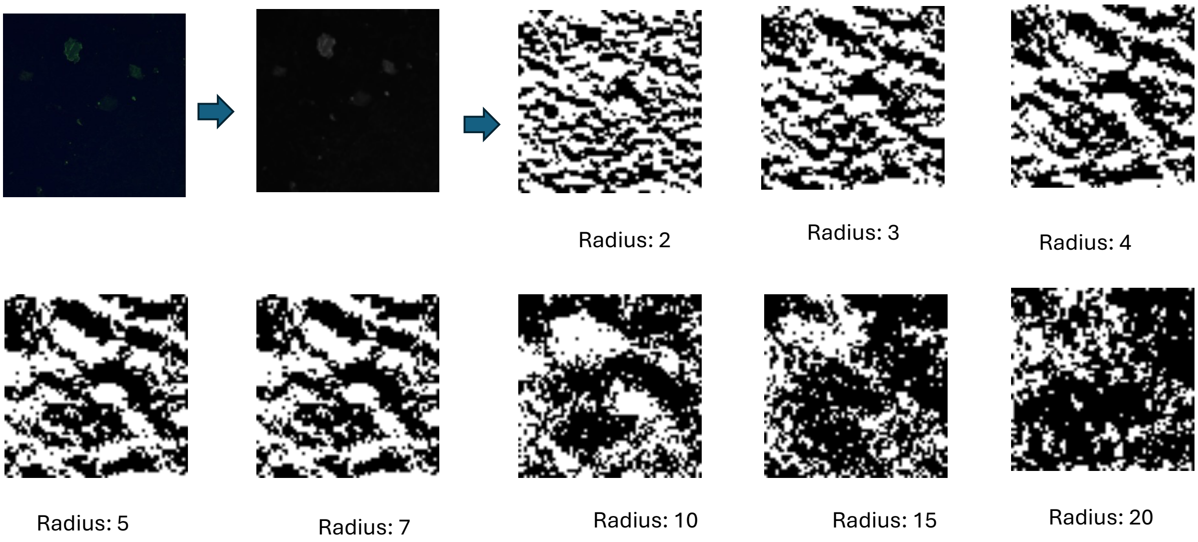

Figure 4.6.1-1 Binary map generation from GQD fluorescence images using the RMLBP method with varying radius values (present sample 1 here). Each row shows the full processing pipeline for a single fluorescence image: the original green-channel image (left), grayscale-converted version, and binary maps generated using RMLBP encoding with increasing radius values r = 2, 3, 4, 5, 7, 10, 15, 20. All images were downsized to 100×100 pixels prior to encoding. As radius increases, local features become progressively smoothed, reducing entropy and pattern sharpness. A radius of 3 offers an optimal trade-off between randomness and robustness for fingerprinting applications.

4.6.2 Binary Maps

To demonstrate the uniqueness and diversity of the fluorescence-based optical physical unclonable function (OPUF) features, a total of 20 photoluminescence (PL) images of electro-sprayed graphene quantum dots (GQDs) were captured under consistent imaging conditions. Each fluorescence image was converted into a binary fingerprint map using the optimized Rotation-Invariant Modified Local Binary Pattern (RMLBP) method with a radius parameter r = 3, which was previously identified as offering the best balance between noise tolerance and feature richness.

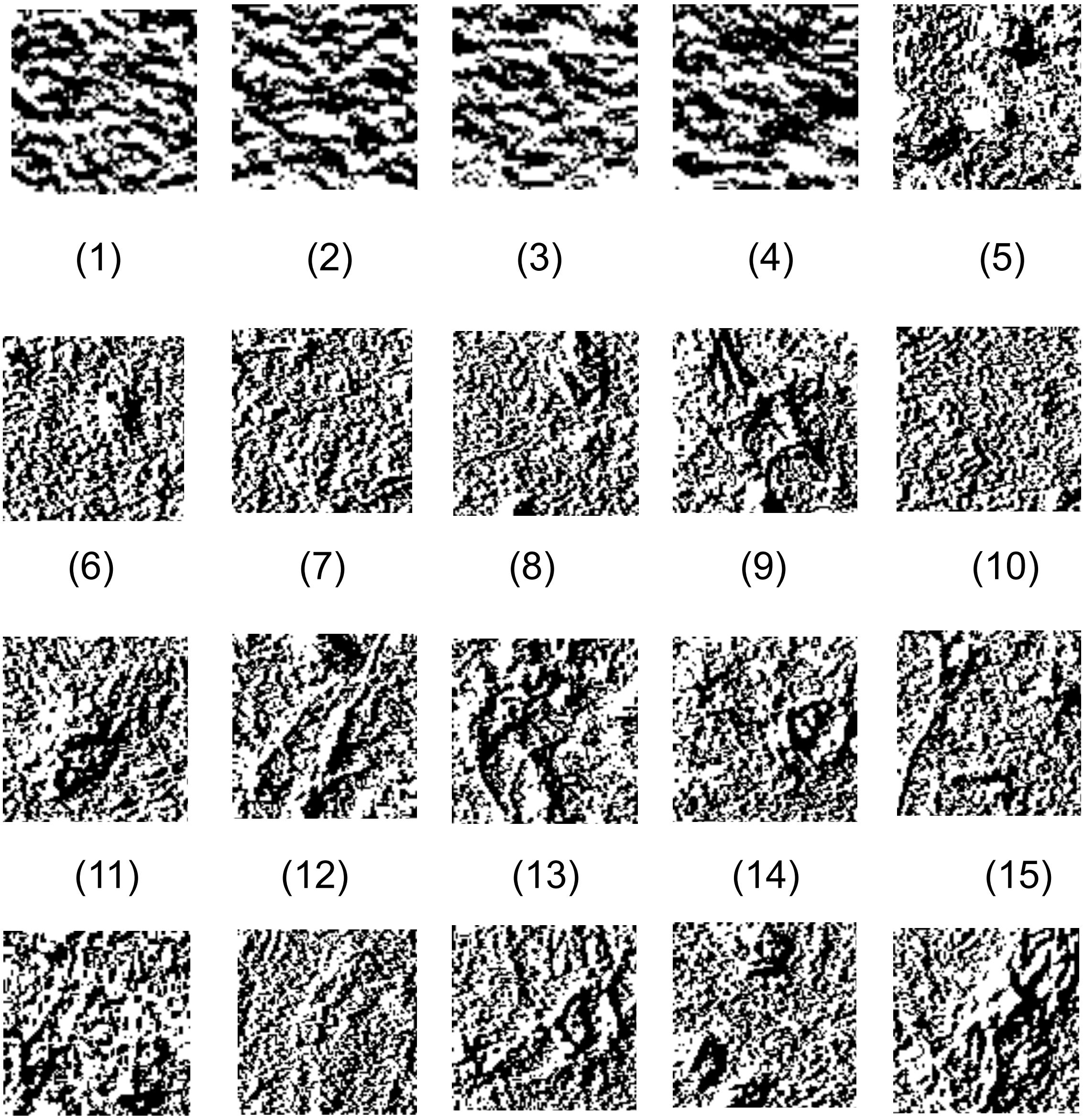
(1) (2) (3) (4) (5)

(6) (7) (8) (9) (10)

(11) (12) (13) (14) (15)

(16) (17) (18) (19) (20)

Figure 4.6.2-1. *binary maps generated using RMLBP (r = 3). Each map shows unique visual features despite identical imaging conditions, demonstrating the spatial randomness of GQD deposition.*

The full set of binary maps is shown in Figure 4.6.2-1, alongside their corresponding fluorescence images for visual reference. The binary maps exhibit distinct, nonrepetitive patterns, confirming that even under identical imaging setups and conditions, the local structural variation of GQD deposition leads to unique binary representations.

This diversity underscores the visual uniqueness of each sample and forms the basis of entropy in the proposed OPUF system. No apparent periodic or repeated structures are observed, supporting the randomness and high inter-device variability essential for secure PUF implementations.

4.6.3 Statistical Evaluation of OPUF Quality

In the literature, the comprehensive assessment of Physical Unclonable Functions (PUFs)—including optical PUFs—relies on multiple statistical and cryptographic metrics to evaluate performance across several dimensions: randomness, uniqueness, stability, reliability, and entropy. Standard metrics include bias, bit aliasing, uniformity, entropy density, key generation rate, and Hamming distances[191,192]. Hamming distance is a core metric that measures bitwise differences, divided into two critical forms: the inter-Hamming distance (inter-HD), which quantifies uniqueness between different devices, and the intra-Hamming distance (intra-HD), which quantifies reproducibility from repeated measurements of the same device and indicates temporal stability (ideally near zero).

Given the proof-of-concept nature of this work, the limited dataset (20 fluorescence images), and time constraints, the evaluation was focused on two foundational statistical parameters: bit bias and inter-Hamming distance. These two metrics serve as essential, baseline indicators of randomness and uniqueness, providing a foundational verification of the optical encoding process and establishing the feasibility of the GQD-based O-PUF. A full assessment of reliability via intra-Hamming distance (intra-HD) will be the focus of future work. As accurate intra-HD analysis requires multiple repeated imaging sessions of each sample under strictly identical optical and environmental conditions to isolate the effects of noise, alignment drift, and photobleaching. Within the available measurement time for this initial study, priority was therefore given to acquiring multiple, statistically independent fluorescence patterns to establish robust proof-of-concept evidence for entropy and uniqueness.

The overall statistical evaluation of the binary maps generated using the RMLBP method demonstrates excellent balance of bias and inter-sample uniqueness (Table 4.5.3-1). The mean bias across all 20 samples was 0.4982 ± 0.0060(n=20, SD), corresponding to a 0.36 % deviation from the ideal unbiased value of 0.5. This result indicates an evenly distributed proportion of binary 0s and 1s, confirming high entropy and the absence of bit-value bias.

The mean inter-Hamming distance was 0.4839 ± 0.0049, representing a 3.22 % deviation from the theoretical ideal of 0.5. This small deviation quantitatively verifies that the generated binary maps exhibit strong pairwise independence and high inter-sample distinctiveness—key attributes required for secure and distinguishable optical identifiers.

Map ID	Bias	Avg. Inter-Hamming Distance
Image 1	0.4892	0.4803
Image 2	0.5012	0.4792
Image 3	0.4931	0.4825
Image 4	0.5032	0.4930
Image 5	0.4924	0.4798
Image 6	0.5112	0.4783
Image 7	0.5021	0.4886
Image 8	0.4990	0.4824
Image 9	0.4873	0.4861
Image 10	0.4958	0.4829
Image 11	0.5037	0.4927
Image 12	0.4939	0.4913
Image 13	0.5041	0.4863
Image 14	0.4987	0.4814
Image 15	0.5010	0.4807
Image 16	0.4965	0.4892
Image 17	0.4933	0.4769
Image 18	0.4976	0.4831
Image 19	0.4942	0.4847
Image 20	0.5056	0.4793

Table 4.6.3-1: Bias and Average Inter-Hamming Distance (Images 1–20)

These results suggest that the binary maps are well-suited as OPUF fingerprints, with bias values tightly centred around 0.5, indicating excellent entropy, and inter-Hamming distances near 0.5, reflecting strong uniqueness across maps. Despite the promising results, several limitations and areas for future improvement remain. First, the extracted binary maps may be sensitive to environmental factors such as lighting conditions, camera focus, or imaging alignment, which could impact reproducibility [193]. Second, the choice of preprocessing steps—including thresholding, denoising, and image resizing—may influence key performance metrics such as bias and inter-Hamming distance. This suggests that preprocessing protocols may need to be tailored to specific imaging setups to ensure consistency. Lastly, for a complete fundamental performance assessment, evaluating the intra-Hamming distance via controlled repeated measurements is a necessary next step to quantify long-term reproducibility and environmental robustness, thereby validating the technology's operational stability.

The evaluation supports that the current binary maps exhibit strong characteristics required for secure and robust OPUF fingerprints. The near-ideal entropy and uniqueness suggest good quality. Future work will involve reproducibility analysis and robustness testing across varying environmental conditions.

4.7 Conclusion

This study demonstrates the feasibility of using electro-sprayed graphene quantum dots (GQDs) to generate distinct and robust fluorescence patterns, which can be reliably transformed into binary maps suitable for Optical Physical Unclonable Functions (OPUFs). The random and spatially unique emission profiles of electro-sprayed GQDs were successfully captured through fluorescence imaging, providing a high-entropy physical basis for secure authentication.

Among the encoding strategies evaluated, the Rotation-Invariant Modified Local Binary Pattern (RMLBP) method with a radius of r = 3 was found to offer the optimal balance between structural detail retention and noise resilience. The resulting binary maps exhibited near-ideal bias values, indicating well-balanced entropy between binary states. High inter-Hamming distances across different samples further confirmed strong uniqueness and low inter-sample correlation—essential characteristics for non-replicable key generation. While preliminary observations indicated good reproducibility, formal intra-Hamming distance analysis remains to be conducted to fully assess temporal stability.

These findings support the potential of GQD-based fluorescence imaging as a hardware-intrinsic, secure randomness source for applications such as cryptographic key storage and device-level authentication. Nonetheless, further work is required to strengthen the security evaluation, including the application of standardized randomness assessment protocols (e.g., NIST statistical test suite) and systematic testing under variable environmental conditions to ensure long-term robustness.

Future work will therefore extend this evaluation framework along two key axes. First, stability and robustness will be assessed by incorporating repeated measurements under controlled variations of temperature, humidity, excitation intensity, optical geometry, and aging. This will allow the quantification of stability metrics such as intra-HD (mean ± SD), bias drift, and bit-error rate, thereby establishing operational stability windows and failure thresholds. Second, cryptographic rigor will be enhanced by expanding the framework to include additional cryptographic metrics such as uniformity, bit aliasing, reliability, entropy density, and key generation capacity. This will enable a more rigorous, system-level performance assessment suitable for practical deployment.

In conclusion, the integration of GQD-based fluorescence with local binary pattern encoding presents a promising pathway toward the development of robust, unclonable physical keys, laying the groundwork for next-generation hardware security systems.

Chapter 5: Optical Fingerprinting with Graphene–MoS_2 van der Waals Heterostructures

While Chapter 4 explored stochastic optical fingerprints derived from graphene quantum dots (GQDs), this chapter presents a complementary approach: deterministic optical fingerprinting based on graphene–MoS_2 van der Waals heterostructures (vdWHs). Unlike GQDs, which rely on randomly distributed emissive sites, vdWHs provide structured, position-specific optical responses arising from controllable stacking geometry, interfacial coupling, and nanoscale strain[194,195]. Graphene–MoS_2 heterostructures uniquely combine the broadband conductivity and Fermi-level tunability of graphene with the strong excitonic emission of monolayer MoS_2. Their interface facilitates charge transfer, dielectric screening, and exciton modulation, all of which are highly sensitive to stacking order, twist angle, and interfacial morphology [194,196]. Importantly, these deterministic features—while inherently sensitive to fabrication conditions—are beneficial for physically unclonable functions (PUFs), as they give rise to fixed, irreproducible optical variations that encode high spatial entropy.

This work investigates how the intrinsic sensitivities of graphene–MoS_2 heterostructures—particularly their dependence on stacking sequence, interfacial strain, and local morphology—can be leveraged to generate spatially encoded optical fingerprints. Photoluminescence (PL) measurements were performed under a range of experimental conditions, including temperature variation from cryogenic (10 K) to room temperature (300 K), changes in excitation power from 1 uW to 12 uW, and spatial scans across multiple positions within the same heterostructure flake. Particular attention is given to the emergence of deterministic PL variations associated with stacking order and intra-flake position. In addition, spatial PL mapping is used to visualize emission inhomogeneity arising from interfacial strain and nanoscale disorder, and to assess its suitability for digital identity encoding through binarization. Although the study focuses on a limited set of devices, it aims to establish a proof-of-concept framework for lithography-free, entropy-rich optical fingerprinting based on van der Waals heterostructures.

This chapter is structured as follows: Section 5.1 provides a state-of-the-art review of optical physical unclonable functions (OPUFs) based on two-dimensional (2D) materials, examining their advantages, limitations, and the emerging motivation for leveraging van der Waals heterostructures as a next-generation OPUF platform. Section 5.2 investigates how stacking order influences PL at room temperature. Section 5.3 extends the analysis to cryogenic temperatures to enhance spectral contrast and fingerprint specificity. Section 5.4 assesses fingerprint stability under environmental perturbations, including laser power and temperature. Section 5.5 presents PL mapping to visualize spatial emission heterogeneity. Section 5.6 introduces a binarization workflow to convert PL maps into digital optical identities. Finally, Section 5.7 evaluates the statistical properties of the resulting binary keys and outlines directions for future scalability and PUF validation.

5.1 State-of-the-Art: 2D Materials applied for Optical Physical Unclonable Functions

Two-dimensional (2D) materials have been widely studied as optical physically unclonable functions (O-PUFs) because they offer a rich, nanoscale-engineerable source of spatially varying optical responses, enabled by the distinctive optical properties that emerge at the atomic scale [197,198]. Current 2D O-PUFs can be broadly categorized into three types—TMDC-based systems, graphene-based PUFs, and plasmon-enhanced 2D PUFs—according to their underlying entropy sources and operating principles [197-199].

TMDC-based O-PUFs (e.g., MoS_2) derive entropy from spatial non-uniformity in PL: local defects and thickness variations (monolayer vs multilayer) perturb the band structure and excitonic recombination, producing position-dependent emission that can be discretised into ON/OFF pixels or encoded as spatial PL maps. In challenge–response operation, the illumination position serves as the challenge, while the response is captured by the emitted intensity and/or spectrally selected PL (via a bandpass filter); related designs further enhance unpredictability by using disordered MoS_2 nanoflakes with randomly distributed TiO_2 aggregates, where photogenerated charge transfer and quenching contrasts are physically “locked in” by the heterostructure.

Graphene-based O-PUFs encode entropy in stochastic morphology and defect/adlayer distributions that translate into spatially heterogeneous Raman fingerprints, enabling high-capacity, unclonable surface “maps” for authentication. For example, CVD-tuned random graphene adlayers combined with polymer de-wetting and oxygen-plasma patterning produces randomly positioned graphene islands that yield distinctive multi-colour Raman maps, while GO–MXene composites form multigenerational microstructures (via moisture-assisted lubrication and cation intercalation) that generate hierarchical, hard-to-replicate topographies readable as robust physical keys [200-202].

Plasmon-enhanced 2D O-PUFs introduce an additional entropy layer by integrating 2D materials with metallic nanostructures, so that localised surface plasmon resonances create strongly position-dependent optical amplification. In practice, the random nanoscale arrangement of plasmonic “hot spots” boosts Raman/optical signals and enables covert, multi-level features (e.g., enhanced spectral patterns or hidden structural motifs) that are difficult to reproduce, strengthening security for optical cryptography and authentication[202,203].

The principal strength of 2D O-PUFs is their ability to translate atomic-scale disorder and nanoscale optical property into high-dimensional, spatially varying responses that are difficult to physically replicate [204,205]. However, several factors can limit practical deployment. For TMDC-based PUFs, the challenge is often restricted to the illumination position (and, in some implementations, the excitation wavelength), while the response is primarily the local PL spectrum and/or intensity; because this response is governed largely by the intrinsic defect and thickness disorder , the accessible CRP space and tunability may be constrained in comparison with architectures that incorporate additional controllable degrees of freedom. In addition, many reported devices enhance randomness through externally introduced disorder (e.g., random nanoparticle deposition) or employ lithographic patterning to define features or readout regions, which increases fabrication complexity and can introduce design-determined elements alongside intrinsic material randomness[199,205]. Scalability and reproducibility also remain non-trivial: maintaining consistent optical performance across large areas and across batches is challenging, particularly when the optical response is sensitive to subtle variations in growth, transfer residues, and environmental adsorbates [201]. Finally, some 2D O-PUF classes—especially plasmon-enhanced or multilayer implementations—may require specialised optical instrumentation (e.g., high-resolution spectral readout or precise alignment), which can complicate translation to low-cost, portable authentication platforms [203,206].

Van der Waals heterostructures—particularly graphene–MoS_2 stacks—offer alternative route to broaden the response space by merging interfacial control with fabrication-locked randomness. By introducing graphene into a vdWH, the challenge space becomes richer because each challenge can probe a different interlayer-coupling state—set by local stacking disorder (twist angle, spacing, trapped residues, wrinkles/strain) and charge-transfer efficiency—so the response (PL intensity/peak position/exciton–trion balance) is modulated by both the TMDC disorder and the graphene–TMDC interaction, expanding the number and separability of CRPs. Third, dry-transfer assembly enables deliberate construction of graphene–MoS_2 heterostructures while minimising solvent exposure during stacking, helping to preserve interfacial coupling and maintain a stable optical response.

In addition, because the entropy can be encoded in fabrication-locked interfacial variations rather than lithographically defined patterns, dry transfer can reduce fabrication complexity and support more scalable production routes for high-entropy O-PUFs. While challenges in large-area transfer control, environmental packaging, and low-complexity readout remain, graphene–TMDC heterostructures offer a interface engineering route to expand the CRP space and improve design flexibility relative to single-layer TMDC PUFs.

This work demonstrates an optical fingerprinting platform based on graphene–MoS_2 van der Waals heterostructures. The systematic characterization of stacking-dependent photoluminescence, cryogenic spectral contrast, and spatial emission mapping establishes a framework for entropy-rich, lithography-free optical physically unclonable functions (OPUFs), which effectively bridges the gap between precisely engineered optoelectronic systems and physically secure authentication protocols.

5.2 Stacking Verification and Interlayer Interaction

Reliable optical fingerprinting requires prior verification of the stacking integrity and interlayer coupling in the fabricated graphene–MoS_2 van der Waals heterostructures. This section employs optical microscopy and Raman spectroscopy to confirm both the physical assembly and the electronic interaction of the 2D heterostructures, establishing a critical foundation for all subsequent photoluminescence-based fingerprinting.

Two stacking sequences—MoS_2-on-graphene and graphene-on-MoS_2—were fabricated via a dry-transfer technique. This solvent-free method uses viscoelastic polydimethylsiloxane (PDMS) stamps to pick up, align, and then place exfoliated flakes onto a target substrate. A controlled peel-off process then releases the stamp, forming a solvent free and clean van der Waals heterostructure (full procedural details are provided in Section 3.1.2). The resulting optical microscopy images of graphene, MoS_2, and the two heterostructure stacking sequences are shown in Figure 5.2-1. Each fabrication route begins with mechanical exfoliation of graphene (a, g) and MoS_2 (c, e) from bulk crystals onto PDMS, followed by sequential transfer onto a Si wafer doped with ~285–300 nm thermally grown SiO_2 (Si/SiO_2) (b, d, f, h). This substrate was selected because its standard oxide thickness maximises thin-film interference contrast for monolayer graphene and MoS_2 under optical microscopy [207], enabling reliable flake identification and precise layer-on-layer alignment, while also providing a flat, low-fluorescence surface compatible with micro-Raman/μ-PL measurements. For the MoS_2–Graphene VdWH, graphene was first transferred onto the Si/SiO_2 substrate, followed by the alignment and placement of the MoS_2 flake on top. For Graphene– MoS_2, MoS_2 is deposited on Si/SiO_2 first and then Graphene aligns on the top.

The final stacked areas measured approximately 4.0 μm × 5.0 μm for the graphene–MoS_2 configuration (Figure 5.1-1-h) and 3.7 μm × 4.6 μm for MoS_2–graphene(d). Due to equipment limitations, all exfoliation, transfer, and optical characterisation steps were performed under ambient conditions, which limits control over interfacial cleanliness and environmental variability during assembly. In addition, manual micromanipulator alignment constrains layer-to-layer alignment to the micron scale and can introduce mild shear during pick-up and release, occasionally producing wrinkles or local strain non-uniformity. Consequently, minor interfacial residues and occasional blisters or bubbles—attributed to trace PDMS oligomers, hydrocarbons, and trapped airborne species such as dust, moisture, or oxygen—were observed in the van der Waals heterostructures (VdWHs), as highlighted in Figure 5.2-1 (panels d and h).

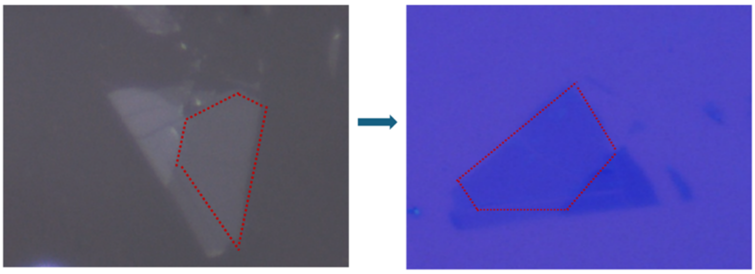

(a) Graphene on PDMS

(b) Graphene on Si/SiO_2

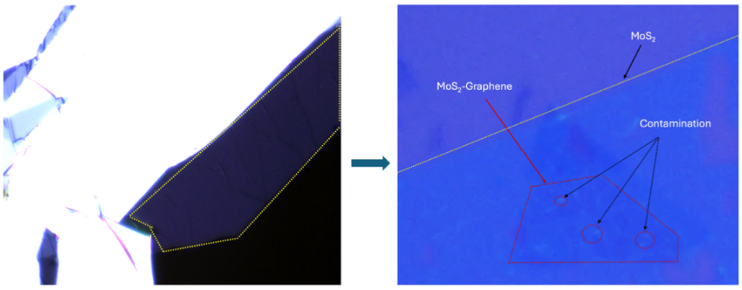

(c) MoS_2 on PDMS

(d) MoS_2 –Graphene on Si/SiO_2

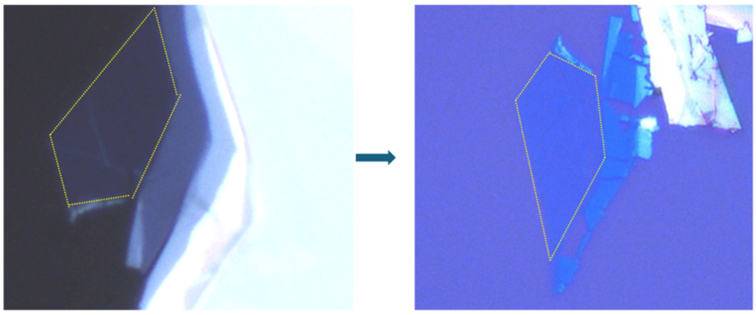

(e) MoS_2 on PDMS

(f) MoS_2 on Si/SiO_2

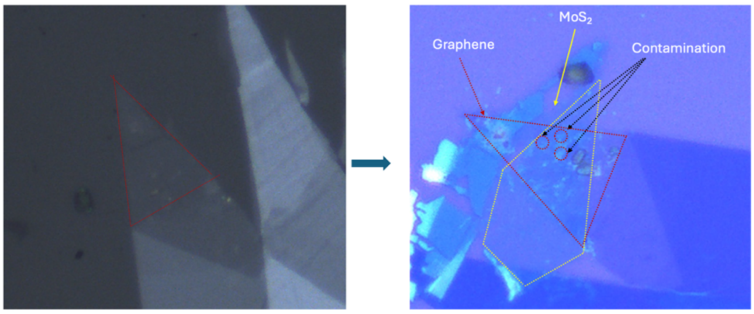

(g) Graphene on PDMS

(h) Graphene – MoS_2 on Si/SiO_2

Figure 5.2-1. Optical microscopy images showing the stepwise fabrication of (a–d) MoS_2-Graphene and (e–h) Graphene-MoS_2 heterostructures on Si/SiO_2. Target flakes are outlined, and regions of visible interfacial contamination in the assembled stacks are highlighted.

Accordingly, two measurement regimes were employed. For spectroscopy aimed at quantifying intrinsic interlayer coupling (Raman and PL at room temperature and low temperature), measurement locations were selected from optically uniform regions and away from obvious wrinkles, bubbles, and particulate contamination, to minimise strain- and doping-related artefacts and ensure that extracted peak shifts, linewidths, and intensity ratios primarily reflected graphene–MoS_2 interlayer coupling effects. For O-PUF readout, wide-area PL maps were acquired without excluding these interfacial non-uniformities, because the resulting spatially varying emission provides the fabrication-locked, high-entropy spatial emission fingerprint used for challenge–response generation. Additionally, characterization measurements (PL and Raman) employed low laser power and short integration times to minimize local heating and photodamage. Optical microscopy images captured at each stage reveal distinct flake boundaries and are used to monitor the stacking process, ensuring reasonably consistent alignment between the transferred layers.

Prior to stacking, the layer identity of each constituent flake was verified to ensure that the assembled van der Waals heterostructures (vdWHs) were formed from monolayer MoS_2 and exfoliated graphene. Monolayer MoS_2 was identified by Raman spectroscopy and further supported by AFM height profiling across a flake edge (Figure 5.2-2). Graphene flakes were identified by their characteristic G and 2D bands in Raman spectrum.

In monolayer MoS_2, the Raman spectrum contains several distinct features, including the first-order modes (E_2g^1 and A_1g), resonance-enhanced second-order and combination bands such as 2LA(M) (~450–460 cm^{-1}), low-frequency interlayer shear and layer-breathing modes (< 50 cm^{-1}), and other symmetry-dependent modes (e.g., E_1g, B_2g^1). Among these, the E_2g^1 and A_1g modes are commonly used for monolayer identification. These two represent the strongest, first-order Raman-active modes in standard backscattering micro-Raman spectroscopy and exhibit a clear, systematic thickness dependence: as layer number increases, the E_2g^1mode typically red-shifts while the A_1g mode blue-shifts [208]. Consequently, the peak separation Δ ($A_1g - E_2g^1$) increases monotonically with thickness, providing a simple and reproducible “fingerprint” that is more robust than intensity-based methods, which are sensitive to alignment, focus, laser power, and optical interference[209-211]. Therefore, this work focuses on the E_2g^1 and A_1g modes for reliable and consistent monolayer identification.

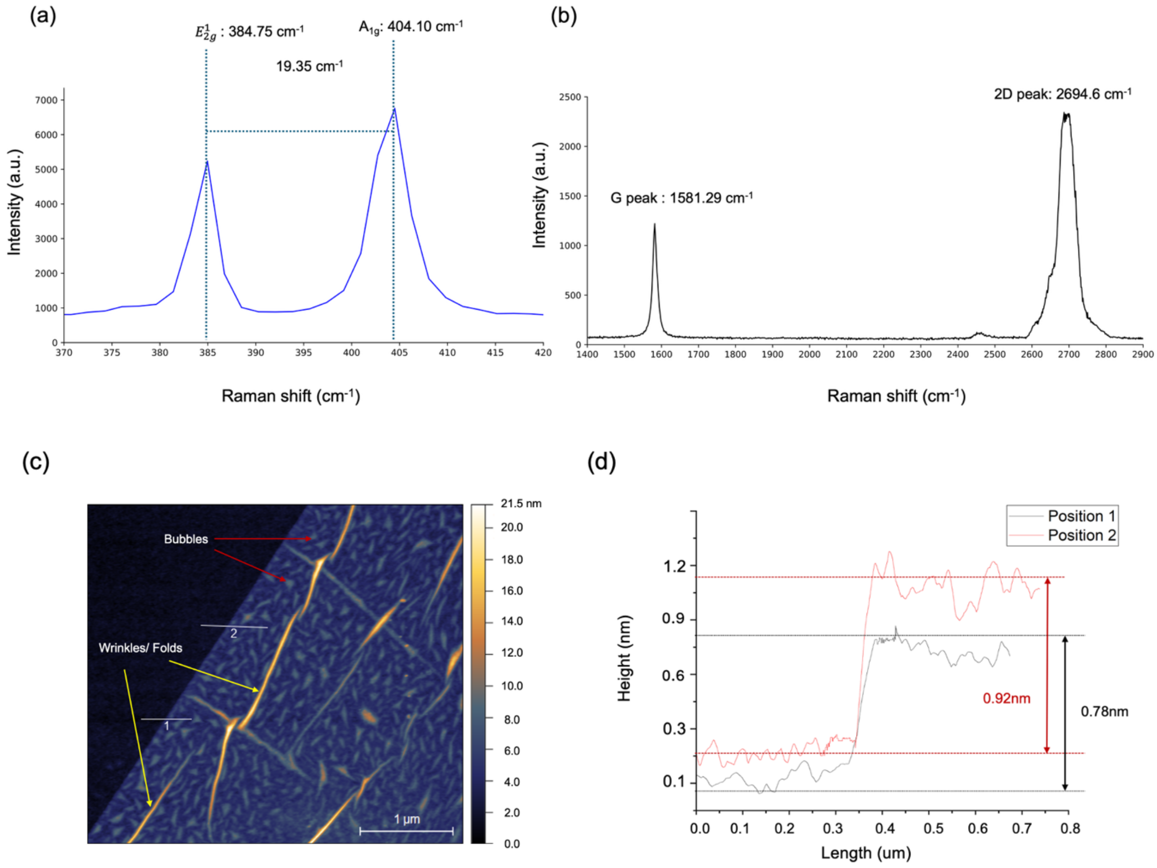

Figure 5.2-2. Pre-transfer identification of constituent monolayers by Raman spectroscopy and AFM. (a-b) Raman spectrum of monolayer MoS_2 (a) on Si/SiO_2 and bilayer graphene (b) on Si/SiO_2, respectively. (c) AFM topography of the MoS_2 flake highlighting transfer-induced surface features such as wrinkles/folds and interfacial bubbles (scale bar: 1 µm). (d) AFM height profiles taken along the marked paths in (c) across the MoS_2 edge, giving apparent step heights of 0.78 nm (Position 1) and 0.92 nm (Position 2).

As shown in Figure 5.2-2(a), the Raman spectrum of monolayer MoS_2 shows the characteristic in-plane E^1_{2g} peak at 384.75 cm^{-1} and the out-of-plane A_{1g} peak at 404.10 cm^{-1}, giving a peak separation of $\Delta \approx 19.35$ cm^{-1}. This value is consistent with the reported $\Delta \approx 19.4$ cm^{-1} for a monolayer MoS_2 [212]. This is attributed to layer-dependent phonon shifts, specifically a stiffening of the A_{1g} mode and a softening of the E^1_{2g} mode caused by interlayer coupling and dielectric screening—a process where adjacent layers reduce long-range Coulomb interactions, weakening the in-plane vibrational restoring forces[208]. While the E^1_{2g} mode is sensitive to in-plane strain and dielectric environment, the A_{1g} mode responds more strongly to out-of-plane coupling, doping, and charge-transfer effects [212]. AFM line profiles acquired across the MoS_2 flake edge yield apparent step heights of 0.78 nm and 0.92 nm (Figure 5.2-2(c-d)), consistent with monolayer MoS_2 on SiO_2[213]. Local surface inhomogeneities, including wrinkles/bubbles and occasional cracks, were observed, which are attributed to transfer-related residues and interfacial trapped contaminants.

For graphene Raman spectrum, the key bands are the G peak (~1580 cm^{-1}; in-plane sp^2 C–C stretching), the D peak (~1350 cm^{-1}; defect/edge-activated), and the 2D (G′) peak (~2670–2720 cm^{-1}; a two-phonon, double-resonance overtone that does not require defects). D′ (~1620 cm^{-1}): defect-activated intravalley mode (another disorder indicator); D+G (~2940–2960 cm^{-1}): combination band, defect-related; 2D′ (~3230–3250 cm^{-1}): second-order overtone of D′ (weaker; sometimes used for strain/doping nuance)[214,215]. Monolayer identification most often relies on G + 2D and the I_{2D}/I_G ratio because (i) 2D line shape/FWHM and intensity change strongly and systematically with layer number due to the evolution of the electronic band structure (monolayer typically shows a single, symmetric 2D band, whereas few-layer becomes broader/structured), and (ii) the ratio is less dependent on absolute signal level than peak intensity alone. (In contrast, D is avoided for layer counting because it mainly reports defects/edges rather than thickness) [216].

The graphene spectrum (Figure 5.2-2(b)) shows a G band at 1581.29 cm^{-1} and a relatively sharp, symmetric 2D band at 2694.6 cm^{-1}. The G peak corresponds to in-plane C–C bond stretching and is sensitive to doping (position and linewidth) and strain (position). The 2D band, a second-order overtone near the K point of the Brillouin zone, is highly sensitive to layer number, strain, and electronic band structure. The measured intensity ratio $I_{2D}/I_G = 1.92$ and the relatively broad 2D peak are consistent with bilayer graphene. The broadened 2D line shape arises from interlayer coupling, which splits the electronic bands and modifies the double-resonance Raman process. The I_{2D}/I_G ratio—decreasing from ~2–3 in monolayer graphene to ~1–2 for bilayer and to ~0.3 in bulk graphite—reflects layer-dependent changes in electronic structure and resonance conditions, although the absolute value can be influenced by substrate interactions, doping, strain, and measurement conditions [216].

Raman spectroscopy was then performed on the stacked regions to evaluate interlayer coupling and stacking order-dependent perturbation. In the MoS_2-Graphene on Si/SiO_2 heterostructure (Figure 5.2-3), the MoS_2 E^1_{2g} mode exhibits a redshift to 384.535 cm^{-1} ($\Delta = -0.215$ cm^{-1}), while the A_1g mode blueshifts by 0.873 cm^{-1} to 404.973cm^{-1}, increasing their separation to 20.44 cm^{-1}. These opposite-direction shifts originate from distinct interfacial mechanisms. The E^1_2g redshift is attributed to long-range dielectric screening from graphene, which weakens in-plane Coulombic forces. In contrast, the A_1g blueshift arises from a van der Waals (vdW)-induced constraint that stiffens out-of-plane vibrations [217,218].

The A_1g shift serves as a direct fingerprint of interfacial vdW coupling strength. In bare MoS_2, the A_1g mode frequency, $\omega(A_1g) \propto \sqrt{}(C_{s2,\ s2})$, is governed by the intralayer "spring" constant between sulfur layers. The presence of graphene introduces an interlayer vdW coupling term, $C_{s2,\ s2}{}^{o}$, such that $\omega(A_1g) \propto \sqrt{}\ (C_{s2,\ s2} + C_{s2,\ s2}{}^{o})$. This term is negligible when the interlayer distances >4 Å, confirming its origin in proximate vdW contact. Consequently, the magnitude of A_{1g} shifts reflects the degree of coupling. This relationship is underscored by the work of Zhou et al., who measured significantly larger shifts (≈ −1 cm^{-1} for E^1_2g and +2 cm^{-1} for A_1g) in optimally coupled regions, conclusively linking the spectral response to direct interfacial contact quality, not merely graphene layer number[219]. The comparatively reduced shifts observed here therefore suggest a less intense or spatially inhomogeneous coupling, likely due to interfacial imperfections (e.g., bubbles or adsorbates) or non-uniform strain transfer during stacking.

The 2D Raman peak in the Graphene-MoS_2 heterostructure shows a compressive-strain signature, evidenced by a blueshift of +4.540 cm^{-1} and linewidth broadening. This is a direct consequence of interlayer coupling, which modifies the double-resonance scattering in graphene through three mechanisms: (i) out-of-plane deformation of graphene layer from transfer-induced conformal contact with MoS_2, (ii) charge redistribution at the interface((electron transfer from graphene to MoS_2), and

(iii) changes in the dielectric environment. The latter—dielectric screening—alters electron–phonon coupling by polarizing the MoS$_2$/SiO$_2$ support, reducing effective Coulomb interactions. In monolayer graphene, the 2D band is highly sensitive to such external screening. In contrast, the bilayer coupling in this heterostructure introduces a degree of “self-screening,” thereby mitigating the substrate’s influence and leading to a weaker overall 2D-band response[220-222].

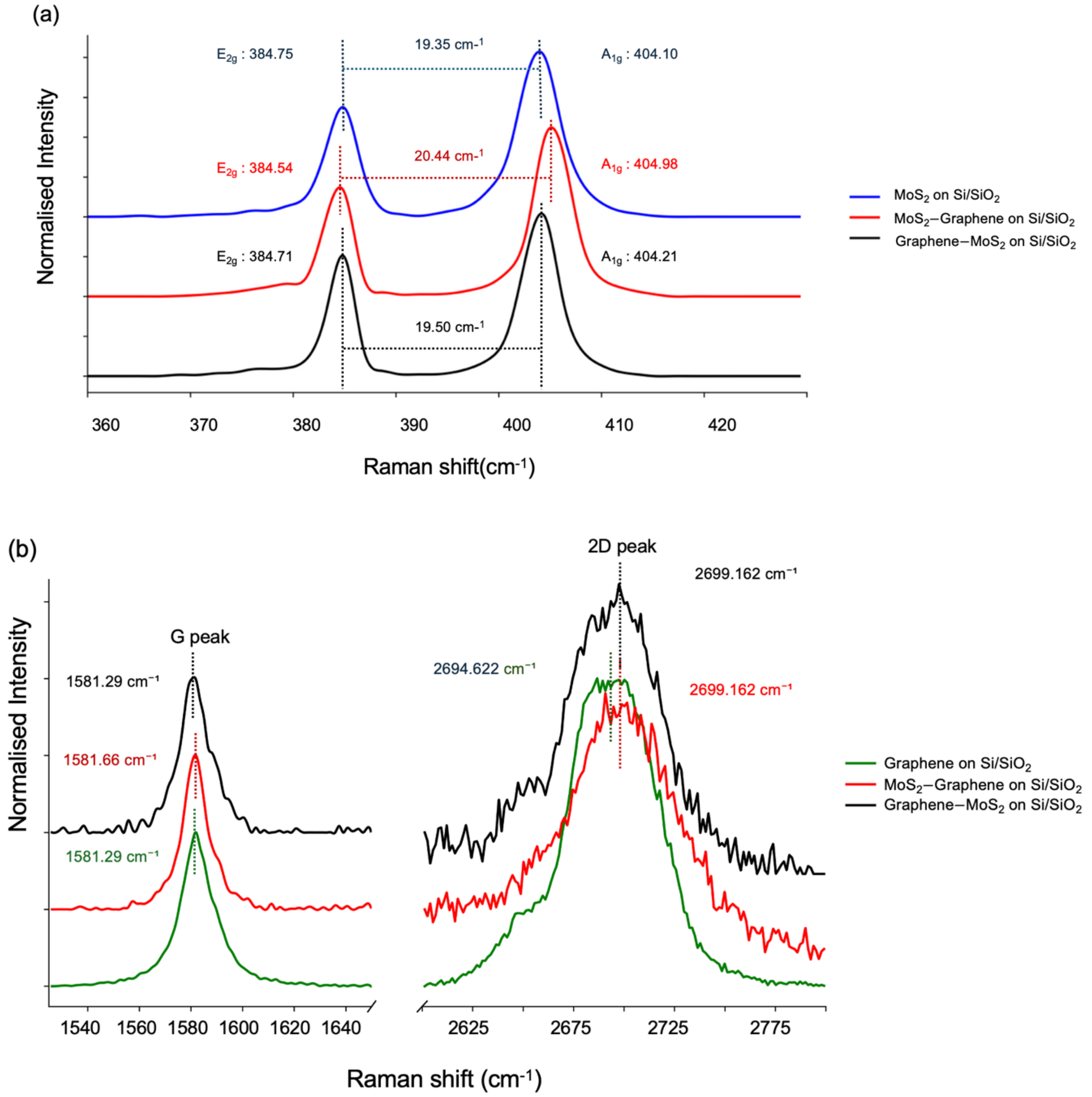

Figure 5.2-3. Raman spectra of monolayer MoS$_2$, bilayer graphene, and their MoS$_2$–Graphene and Graphene–MoS$_2$ heterostructures on Si/SiO$_2$. (a) Comparison of MoS$_2$ first-order modes (E$^1_{2g}$ and A$_{1g}$ in the 360–430 cm^{-1} region. (b) Comparison of graphene G and 2D bands (1525–1650 cm^{-1} and 2600–2800 cm^{-1}) for graphene on Si/SiO$_2$ and both heterostructure stacking orders.

These subtle yet consistent spectral modulations suggest interfacial coupling in both stacking geometries, caused by a combination of vertical strain, electron transfer from MoS_2 to graphene, and dielectric screening. Collectively, these signatures confirm that the layers are electronically coupled rather than simply physically stacking—an essential prerequisite for interpreting photoluminescence behaviour in subsequent sections[223-225].

5.3 Room-Temperature Photoluminescence: Influence of Stacking Order

To investigate how stacking order modulates excitonic properties in van der Waals heterostructures (vdWHs), room-temperature photoluminescence (PL) spectra were measured for three configurations: monolayer MoS_2 on SiO2/Si, MoS_2−Graphene on SiO2/Si and Graphene–MoS_2 on SiO2/Si. The photoluminescence (PL) spectrum of monolayer MoS_2 on SiO_2 (Fig. 5.3-1(b)) was deconvolved using Lorentzian functions, resolving three excitonic features. The dominant neutral exciton resonances are assigned to the A and B transitions at 1.882599 eV (658.66 nm) and 2.018067 eV (614.45 nm), respectively; their energy separation is consistent with the spin–orbit splitting of the valence band at the K/K′ points in monolayer MoS_2 [226,227].

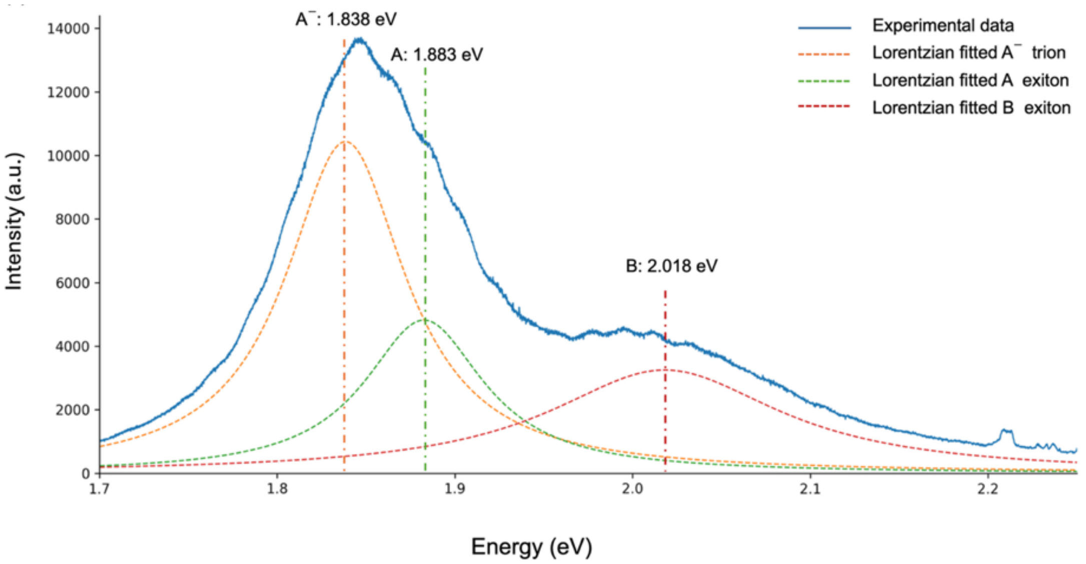

Figure 5.3-1. Photoluminescence (PL) spectra and Lorentzian peak deconvolution of monolayer MoS_2 on SiO_2/Si. Representative 3-peak Lorentzian fits (A^- trion (orange dash line), A exciton (green dash line), and B exciton (black dash line)) to the experimental PL spectra for MoS_2/SiO_2, and vertical dashed lines mark the extracted peak centres.

In addition, a lower-energy feature A^- appears at 1.838479 eV (674.47 nm), which is commonly attributed to charged-exciton (trion) emission, arising from the radiative recombination of a three-particle bound state in MoS_2[228]. Because MoS_2 on SiO_2 is typically electron-rich (n-type), negative trions (A^-) are abundant, giving rise to a pronounced A^- intensity in the deconvolved PL spectrum. Accordingly, the presence and relative intensity of A^- are strongly governed by carrier density and disorder (inhomogeneous broadening) and are therefore widely used as a qualitative indicator of doping in monolayer MoS_2[226,227,229]. Overall, the extracted peak structure and positions are consistent with the established PL signature of monolayer MoS_2 on SiO_2 [226,229].

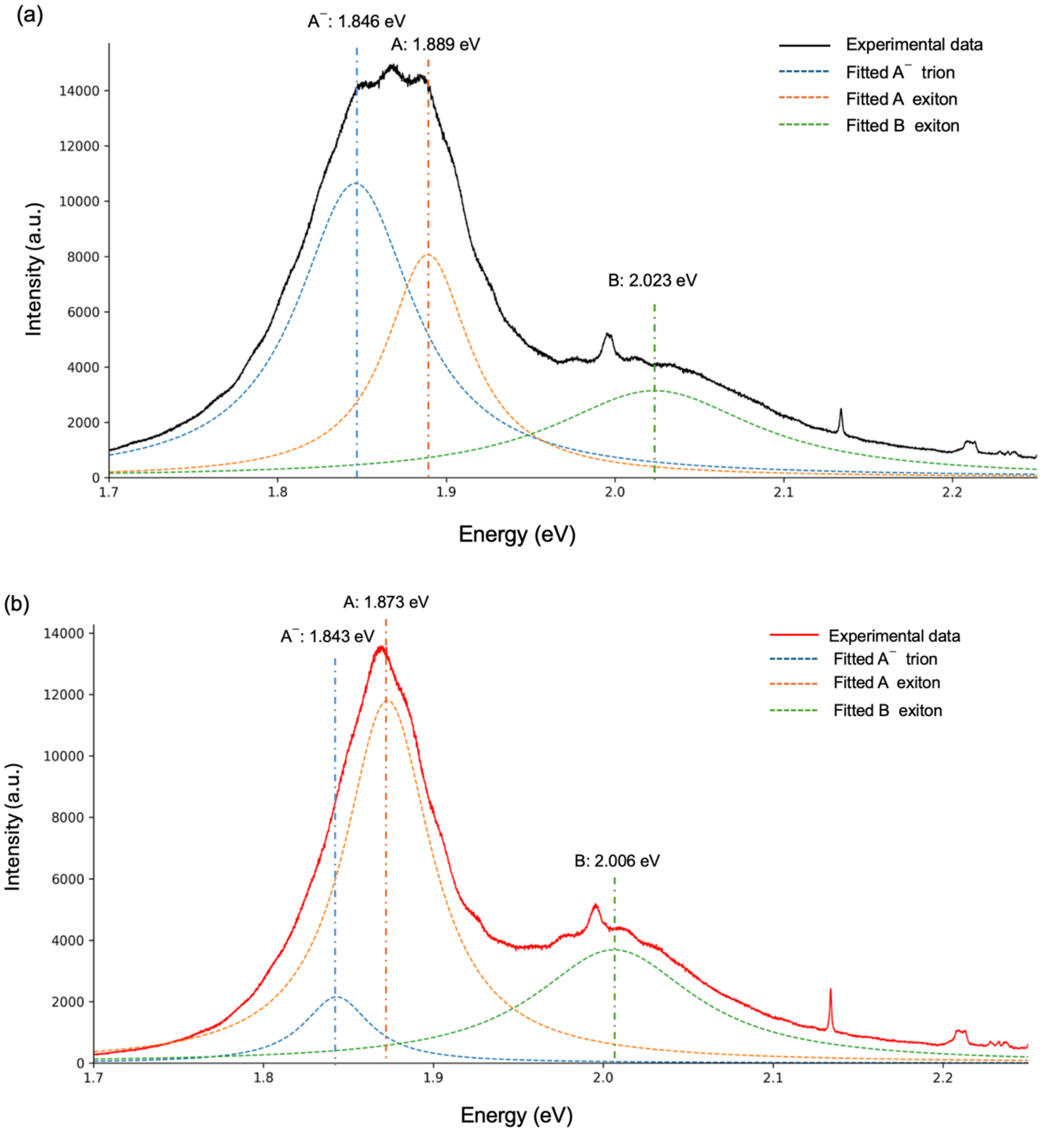

Figure 5.3-2. Photoluminescence (PL) spectra with Lorentzian peak deconvolution of Graphene–MoS_2 heterostructures (a), and MoS_2-Graphene(b) on SiO_2/Si.

When graphene is introduced, the photoluminescence (PL) intensity remains largely unchanged in both stacking configurations (5.3-2), with no significant quenching observed. This contrasts with prior assumptions of strong PL suppression due to interfacial charge transfer, suggesting that the coupling in these samples may be relatively weak or that recombination pathways remain largely intact[230].

While the overall PL intensity is not significantly quenched at room temperature, the introduction of graphene substantially alters the MoS_2 excitonic environment through dielectric screening—changing the effective dielectric surroundings of MoS_2 from "SiO_2 + air" to "SiO_2 + graphene", and through interfacial charge-transfer/electrostatic doping, which tune exciton–trion energetics and shift the relative population balance between neutral excitons and trions[231-236].

In the PL of both heterostructures (Figure 5.3-2), the A^- trion blueshifts (from 1.838 eV in MoS_2/SiO_2 to 1.843 eV in MoS_2–Graphene and 1.846 eV in Graphene–MoS_2). The observed A^- trion blueshift follows from the relationship $\Delta E_{PL} \approx \Delta E_g - \Delta E_b^T$, where the ΔE_{PL} arises because the reduction in trion binding energy ($\Delta E_b^T < 0$) dominates band-gap renormalization (ΔE_g). This decrease in E_b^T is driven by two effects of coupling with graphene: (i) enhanced dielectric screening, which increases the effective dielectric constant (ε_{eff}) and scales approximately as $E_b \propto 1/\varepsilon_{eff}^2$, and (ii) increased electron density from interfacial charge transfer, which strengthens free-carrier screening via the Thomas-Fermi wavevector ($q_{TF} \propto \sqrt{n}$). Both mechanisms weaken the Coulomb potential, lowering E_b^T and producing the observed blueshift that quantifies the modified electrostatic environment. Concurrently, the neutral A exciton contribution increases (A peak intensity: 4818.98 → 11806.48 in MoS_2–Graphene and → 8064.94 in Graphene–MoS_2), as expected from doping-controlled studies where carrier density shifts the PL balance from trion- to exciton-dominated emission [232, 233,235-236].

Furthermore, stacking order introduces additional asymmetry by modulating how strongly the SiO_2 substrate perturbs MoS_2, since SiO_2 is a source of charged-impurity disorder and trap-induced electrostatic fluctuations that can locally gate 2D semiconductors [235,237-239]. In MoS_2–G, MoS_2 is in direct contact with SiO_2, whereas in G–MoS_2, an intervening graphene layer partially screens and spatially redistributes substrate-induced fields, altering the interfacial electrostatics of MoS_2.

This structural difference leads to distinct spectral signatures: G–MoS_2 exhibits systematically higher peak energies than MoS_2–G, with $\Delta E = +0.00296$ eV (A^-), +0.01609 eV (A), and +0.01700 eV (B), indicating a stronger blueshift when MoS_2 is supported by graphene. The emission balance also reverses: G–MoS_2 is more trion weighted, with a markedly larger A^- peak area but a reduced A peak area compared to MoS_2–G, consistent with carrier-density–dependent redistribution between trion and exciton-dominated emission channels [235,237,238,240,241]. Collectively, the observations confirm that interfacial dielectric screening and charge redistribution—though subtle—can deterministically reshape the excitonic emission profile of monolayer MoS_2 in vdWHs [242].

5.4 Low-Temperature PL: Spectral Fingerprinting of Graphene–MoS_2 Heterostructures

To uncover fine excitonic structure and assess the spatial fidelity of emission-based optical fingerprints, low-temperature photoluminescence (LT-PL) measurements were performed at 10K on both MoS_2–graphene and graphene–MoS_2 heterostructures. These experiments test whether the spatial and stacking-dependent PL modulations observed at room temperature persist with enhanced contrast at low temperatures, thereby validating their deterministic nature for physically unclonable function (PUF) applications.

Cryogenic photoluminescence (PL) spectroscopy enhances the spectral resolution of monolayer MoS_2 and its heterostructures with graphene by suppressing thermally activated broadening and non-radiative loss pathways, thereby enabling the reliable identification of weak spectral shoulders, line shape asymmetries, and subtle peak shifts. This enhancement originates from the cryogenic modification of three principal temperature-dependent phenomena: (i) the renormalization of the electronic band structure, (ii) the suppression of dephasing and scattering processes, and (iii) the rebalancing of radiative versus non-radiative recombination dynamics**.** First, excitonic transition energies exhibit temperature dependence arising from bandgap renormalization driven by electron–phonon coupling and lattice thermal expansion—a behaviour commonly parameterized by the Varshni relation:

$$E(T) = E(0) - \frac{\alpha T^2}{\beta + T} \quad \text{, (Equation 5.4-1)}$$

where *E(T)* is the transition energy at temperature *T, E (0)* is the extrapolated *0 K* energy, and α and β are material-specific empirical parameters obtained from fitting. Second, spectral linewidths are governed by dephasing and scattering processes that scale with the phonon population. The average phonon occupation $n(\omega, T)$, described by the Bose–Einstein distribution decreases at low temperatures.

$$n(\omega, T) = \frac{1}{\exp\left(\frac{\hbar\omega}{\kappa_B\ T}\right) - 1} \quad \text{, (Equation 5.4-2)}$$

Here, ω is the phonon frequency, $\hbar$ is the reduced Planck constant and κ_B is the Boltzmann constant. This reduction weakens phonon-assisted dephasing and exciton–phonon scattering, yielding sharper excitonic features with improved spectral separability. Third, cooling rebalances radiative and non-radiative recombination dynamics. Thermally activated non-radiative channels can be phenomenologically described by an Arrhenius-type quenching model:

$$I(T) = \frac{I_0}{1 + A_1 \exp\left(\frac{E_{T1}}{T\kappa_B}\right) + A_2\ \exp\ (\frac{E_{T2}}{T\kappa_B})} \qquad \text{(Equation 5.4-3)}$$

Where $I(T)$ is *the* PL intensity; I_0 is the low temperature limiting intensity; A_i and E_i are the prefactors and activation energies distinct non-radiative pathways [243].

Together, these relations rationalize the frequent enhancement of PL quantum yield and the emergence of weak radiative channels at cryogenic temperatures as thermally activated losses are suppressed [244-248]. Finally, by amplifying static disorder, reduced thermal fluctuations intensify low-energy bound-exciton emission and alter the exciton–trion equilibrium [244-246].

5.4.1 MoS_2-Graphene on Si/SiO_2

The temperature-dependent photoluminescence response of MoS_2–Graphene heterostructure is investigated at 300 K and 10 K. Through multi-Lorentz deconvolution, changes in exciton peak energies, linewidths, and the exciton–trion balance are quantified. Furthermore, the intra-flake spatial homogeneity of MoS_2–G is assessed to determine whether graphene introduces reproducible, position-dependent modulation of excitonic fingerprints across the heterostructure.

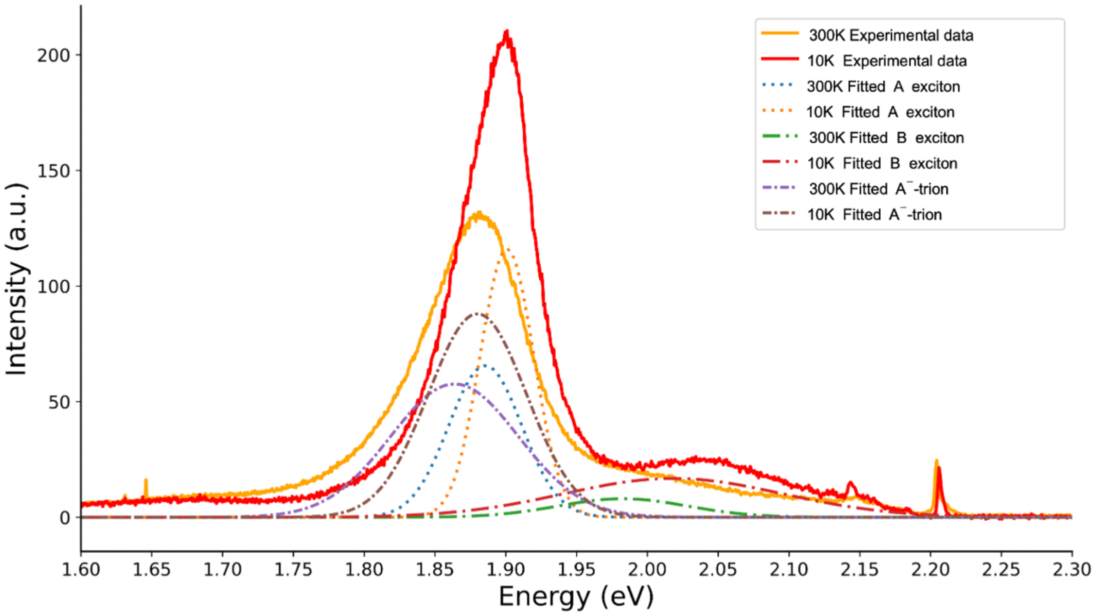

Figure 5.4.1-1 Temperature-dependent PL spectra of the MoS_2–Graphene heterostructure measured at 300 K (black) and 10 K (red), shown with Lorentz deconvolution of the A exciton, A^- trion, and B exciton contributions (dashed/dotted curves).

In the MoS_2–graphene heterostructure (Figure 5.4.1-1), cooling from 300 K to 10 K results in a pronounced enhancement and spectral sharpening of the A-band emission. This evolution is consistent with the suppression of intrinsic MoS_2 loss channels—phonon-assisted dephasing and thermally activated non-radiative decay—which govern the low-temperature spectral sharpening despite the influence of the adjacent graphene layer. At 300 K, the spectrum comprises overlapping A^- and A exciton peaks centred at 1.864 eV and 1.886 eV, respectively, corresponding to a splitting of 21.73 meV. Both peaks are broad, with FWHM values of 0.10628 eV (A^-) and 0.06062 eV (A) and exhibit comparable intensities (~65.54 a.u. and ~57.64 a.u.). By 10 K, the transitions blueshift by approximately +15 meV (A: 1.90092 eV; A^-: ≈1.88 eV) and narrow significantly (FWHM(A): 0.04444 eV; FWHM(A^-): 0.08152 eV). Concurrently, the integrated intensities increase for both peaks, with the A exciton rising from ~65.54 a.u. to ~115.80 a.u. and the A^- trion from ~57.64 a.u. to ~87.97 a.u. This yields an A/A^- intensity ratio that increases from ~1.14 at 300 K to ~1.32 at 10 K, indicating a rebalancing of the exciton–trion equilibrium toward exciton-dominated emission at low temperature. Furthermore, the B exciton, which is not detectable at room temperature, emerges as a weak peak at 1.98258 eV (16.73 a.u.) at 10 K—in agreement with the behaviour observed in isolated monolayer MoS_2 in 10K.

Five distinct spatial positions on the MoS_2–Graphene heterostructure were selected to evaluate the intra-flake spatial homogeneity (Figure 5.4.1-2). At 10 K, the PL spectra from all positions demonstrate consistent changes compared to the monolayer MoS_2—quenching of the A-band intensity and a blueshift of the A and A^- excitonic energies—but with clear spatial dispersion in the magnitude of these effects, revealing position-dependent coupling to the graphene layer. Most notably, the the A-exciton emission shows significant quenching, with intensity varying from ~116 to 185 a.u. across the heterostructure compared to ~238 a.u. in the monolayer MoS_2. This quenching is attributed to non-radiative charge and energy transfer to graphene, and its spatial variation points to local differences in interlayer coupling.

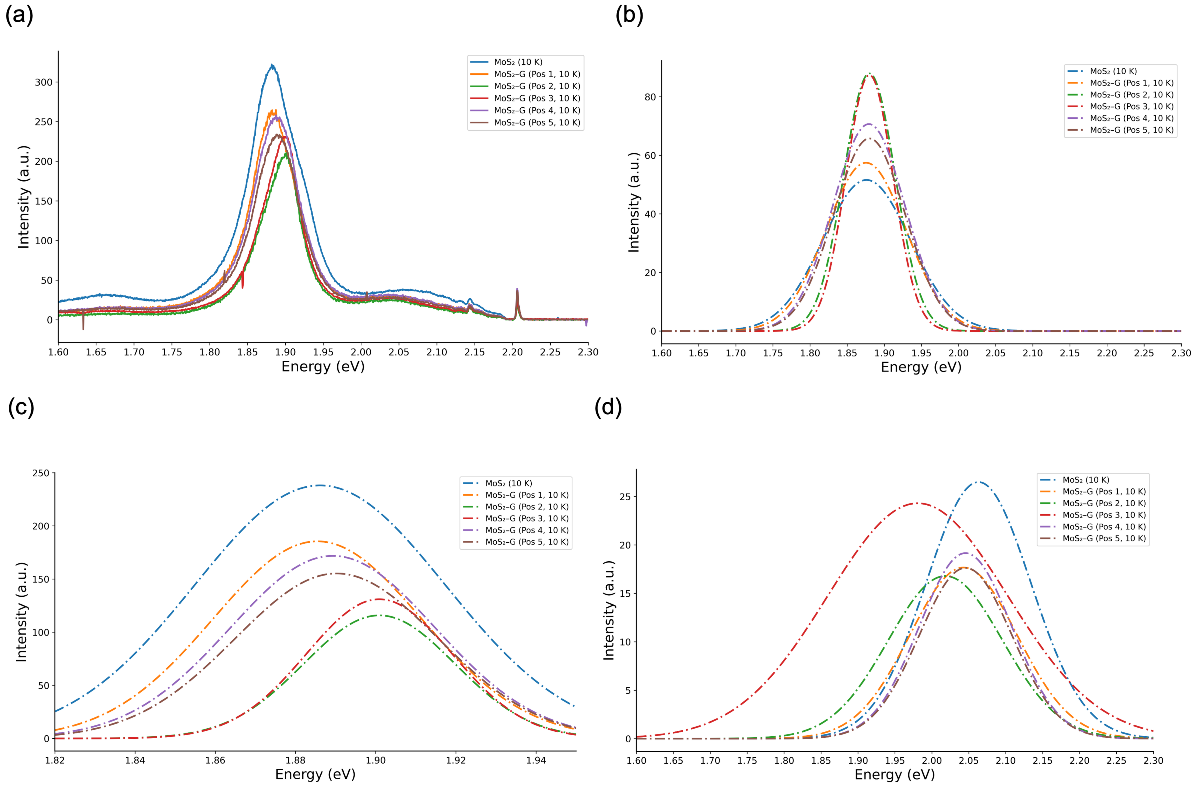

Figure 5.4.1-2 Low-temperature (10 K) PL comparison between monolayer MoS_2 on Si/SiO_2 and the MoS_2–graphene heterostructure measured at five spatial positions. (a) PL spectra for MoS_2 (reference) and MoS_2–G (Pos. 1–5). (b,c) Lorentz-deconvolved A^- trion (b) and A exciton (c) contributions for MoS_2 and MoS_2–G (Pos. 1–5), showing the relative evolution of the A-region emission across the heterostructure. (d) Lorentz-deconvolved B-exciton contributions, illustrating the weak but spatially variable B feature across the measured positions.

The excitonic peak positions across the heterostructure also display clear spatial dispersion. The A exciton spans 1.885–1.901 eV (~15.5 meV spread), while the A^- trion varies across a narrower range of 1.875–1.880 eV (~4.5 meV)—both slightly blue-shifted relative to the MoS_2 monolayer. This positional modulation alters the splitting of A-A^-. For instance, positions 2 and 3 exhibit a larger splitting of ~20.9 meV compared to the ~10 meV in isolated MoS_2, indicating spatial variation in the local exciton–trion balance governed by differences in carrier density and dielectric screening. In contrast, the fitted B-exciton shows the largest apparent energy variation (1.981–2.046 eV, ~64.8 meV spread) and is consistently lower in energy than in the monolayer. However, as the B-exciton is weak and broad, it is highly sensitive to spectral background and fitting parameters, making it a less robust spatial signature than the sharp A and A^- peaks.

The extent of PL quenching was quantified using two complementary metrics: (i) the integrated PL area (1.70–2.20 eV) for total emission, and (ii) the total fitted A and A^- areas for the excitonic channel. The integrated intensity shows an overall suppression of ~21–40% (mean ~29.8%) while the total excitonic (A + A^-) emission shows consistently stronger quenching of ~24–51% (mean ~36.6%) across the five positions. Both metrics show that positions 2 and 3 exhibit the strongest quenching (~40–51%), while positions 1 and 4 show the weakest (~21–25%). This quantifies the pronounced heterogeneity in graphene-induced non-radiative transfer efficiency.

Reproducible spatial variations in the exciton peaks indicate position-dependent modulation of the A/A^- emission, consistent with local fluctuations in strain, electrostatic doping/screening, and MoS_2–graphene coupling across the flake [249,250]. These variations are primarily from transfer-induced interfacial heterogeneity—such as residues, blisters/voids, and wrinkles/folds—which locally changes the MoS_2–graphene separation and strain field, thereby altering dielectric screening and the efficiency of non-radiative energy/charge transfer to graphene. Secondary contributions may arise from SiO_2 charge disorder (trap states/charged impurities) and intrinsic MoS_2 point defects (e.g., S-vacancy/oxygen-related sites), which locally modulate carrier density and recombination pathways, leading to measurable changes in the A/A^- balance and linewidth. The fact that these differences become clearly resolvable only at low temperature—yet remain consistent across repeated scans—supports deterministic intra-flake heterogeneity in the heterostructure.

5.4.2 Spatial and Temperature-Dependent Photoluminescence in Graphene–MoS$_2$ Heterostructures

Temperature-dependent PL of G–MoS$_2$ was measured at 300 K and 10 K under identical acquisition conditions and analysed using the same multi-Lorentz deconvolution procedure applied to monolayer MoS$_2$ (Figure 5.4.2-1). A direct comparison between G–MoS$_2$ and MoS$_2$ at 10 K is presented in Figure 5.4.2-2. Spatial homogeneity across the heterostructure is assessed using eight positions to quantify position-dependent modulation of excitonic fingerprints and the corresponding PL quenching relative to MoS$_2$ (Figure 5.4.2-3).

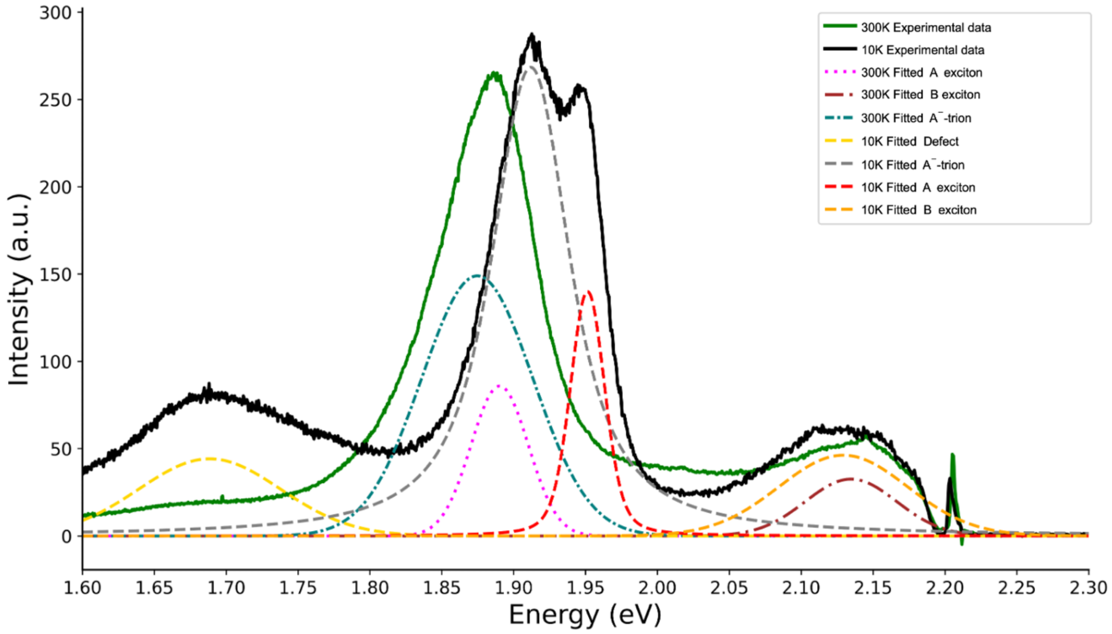

Figure 5.4.2-1. Temperature-dependent PL spectra of the graphene–MoS$_2$ heterostructure (G–MoS$_2$) at 300 K (green) and 10 K (black). The spectra are decomposed using Lorentz peak fitting to resolve the A exciton, A$^-$ trion, and B exciton at both temperatures, with an additional low-energy defect-related emission included in the 10 K fit.

As shown in Figure 5.4.2-1, At 10 K, the G–MoS$_2$ PL undergoes a significant restructuring relative to 300 K: the A-family peaks blue-shifts, narrows, and intensifies, and a new low-energy band in the 1.6–1.8 eV window emerges (assigned to a bound/localised exciton, X$_L$). Compared with 300 K, the A$^-$ trion shifts from 1.8747 →

1.9119 eV (+37.2 meV) and its linewidth narrows from 0.0911 → 0.0651 eV (−28.5%), while its amplitude increases from 148.9 → 268.4 a.u. (+80%); the A exciton shifts from 1.8903 → 1.9514 eV (+61.1 meV) and narrows from 0.0470 → 0.0284 eV (−39.5%), with the A–A^- splitting increasing from 15.6 meV to 39.5 meV, consistent with reduced thermal broadening and a more clearly resolved exciton–trion balance at cryogenic temperature. The B exciton remains near ~2.13 eV (2.1346 eV at 300 K vs 2.1293 eV at 10 K; −5.4 meV), but becomes more prominent in integrated weight (area 2.59 → 5.25 a.u.·eV, ~×2) and is fitted with a broader linewidth (0.0749 → 0.1059 eV), indicating that the high-energy shoulder carries increased spectral weight at low temperature even though its position is largely unchanged. Crucially, a distinct X_L (defect/bound exciton) band appears at 1.6886 eV (FWHM 0.116 eV, height 44.2 a.u., area 5.46 a.u.·eV), which is absent (or not separable) at 300 K and is characteristic of exciton localisation at defects/potential fluctuations.

This emergence of X_L is commonly explained by a three-state model for monolayer MoS_2 [248,251-252] in which carriers relax into trapped (localised) states; at high temperature they can thermally re-excite to higher-energy states and predominantly radiate via the A exciton channel, whereas at low temperature thermal activation is suppressed and a larger fraction recombines directly from trapped states to emit X_L, with both A and X_L intensities further enhanced by the reduction of phonon-assisted non-radiative pathways.

The direct comparison between G–MoS_2 and monolayer MoS_2 (Figure 5.4.2-2) shows that introducing graphene strongly reshapes the excitonic balance and improves spectral separability [253-255]. Relative to MoS_2, all fitted peak centres in G–MoS_2 are blue-shifted: A^- moves from 1.87588 → 1.91191 eV (+36.0 meV) and A from 1.88588 → 1.95138 eV (+65.5 meV), while B peak shifts from 2.06286 → 2.12926 eV (+66.4 meV), consistent with interfacial charge-transfer/screening effects that can renormalise optical transition energies in supported/stacked MoS_2 systems [253,254,256]. Concomitantly, the A-manifold becomes much more clearly split in Graphene-MoS_2, with the A–A^- splitting increasing from ~10.0 meV (monolayer MoS_2) to ~39.5 meV (G–MoS_2), and both A-related peaks narrowing substantially (e.g., A exciton FWHM: 0.0736 eV → 0.0284 eV; A^- FWHM: 0.1381 eV → 0.0651 eV), aligning with the well-established sensitivity of the exciton–Trion balance and linewidths to carrier density and dielectric environment.

Most notably, graphene drives the spectrum into a trion-dominated regime: in MoS_2 the integrated areas give $A^-/A \approx 0.41$ (7.58 vs 18.65 a.u.·eV), whereas in G–MoS_2 $A^-/A \approx 5.42$ (25.77 vs 4.75 a.u.·eV), i.e., the neutral A exciton is strongly suppressed while the trion contribution dominates—consistent with the known evolution from exciton to trion dominated PL under increased electron density (via doping/gating/charge transfer)[253,255,257]. The B exciton is present in both cases but remains much broader in MoS_2 (FWHM 0.167 eV) than in G–MoS_2 (0.106 eV), consistent with broader/less-resolved excitonic features under different local electrostatic environments and interfacial coupling conditions [254,256].

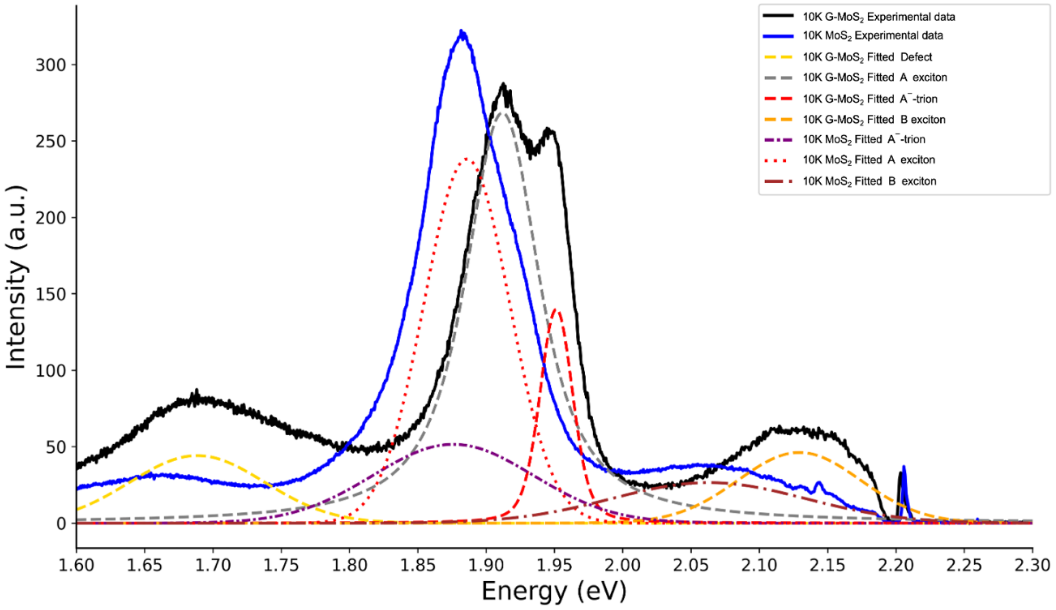

Figure 5.4.2-2. Comparison of low-temperature PL spectra measured at 10 K for G–MoS_2 (black) and monolayer MoS_2 (blue). The spectra are fitted using Lorentz peak decomposition to extract the A exciton, A^- trion, and B exciton contributions; an additional low-energy defect-related emission is included for G–MoS_2 to capture the enhanced sub-bandgap feature observed in the heterostructure.

In addition, G–MoS_2 exhibits an extra low-energy band at 1.68855 eV (FWHM 0.116 eV) assigned to a localised/bound exciton (X_L), consistent with defect-/trap-assisted sub-bandgap emission widely reported in monolayer TMDs (including MoS_2) at low temperature[256,258]. Thus, graphene-induced modification of the local carrier environment (charge transfer and screening) that enhances trion formation and suppresses neutral-exciton emission, together with interfacial heterogeneity that promotes localised-exciton pathways at cryogenic temperature, provides a physically consistent framework for the observed spectral redistribution in the heterostructure.

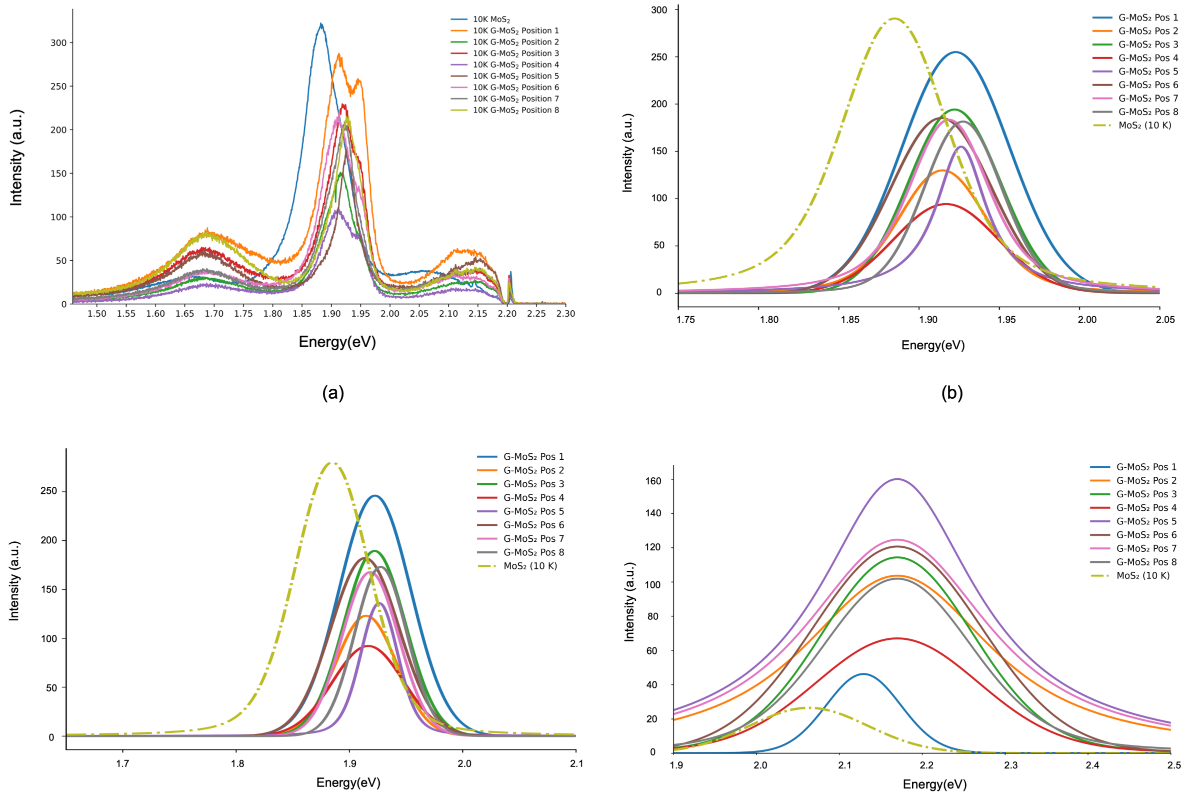

(a)

(b)

(c)

(d)

Figure 5.4.2-3. Spatially resolved 10 K PL spectra comparing monolayer MoS_2 (dash–dot, yellow) with the G–MoS_2 heterostructure measured at eight locations (Positions 1–8). (a) Full PL spectra showing the overall spectral evolution. (b–c) Enlarged views of the A-band (A^-/A) energy range, revealing position-dependent changes in peak shape, relative intensity, and spectral shift across the heterostructure compared with MoS_2. (d) Enlarged view of the B-exciton region across Positions 1–8 relative to MoS_2.

Analysis of spatial homogeneity (Figure 5.4.2-3) shows that the PL response of G–MoS_2 exhibits consistent graphene-associated modifications across all measured positions relative to monolayer MoS_2. The neutral A-exciton peak is systematically blue-shifted with respect to MoS_2 (1.886 eV), spanning ~1.916–1.953 eV across the eight locations, while the A^- trion energy remains in a comparable range and spans both slightly below and above the MoS_2 reference (1.876 eV), ~1.857–1.927 eV. In addition to these spectral shifts, the total integrated PL intensity (1.70–2.20 eV) is reduced by ~30–78% compared to MoS_2 across all positions, consistent with graphene introducing additional non-radiative relaxation pathways (e.g., via interlayer charge/energy transfer) and/or modifying the local dielectric and doping environment [259-262]. Deconvolution of the A-manifold further indicates that the neutral A component is strongly suppressed at most positions, whereas the A^- contribution can be enhanced at selected locations, revealing a position-dependent exciton–trion balance that likely reflects spatial variations in local carrier density, strain, and interfacial coupling within the heterostructure [261-263].

Although the same qualitative trends are observed across the heterostructure, the magnitude of these effects varies substantially with position. The total integrated PL quenching ranges from ~30% at Pos1 to ~78% at Pos 8, indicating strong spatial variation in graphene coupling efficiency. The fitted A-exciton area spans from modest quenching (~16% at Pos2) to near-complete suppression (>94% at Pos3 and Pos6). In contrast, the A^- trion response is highly non-uniform: it is strongly enhanced at some positions (e.g., Pos1, Pos3, Pos6) but is effectively suppressed where the trion peak becomes extremely weak (notably Pos4). The extracted A–A^- splitting also shows clear spatial dispersion (e.g., ~39.5 meV at Pos1 versus ~47.9 meV at Pos8), consistent with a locally varying exciton–trion landscape driven by position-dependent doping/screening and interfacial disorder. Finally, the B-exciton—often appearing only as a weak, high-energy shoulder in MoS_2 PL and more difficult to resolve clearly than the A-manifold—remains broadly centred near ~2.17 eV across Positions 2–8 but shows very large fitted area variations in our dataset (up to ~12× at Pos5), making it less reliable as a spatial probe than the A/A^- features[264-267].

Quantitative quenching analysis highlights that overall PL (integrated intensity) is quenched at every measured position, but the fitted A-manifold (A + A^-) does not follow the same trend. The strongest integrated quenching occurs at Pos5 and Pos8 (~78%), whereas the fitted (A + A^-) contribution is most strongly suppressed at Pos4 (~66%) and remains substantially quenched at Pos8 (~55%). Conversely, Pos1 (and Pos5) show comparable or enhanced fitted (A + A^-) weight because the spectrum becomes increasingly trion-dominated, even though the total integrated PL remains quenched [255-257]. This decoupling between total intensity and fitted excitonic weight emphasises that interlayer coupling is spatially heterogeneous, likely due to interfacial inhomogeneities (residues, wrinkles, bubbles/strain gradients) that modulate both non-radiative transfer rates and the local carrier environment across the G–MoS_2 interface [256,268-270].

5.5: Environmental Robustness

For optical physically unclonable functions (PUFs) to be viable in real-world applications, their spectral signatures must remain stable under varying environmental conditions. Their response to changes in excitation power and operating temperature is critical for ensuring long-term reliability and resistance to tampering or environmental noise. While the previous section demonstrated that spectral uniqueness arises from interfacial complexity, this section evaluates whether these unique optical fingerprints are robust against two key stressors: laser power variation and thermal fluctuation. These tests simulate realistic operating conditions for optical reading systems and challenge–response protocols.

5.5.1 Laser power dependent low temperature Photoluminescence

To establish a detailed understanding of how the optical fingerprint responds to varying excitation conditions, Position 1 of the Graphene–MoS_2 heterostructure was selected for a full-range laser power study from 1 uW to 12 uW. As shown in Figure 5.5.1-1, the PL spectra across this power range reveal a stable and well-defined excitonic emission peak centred near 1.88 eV. With increasing laser power, a progressive redshift of the peak is observed, particularly above ~9 uW, accompanied by a minor loss of shoulder resolution. This behaviour is consistent with laser-induced local heating. Increasing local temperature leads to a reduction in the excitonic optical transition energy through lattice expansion and electron–phonon coupling, and simultaneously increases linewidths, which can diminish the apparent shoulder resolution.

Laser-power dependent redshifts in monolayer MoS_2 PL/Raman attributable to local heating have been widely reported[271]. As introduced in Section 5.4, the temperature dependence of the transition energy is commonly parameterised by the Varshni relation(equation 5.4-1), in the graphene–MoS_2 heterostructure, while the power dependent redshift is attributed to local heating, the overall PL response is measured in a heterostructure where band alignment can be modulated by promoting interfacial charge transfer and redistribution the exciton/trion population(see band structure details in Figure 2.1.3.3-2).

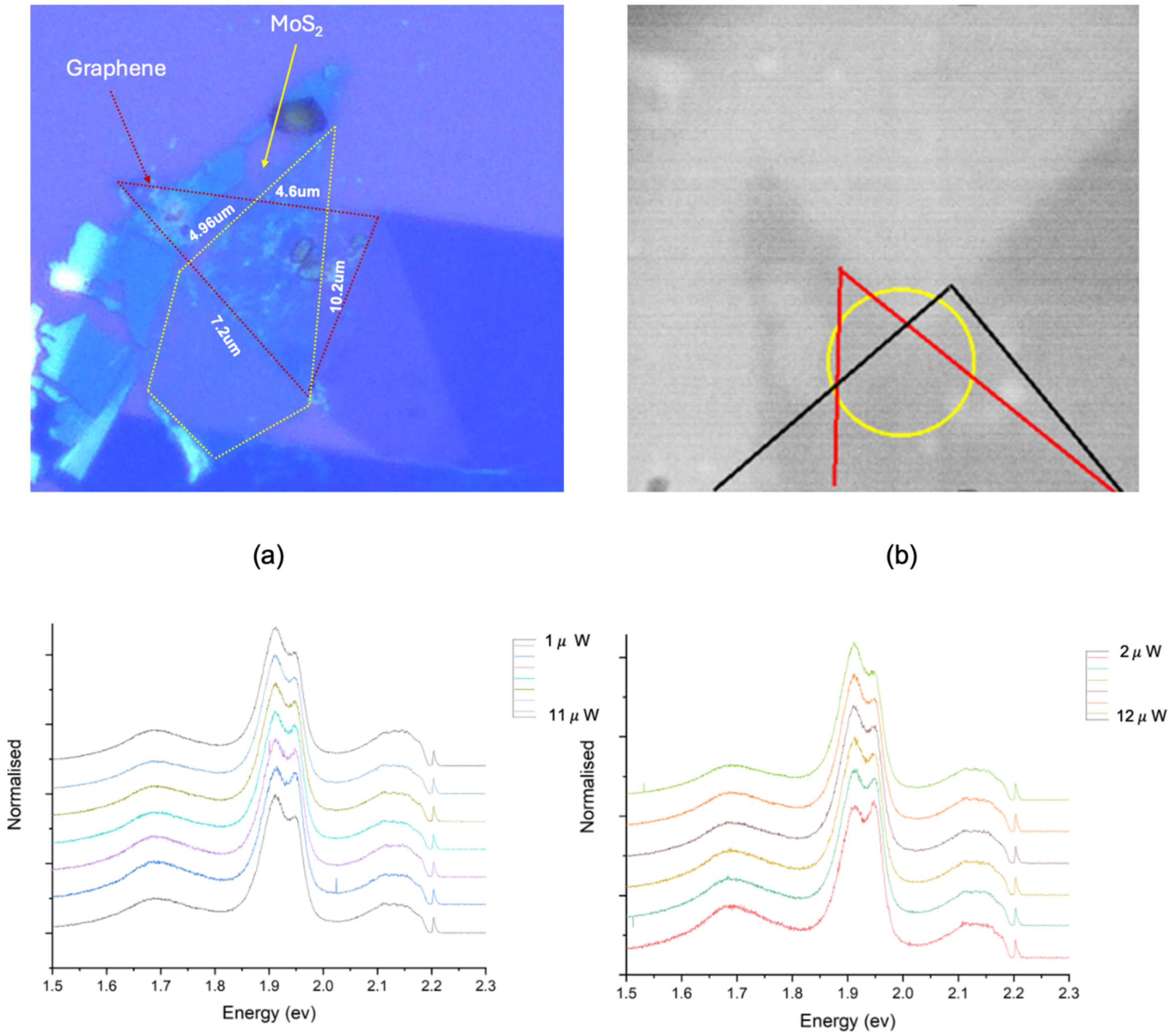

(a) (b)

(c) (d)

Figure 5.5.1-1 laser power-dependent PL measurements of position 1 in Graphene–MoS_2 heterostructure (a, b) Optical and microscope images showing the triangular MoS_2 flake with graphene overlay and the exact position (Position 1) measured in the μ-PL system. (c-d) Low-temperature PL spectra at Position 1, collected from 1 uW to 13 uW. To visualize thermal evolution, the data are split into two subsets: odd-numbered (1-11 uW) and even-numbered (2-12uW). The excitonic peaks sharpen progressively at lower laser power, with only minor redshifts and no distortion in overall shape.

Despite these power-dependent spectral shifts, the overall fingerprint shape remains intact. No photobleaching—an irreversible, exposure-induced loss of PL intensity and/or permanent spectral distortion due to photo-induced chemical/structural changes—was observed within the acquisition conditions, as the key features remained reproducible across the full power range. The consistent presence of the same spectral components under a 12× change in excitation power indicates that the fingerprint at Position 1 is optically resilient and robust against moderate excitation fluctuations.

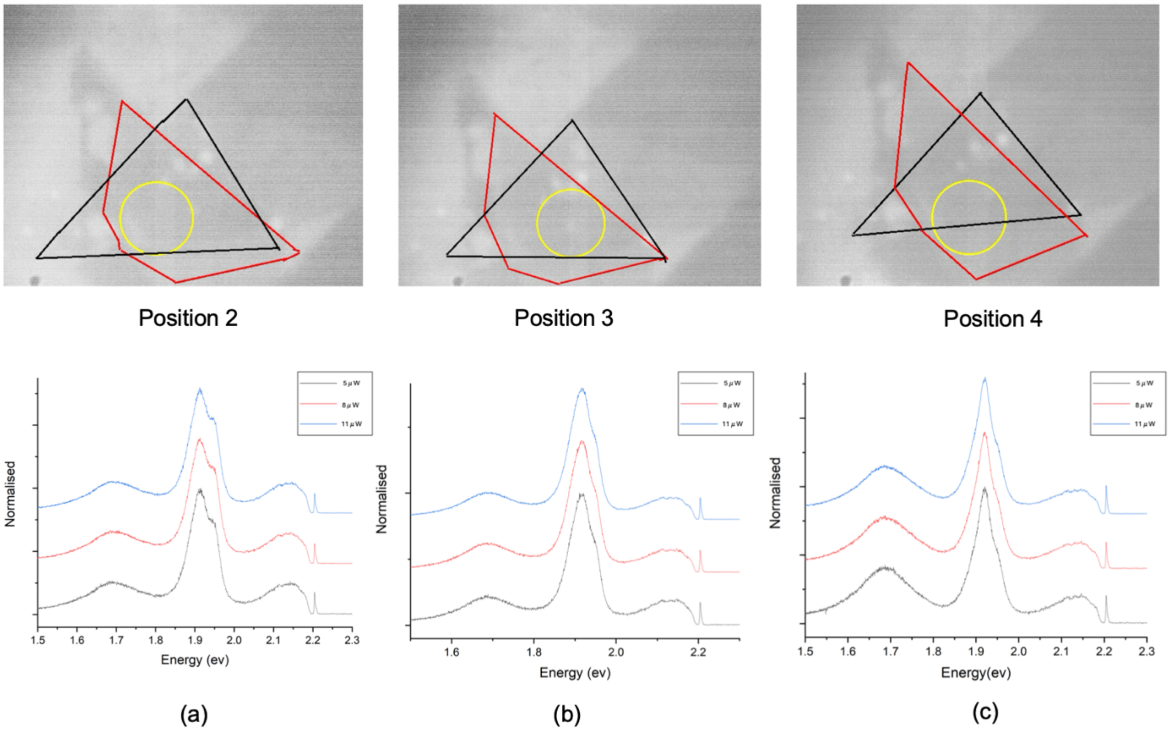

Figure 5.5.1-2 PL spectra at Positions 2(a), 3(b), and 4(c) collected at 5, 8, and 11 uW. These measurements confirm that the relative fingerprint at each position is preserved as laser power increases. The consistency of spectral shape and peak structure across a range of laser power demonstrates strong thermal robustness—essential for ensuring stability in temperature-variable authentication environments.

To validate this robustness across the heterostructure, additional PL measurements were performed at three other locations (Positions 2–4), each under three representative power levels: 5 uW, 8 uW, and 11 uW. These powers were chosen to span the low, moderate, and high excitation regimes identified in the full-range study of Position 1. This allowed for efficient probing of spectral stability without requiring exhaustive repetition. As shown in Figure 5.5.1-2, all three positions exhibit consistent PL spectral shapes across the selected powers, with only minor redshifts or amplitude variations—again attributed to localized thermal effects[272]. No evidence of photobleaching, feature disappearance, or irreversible distortion was observed.

The results from Positions 2–4 demonstrate that fingerprint stability is not limited to a single region but is rather a general property of the Graphene–MoS_2 system. The spectral identity at each location remains consistent even under thermal and photonic perturbation, confirming the spatial reproducibility and power-invariance of the optoelectronic response. This ensures that unique fingerprints derived from each site remain reliable and unclonable under realistic operating conditions, further reinforcing the viability of these heterostructures for practical PUF applications.

5.5.2 Temperature-Dependent Photoluminescence of Graphene–MoS_2 Heterostructures

Alongside the exciton energy shift, the μ-PL intensity of the graphene–MoS_2 heterostructure exhibits a strong temperature dependence. The full temperature sweep was recorded from 10–300 K; however, the 10–210 K dataset is presented here because it captures the regime where the A-exciton remains sufficiently narrow, and the low-energy defect-bound/localised exciton emission is still observable and then thermally suppressed[273]. In MoS_2, such bound-exciton (often denoted X_L) features are typically only observed at low temperatures (<~150 K) and become indistinguishable as temperature rises due to thermal escape from trapping potentials. As shown in Figure 5.5.2-1, the A-exciton peak redshifts and broadens with increasing temperature. The redshift is the expected consequence of bandgap renormalisation driven by lattice expansion and electron–phonon coupling. In parallel, the increasing linewidth with temperature is consistent with stronger exciton–phonon scattering and phonon-induced dephasing, which progressively reduces the visibility of weak spectral contributions at elevated temperature.

To examine the crossover regime in more detail, Figure 5.5.2-1(b) highlights the intermediate range of 70–140 K, where the A-exciton redshift and moderate broadening are clearly resolved while the spectra remain sufficiently well-defined for reliable Lorentz analysis. This temperature window is also where weak low-energy emission (X_L) begins to diminish rapidly, consistent with the onset of thermally activated loss pathways that compete with radiative recombination.

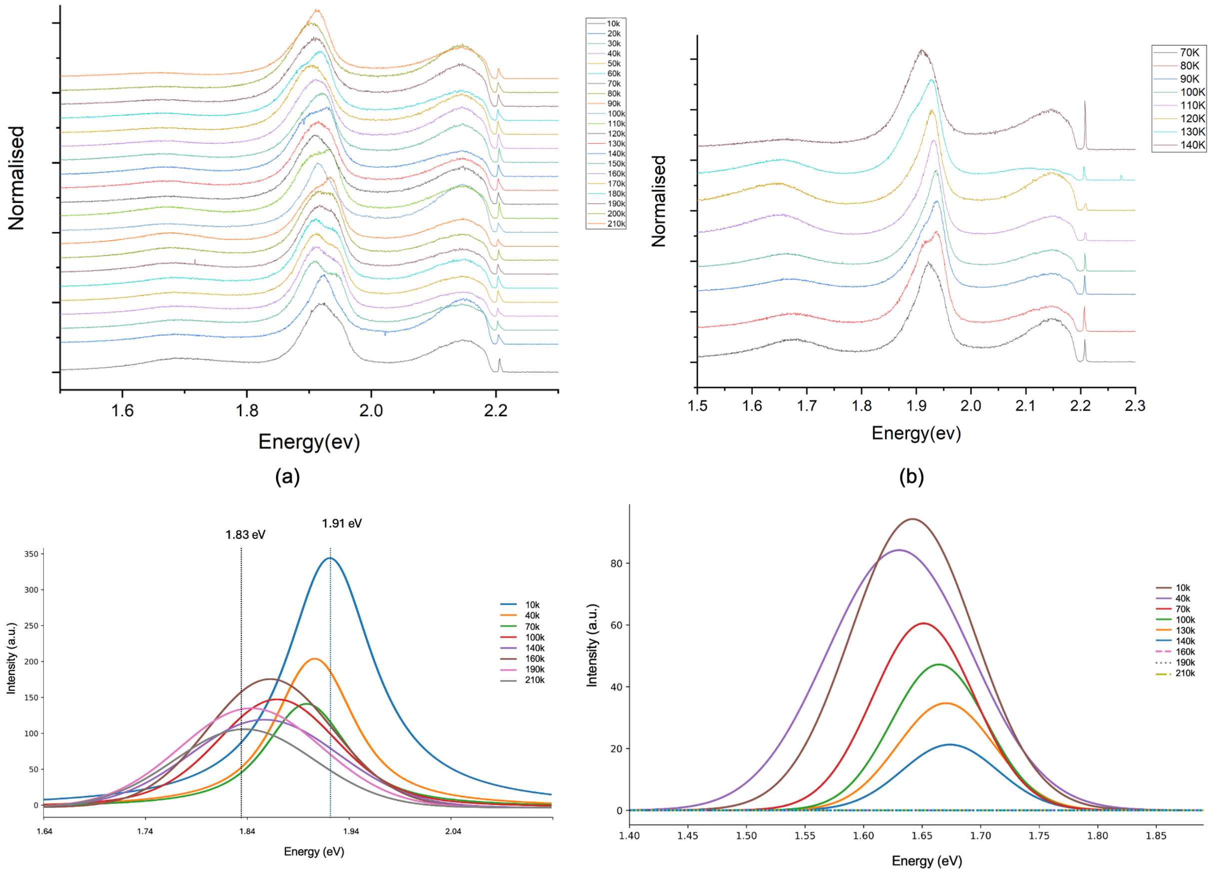

(a) (b)

(c) (d)

Figure 5.5.2-1. Temperature-dependent µ-PL evolution of the graphene–MoS_2 heterostructure and Lorentz peak analysis (10–210 K). (a) Stacked normalised µ-PL spectra measured from 10–210 K, highlighting progressive linewidth broadening and the temperature-driven redshift of the A-exciton emission.(b) Expanded view of the normalised spectra from 70–140 K, emphasising the intermediate-temperature regime where the A-exciton redshift and broadening are most clearly resolved and where the low-energy defect-related contribution weakens. (c) Lorentz fits to the unnormalized A-exciton band at representative temperatures (10–210 K), showing a systematic redshift and thermal quenching of the A-exciton intensity together with broadening, consistent with bandgap renormalisation and increasing nonradiative recombination at elevated temperature.(d) Lorentz fits to the unnormalized low-energy band (≈1.6–1.8 eV), assigned to defect bound/localised exciton emission arising from exciton localisation at defect/trap potentials (commonly associated with vacancy/impurity/disorder-related states in MoS_2).

The A-exciton intensity was quantified using the fitted peak amplitude obtained from Lorentz fits to the raw (unnormalized) spectra (Figure 5.5.2-1(c)). The fitted A-peak amplitude decreases from 341.68 a.u. at 10 K to 65.17 a.u. at 210 K, corresponding to an 80.93% reduction relative to 10 K. This behaviour is consistent with thermally activated suppression of radiative emission as nonradiative pathways become increasingly competitive with rising temperature.

The extent of PL quenching of the excitonic channel A-exciton at temperature *T is* defined as:

$$Q_A\ (T) = 1 - \frac{I_A\ (T)}{I_A\ (10K)}, \text{ (Equation 5.5.2-1)}$$

where: $I_A(T)$ is the fitted A-exciton peak intensity (integrated A-A$^-$) at temperature T, taken here as the Lorentz peak amplitude (units: a.u.) extracted from fits to the raw (unnormalized) PL spectra. $I_A\ (10K)$ is the reference integrated A-exciton peak intensity at 10 K (same definition/units as $I_A(T)$, used to normalise the quenching to the lowest temperature in the dataset.

Using Eq. 5.5.2-1 gives Q_A=0.028 (40 K), 0.357 (70 K), 0.602 (100 K), 0.721 (140 K) and 0.809 (210 K). The significant drop occurs below ~140 K, followed by a more gradual decrease between ~140–190 K, indicating that the dominant nonradiative channels become established by ~140 K, with additional quenching occurring more gradually thereafter. This trend can be interpreted using the radiative–nonradiative competition model introduced in Section 5.4 (Eq. 5.4-4), in which the PL intensity reflects the temperature-dependent balance between $K_{nr}(T)$ and $K_r\ (T)$. Approximating I_0 by the lowest-temperature value (10 K), the relative increase of nonradiative dominance can be estimated as:

$$K(T) \approx \frac{I(10K)}{I(T)} - 1, \text{ (Equation 5.5.2-2)}$$

yielding K ≈0.029 (40 K), 0.555 (70 K), 1.512 (100 K), 2.591 (140 K) and 4.243 (210 K). The monotonic increase in $K(T)$ indicates that $K_{nr}(T)/K_r\ (T)$ rises strongly with temperature, consistent with thermally activated loss processes such as enhanced phonon scattering and defect-mediated trapping[273].

In addition to the main integrated A-exciton, a weak low-energy contribution in the 1.6–1.8 eV region is visible at low temperature but becomes indistinguishable by 150 K (Figure 5.5.2-1d). This band is assigned to defect-bound/localised exciton emission (often denoted X_L), arising from exciton localisation in defect/trap potentials. Bound-exciton emission is widely reported to be restricted to low temperatures (typically <~150 K), because increasing temperature enables excitons to escape trapping potentials and return to free-exciton recombination, while nonradiative pathways become more competitive. The disappearance of the 1.6–1.8 eV band in this temperature range is therefore consistent with thermal delocalisation (de-trapping) of bound excitons together with increasing nonradiative recombination at elevated temperature[273].

Overall, the temperature-dependent µ-PL confirms that the heterostructure's excitonic response is highly sensitive to thermal variation in the cryogenic-to-intermediate regime, exhibiting (i) a bandgap-renormalisation-driven redshift, (ii) phonon-driven linewidth broadening, and (iii) strong thermal quenching of emission intensity accompanied by the suppression of defect-bound exciton signatures[273-275]. These observations motivate the subsequent spatial mapping analysis, where interfacial inhomogeneity and disorder are examined as the microscopic origin of entropy-rich optical textures suitable for PUF encoding[276,277].

Similarly, under varying laser excitation power, the PL response remains stable, with no evidence of irreversible photobleaching or structural degradation. Minor redshifts and intensity changes occur at higher excitation levels, consistent with local heating effects, but the spectral fingerprints retain their characteristic peak shapes and position-specific features. This confirms that the optical emission from the heterostructure is both environmentally robust and reproducible, key requirements for physically unclonable function (PUF) implementations. Overall, the spatial PL signatures in graphene–MoS_2 heterostructures demonstrate high thermal and photonic resilience, validating their suitability for encoding stable, high-fidelity optical identifiers.

Having established both the uniqueness and robustness of the PL fingerprints at discrete spatial points, the temperature-dependent evolution of the excitonic and defect-bound contributions, the next section examines spatially resolved PL maps across the heterostructure to visualise how interfacial disorder and coupling variations translate into entropy-rich optical textures suitable for PUF encoding.

5.6 PL Mapping: Inhomogeneous Optical Identity

To complement the spectral analysis of excitonic behaviour, photoluminescence (PL) mapping was performed to visualize the spatial heterogeneity of the graphene–MoS_2 heterostructure. While temperature-dependent photoluminescence (PL) reveals distinct spectral fingerprints across thermal regimes, spatially resolved PL mapping provides the complementary optical identity across the surface. Together, these techniques create the essential bridge between complex spectral data and the spatial binarization required for robust Physically Unclonable Function (PUF) devices.

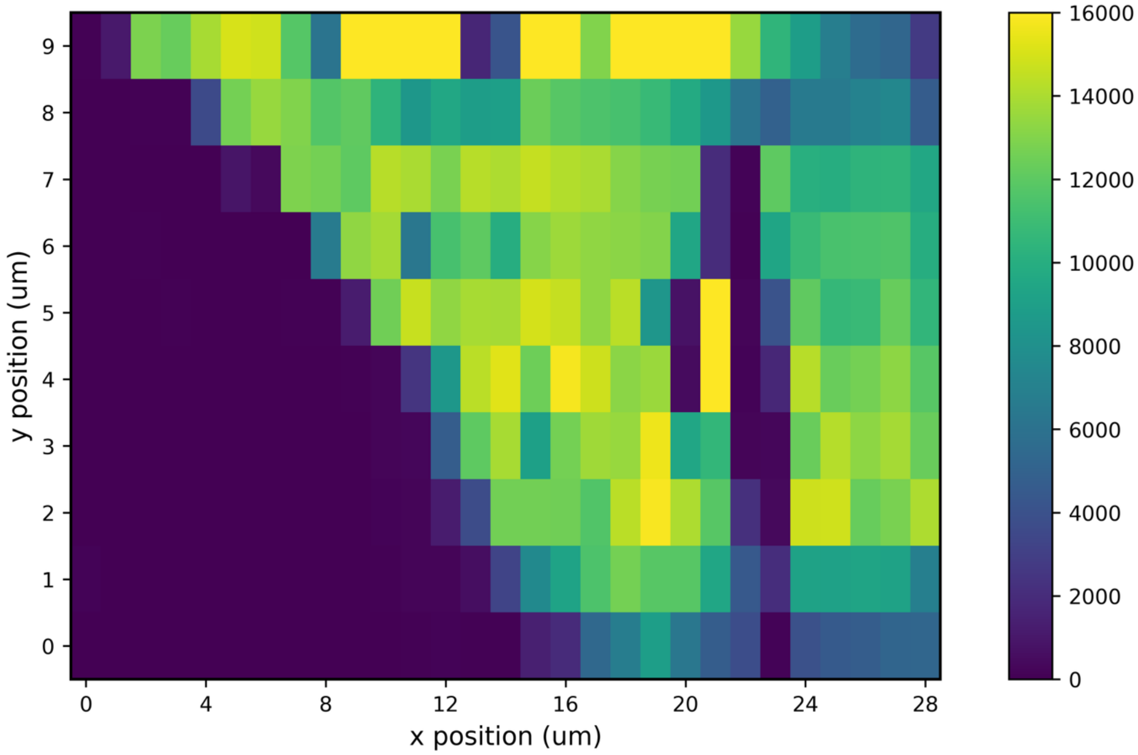

Figure 5.6-1. Spatial PL intensity map of the graphene–MoS_2 heterostructure. Variations in emission intensity reflect underlying physical features such as wrinkles, bubbles, and strain fields, establishing a spatially inhomogeneous optical profile.

Figure 5.6-1 presents a spatial PL intensity map of the heterostructure, revealing pronounced microscale intensity variations indicative of local fluctuations in radiative efficiency. The pronounced spatial inhomogeneity, together with the associated variability in atomic defect populations, is attributed to fabrication-induced morphological and strain-related non-uniformities—such as wrinkles, interfacial bubbles/residue pockets, and local strain fields—introduced during preparation of the MoS_2 layer and assembly of the heterostructure interface[278].

The sources of interfacial disorder are strongly fabrication-route dependent, with different synthesis and assembly methods imprinting distinct patterns of defect density, strain distribution, and interfacial coupling across van der Waals heterostructures (vdWHs). For instance, in CVD-grown graphene–MoS_2 heterostructures, PL inhomogeneity originates from growth-induced microstructural and electronic non-uniformity, including grain boundaries, spatially varying strain, and position-dependent doping[279-282]. These features are controlled by growth kinetics (temperature, precursor flux, pressure. carrier-gas flow,) substrate interactions (thermal expansion mismatch, surface chemistry), together with oxygen/water-related defect passivation and charge-transfer effects[283-287]. In PVD-fabricated (magnetron-sputtered) MoS_2 films, disorder is governed primarily by deposition-defined polycrystallinity and defect formation, which are strongly controlled by substrate temperature, sputter power, working pressure/Ar flow, substrate bias, and target–substrate distance, as well as by deposition time (thickness) and subsequent post-deposition sulfur annealing/sulfurization conditions (temperature, duration and ambient)[288,289].

In contrast, for the mechanically assembled van der Waals heterostructures in this work, the disorder is introduced during the exfoliation, transfer, and stacking processes. This results in non-uniform interfacial contact that leads to the aggregation of trapped adsorbates and polymer residues into discrete pockets, while adjacent regions form comparatively cleaner, closer contact [290-292]. This fabrication-induced disorder in the interface morphology produces heterogeneous optical coupling, thereby encoding a high-dimensional PL fingerprint through the modulation of key optical parameters: intensity, A-exciton energy, linewidth, and trion fraction. The resulting map generates a unique pattern that is impossible to replicate yet permits repeatable readout under consistent measurement conditions—forming the basis for a cryptographic identity. Local strain fields from wrinkles or bubbles shift the MoS_2 optical bandgap and can spatially redistribute exciton recombination (e.g., via exciton funnelling), directly altering local intensity and emission energy [293].

Concurrently, variable interlayer separation and contact quality govern coupling strength: regions of strong coupling to graphene favour efficient nonradiative loss via charge transfer, producing quenched (darker) domains, whereas bubble-separated regions exhibit partial decoupling and brighter emission [294]. Finally, residue- and adsorbate-induced electrostatic disorder—from trapped charges and local doping—further perturbs the exciton/trion balance and introduces spatially varying nonradiative trapping. This amplifies the overall heterogeneity of the PL map [290,291], enhancing the unique spatial fingerprint essential for PUF applications.

The strong microscale variation confirms that the optical response is highly heterogeneous, even within nominally uniform overlap regions. This is corroborated by the optical microscope image in Figure 5.6-2, collected in PL detection mode, where localized bright-red emission highlights specific emission-rich zones against a weakly emissive background. These high intensity domains correspond to areas of efficient exciton generation and recombination[295], directly evidencing spatial heterogeneity in optical properties. This nanoscale variability enables the generation of unique, irreproducible photonic identities, where fabrication induced emission inhomogeneity functions as a physically unclonable emitter for secure digital fingerprinting.

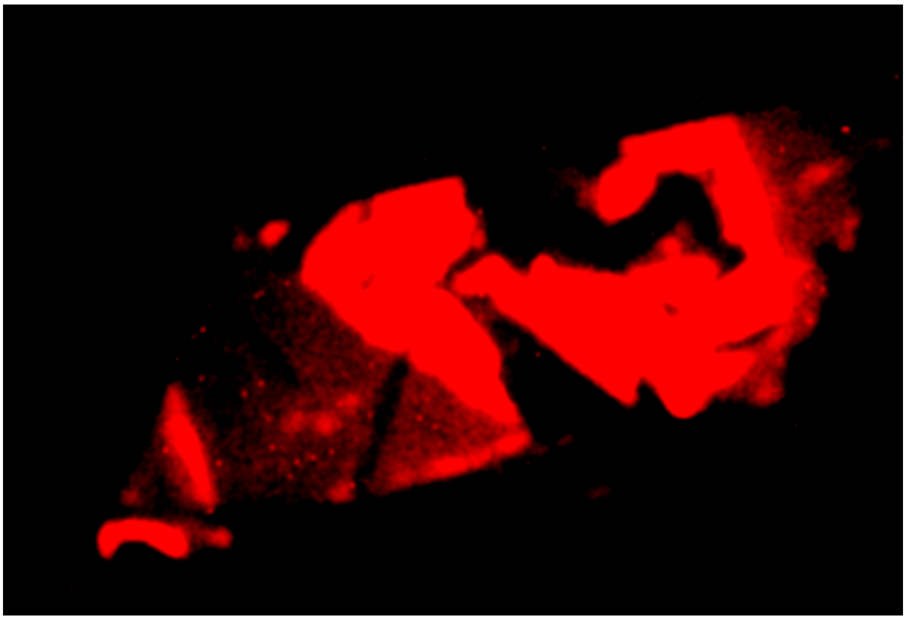

Figure 5.6-2. PL-mode microscope image of the heterostructure showing localized red emission. Bright regions correspond to high-intensity PL zones seen in the PL map, confirming optical spatial complexity.

Collectively, the persistence of PL contrast and peak-energy patterns under thermal and power cycling confirms the stability of the interfacial coupling and optical properties. The PL map visualises a unique spatial fingerprint governed by the assembly-imprinted interfacial microstructure, comprising local strain gradients, trapped interfacial contaminants (e.g., residue/bubble pockets), and position-dependent interlayer coupling [290-294].

Together, these observations demonstrate that graphene–MoS_2 interface fabrication induces deterministic spatial inhomogeneity, producing a random distribution of emission intensities governed by local variations in strain, interlayer contact quality, and residue/bubble morphology. In conventional optoelectronics, such features are treated as imperfections; in PUF devices, however, they become functionally valuable, providing the microscale disorder that enables high-entropy, irreproducible optical fingerprints. The random spatial arrangement of wrinkles, bubbles, and residue pockets is locked in during fabrication and is practically impossible to replicate. This interfacial disorder thus enables a unique cryptographic identity while permitting repeatable readout, provided the interfacial morphology remains stable under measurement conditions [292,294]. Consequently, these fabrication-induced features form a robust entropy source for a reliable optical PUF (OPUF). This stability enables the quantization of the spatial pattern into a unique digital fingerprint, which requires a low intra-device Hamming distance (ensuring reliability) and a high inter-device Hamming distance (guaranteeing uniqueness).

5.7 Optical Binarization: From Spatial Complexity to Digital Identity

Building upon the spatially resolved photoluminescence (PL) mapping in Section 5.6, a direct transformation of the measured emission heterogeneity into a reproducible binary optical identity is presented. This is achieved through optical binarization, which converts complex PL intensity textures into a binary matrix that can function as a digital key for physically unclonable functions (PUFs). The method exploits the fabrication-imprinted inhomogeneity of the graphene–MoS_2 heterostructure—arising from spatial variations in strain, wrinkles, and interfacial contact quality—as a source of intrinsic entropy for robust optical identification.

The binary fingerprint was constructed from PL map by extracting pixel-wise within the

G-MoS_2 heterostructure region. The generation of the final 256-bit PUF response followed a deterministic five-step workflow. The initial and critical step was the creation of a precise heterostructure mask. This was achieved by first inspecting optical and macro-PL images to locate the flake overlap region. An initial mask was obtained by thresholding a quick peak-intensity map at the 30th percentile of its positive values to preserve dim yet valid signal areas. This mask was then refined through hole-filling and a two-iteration morphological closing operation with a 3×3 structuring element, before finally retaining only the largest connected component to define the active region for all subsequent analysis. Following this masking, the workflow proceeded through trusted-pixel selection, binarization, interleaved readout, and cryptographic hashing. The complete, detailed protocol is enumerated in Appendix 2.

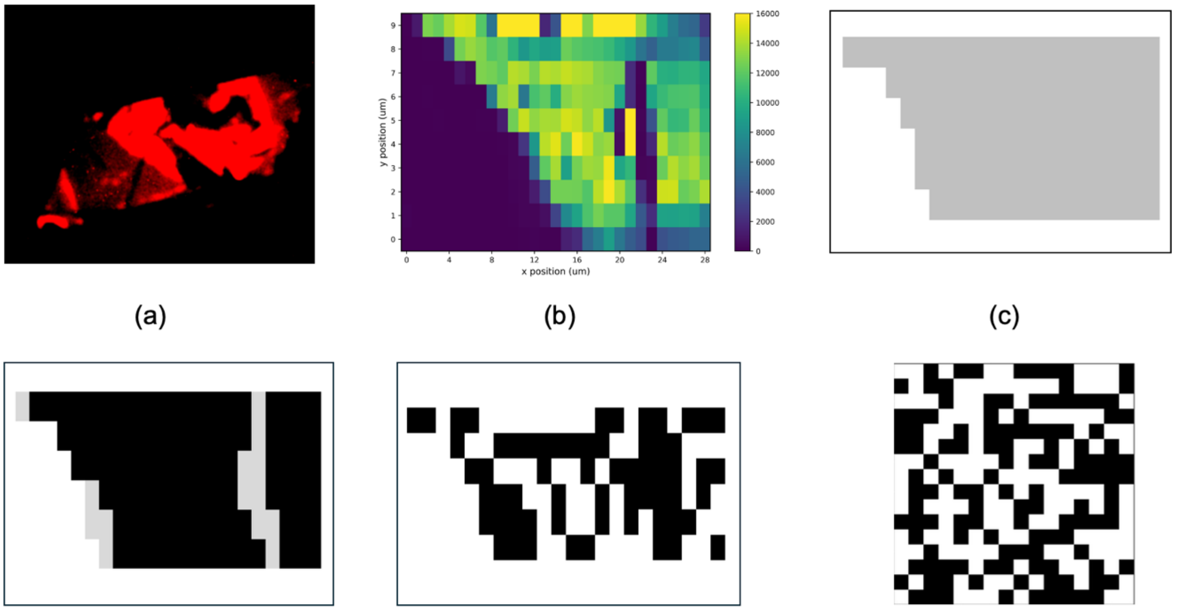

(a) (b) (c)

(c) (d) (e)

Figure 5.7-1 Workflow for generating a binary fingerprint from room-temperature PL maps of the g–MoS_2 heterostructure start by masking, trusted-pixel selection, centred binarization, interleaved sampling, and hashing to a 256-bit response. (a) Macro-PL image of G-MoS_2 used as reference for the HS masking. (b) Integrated PL intensity map; (d) Heterostructure (HS) mask obtained by thresholding and morphological refinement of the intensity map to isolate the overlap region. (c) Trusted-pixel selection within the HS region based on fit quality and stability criteria (R^2 threshold and minimum trion contribution. (d) Example bit-plane derived from the locally normalised intensity feature map. (e) Final 16 × 16 binary response matrixes after applying parity-interleaved sampling and selecting a fixed-length response (post-hash 256-bit key).

Figure 5.7-1 summarises the complete workflow used to generate a binary fingerprint from the room-temperature PL map of the G–MoS_2 heterostructure. Using the trusted heterostructure mask, a total of N = 99 pixels remain for encoding. Across these trusted pixels, multiple fitted peaks exhibit broad, non-degenerate distributions with measurable spatial variation: the locally normalised intensity feature $\log (I/\bar{I}_{3\times3,\ \mathrm{HS}})$ displays a wide distribution with a mean of –0.056 ± 0.680 across 98 trusted pixels.

Collectively, these statistical spreads confirm that the heterostructure's optical property stem from a multiplicity of local, uncontrolled variations rather than a uniform interfacial state. Spatial correlation analysis further supports the low predictability of the fingerprint—a core requirement for physical un-clonability. The locally normalised intensity map is effectively decorrelated at lag-1 ($r \approx 0.007$), with a neighbour-agreement rate of ~0.45—statistically indistinguishable from randomness. This decorrelation is expected because the 3×3 median normalisation suppresses smooth illumination/collection trends while emphasising local texture.

These quantitative findings—broad intensity distributions and low spatial predictability—demonstrate that the PL-derived fingerprint originates from irregular, nanoscale fluctuations in the as-formed heterostructure interface. This spatial complexity, which emerges from stochastic variations in local charge transfer, dielectric screening, strain, and interfacial registry, is extremely difficult to reproduce under nominally identical fabrication conditions. Even under the same fabrication parameters, the detailed nanoscale arrangement of strain, defects, trapped charges, residues, and interfacial contact quality will inevitably vary between devices—and often between regions within the same device. Since the optical response is directly derived from these spatially heterogeneous properties, reproducing the exact emission map at the pixel level is practically infeasible without explicit nanoscale patterning and precise control over interfacial microstructure.

Furthermore, the extracted feature maps can be converted into a compact cryptographic output a deterministic digital readout procedure. In this work, the raw two-dimensional feature maps were down-sampled by restricting the readout to a threshold defined subset of trusted pixels within the heterostructure and serialising them in a fixed, parity-interleaved order to form a reproducible pre-hash bitstream. This bitstream is then hashed using SHA-256 to produce a fixed-length 256-bit response, which standardises the output length and reduces residual spatial correlation in the raw bitstream. Beyond a single fixed response, the same framework can be extended to a challenge–response setting by define the challenge as a sampling instruction (ROI selection, pixel subset/permutation seed, feature subset, quantization mode) and the response as the extracted pre-hash bitstream and/or hashed key. Implementing and validating a large CRP set would require repeated measurements of the same device and multiple devices to quantify reliability (intra-device stability) and uniqueness (inter-device separation) across challenges. Taken together, this binary map generation approach yields a reproducible digital key without external patterning or lithographic steps; the encoded complexity instead arises from the fabrication imprinted heterostructure microstructure and interfacial charge/strain distributions (including local environmental contributions).

5.8 Statistical Evaluation of PUF Quality

While the optical binarization process described in Section 5.6 successfully transforms spatial emission patterns into a binary digital identity, it is essential to evaluate the statistical quality of the resulting binary key for it to be considered a valid and secure physically unclonable function (PUF). PUFs must exhibit high entropy, low bias, and strong inter- and intra-device uniqueness to ensure unpredictability and resistance to cloning.

Due to the limited number of devices characterised, classical PUF metrics that require statistical analysis across multiple devices (e.g., uniqueness, inter-device Hamming distance) or repeated measurements (e.g., reliability, intra-device Hamming distance) could not be evaluated directly. Instead, the extracted 256-bit response is assessed using (i) response uniformity and (ii) algorithmic robustness to controlled perturbations applied to the same measurement. Bias is defined as:

$$Bias = | N_1 / N |$$

where N_1 is the number of ‘1’ bits and N is the total number of bits. An ideal PUF would have a bias close to 0.5, meaning an equal probability of 0 and 1 across the output.

In this work, the binary matrix consisted of a total of 256 bits, among which 179 bits were ‘1’ and 77 bits were ‘0’, resulting in a bias of 0.6992, which is relatively high, indicating a skew toward ‘1’ values.

This imbalance likely results from the application of a single global threshold to an intensity field with a strong gradient and uneven illumination. Additionally, asymmetries in the sample's photoluminescence (PL) emission may contribute, indicating that the current binarization output is sub-optimal for generating spatially random keys. To mitigate these issues, local adaptive thresholding methods could be employed. These adjust the binarization threshold based on local intensity distributions within a defined window, better preserving spatial randomness and reducing structural bias. For a PUF system, however, any such method must be implemented as a device-agnostic, pre-defined rule (e.g., local median thresholding with a fixed window size). This ensures objectivity and reproducibility, as per-sample tuning would introduce unwanted variability and complicate cross-device validation.

Additional key metrics such as Hamming distance—which quantifies the difference between PUF outputs from different devices (inter-device) or under repeated measurements (intra-device)—are planned for future experiments. A reliable PUF should show high Hamming distance between devices and low Hamming distance for repeated reads of the same device, ensuring both uniqueness and stability. Moreover, an assessment of entropy will be required to validate the cryptographic strength of the output. While not yet fully completed, this can be pursued using either: Shannon entropy, which evaluates the average information content per bit; Or NIST randomness tests, which offer a comprehensive suite of statistical evaluations for binary data streams.

Together, these metrics will form a complete profile of the PUF’s quality and resilience. Although the current statistical assessment is still in its early stages, it establishes a foundation for further optimization and future work.

5.9 Summary and Outlook

In this chapter, graphene–MoS_2 heterostructures are demonstrated to offer a rich and reproducible source of spectral and spatial entropy suitable for optical physically unclonable functions (PUFs). Stacking verification and low-temperature photoluminescence (PL) measurements confirm that both stacking order and spatial position strongly influence excitonic emission, producing deterministic yet unique spectral fingerprints. These optical identities remain robust across variations in laser power and temperature, establishing their environmental stability. Moving from spectral to spatial domains, PL mapping revealed microscale emission heterogeneity shaped by strain, wrinkles, and interfacial disorder—laying the groundwork for digital binarization. Through a systematic pipeline, this optical complexity was successfully translated into binary maps that encode the randomness of the material into secure digital keys. Although bias analysis revealed a skewed bit distribution (bias = 0.6988), future improvements—such as adaptive thresholding and entropy optimization—will enhance statistical quality and randomness. Overall, these results establish the graphene–MoS_2 heterostructure as a promising platform for robust, scalable, and tamper-resistant optoelectronic security.

Chapter 6: Raman Investigation of HOPG and Solvation Structures in Li-Ion Batteries

Understanding interfacial chemistry in lithium-ion batteries is essential for improving long-term performance, safety, and cycle stability. This chapter explores the application of Raman spectroscopy to investigate two critical aspects: the structural evolution of Highly Oriented Pyrolytic Graphite (HOPG) electrodes and the solvation environment of lithium ions in liquid electrolytes. As a non-destructive vibrational technique, Raman spectroscopy provides molecular-level insights into carbon bonding, structural disorder, and ion coordination—making it a powerful tool for probing both electrode surfaces and electrolyte interactions.

The first part of this chapter focuses on the structure of HOPG electrodes, examining how mechanical polishing, thermal annealing, and plasma treatment affect the crystallinity and reactivity of basal and edge planes. A combination of ex situ and operando Raman studies is used to evaluate defect evolution, lithium intercalation behaviour, and SEI formation dynamics under cathodic polarization. While some of the operando Raman data were collected as part of a collaborative project and published in the supplementary information of a *published* paper, the detailed analysis and interpretation—particularly the correlation of spectral shifts with distinct lithium intercalation stages and SEI growth—are presented here for the first time.

In the second part, the focus shifts to the electrolyte environment, where Raman spectroscopy is used to analyse how different solvent systems (EC/DMC vs. DX), salt chemistries ($LiPF_6$ vs. LiFSI), and concentration ranges (0.1 M to 6 M) influence lithium-ion solvation structures. These observations reveal critical differences in solvation shell composition and coordination trends, which directly impact interfacial decomposition behaviour and SEI chemistry.

The chapter is structured as follows: Section 6.1 reviews the state of the art on SEI formation at graphite electrodes and motivates the Raman-based measurement strategy implemented throughout the remainder of this chapter. Section 6.2 characterizes the Raman features of polished HOPG surfaces, focusing on basal vs. edge plane differences. Section 6.3 examines the effects of post-polishing treatments.

Section 6.4 presents the operando Raman analysis of SEI formation and lithium intercalation. Sections 6.5 and 6.6 investigate bulk and interfacial solvation structures in EC-based and DX-based electrolytes, while Section 6.7 explores the impact of salt concentration on solvation and SEI behaviour. Together, these findings provide multi-scale insights into interfacial design strategies, bridging surface structure and electrolyte chemistry to guide the development of more stable and efficient lithium-ion battery systems.

6.1 Introduction

In lithium-ion batteries, the solid electrolyte interphase (SEI) formed on graphite anodes is a critical passivation layer: it conducts Li^+ while blocking electrons, thereby suppressing continuous electrolyte reduction. This layer governs long-term performance metrics such as capacity retention, rate capability, and safety [296,297]. SEI formation is influenced by both the intrinsic surface properties of the graphite electrode—including defect density, crystallographic orientation, and chemical functionality—and the Li^+ solvation structure in the bulk electrolyte and at the electrode–electrolyte interface. Although extensive research has been devoted to understanding SEI formation mechanism, chemical composition and structural evolution[298,299], the complex interplay between anode materials, electrolyte chemistry, and interfacial dynamics remains incompletely understood, despite its pivotal role in determining SEI stability and functionality.

From the anode perspective, the distinct roles of Highly Oriented Pyrolytic Graphite (HOPG) basal and edge planes in SEI formation are well recognized. However, achieving precise and independent modification of these planes remains challenging. Conventional surface treatments—such as mild oxidation[300,301], chemical oxidation [302], or combined argon cleaning with reactive gas exposure [303,304]—often affect both planes simultaneously, lacking the selectivity needed for optimal SEI formation and interfacial stability. Recently, beam-exit cross-sectional polishing (BEXP) has emerged as a promising alternative [305]. By aligning the ion beam at a shallow exit angle, BEXP produces ultra-flat, nanoscale cross-sections with minimal roughness. When coupled with post-treatment methods like annealing [306] or plasma processing [307], it enables controlled and uniform modification of HOPG surfaces.

On the electrolyte side, research has mainly focused on how bulk and interfacial solvation structures impact SEI properties. Electrolyte engineering—through adjustments in salt type, concentration, and solvent system—offers a powerful lever to alter SEI composition and enhance battery performance. For instance, varying salt concentration has proven effective in modifying reduction pathways at the electrode interface. High-concentration electrolytes (HCEs)[308], and localized high-concentration electrolytes (LHCEs)[309] promote preferential anion decomposition, leading to inorganic-rich SEIs composed primarily of lithium fluorides and oxides, which exhibit superior stability and ionic conductivity [310]. In contrast, low-concentration electrolytes favour solvent reduction, resulting in organic-rich SEIs that are less stable and prone to degradation over time, negatively impacting battery longevity [311]. Beyond salt concentration, the development of alternative solvents has emerged as a promising strategy in electrolyte design. Weakly solvating electrolytes (WSEs), typically DX-based formulations characterised by low-polarity solvents, have gained attention for their ability to enhance anion coordination with lithium ions, promote ion-pair formation and facilitate favourable Li–F interactions within the solvation sheath [312]. For example, Yao et al. (2020) demonstrated that low-polarity solvents improve anion-driven SEI formation by stabilising the solvation sheath [313].

Despite these advances, several critical questions remain unclear regarding the role of initial bulk and interfacial solvation structures at the electrode–electrolyte interface in SEI evolution. In particular, the dynamic interactions between electrolyte components—such as solvents, salts and additives—and anode materials during electrochemical cycling are not yet fully understood. Furthermore, current research often examines the factors influencing SEI composition—such as bulk electrolyte properties, interfacial structure and dynamics individually, whereas fundamental understanding of how these components interact and function synergistically as a unified electrochemical system remains poorly explored. In addition, the effect of lithium salt concentration on electrolyte solvation behaviour, especially in EC-based and DMC-based electrolytes, requires further investigation to clarify its impact on SEI stability, composition and overall battery performance.

Addressing these challenges requires a comprehensive understanding that connects HOPG surface properties, electrolyte composition (salt type and concentration), and bulk and interfacial solvation structures under operando conditions. To this end, this work employs a combined ex situ and operando Raman spectroscopy approach. First, ex situ measurements are used to establish how mechanical polishing and subsequent annealing or plasma treatments modify the structure and defect density of HOPG basal and edge planes, with the goal of optimising surface preparation for enhanced anode performance (Sections 6.2–6.3). Next, operando Raman spectroscopy provides real-time, molecular-level insight into lithium intercalation stages and SEI evolution during electrochemical cycling (Section 6.4). Finally, systematic Raman analysis of EC-based and DX-based electrolytes across a range of salt concentrations quantifies how solvation structures—both in the bulk and at the interface—are reshaped by electrolyte chemistry, thereby linking solvation motifs to interfacial decomposition pathways and SEI development (Sections 6.5–6.7).

6.2 Raman Characterization of HOPG after Polishing Treatment

To produce a smooth, contamination-free, and uniform surface essential for accurate electrochemical and nanoscale measurements, Beam-Exit Cross-Sectional Polishing (BEXP) was applied to freshly cleaved HOPG. This process yielded two distinct regions: the basal plane, corresponding to the flat, layered surface of graphene sheets, and the edge plane, where the graphene layers are exposed perpendicularly due to mechanical termination. The basal planes are composed of smooth, crystalline, and highly ordered layers of carbon atoms arranged in a hexagonal lattice. This structure facilitates the efficient intercalation and de-intercalation of lithium ions during charging and discharging cycles, ensuring effective energy storage and release[314]. In contrast, the edge plane exhibit structural irregularities and higher chemical reactivity. These features make them effective active sites for lithium-ion interaction, complementing the energy storage function of the more inert basal planes. This structural and chemical contrast between basal and edge planes is critical for understanding lithium-ion intercalation mechanisms in graphite-based systems.

Figure 6.2-1(a) illustrates the polishing process and the resulting geometric configuration of the basal and edge planes. Figure 6.2-1(b) shows an optical image of the polished HOPG cross-section, highlighting the three regions used for Raman analysis: the natural cross-section, the polished basal plane, and the inclined slope (edge plane). The total sample area was approximately 3 mm × 3 mm. Raman spectra were collected at representative three points in each region, baseline-corrected, and normalized to the G-peak intensity to enable direct comparison. Figure 6.2-2 compares these spectra, highlighting the structural differences between the natural cross section, basal plane, and edge plane.

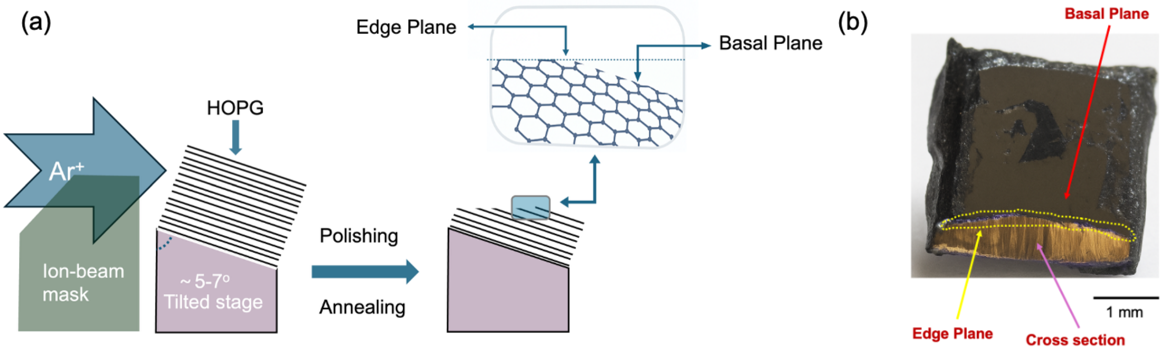

Figure 6.2-1. (a) Schematic of HOPG surface preparation: an Ar^+ ion beam is directed through an Ion-beam mask onto HOPG mounted on a ~5–7° tilted stage to define an exposed cross-section region; subsequent mechanical polishing and thermal annealing produce a model surface containing both the basal plane and a well-defined edge plane (inset illustrates the crystallographic orientation of basal vs edge planes). (b) Optical micrograph of the resulting cross-section HOPG model sample, indicating the basal plane (red arrow), the exposed edge plane region (yellow dashed outline), and the cross-section (purple arrow); scale bar: 1 mm.

The cross-sectional Raman spectrum reveals three prominent peaks that characterize the structural integrity of HOPG. The G peak, located at approximately 1580 cm^{-1}, corresponds to the E_{2g} phonon mode of sp^2-hybridized carbon atoms and is indicative of strong in-plane crystallinity[315]. The sharpness and intensity of this peak suggest well-ordered graphitic domains. The 2D peak, appearing near 2700 cm^{-1}, is a second-order overtone of the D peak and originates from a double-resonance process involving phonons with opposite momentum [316,317]. Its relatively narrow shape confirms well-aligned graphitic layers, although slight broadening suggests minor deviations from ideal stacking [316]. The D peak observed around 1350 cm^{-1}, arises from disorder-induced phonon scattering in sp^2 rings. Its weak intensity suggests that defect density is low, with minor contributions potentially stemming from surface exposure or edge effects introduced during sample preparation [318]. Overall, these features reflect a highly crystalline, low-defect graphitic structure characteristic of pristine HOPG bulk.

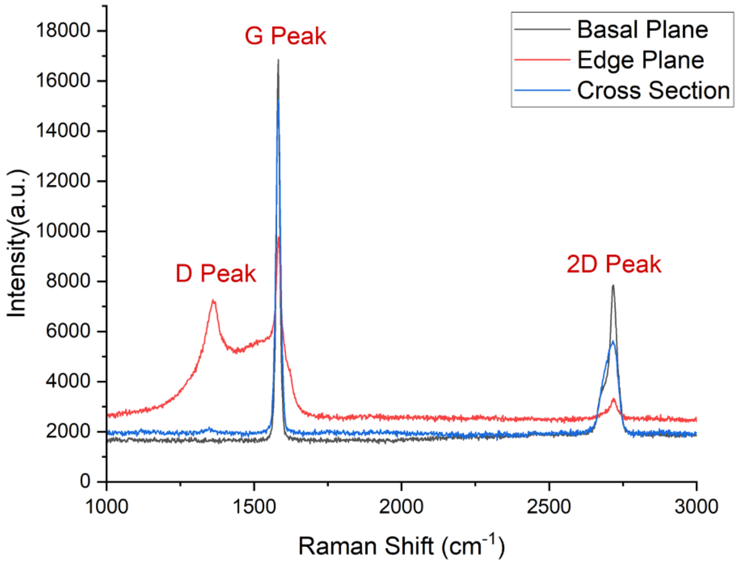

Figure 6.2-2 Raman spectra comparison of cross-section(blue), basal plane(black), and edge plane (red) of HOPG after polishing.

In the Raman spectrum of the polished basal plane, the G peak remains intense and sharp, consistent with a highly ordered in-plane structure. The 2D peak, also sharp and symmetric, shows a slight enhancement in intensity compared to the cross-section, indicating further reduction in stacking defects. Crucially, the D peak is not observed in this region, suggesting that the basal plane is virtually free of structural defects. These observations demonstrate that the polishing process effectively removes residual surface irregularities, thereby restoring a clean, crystalline graphitic surface with enhanced structural order.

By contrast, the Raman spectrum collected from the edge (slope) plane shows significant changes indicative of structural disorder. The most prominent feature is a strong D peak at ~1350 cm^{-1}, which signals a high density of defects such as edge terminations, vacancies, and amorphous carbon. The G peak becomes noticeably broader and less intense, reflecting a decline in in-plane order and increased phonon scattering. Additionally, the 2D peak is both weaker and broader compared to the basal and cross-sectional regions, suggesting compromised interlayer stacking and reduced crystallinity. These spectral signatures confirm that while polishing preserves the integrity of the basal plane, it simultaneously introduces significant structural disruption at the exposed edge plane.

Table 6.2.1 summarizes the key Raman spectral features for the three investigated regions. The basal plane maintains sharp G and 2D peaks with no D peak, indicating low disorder and high crystallinity. The cross-section exhibits similar features with minor D peak presence due to edge exposure. The edge plane, however, displays significant disorder reflected in the high D/G ratio, broader peaks, and reduced spectral intensity. Thus, the Raman analysis reveals the dual effect of polishing—enhancing structural order on the basal plane while inducing defect-rich, disordered regions along the edge plane.

Region	G Peak	D Peak	2D Peak	Defect Density	Crystallinity
Cross-Section	Sharp, strong	Weak	Moderate, sharp	Low	High
Basal Plane	Sharp, very strong	Absent	Sharp, symmetric	Very low	Very high
Edge Plane (Slope)	Broad, weaker	Strong	Broad, weak	High	Low

Table 6.2.1 Comparison of Raman spectral features and structural characteristics of HOPG surface regions after polishing.

6.3 Raman of HOPG after Annealing Treatment

To address the defects introduced during polishing and enhance the quality of Highly Oriented Pyrolytic Graphite (HOPG), two post-treatment strategies were investigated: annealing and plasma treatment. These methods aim to improve the structural and surface properties of HOPG for high-performance for lithium-ion batteries. Annealing, which involves heating the material to 500–800°C in an inert atmosphere like argon, facilitates the rearrangement of carbon atoms, thereby restoring the graphitic structure and significantly reducing the structural defect in HOPG. Conversely, plasma treatment uses gases such as hydrogen or argon to selectively remove surface defects and contaminants, enhancing crystallinity and allowing precise modification of surface properties.

The Raman spectra, displayed in Figures 6.3-1, show significant changes in both the slope and basal planes of HOPG following these treatments. For the slope(edge) plane, annealing at 500°C for 30 minutes decreases the D-band's intensity, suggesting a reduction in defects, although some remain as indicated by the band's persistence. Extending the annealing to 60 minutes eliminates the D-band, showcasing effective defect removal and restoration of the graphitic structure. The G and 2D bands become sharper and more intense, indicating improved in-plane graphitic order and restoration of graphene layer stacking.

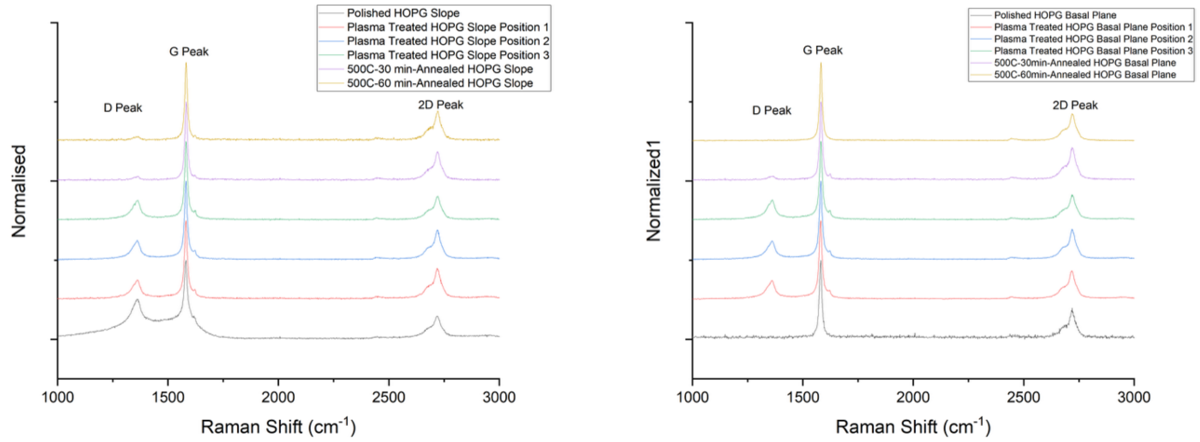

Figure 6.3-1: Raman Spectrum of the HOPG edge plane(a) and basal plane (b)after Annealing and Plasma Treatment

In contrast, plasma treatment results in sharper and more intense G and 2D bands but fails to eliminate the D-band, indicating that while it can enhance the graphitic structure, it is less effective in removing defects. This is particularly evident in the basal plane where plasma treatment introduces noticeable defects, demonstrated by a prominent D peak. The broader G and 2D peaks imply reduced graphitic order and disruptions in stacking, confirming the detrimental effects of plasma treatment on structural quality. Overall, annealing at 500°C for 60 minutes proves to be highly effective in enhancing both the basal and edge planes of HOPG by removing amorphous carbon layers, eliminating defects, and restoring a highly graphitized structure.

6.4 Raman of HOPG during the First Cathodic Polarization

To investigate early-stage SEI formation and lithium intercalation dynamics on the edge plane of HOPG, operando Raman spectroscopy was performed on the edge plane of HOPG using a custom-built electrochemical cell. The electrolyte consisted of 1 M $LiPF_6$ in EC/DMC (1:1). Raman measurements were collected from open-circuit potential (OCP) down to 0.01 V vs. Li/Li^+.

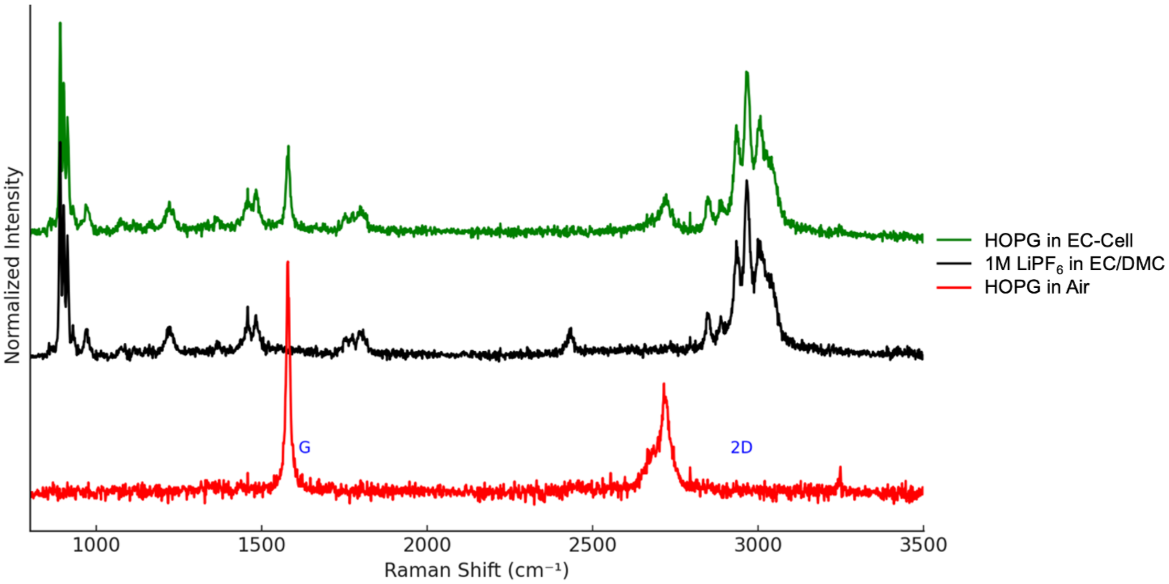

Figure 6.4-1 Raman spectra of HOPG measured in air (red), in the electrochemical cell filled with 1 M $LiPF_6$ in EC/DMC under open-circuit potential (green), and of the neat 1 M $LiPF_6$ in EC/DMC electrolyte recorded in the same cell without HOPG (black). The green trace therefore represents HOPG in contact with the electrolyte, the black trace isolates vibrational modes of the EC/DMC–$LiPF_6$ solution, and the red trace corresponds to pristine HOPG in air. Comparison of these spectra allows the graphitic G (~1580 cm^{-1}) and 2D (~2720 cm^{-1}) bands of HOPG to be distinguished from solvent- and electrolyte-related peaks and reveals the shifts and intensity changes of the G/2D bands upon electrolyte immersion.

As shown in Figure 6.4-1, the Raman spectrum of HOPG in the electrochemical cell under open-circuit potential (green line) exhibits distinct features corresponding to both the electrolyte solvents—ethylene carbonate (EC) and dimethyl carbonate (DMC)—as well as the characteristic graphitic bands. Notable solvent-related peaks include those from EC at 893, 916, 973, 1220, 1487, and 1808 cm^{-1}, and from DMC at 904, 973, 1455, 1750, and in the range of 2849 – 3002 cm^{-1}[319-321]. The carbonyl (C=O) stretching vibrations are observed near 1760 cm⁻¹ for DMC and around 1805 cm⁻¹ for EC.

In addition to these solvent signatures, subtle shifts are evident in the G and 2D bands of HOPG—specifically, the G peak shifts from 1579.3 to 1580.87 cm⁻¹ and the 2D peak from 2715.5 to 2722.2 cm⁻¹. These spectral changes are accompanied by a decrease in the intensity ratio of I_G/I_{2D} from 2.04 to 1.72. Together, these shifts suggest early electronic interaction between the HOPG surface and solvated lithium ions.

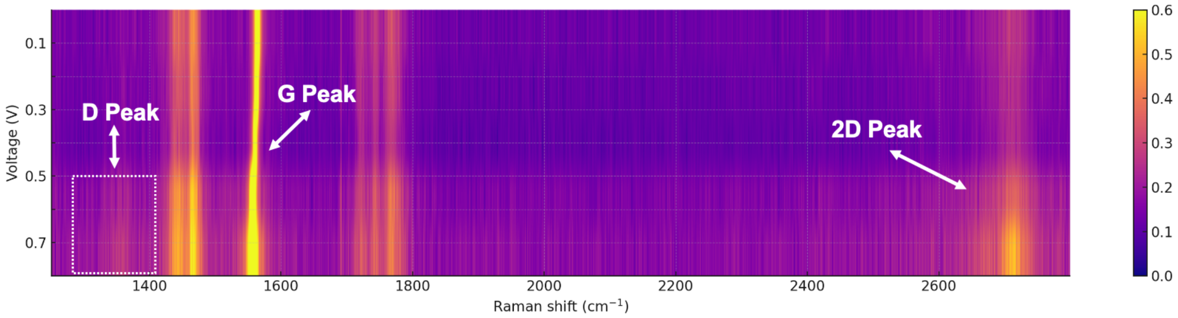

Figure 6.4-2. Operando Raman intensity map acquired on the HOPG edge plane during the first lithiation in 1 M $LiPF_6$ in EC/DMC, shown as a function of Raman shift (x-axis) and applied potential (y-axis). The colormap gives the normalized Raman intensity. The characteristic graphite bands are labelled, including the D band (~1350 cm⁻¹), the G band which shifts from 1579.3 to 1580.87 cm⁻¹, and the 2D band which shifts from 2715.5 to 2722.2 cm⁻¹ over the polarization range. The dashed box marks the spectral window around the D band where a pronounced decrease in intensity is observed during the early stages of cathodic polarization, indicating rapid suppression of defect/edge-activated scattering as the interface evolves.

The full operando spectra are shown in Figure 6.4-2, capturing the evolution of key graphitic bands (D, G, 2D) as lithium intercalates into HOPG from 0.9 V to 0.01 V. As shown in Figure 6.4-3(a), during the initial phase of lithiation, a pronounced decrease in the D-band intensity is observed at the HOPG edge plane once the potential falls below ~0.7 V. Between ~0.7 V and 0.5 V, the D band progressively approaches the noise level, while the G and 2D bands remain visible, indicating that bulk graphite intercalation has not yet become dominant. In the literature, attenuation of the D band in this potential window has been linked to surface passivation at edge sites, changes in stacking order and modifications of the Raman resonance conditions as lithium accumulates, and its precise microscopic origin remains debated [322,323]. In this work, the D-band decay is therefore interpreted as an indirect signature of surface passivation and evolving local electronic structure at defect-rich edge planes, rather than as a reduction in the number of structural defects in the graphite lattice. This interpretation is consistent with complementary EC-AFM, 3D nano-rheology microscopy and XPS measurements on the same HOPG / 1 M $LiPF_6$ in EC/DMC model system, which show that SEI first nucleates and thickens at the edge plane within the same 0.7–0.5 V window, while only a thinner and more uniform SEI forms on the basal plane [324].

As lithium intercalation progresses, the G band (Figure 6.4-3 (b)) exhibits a significant shift from 1580 cm^{-1} to 1590 cm^{-1} as the potential decreases to ~0.5 V. This shift reflects an increase in the force constants of the in-plane C–C bonds, a direct result of lithium ions embedding within the graphite layers. Between 0.5 and 0.2 V, the G band (Fig. 6.4-4) shifts linearly with a slope of 28 ± 1 cm^{-1} V^{-1}, in close agreement with Shi et al. (29 cm^{-1} V^{-1}) for KS44 graphite [325]. The G band undergoes notable changes in its shape during this process, first narrowing between 0.45 V and 0.35 V and then broadening between 0.35 V and 0.27 V. The narrowing and shift of the G band both initiate below 0.5 V, corresponding to the onset of lithium insertion at approximately 0.5 V. The dilute stage 1 persists until 0.2 V, below which the formation of lower-stage intercalation compounds begins, causing further broadening of the G band.

Meanwhile, the 2D band (Figure 6.4-3 (c)) gradually weakens and broadens between 0.7 V and 0.2 V. This broadening reflects the dense packing of lithium ions within the graphite layers, significantly altering the graphite's electronic structure. The weakening of the 2D band is consistent with progressive saturation of the graphite galleries and the transition to lower-stage graphite intercalation compounds (GICs), in which the electronic structure of the graphitic layers is substantially modified.

As the voltage drops below ~0.05 V, both the G and 2D bands progressively diminish and eventually become undetectable. Figure 6.4.5 compares the Raman spectra of the HOPG sample in the EC cell before and after the first lithiation. After lithiation, the characteristic graphitic G and 2D bands have disappeared, while the solvent-related modes remain visible. This behaviour is consistent with the formation of low-stage (stage 2 and stage 1) graphite intercalation compounds, in which the graphene galleries are densely filled with Li$^+$ and the material becomes highly metallic. The resulting increase in electrical conductivity reduces the optical skin depth, effectively quenching the Raman response from the intercalated graphite and leading to the loss of detectable graphitic bands [326].

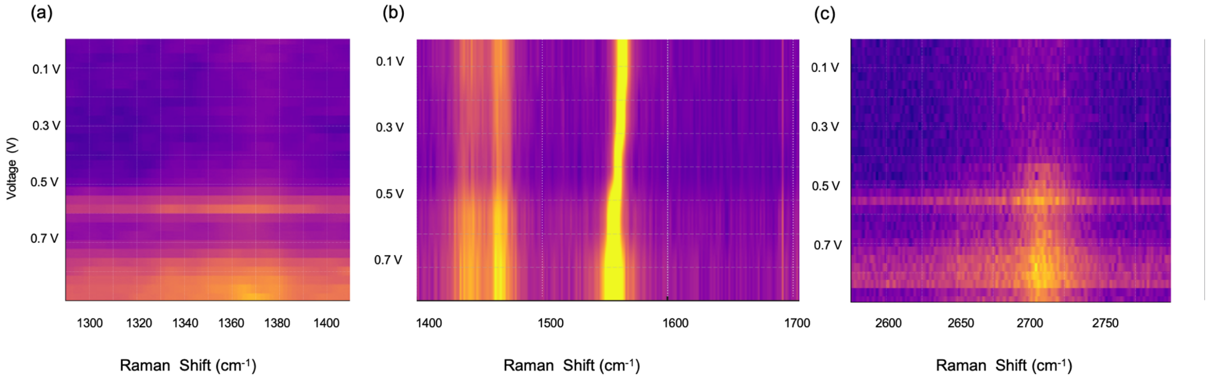

Figure 6.4-3. Raman spectra of the D peak (a), G peak (b), and 2D peak (c) for the edge plane of HOPG during the first cathodic polarization.

In 1 M LiPF$_6$ in EC/DMC, the SEI formed on graphite is generally described as an inorganic-rich inner layer (primarily Li_2CO_3, LiF and LixPOyFz, with minor Li_2O/LiOH) covered by an organic outer layer containing alkyl lithium carbonates $ROCO_2Li$, lithium ethylene di-carbonate (LEDC, $(CH_2OCO_2Li)_2$), lithium ethylene mono-carbonate (LEMC), polymeric $(–CH_2–CH_2–O–CO_2Li–)_n$ species and Li–alkoxides (ROLi)[326,327]. Raman-active modes associated with these species are typically reported at ~740 cm^{-1} (PF_6^- / LixPOyFz), ~1090 cm^{-1} (C–O stretch in Li_2CO_3 / $ROCO_2Li$), ~1450 cm^{-1} (CH_2 deformation / carbonate modes) and ~1650 cm^{-1} (C=O in semi-carbonates [328]. This stratified composition has been established primarily by ex situ FTIR, XPS, EDAX, GC–MS and related spectroscopic/electrochemical studies on lithiated graphite and model electrodes [329-332].

In the present HOPG / 1 M LiPF$_6$ in EC/DMC system, no additional SEI-related bands can be unambiguously resolved (Fig. 6.4-5) , this is attributed to the combination of a very thin SEI (a few nanometres), which gives a small Raman scattering volume compared with the bulk electrolyte and graphite, and the fact that the strongest SEI carbonate modes lie in the 1000–1600 cm^{-1} region, where they are spectrally buried beneath the intense EC/DMC solvent bands.

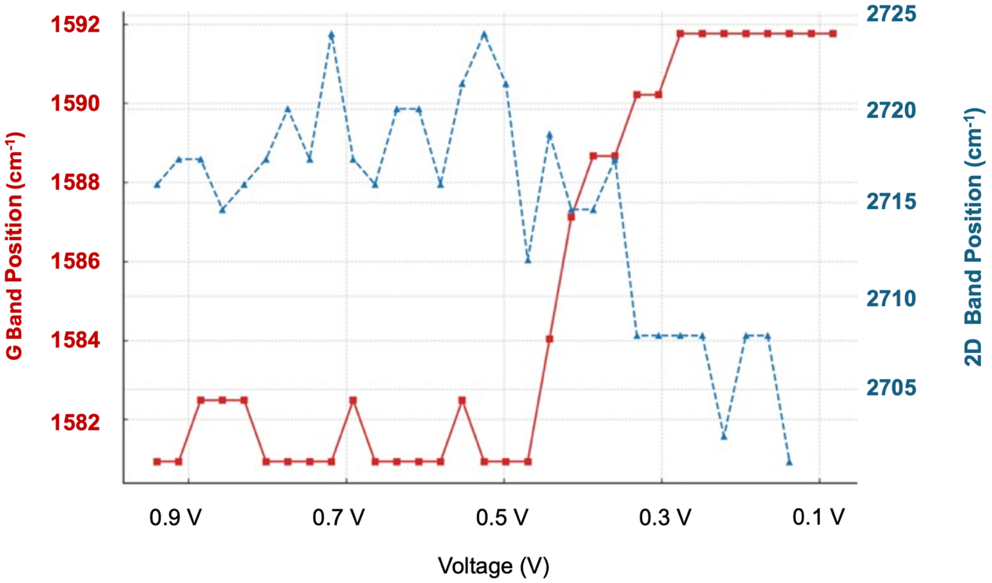

Figure 6.4-4: Variation of the G band and 2D peak positions from 0.9 V to 0.05 V vs. Li/Li^+ during the first lithiation cycle of HOPG.

Overall, the potential-dependent evolution of the D, G and 2D bands provides indirect signatures of both SEI formation and graphite intercalation. Between 0.7V to 0.5 V, attenuation of the D band before pronounced G- and 2D- band evolution indicates changes localised at defect-rich edge planes and is interpreted as passivation and electronic screening of edge defects by nascent SEI species, which suppress defect-related double-resonance scattering rather than removing structural defects from the lattice. At intermediate potentials (0.5–0.2 V), the evolution of the G and 2D bands is consistent with progressive staging and associated changes in electronic structure and layer stacking. At the lowest potentials (below ~0.05 V), the disappearance of the graphite Raman bands is consistent with the formation of highly conductive stage 1 GICs, where the reduced optical skin depth limits laser penetration and obscures signals from both graphite and the underlying SEI.

Taken together, these operando Raman measurements on the HOPG edge plane act as a time-resolved probe of graphite intercalation and near-surface electronic structure, thereby defining the potential window over which SEI-related processes occur. When the Raman observations are combined with collaborative measurements on the same HOPG / 1 M $LiPF_6$ in EC/DMC model system, where EC-AFM, 3D nano-rheology microscopy (3D-NRM) and XPS characterise SEI morphology, mechanics and chemistry on both edge and basal planes, a consistent sequence of SEI nucleation and growth emerges. EC-AFM shows that nanoscale SEI domains nucleate and grow preferentially along the edge section within the same 0.7–0.5 V window in which the D band decays, while only a thin layer develops on the basal terrace. 3D-NRM and XPS further reveal that the edge-plane SEI is thicker, more mechanically heterogeneous and organic-rich, whereas the basal-plane SEI is thinner and more uniform [324]. In this integrated picture, SEI nucleation at defective edge sites begins around 0.7–0.5 V, bulk lithium intercalation into the galleries dominates between 0.5 V and 0.2 V, and the highly conductive stage 1 GICs formed below ~ 0.05 V render both graphite and SEI effectively Raman-silent.

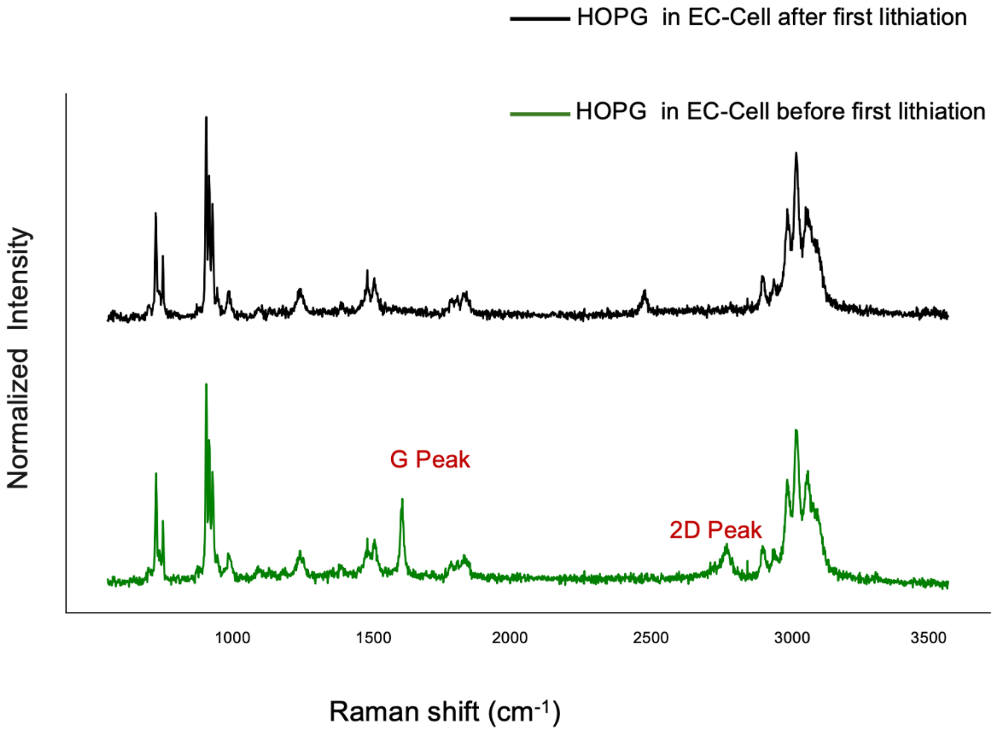

Figure 6.4-5: Raman spectra of the edge plane of HOPG before and after the first lithiation

6.5 Lithium-Ion Solvation Structures in EC-Based Electrolytes

In lithium-ion battery electrolytes, dissolved lithium salts form a solvation shell (or sheath) around each Li^+ ion [334]. The solvation sheath can be described in three regimes (Fig. 6.5-1(a)). In the primary solvation sheath, the central Li^+ ion forms the strongest interactions with solvent molecules, maintaining a stable sheath structure as it moves through the electrolyte. Beyond this, the secondary solvation sheath consists of solvent molecules that weakly associate with Li^+, resulting in dynamic fluctuations that can disrupt the stability of the primary sheath. Solvent molecules outside these regions remain largely undisturbed and distant from the central ion, exerting only a minor influence on solvation dynamics.

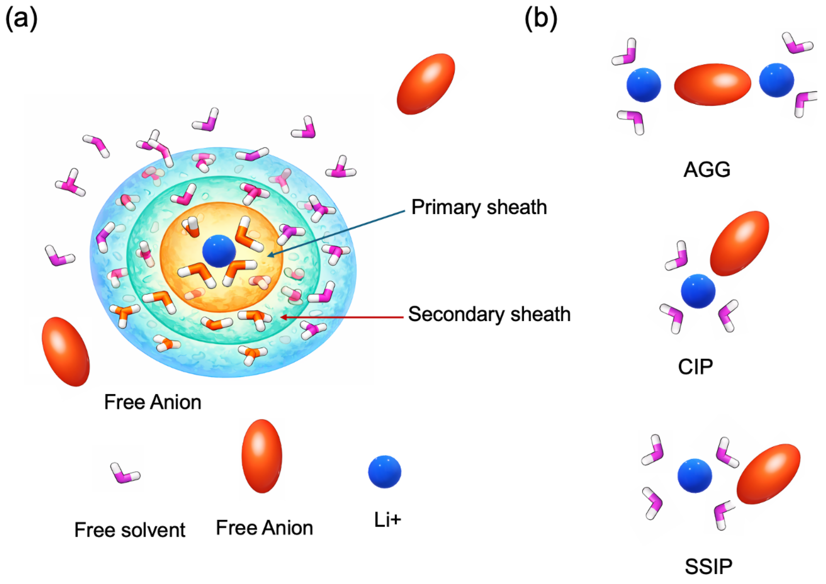

Figure 6.5-1. Schematic illustration of Li^+ solvation and ion-pairing motifs in liquid electrolytes. (a) A representative solvation structure showing the Li^+ primary solvation sheath and secondary sheath, together with free solvent molecules and free anions in the surrounding electrolyte. Adapted from Borodin, O. et al. Uncharted Waters: Super-Concentrated Electrolytes, Joule, 4(1), 69–100 (2020), with permission from Elsevier [343]. (b) Common ion-association states: solvent-separated ion pairs (SSIP), contact ion pairs (CIP), and larger ion aggregates (AGG), highlighting the increasing participation of anions in the first coordination environment of Li^+.

The primary-shell structure varies with electrolyte conditions and is commonly rationalised in terms of three limiting solvation motifs, defined by the arrangement of Li^+, anions and solvent molecules: solvent-separated ion pairs (SSIPs), contact ion pairs (CIPs) and aggregates (AGGs) (Fig. 6.5-1(b)). In SSIPs, Li^+ is fully surrounded by solvent molecules while the anion remains outside the first solvation shell, creating a loosely bound, solvent-dominated environment with relatively weak ion–ion interactions and high Li^+ mobility [335-338]. In CIPs, the anion enters the primary solvation shell and coordinates directly to Li^+, producing a more compact structure with stronger ion–ion interactions and reduced ionic conductivity [339-341]. AGGs involve multiple Li^+ ions and anions sharing coordinating solvent molecules, forming extended Li^+–anion clusters that can slow Li^+ transport but also strongly influence SEI formation [342-345]. Changes in solvent polarity, salt type and concentration therefore alter the balance between SSIPs, CIPs and AGGs, and in turn modulate electrolyte transport and interfacial reactivity.

To investigate how solvent polarity, salt type and concentration modify the local environment of Li^+, two distinct solvent systems were examined: a polar solvent mixture of ethylene carbonate (EC) and dimethyl carbonate (DMC), and a low-polarity solvent, 1,4-dioxane (DX) (see Section 6.5). The EC/DMC (1:1 v/v) mixture was chosen as a representative commercial carbonate electrolyte for $LiPF_6$: it mitigates graphite surface damage associated with co-intercalation in other polar solvents such as propylene carbonate (PC) or diethylene carbonate (DEC), and its relatively weak solvation properties and specific Li^+ interactions favor the formation of a stable passivating SEI. In particular, EC has a high dielectric constant and cyclic structure, which promote strong coordination with Li^+, while DMC acts as a lower-viscosity diluent that enhances ionic conductivity but binds Li^+ weaker. In such carbonate-based systems, Li^+ is therefore expected to adopt a solvent-dominated solvation shell primarily coordinated by EC, with a smaller contribution from DMC. In contrast, 1,4-dioxane is a low-dielectric, weakly coordinating solvent in which Li^+ is expected to adopt an anion-rich solvation shell dominated by FSI^- CIPs and AGGs. This weaker solvation reduces the de-solvation energy barrier, inhibits solvent co-intercalation and helps prevent carbon layer exfoliation and sample damage.

Raman spectroscopy was performed on pure EC, pure DMC, pure LiFSI and 1 M solutions of $LiPF_6$ and LiFSI in EC/DMC to resolve how EC and DMC coordinate to Li^+ and to define the solvent-dominated solvation shell in carbonate electrolytes. $LiPF_6$ was selected as a benchmark salt owing to its excellent ionic conductivity and widespread commercial use, whereas LiFSI offers superior thermal stability and can promote more robust SEI formation [346]. A parallel set of measurements on 1 M LiFSI in DX (Section 6.6) then reveals how a weakly coordinating solvent shifts the balance towards anion-rich CIPs and AGGs. The influence of salt concentration on these solvation motifs is further examined in Section 6.7. Taken together, these measurements provide a direct experimental comparison between solvent-dominated and anion-dominated solvation shells and their implications for SEI formation.

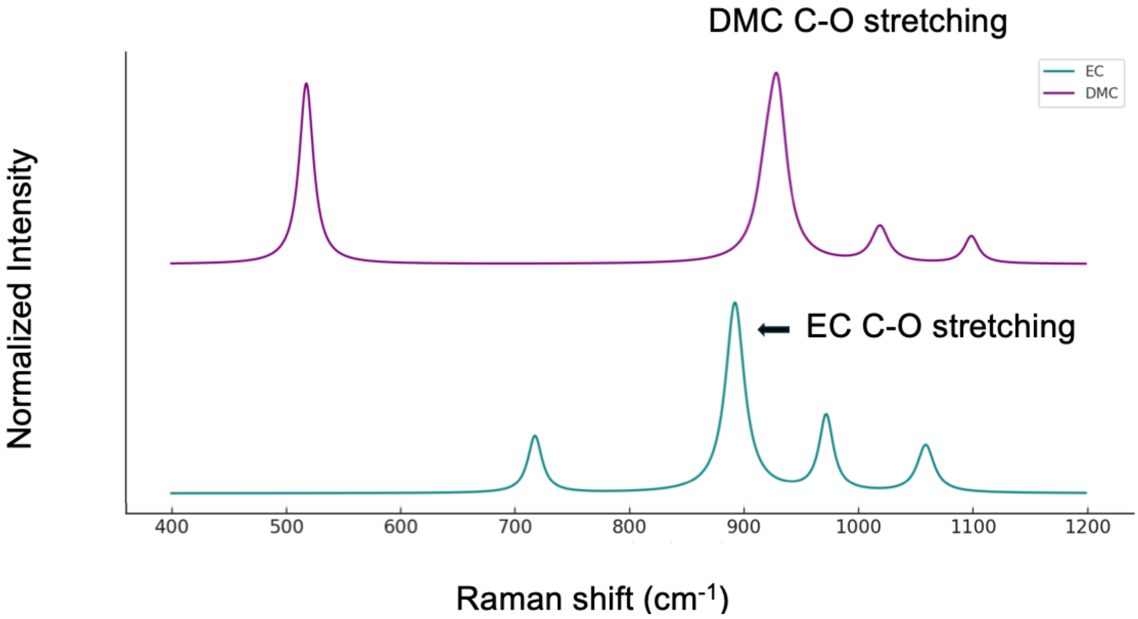

Figure 6.5-2. Raman spectrum of pure EC and DMC.

Figure 6.5-2 presents the Raman spectra of pure EC and DMC. Both solvents exhibit prominent C=O stretching peaks, with EC's peak at 893 cm^{-1} and DMC's slightly higher at 930–950 cm^{-1}, reflecting their distinct carbonyl vibrational modes [347]. For EC, additional features include ring deformation modes at 718 cm^{-1} and 973 cm^{-1}, as well as asymmetric C–O stretching vibrations near 1060 cm^{-1}, which emphasize its cyclic carbonate structure. In contrast, DMC displays a notable peak at 518 cm^{-1} corresponding to the bending or deformation of its molecules, along with smaller peaks between 900–1100 cm^{-1} associated with the symmetric stretching of its C–O–C bonds [348]**.** These features establish the spectral baseline needed to track coordination changes upon salt addition.

When $LiPF_6$ is introduced to the EC/DMC solvent mixture (1M concentration), the Raman spectrum reveals significant peak shifts and new features (see Figure 6.5-3). The C=O stretch of EC shifts from ~893 to ~915 cm^{-1}, and that of DMC from ~930 to ~933 cm^{-1}, indicating lithium-ion coordination. These coordinated EC and DMC molecules constitute the primary lithium-ion solvation shell, the first coordination sphere of ligands that move with Li^+ and define its local chemical environment. This solvation shell is critical for ion transport, by setting the effective size and de-solvation barrier of Li$^+$, and for SEI formation, because the coordinated species are the first to be reduced at the negative electrode. The intensity ratio of coordinated to free EC (I_{Coor}/I_{Free} ~0.71) is significantly higher than that of DMC (I_{Coor}/I_{Free} ~0.21), highlighting the preferential coordination of EC to lithium ions. Nevertheless, the coordination of DMC is not negligible, as evidenced by the broad coordination band at ~933 cm^{-1}. Additionally, the sharp peak at ~740 cm^{-1} is attributed to the PF_6^- anion, arising from the symmetric Phosphorus-Fluorine bond's stretching vibration [333].

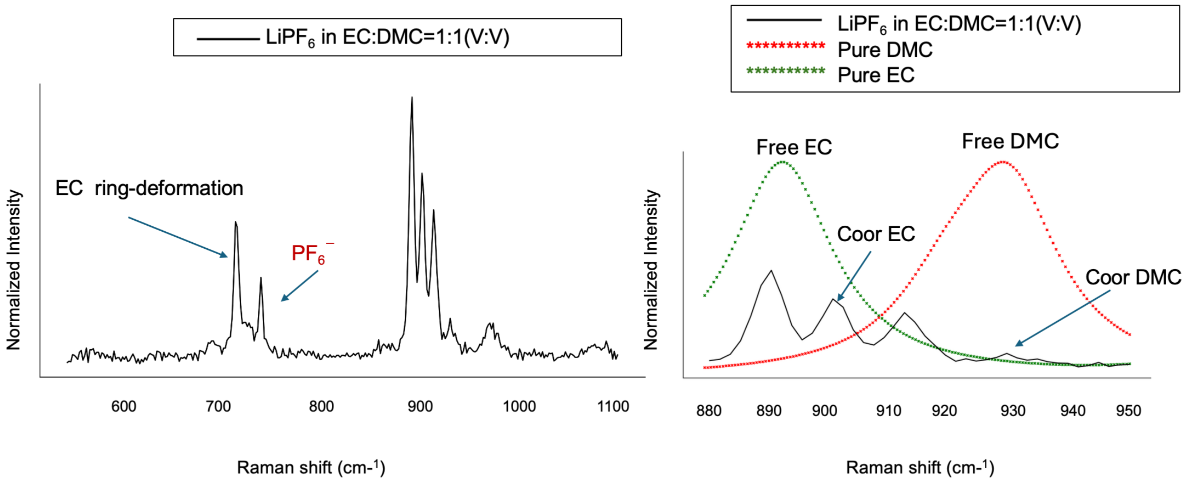

Figure 6.5-3. Lithium-ion's solvation structures in EC-based electrolytes without negatively charging the electrode**.** (a) and (b) Raman spectra of pure EC, DMC and 1M $LiPF_6$ in EC: DMC = 1:1 electrolyte.

The Raman measurements are complemented by MD simulations of the same 1 M $LiPF_6$ in EC/DMC electrolyte, yielding a consistent picture of the Li$^+$ primary solvation structure. The preferential coordination of Li$^+$ by EC, inferred from Raman analysis of the EC/DMC C=O bands, is quantitatively supported by MD-derived radial distribution functions and running coordination numbers (Figure 6.5-4). These simulations—performed by Yue Chen and Wenkai Wu—reveal that in both the bulk electrolyte and the electrical double layer (EDL), each Li$^+$ is predominantly solvated by several EC molecules, accompanied by approximately one to two DMC molecules and one PF_6^- anion in the first coordination shell [324].

A parallel analysis was carried out using LiFSI as the salt, with the Raman spectra displayed in Figure 6.5-5, the S–N–S bending vibration ($\delta_{S\text{-}NS}$) in LiFSI, representing the bending motion within the $N(SO_2F)_2$ structure, is a prominent feature in the Raman spectrum of LiFSI powder (Fig.6.4.3a). In the 1M EC/DMC electrolyte solution, FSI$^-$

anions interact with Li^+ ions, with shifts in the S–N–S bending peak and changes in intensity indicating coordination. Specifically, the peak at ~732 cm^{-1} corresponds to coordinated FSI^-, confirming direct coordination between FSI^- and Li^+. However, the spectrum lacks the ~747 cm^{-1} band associated with aggregated ion clusters, indicating that Li^+ remains primarily in solvent-separated or contact ion pair configurations, rather than forming large aggregates.

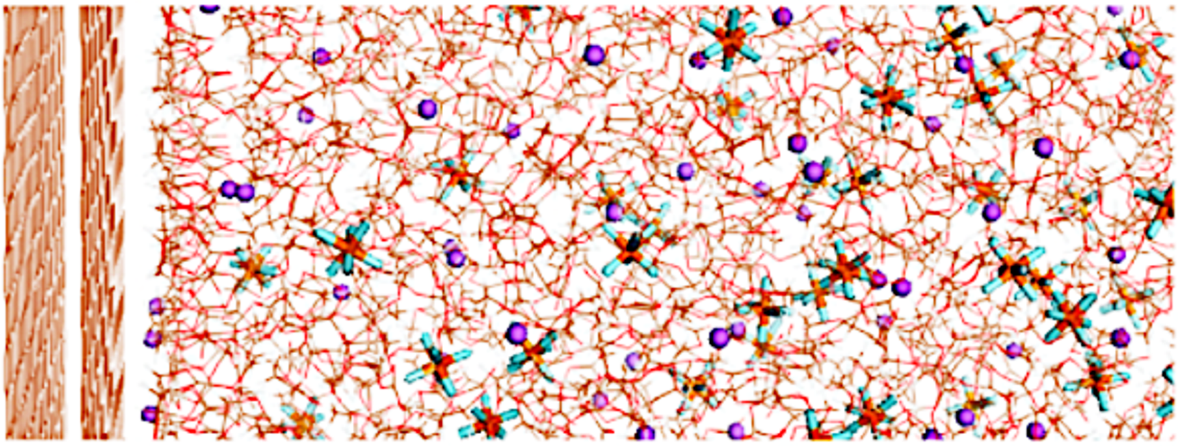

Figure 6.5-4 Snapshots of molecules/ions arrangement near the negatively charged electrode surface in 1M LiPF6 in EC: DMC by MD simulations. Reproduced from Chen *et al.* (2023) under the Creative Commons Attribution 4.0 International License (CC BY 4.0) [324]

Additionally, the Raman spectrum exhibits strong coordination peaks for EC at ~723 cm^{-1} and ~915 cm^{-1}, reflecting the preferential interaction between EC—a high dielectric constant solvent—and lithium ions, rather than FSI^- anions [349]**.** This behaviour is consistent with the solvation structure observed in 1 M $LiPF_6$ in EC/DMC electrolytes, where lithium ions are predominantly solvated by solvent molecules in the first solvation shell. These findings suggest that the nature of the decomposition layer on the lithium anode is primarily governed by the solvent environment rather than the specific anion species (PF_6^- or FSI^-). Ultimately, it is the solvation structure—not the anion chemistry—that determines the preferential decomposition pathways and plays a crucial role in influencing electrochemical performance.

The combined results emphasise that lithium-ion solvation in EC-based electrolytes is dominated by solvent properties. EC forms strong, stable complexes with Li^+, while DMC exhibits weaker or negligible coordination. Although the presence of PF_6^- or FSI^- contributes anion-specific vibrational modes, it does not significantly alter the primary solvation landscape. Building on the ion–solvent complex model of Chen and co-workers, in which Li$^+$–(solvent)$_n$ clusters are analysed by DFT, strong Li$^+$–EC coordination is found to withdraw electron density from the carbonyl oxygen, stabilise (lower) the EC LUMO by approximately 1–2 eV relative to free EC, and produce a LUMO shift that scales with Li$^+$–EC binding energy, thereby shifting the onset of solvent reductive decomposition towards higher potential [350,351]. As solvent decomposition initiates from molecules directly coordinated to Li$^+$, understanding and controlling the solvation environment is key to tuning interphase chemistry. These findings indicate that tuning solvent composition and dielectric properties may offer a more effective strategy for optimising SEI behaviour than modifying the anion alone.

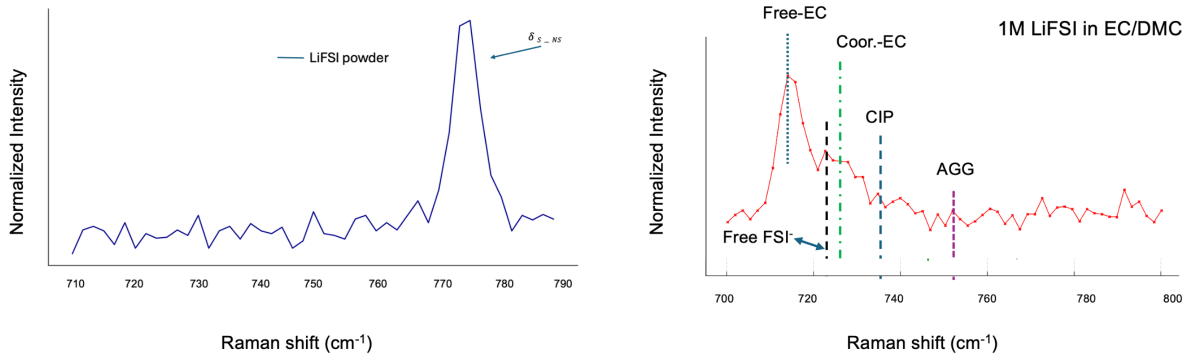

(a)

(b)

Figure 6.5-5. Raman spectra of LiFSI powder(a), showing the characteristic FSI$^-$ $\delta_{S\text{-}NS}$ mode, and (b) 1 M LiFSI in EC/DMC (1:1 v/v), highlighting different coordination states of the FSI$^-$ anion. In (b), the free FSI$^-$ corresponds to anions not directly coordinated to Li$^+$, the CIP (contact ion pair) arises from Li$^+$–FSI$^-$ pairs, and the AGG (aggregate) is attributed to Li$^+$–(FSI$^-$) ^{n} ion clusters. Vertical lines also mark the contributions from free EC and Li$^+$-coordinated EC species.

6.6 Lithium-Ion Solvation Structures in DX-Based Electrolytes

To contrast the coordination environment of lithium ions in carbonate-based electrolytes, I then explored their solvation behavior in 1,4-dioxane (DX), a non-polar, low-dielectric solvent. Due to its weaker solvating ability, DX is expected to favor anion-rich solvation shells and suppress solvent co-intercalation—making it a promising candidate for electrolyte systems aiming to stabilize the graphite–electrolyte interface and minimize exfoliation or SEI instability.

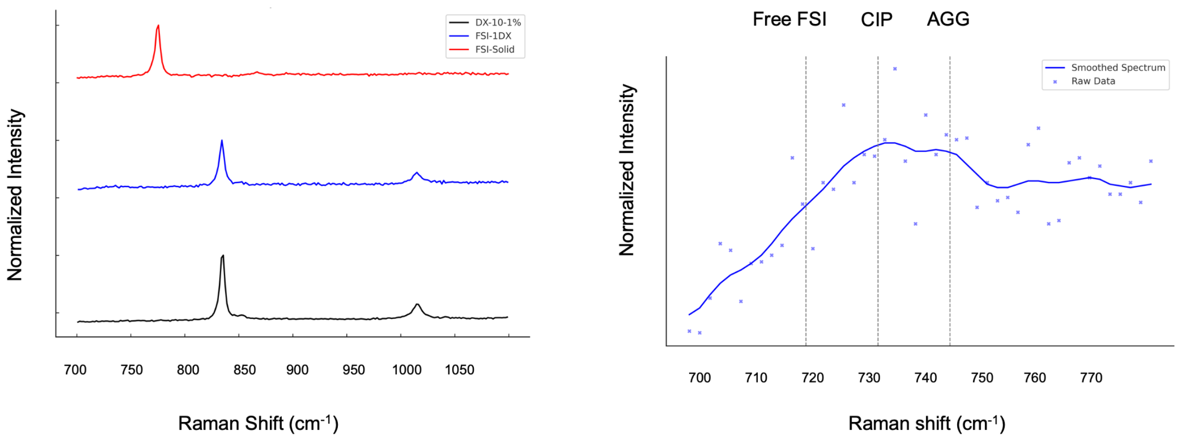

(a) (b)

Figure 6.6-1: (a) Comparison of Raman spectra for pure DX, LiFSI powder, and 1M LiFSI in DX electrolytes. (b) Deconvoluted symmetric-antisymmetric stretch band of 1M LiFSI in DX electrolyte. the free FSI^- corresponds to anions not directly coordinated to Li^+, the CIP (contact ion pair) arises from Li^+–FSI^- pairs, and the AGG (aggregate) is attributed to Li^+–$(FSI^-)^n$ ion clusters.

Figure 6.6-1(a) presents the Raman spectrum of pure DX, where two dominant peaks are observed: the symmetric C–O–C stretching mode at ~835.6 cm⁻¹ and the C–C stretching mode at ~1016.3 cm⁻¹ [352]. In 1M LiFSI in DX, both the C–O–C and C–C stretching peaks remain strong at the same wavenumbers, indicating that a large portion of DX molecules remain free and uncoordinated, even at this relatively high salt concentration. However, subtle broadening of the C–O–C and C–C stretching peaks points to some degree of coordination between DX molecules and Li^+ ions. Specifically, the full width at half maximum (FWHM) of the C–O–C stretch increases slightly from 3.31 to 3.40 cm⁻¹, and the C–C symmetric stretch from 6.08 to 6.18 cm⁻¹. These slight broadenings suggest weak and partial coordination between DX molecules and lithium ions.

Additionally, the Raman spectrum of 1M LiFSI in DX exhibits a distinct S–N–S stretch-related peak (~720–760 cm⁻¹) arising from FSI^- anions. This peak(Fig. 6.6-1.b), observed at 775.65 cm⁻¹, was deconvoluted into three distinct bands: free anions (~721 cm⁻¹, non-coordinated FSI^-), contact ion pairs (CIP, ~733 cm⁻¹, one FSI^- coordinating with one Li^+), and ion aggregates (AGG, ~745 cm⁻¹, one FSI^- coordinating with two or more Li^+)[353,354]. This confirms the presence of FSI^- ions in the electrolyte, as well as the formation of contact ion pairs and aggregates. The ratio of free FSI⁻ anions is significantly lower than that of CIPs and AGGs, suggesting a predominant interaction between FSI⁻ and Li^+ ions. Moreover, the S–N–S Raman shift of AGG is only ~31 cm^{-1} away from the S–N–S vibration mode observed in LiFSI powder (~775.65 cm^{-1}) [355]**,** indicating a strong coordination interaction between FSI⁻ and lithium ions in DX-based electrolytes.

Moreover, the S–N–S stretch peak associated with aggregated Li-FSI coordination (~747 cm^{-1}) is absent in EC/DMC-based electrolytes. This confirms that in 1M LiFSI mixed with DX, lithium ions predominantly form ion aggregates. Due to the relatively weaker coordination effect of DX with lithium compared to the stronger interaction between FSI⁻ and lithium, FSI⁻ dominates the first solvation shell within the electric double layer (EDL). Thus, lithium ions in DX-based electrolytes are primarily solvated by FSI⁻ anions, leading to the formation of contact ion pairs and aggregates.

Overall, these results confirm that lithium ions in DX-based electrolytes are not primarily solvated by the solvent itself, but instead by the FSI⁻ anions. This anion-dominated solvation structure may influence the resulting interfacial chemistry, reduce solvent-driven decomposition and minimize co-intercalation into graphite electrodes. In weakly solvating, anion-coordinated electrolytes of this type, Li^+ is surrounded by FSI⁻ in the primary shell, so interphase formation is dominated by anion-derived decomposition products that form inorganic, LiF-rich SEI/CEI layers. These anion-derived interphases are more resistant to oxidative breakdown and transition-metal dissolution at elevated potentials, thereby enabling more stable cycling at higher upper cut-off voltages and over extended cycle numbers [356-362]. Such solvation behavior therefore supports the potential use of DX as a co-solvent or additive in electrolyte formulations tailored for high-voltage or long-cycle lithium-ion batteries.

6.7 Effects of Salt Concentration on Lithium-Ion Solvation Structure

Understanding how electrolyte concentration influences lithium-ion solvation is essential for tuning solid electrolyte interphase (SEI) formation and overall battery performance. At the electrode–electrolyte interface, this influence is mediated through the electric double layer (EDL), which consists of a compact layer of specifically adsorbed ions and solvent molecules adjacent to the electrode and a diffuse region of counter-ions extending into the bulk [363-367]. Its structure is governed by electrostatic attraction between the charged surface and counter-ions, together with solvent reorganization and specific ion adsorption, which modify the local dielectric environment and ion distribution. Within this EDL, the local solvation structure—set by the interplay between salt concentration, anion coordination and solvent interactions—directly impacts the formation, composition and stability of the SEI. High salt concentrations promote the preferential decomposition of anions over solvents, forming a SEI enriched with inorganic species that are mechanically robust and ionically conductive [382-383].

To investigate these effects, Raman spectroscopy was performed on LiFSI dissolved in two solvent systems—EC/DMC (1:1) and DX—across varying salt concentrations. The concentration range extended from 0.1 M to 6.0 M in EC/DMC, and from 0.5 M to 1.0 M in DX.

As shown in Figure 6.7-1, the Raman spectra of 0.5 M and 1.0 M LiFSI in DX confirm a solvation environment dominated by FSI^- coordination. At 0.5M, the C–O–C symmetric stretch peak (~835.65 cm^{-1}) remains strong and unchanged, indicating that most DX molecules are in their free state with minimal coordination to Li^+ ions. At 1M LiFSI, while the C–O–C peak position remains constant, slight broadening suggests weak interactions between Li^+ ions and DX molecules [381]. Notably, the S–N–S stretch-related band (~720–760 cm^{-1}) emerges at this concentration, confirming the increased FSI^-–Li^+ coordination. Deconvolution of this band reveals the presence of free FSI^-, contact ion pairs (CIP), and aggregates (AGG)[380], indicating that lithium ions are predominantly solvated by FSI^- anions rather than DX. The weak coordination ability and low dielectric constant of DX suppress extensive aggregation, resulting in a solvation structure dominated by anion interactions [379]. This weak solvation shell may reduce solvent decomposition at the graphite interface while maintaining high ion mobility, offering a design advantage in electrolyte systems seeking to suppress SEI instability and solvent co-intercalation.

In contrast, the Raman spectra of LiFSI-EC/DMC electrolytes show a stronger dependence on salt concentration (as shown in Figure 6.7-2.), with the solvation structure evolving significantly as the concentration increases. The prominent EC-Li^+ coordination peaks at approximately 723 cm^{-1} and 915 cm^{-1} in LiFSI-EC/DMC electrolytes (1M to 6M) highlight the strong coordination ability of the high-dielectric-constant EC solvent compared to FSI^- anions [378].

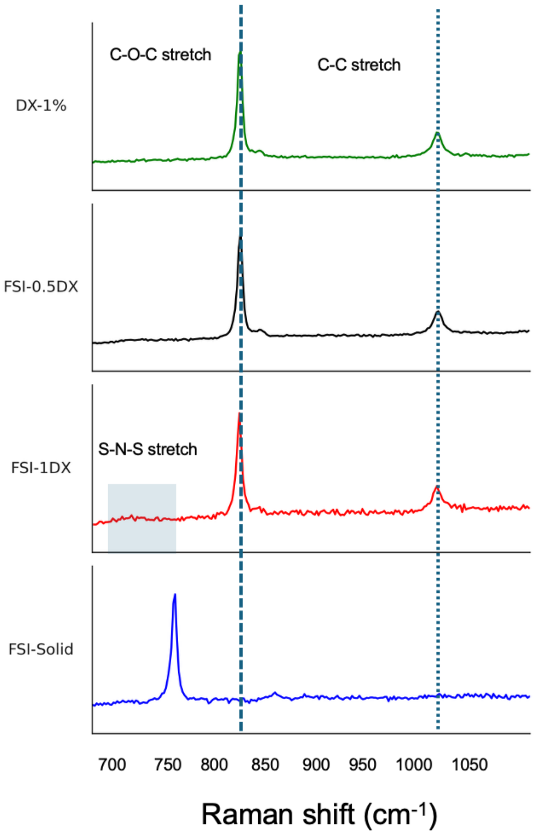

Figure 6.7-1. Raman spectrum of Pure DX, 0.5M LiFSI in DX; 1M LiFSI in DX.

At low concentrations (0.1M–1.0M), the free EC peaks at 714.8 cm^{-1} and 892.9 cm^{-1} remain unshifted but exhibit increased intensity and broadening, indicating the gradual interaction between EC molecules and Li^+ ions. At the same time, the coordinated-EC (Coor-EC) peak emerges at ~914.7 cm^{-1} at 0.1M and shifts slightly to ~916.4 cm^{-1} by 0.5M–1.0M, reflecting the initial formation of Li^+-EC coordination. By 1M, a Coor-EC peak near 723 cm^{-1} becomes visible, marking the onset of stronger Li^+-EC interactions.

As the concentration increases from 1M to 6M, the ratio of I free/Icoor around 723 cm^{-1} and 892 cm^{-1} decreases, indicating the progressive reduction of free EC molecules as they coordinate with Li$^+$ ions. By 6M, the free EC peaks vanish completely, confirming that nearly all EC molecules are involved in coordination. At higher concentrations (3M–6M), the Coor-EC peak at ~723 cm^{-1} broadens, while the peak at 916.4 cm^{-1} becomes sharper. Both peaks display a noticeable increase in intensity, reflecting the formation of contact ion pairs (CIP) and larger aggregates as the solvation environment becomes increasingly crowded. This dense and highly coordinated structure, where nearly every oxygen atom in EC interacts with Li$^+$, limits the solvent's ability to screen the ions fully, leading to the participation of FSI$^-$ anions in the first solvation shell. As a result, we suggest that the solvation structure—arising from the competitive coordination of solvents and anions with Li$^+$ ions—plays a more decisive role in driving the preferential electrolyte decomposition process, rather than the specific anion species.

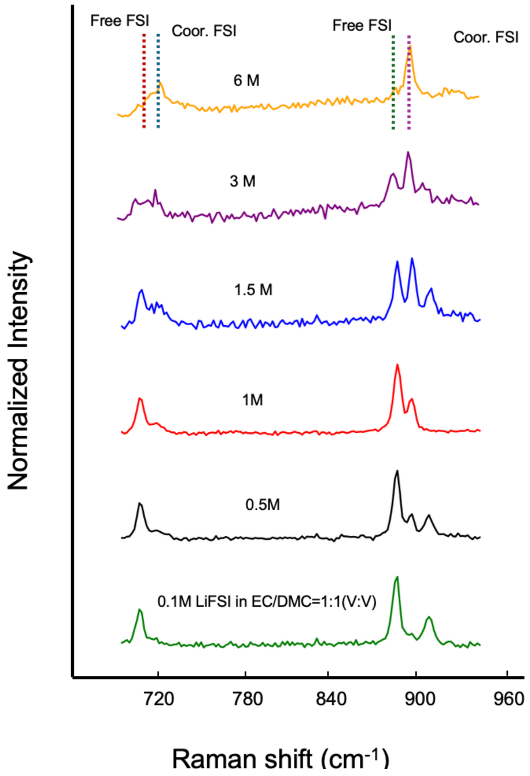

Figure 6.7-2. Raman Spectra of LiFSI in EC/DMC Electrolytes at Various Concentrations (0.1M–6.0M).

The key difference between EC-based and DX-based electrolytes lies in the balance between solvent and anion coordination, which significantly influences the solvation structure and electrolyte behavior. In DX-based electrolytes, the weaker Li^+-DX interactions result in a solvation structure dominated by FSI^- aggregates rather than solvent-separated ion pairs. The presence of the S–N–S stretch peak (~747 cm^{-1}) highlights the stronger involvement of FSI^- anions, while a significant number of free DX molecules persist even at 1M, indicating a loosely packed solvation shell. This relatively open structure may support higher ion mobility but reduces the extent of solvent-driven solvation shell formation.

In contrast, EC-based electrolytes exhibit much stronger solvent-Li^+ interactions, as evidenced by the rapid disappearance of free EC peaks and the growth of coordinated-EC peaks with increasing salt concentration. This leads to the formation of a dense and tightly packed solvation shell, accompanied by extensive ion pairing and aggregate formation at higher concentrations. While this compact structure enhances ionic interactions and promotes competitive coordination between EC and FSI^- anions, it may hinder ion transport efficiency compared to the more open DX-based system. The evolution of EC-based systems from free EC dominance at low concentrations to a highly coordinated solvation environment at high concentrations highlights the critical role of EC-Li^+ interactions in determining solvation structure, lithium-ion transport, and SEI formation. This indicates that the solvation structure—driven by the competitive effects between solvents and anions—rather than the specific anion species, plays a dominant role in governing the preferential electrolyte decomposition process [375-377].

These findings emphasize that the composition of the lithium-ion solvation shell—not simply the salt or solvent used—plays a dominant role in guiding electrolyte decomposition pathways and SEI structure. By carefully selecting both the solvent system and salt concentration, the solvation structure can be engineered to modulate lithium-ion transport, SEI chemistry, and interfacial stability—offering a rational pathway for next-generation electrolyte design.

6.8 Conclusion

This chapter presents a detailed investigation into the mechanisms of SEI formation and lithium intercalation at the graphite–electrolyte interface, using Raman spectroscopy as a central analytical technique. While some of the operando Raman data were generated as part of a collaborative study and published in the supplementary section of a paper by Chen et al. (2023)[324], the analysis presented here — particularly the identification of lithiation stages and solvation structure dynamics — is original to this work and expands the scientific understanding of graphite–electrolyte interactions.

The results demonstrated that mechanical polishing of HOPG produces a strong contrast between the ordered basal plane and the disordered, defect-rich edge plane. Raman spectroscopy confirmed this via sharp G and 2D bands in the basal region, and a pronounced D band at the edge. Post-treatment by annealing at 500 °C effectively restored graphitic order, especially at the edge, while plasma treatment introduced new defects on the basal surface. Operando Raman during the first lithiation cycle revealed that SEI formation begins at 0.7–0.5 V, prior to bulk intercalation, marked by D-band suppression and early G/2D shifts. As voltage decreased, stage-wise lithium intercalation was tracked through spectral changes, with complete signal loss at voltages below 0.05 V indicating Stage 1 compound formation. Operando Raman during the first lithiation cycle showed that attenuation of the D band in the 0.7–0.5 V window at the HOPG edge plane, occurring before pronounced G- and 2D-band evolution, is consistent with the onset of SEI nucleation inferred from complementary EC-AFM/3D-NRM/XPS measurements. As the potential decreased further, stage-wise lithium intercalation was tracked through systematic changes in the G and 2D bands, and the complete loss of graphite Raman features at voltages below ~0.05 V indicated the formation of highly conductive stage-1 graphite intercalation compounds that render both graphite and the overlying SEI effectively Raman-silent.

In the electrolyte studies, EC-based systems (1M $LiPF_6$ or LiFSI in EC/DMC) exhibited strong solvent-dominated Li^+ solvation, while DX-based systems revealed anion-dominated structures with FSI$^-$ forming contact ion pairs and aggregates even at low concentrations. Increasing salt concentration (3–6 M) further altered solvation: EC/DMC systems transitioned from solvent-separated to contact-ion-pair-dominated shells whereas DX maintained FSI$^-$ coordination throughout. These distinct solvation trends have direct implications for SEI composition and interfacial stability. Collectively, this work shows that Raman spectroscopy — particularly operando — is a powerful molecular probe for simultaneously tracking structural evolution of electrodes and solvation chemistry in electrolytes. The findings provide critical insights into how surface treatments, electrolyte composition, and ion coordination mechanisms govern SEI formation and lithium-ion transport. This offers a unified framework for interfacial design in high-performance lithium-ion battery systems.

Future work could build on this foundation in several directions. First, although this study focused on early-stage SEI formation, combining operando Raman with high-resolution techniques such as cryo-TEM, EC-AFM and XPS would allow simultaneous tracking of morphological and chemical evolution over extended cycling windows. Second, because SEI vibrational modes are not directly resolved under the conventional confocal Raman conditions used here, recent developments in plasmon-enhanced and tip-enhanced Raman spectroscopy (e.g. SERS, SHINERS and TERS) – which have demonstrated direct access to SEI vibrational fingerprints and nanoscale chemical heterogeneity on lithium and silicon-based electrodes – suggest that implementing such enhanced schemes on HOPG or other model carbon anodes could overcome the sensitivity limitations encountered in this work and provide a more complete vibrational picture of early SEI formation[368-374]. Third, applying the combined intercalation–solvation framework established here to other anode materials, such as silicon, lithium metal or hard carbons, would test the generality of the observed links between solvation structure, SEI evolution and intercalation behaviour. Fourth, machine-learning approaches could assist in deconvoluting large Raman datasets across wide electrolyte libraries, enabling rapid screening of solvation environments and their impact on graphite and SEI signatures. Finally, deeper characterisation of electrolyte–SEI coupling under dynamic cycling—integrating operando Raman with electrochemical modelling and impedance analysis—could help bridge the gap between molecular-level solvation behaviour and long-term interfacial stability in practical lithium-ion cells.

Chapter 7: Conclusion and Future Work

This thesis investigated the influence of material dimensionality—ranging from zero-dimensional graphene quantum dots (GQDs) to two-dimensional graphene–MoS_2 van der Waals heterostructures (vdWHs), to bulk highly oriented pyrolytic graphite (HOPG)—on optical properties and interfacial behaviours. By integrating nanoscale fabrication, photonic encoding, and operando spectroscopic analysis, the work provides a comprehensive understanding of how graphene-based systems can be engineered for physically unclonable functions (PUFs) and lithium-ion battery (LIB) interface optimization.

In the GQD system, I demonstrated that electrospray-deposited GQDs derived from spent tea leaves generate high-entropy, excitation-dependent fluorescence patterns that are well suited for PUF applications. Through rotationally invariant local binary pattern (RMLBP) encoding, these patterns were transformed into binary maps with strong randomness, balance, and inter-sample uniqueness. Optimizing deposition concentration and imaging parameters further enhanced the stability and reproducibility of the optical fingerprints, establishing a green, scalable, and tamper-resistant photonic platform.

The graphene–MoS_2 heterostructure study explored deterministic optical fingerprints based on stacking geometry, interfacial strain, and excitonic modulation. Spatially resolved photoluminescence (PL) measurements, performed across temperatures and excitation powers, revealed unique emission signatures that varied across the flake yet remained reproducible under perturbation. Binary maps generated from PL intensity distributions showed the feasibility of deterministic PUFs derived from controlled interlayer interactions, expanding the scope of optically encoded security.

For the HOPG system, operando Raman spectroscopy revealed the sequence of solid electrolyte interphase (SEI) formation and lithium intercalation at graphite electrodes. The suppression of the D-band between 0.7 and 0.5 V indicated that SEI formation initiates at defect-rich edge planes before lithium intercalation dominates below 0.5 V. Comparative electrolyte studies showed that EC-based solvents promote solvent-dominated Li^+ coordination, while DX-based solvents result in anion-dominated solvation shells. Increasing salt concentration in EC/DMC shifted the solvation structure toward aggregate formation, modulating SEI chemistry and potentially improving battery stability.

This work makes several key contributions to the field. It introduces a sustainable fabrication strategy for GQD-based optical fingerprints, achieving near-ideal entropy metrics without lithography. It demonstrates, for the first time, that interlayer exciton coupling in vdWHs can produce deterministic, high-resolution optical signatures suitable for PUFs. It also provides new operando insights into the electrochemical behavior of HOPG, highlighting the role of solvation structures in guiding SEI formation and lithium-ion dynamics. Together, these results bridge optical security and energy storage, showing how nanoscale structure determines function across disciplines.

Despite its strengths, the work has limitations. The GQD PUFs were not tested under environmental or mechanical stress, which could affect real-world durability. The deterministic vdWH fingerprints, though consistent across controlled regions, require further validation across multiple fabrication batches to assess scalability. In the electrochemical study, only early-cycle interfacial behaviour was examined, and additional tools such as cryo-TEM or XPS would be needed to confirm SEI composition and thickness. Future research should explore the robustness of PUFs under mechanical bending, humidity, or temperature cycling to simulate practical use cases. Expanding the material palette to include other 2D semiconductors or heterostructures with rotational misalignment may increase entropy and broaden optical encoding applications. Coupling operando Raman with advanced imaging methods could offer richer, multidimensional views of SEI evolution. Moreover, machine learning models trained on spectral and imaging data could accelerate electrolyte optimization and fingerprint authentication protocols.

In conclusion, this thesis demonstrates how dimensionality in carbon-based nanomaterials can be harnessed to engineer both optical identity and interfacial behaviour. From zero-dimensional randomness to two-dimensional determinism, and from molecular solvation to bulk electrode function, this work offers new strategies for secure hardware authentication and high-performance battery design. It also reflects the creative possibilities unlocked when nanoscale material science meets interdisciplinary engineering.

Appendix

1.1 Binary Map Generation Manual

The processing framework includes data capture → pre-processing → fingerprint generation → output, the workflow comprised (i) ROI cropping, (ii) contrast boosting via global histogram equalisation (MATLAB *histeq*), and (iii) downsizing prior to R-MLBP encoding. Pre-processing began by converting each raw fluorescence image to 8-bit grayscale (L=256 intensity levels) to eliminate colour-channel variability. A 284 × 284 px square region of interest (ROI) was then cropped from the centre of the emission region to retain the highest-signal area while minimising background artefacts. Global histogram equalisation was applied to all cropped ROIs to better highlight contrasting pixels and yield more reliable, unique fingerprints by using MATLAB:

$$I_{eq} = histeq(I_{roi}, 256);$$

where 256 bins match the 8-bit dynamic range. The *histeq* operation remaps intensities so that the output histogram approximately matches a near uniform distribution, thereby enhancing contrast across the ROI. The equalised ROI (I_{eq})was then passed to the subsequent steps.

The cropped ROI was then pre-smoothed with a Lorentz filter following histogram equalization; this step attenuates high-frequency noise—such as camera read noise, photon shot noise, and hot pixels—and bandlimits the signal to prevent aliasing artifacts during subsequent resampling. Then this pre-smoothed ROI was then down sampled to a fixed resolution of 100×100 pixels. down sampled to 100×100 pixels to (i) accelerate fingerprint generation by reducing the number of pixels (and hence per-pixel neighbourhood iterations) processed by the encoder, and (ii) suppress pixel-scale noise, particularly isolated single-pixel fluctuations that can destabilise local texture comparisons; The fixed 100×100 size also standardises the feature grid/bit-length across devices, which is required for valid Hamming-distance comparisons because Hamming distance is defined for equal-length strings/vectors.

Following preprocessing, each fluorescence image was converted into a binary fingerprint using Reduced-Modified Local Binary Patterns (R-MLBP) method. This process transforms a 100×100-pixel ROI into a binary output image of identical dimensions, where each pixel's value is determined by intensity comparisons within a local circular neighbourhood defined by two parameters: the neighbourhood radius r and the number of sampling points *N*.

Parameterisation. The radius r controls the spatial scale while the even integer *N* specifies the angular sampling density. For this work, a fixed neighbourhood of *N*=16 sampling points was selected. This provides N/2 = 8 diametrically-opposed gradient comparisons plus a centre-to-mean contrast bit, yielding sufficiently dense angular sampling while retaining the noise-robust modal reduction inherent to R-MLBP. To assess neighbourhood-size sensitivity to spatial scale, the radius was varied across $\Upsilon \in \{2,3,4,5,7,10,15,20\}$ pixels.

Pixel-wise R-MLBP computation. For each centre pixel α_0, the binary output bit is obtained as follows:

(1) Sample circular neighbours. The intensities $\{\alpha_i\}_{i=1}^{N}$ are sampled on a circle of radius r centred at α_0. The circle is divided into right and left halves, with the right half is defined as the first N/2 points moving clockwise from the point on the positive y-axis (the "upper" neighbour).

(2) Form the MLBP feature vector (length N/2+1):

- Gradient bits (first N/2 bits): For each diametrically-opposed pair k, starting from the upper neighbour and proceeding clockwise, the gradient bit is

$$b\kappa = \begin{cases} 1, \alpha_{R,\kappa} \geq \alpha_{L,\kappa} \\ 0, otherwise \end{cases}$$

  where $\alpha_{R,\kappa}$ and $\alpha_{L,\kappa}$ are the intensities of the κ-th right-half and left half sample, respectively. Concatenating $\{b\kappa\}_{\kappa = 1}^{N/2}$ yields the gradient component.

- Contrast bit (final bit): the mean intensity of all neighbours is computed as

$$\mu = \frac{1}{N} \Sigma_{i = 1}^{N} \alpha_i$$

and the centre pixel is compared to this mean μ:

$$b_c \quad = \begin{cases} 1, & \alpha_0 \geq \mu \\ 0, & otherwise \end{cases}$$

The resulting (N/2+1)-bit MLBP vector reduces sensitivity to a noisy centre pixel because the centre contributes only one bit, while the neighbourhood average suppresses single-pixel fluctuations.

(3) Reduce to a single output bit (R-MLBP): the final output bit for α_0 is defined as the modal value (majority bit) of the (N/2+1)-bit MLBP feature vector. This modal reduction further suppressed pixel-level noise on the final fingerprint, since isolated corrupted comparisons are less likely to alter the majority outcome.

1.2 Binary Map Generation Based on Additional Samples

To validate the robustness and generalizability of the R-MLBP encoding method described in Section 4.6.1, binary fingerprint maps were generated for three additional GQD samples (designated S2, S3, and S4). These samples were prepared under identical synthesis and deposition conditions as the primary sample (S1) detailed in Section 4.6.1, ensuring consistency in material properties while introducing inherent stochastic variability from the green hydrothermal process and electrospray deposition.

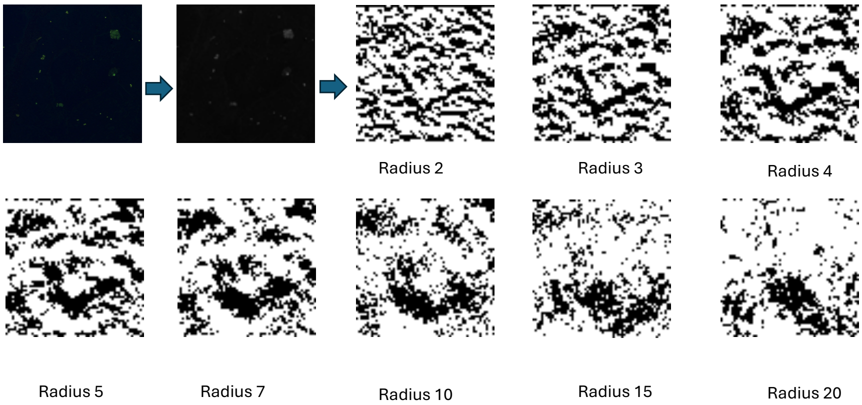

Sample 2

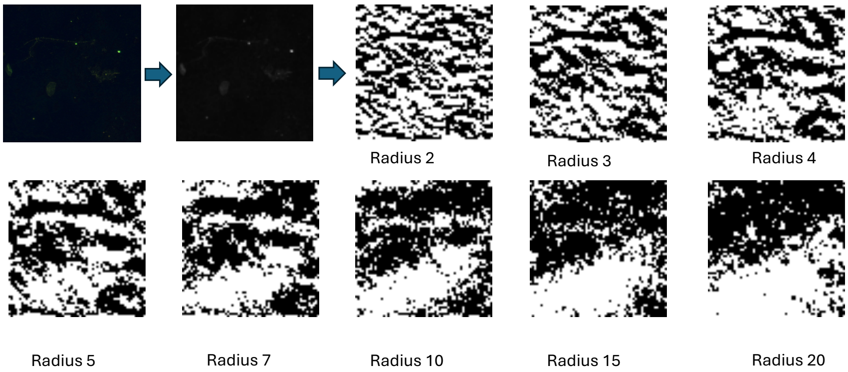

Sample 3

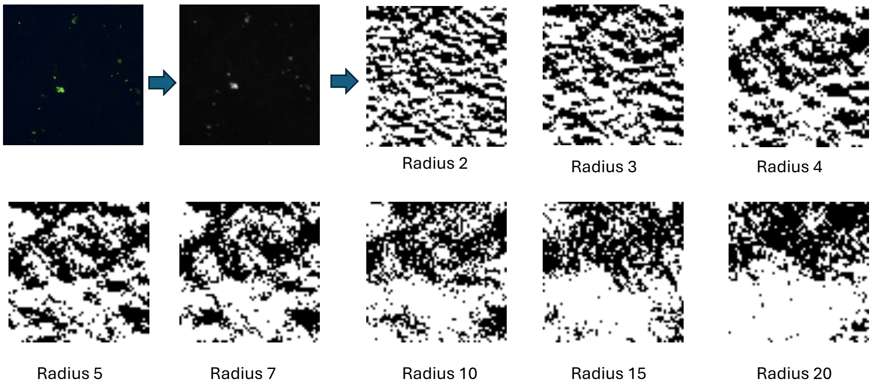

Sample 4

Figure 1.2-1 Binary map generation from GQD fluorescence images using the RMLBP method with varying radius values (present sample 2-4 here). Each row shows the full processing pipeline for a single fluorescence image: the original green-channel image (left), grayscale-converted version, and binary maps generated using RMLBP encoding with increasing radius values r = 2, 3, 4, 5, 7, 10, 15, 20. All images were downsized to 100×100 pixels prior to encoding. As radius increases, local features become progressively smoothed, reducing entropy and pattern sharpness. A radius of 3 offers an optimal trade-off between randomness

1.3 Fluorescence Images of the 20-Sample Dataset for Binary Map Extraction

To statistically validate the reproducibility and uniqueness of GQD-based optical fingerprints, a larger dataset of 20 independent samples was prepared under consistent synthesis and deposition conditions. This section presents the fluorescence images acquired from these samples, which serve as the raw input for the binary map extraction pipeline detailed in Section 4.6.2.

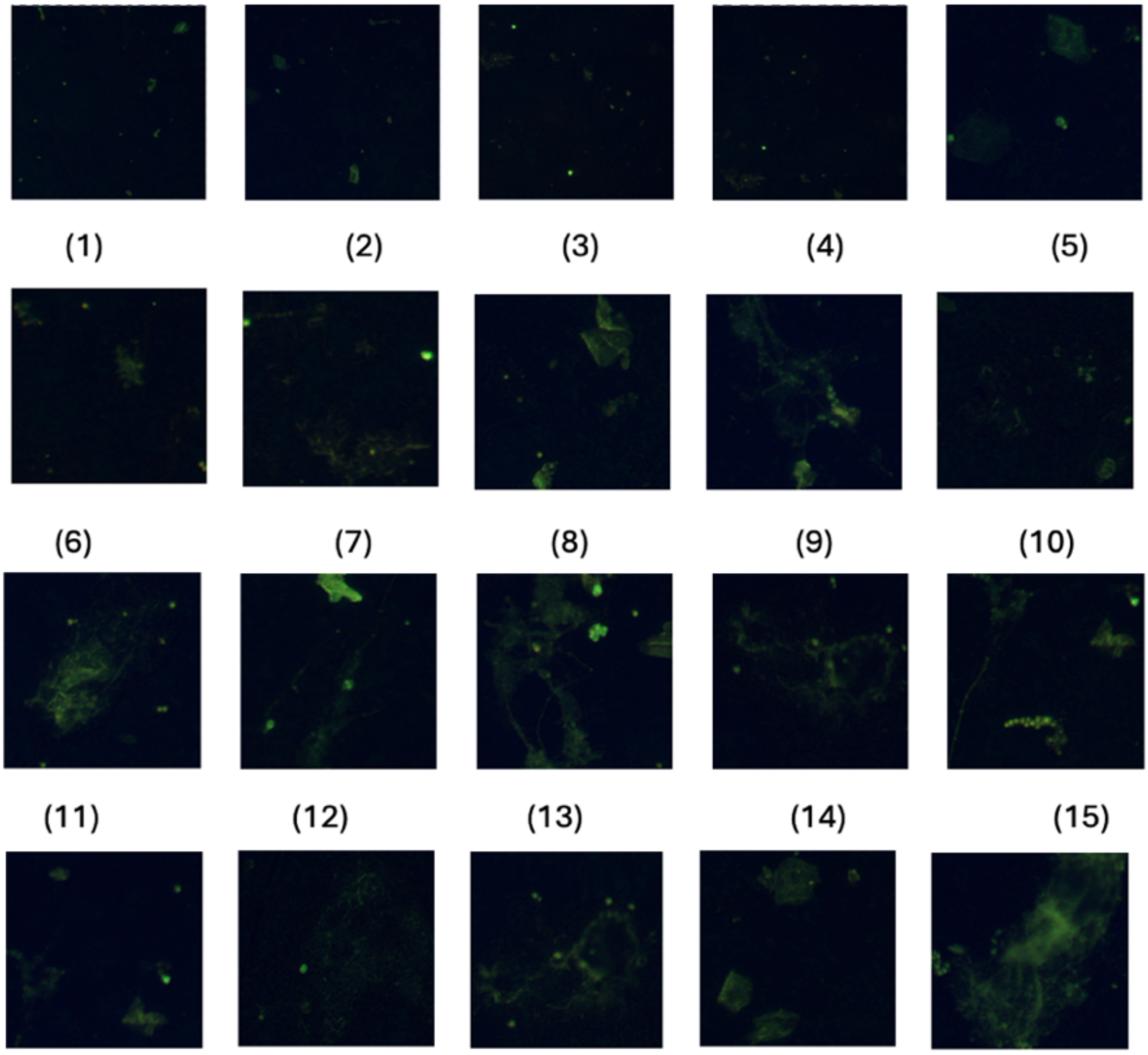

(1) (2) (3) (4) (5)

(6) (7) (8) (9) (10)

(11) (12) (13) (14) (15)

(16) (17) (18) (19) (20)

Figure 1.3-1 Fluorescence images of the 20 samples

All samples were fabricated following the green hydrothermal synthesis route described in Section 3.1.1, using spent oolong tea waste as the carbon precursor. Electrospray deposition was employed to create spatially stochastic GQD films on silicon substrates, ensuring that each sample exhibited inherent, unrepeatable morphological variability while maintaining comparable optical density and fluorescence intensity.

1.4 Hamming Distance and Bias Analysis Across Radii for 20 Samples

To optimize the R-MLBP encoding parameters for GQD-based optical PUFs, evaluation of bias and inter-sample Hamming distance (HD) was conducted across eight neighbourhood radii: $r \in \{2, 3, 4, 5, 7, 10, 15, 20\}$ pixels. The analysis was performed on binary fingerprints extracted from additional 16 GQD samples (S05–S20) using the pre-processing and encoding pipeline described in section 1.1.

Based on the 20-sample statistics, R = 3 provides the most balanced operating point between bit balance and inter-device separability because it achieves the smallest deviation of the mean inter-device Hamming distance from the ideal value of 0.5, while keeping the bias deviation low. Specifically, R = 3 yields a mean inter-Hamming distance of 0.4839 ± 0.0049, corresponding to a 3.22% deviation from 0.5 (relative to 0.5), which is smaller than 3.98% (R = 2), 4.20% (R = 4), 4.80% (R = 5), 5.20% (R = 7), 5.98% (R = 10), 6.22% (R = 15), and 10.94% (R = 20), indicating the strongest inter-device separability among the tested settings. In parallel, the mean bias at R = 3 is 0.4982 ± 0.0060, giving a 0.36% deviation from 0.5 (relative to 0.5), which remains similarly low to the other small-R cases. Therefore, R = 3 is selected because it minimises the inter-Hamming deviation from 0.5 (maximising uniqueness) without compromising bias stability.

Sample	R=2	R=3	R=4	R=5	R=7	R=10	R=15	R=20
S1	0.5047	0.4892	0.5048	0.5050	0.5061	0.5062	0.5099	0.5166
S2	0.4923	0.5012	0.4920	0.4910	0.4895	0.4878	0.4827	0.4678
S3	0.5047	0.4931	0.5048	0.5050	0.5061	0.5062	0.5099	0.5166
S4	0.4923	0.5032	0.4920	0.4910	0.4895	0.4878	0.4827	0.4678
S5	0.5047	0.4924	0.5048	0.5050	0.5061	0.5062	0.5099	0.5166
S6	0.4923	0.5112	0.4920	0.4910	0.4895	0.4878	0.4827	0.4678
S7	0.5047	0.5021	0.5048	0.5050	0.5061	0.5062	0.5099	0.5166
S8	0.4923	0.4990	0.4920	0.4910	0.4895	0.4878	0.4827	0.4678
S9	0.5047	0.4873	0.5048	0.5050	0.5061	0.5062	0.5099	0.5166
S10	0.4923	0.4958	0.4920	0.4910	0.4895	0.4878	0.4827	0.4678
S11	0.5047	0.5037	0.5048	0.5050	0.5061	0.5062	0.5099	0.5166
S12	0.4923	0.4939	0.4920	0.4910	0.4895	0.4878	0.4827	0.4678
S13	0.5047	0.5041	0.5048	0.5050	0.5061	0.5062	0.5099	0.5166
S14	0.4923	0.4987	0.4920	0.4910	0.4895	0.4878	0.4827	0.4678
S15	0.5047	0.5010	0.5048	0.5050	0.5061	0.5062	0.5099	0.5166
S16	0.4923	0.4965	0.4920	0.4910	0.4895	0.4878	0.4827	0.4678
S17	0.5047	0.4933	0.5048	0.5050	0.5061	0.5062	0.5099	0.5166
S18	0.4923	0.4976	0.4920	0.4910	0.4895	0.4878	0.4827	0.4678
S19	0.5047	0.4942	0.5048	0.5050	0.5061	0.5062	0.5099	0.5166
S20	0.4923	0.5056	0.4920	0.4910	0.4895	0.4878	0.4827	0.4678
Mean	0.4985	0.4982	0.4984	0.4980	0.4978	0.4970	0.4963	0.4922
SD	0.0064	0.0060	0.0066	0.0072	0.0085	0.0094	0.0140	0.0250

Table 1: Individual Bias Values for 20 samples

Sample	R=2	R=3	R=4	R=5	R=7	R=10	R=15	R=20
S1	0.4824	0.4803	0.4840	0.4825	0.4811	0.4777	0.4773	0.4609
S2	0.4734	0.4792	0.4863	0.4695	0.4669	0.4625	0.4605	0.4297
S3	0.4853	0.4825	0.4740	0.4825	0.4811	0.4777	0.4773	0.4609
S4	0.4866	0.4930	0.4717	0.4695	0.4669	0.4625	0.4605	0.4297
S5	0.4673	0.4798	0.4840	0.4825	0.4811	0.4777	0.4773	0.4609
S6	0.4716	0.4783	0.4740	0.4695	0.4669	0.4625	0.4605	0.4297
S7	0.4812	0.4886	0.4863	0.4825	0.4811	0.4777	0.4773	0.4609
S8	0.4782	0.4824	0.4717	0.4695	0.4669	0.4625	0.4605	0.4297
S9	0.4802	0.4861	0.4740	0.4825	0.4811	0.4777	0.4773	0.4609
S10	0.4746	0.4829	0.4840	0.4695	0.4669	0.4625	0.4605	0.4297
S11	0.4862	0.4927	0.4717	0.4825	0.4811	0.4777	0.4773	0.4609
S12	0.4855	0.4913	0.4863	0.4695	0.4669	0.4625	0.4605	0.4297
S13	0.4808	0.4863	0.4840	0.4825	0.4811	0.4777	0.4773	0.4609
S14	0.4878	0.4814	0.4740	0.4695	0.4669	0.4625	0.4605	0.4297
S15	0.4834	0.4807	0.4717	0.4825	0.4811	0.4777	0.4773	0.4609
S16	0.4746	0.4892	0.4863	0.4695	0.4669	0.4625	0.4605	0.4297
S17	0.4828	0.4769	0.4740	0.4825	0.4811	0.4777	0.4773	0.4609
S18	0.4739	0.4831	0.4840	0.4695	0.4669	0.4625	0.4605	0.4297
S19	0.4862	0.4847	0.4863	0.4825	0.4811	0.4777	0.4773	0.4609
S20	0.4800	0.4793	0.4717	0.4695	0.4669	0.4625	0.4605	0.4297
Mean	0.4801	0.4839	0.4790	0.4760	0.4740	0.4701	0.4689	0.4453
SD	0.0058	0.0049	0.0064	0.0067	0.0073	0.0078	0.0086	0.0160

Table 2: inter-hamming distance of 20 samples

2. Binary Map Generation from Graphene-MoS_2

The binary matrix (and final 256-bit PUF response) was generated using a five-step workflow, progressing from spatial region selection and spectral fitting to feature-map construction, binarization, correlation-reduced readout, and cryptographic hashing. Briefly, the workflow comprises: (1) ROI/heterostructure region selection and masking, (2) trusted-pixel selection within the heterostructure, (3) 2×2 parity interleaved pixel readout to reduce spatial correlation, (4) concatenation of a fixed-order pre-hash bitstream, and (5) SHA-256 hashing to produce a fixed-length 256-bit response. The details of these steps are listed as follows:

Step 1: ROI region selection:

1. The optical microscope image and the macro-PL image were inspected to identify the physical outline of the flake(s) and the approximate overlap/heterostructure region.
2. Flake masking: The initial mask was obtained by thresholding the quick peak-intensity map. The threshold was set to the 30th percentile of the positive intensity values ($I > 0$) to avoid over-clipping dim but valid HS regions. Pixels with intensity greater than this threshold were marked as 1, otherwise 0. The initial mask was then refined by (i) filling holes to preserve internal regions that may appear dim, and (ii) applying a binary morphological closing operation using a 3×3 structuring element for two iterations. After refinement, only the largest connected component was retained to remove small, isolated islands.

Step 2: Trusted-pixel selection within HS:

1. Rationale: a ‘trusted’ pixel subset was defined using objective fit-quality and stability thresholds.
2. Set thresholds: Pixels were classified as trusted only if (i) they lie inside the HS mask, (ii) the fit converged to finite parameters, (iii) the goodness-of-fit exceeded $R^2 > 0.95$. The trusted mask is therefore defined as:

   $$Mtrusted = MHS \cap (R^2 > 0.95) \cap (HA - / HA > 0.05).$$

   Only pixels with $M_{trusted} = 1$ are used for encoding. All subsequent feature extraction and binary encoding were performed only on trusted pixels. Pixels inside HS but marked untrusted were excluded from sampling (or treated as missing values for plotting), preventing unreliable spectra from dominating the final bitstream and hashed 256-bit response.

Step 3 — Centred-feature binarization: for feature $f_{k,}$ compute the median over trusted pixels m_k and centre

$$f'k \ = \ fk \ - median\ (f)$$

then, binarize each feature with a fixed threshold at 0: $bk \ = \ 1\ if\ f'k \ > \ 0\ else\ 0$.

Step 4 — Interleaved pixel readout (reduce spatial correlation): read out trusted pixels using 2×2 parity interleaving based on (y mod 2, x mod 2), cycling sublattices 00 → 01 → 10 → 11 until all trusted pixels are listed.

Step 5— Hash to 256-bit response: compute K = SHA-256(B) and output the 256-bit digest as the final PUF response.

References

1. Li, L., Wu, G., Yang, G., Peng, J., Zhao, J. and Zhu, J.J., 2013. Focusing on luminescent graphene quantum dots: current status and future perspectives. *Nanoscale*, *5*(10), pp.4015-4039.
2. Geim, A.K. and Grigorieva, I.V., 2013. Van der Waals heterostructures. *Nature*, *499*(7459), pp.419-425.
3. Vithalani, R., Patel, D., Modi, C.K. and Suthar, D.H., 2020. Glowing photoluminescene in carbon-based nanodots: current state and future perspectives. *Journal of materials science*, *55*(21), pp.8769-8792.
4. Maes, R. and Verbauwhede, I., 2010. Physically unclonable functions: A study on the state of the art and future research directions. *Towards Hardware-Intrinsic Security: Foundations and Practice*, pp.3-37.
5. Nocentini, S., Rührmair, U., Barni, M., Wiersma, D.S. and Riboli, F., 2024. All-optical multilevel physical unclonable functions. *Nature materials*, *23*(3), pp.369-376.
6. Xu, K., 2014. Electrolytes and interphases in Li-ion batteries and beyond. *Chemical reviews*, *114*(23), pp.11503-11618.
7. Agubra, V.A. and Fergus, J.W., 2014. The formation and stability of the solid electrolyte interface on the graphite anode. *Journal of Power Sources*, *268*, pp.153-162.
8. Lim, J.N., Lim, G.J., Cai, Y., Chua, R., Guo, Y., Yan, Y. and Srinivasan, M., 2023. Electrolyte designs for safer lithium-ion and lithium-metal batteries. *Journal of Materials Chemistry A*, *11*(42), pp.22688-22717.
9. Xie, S., Ni, K. and Zhu, Y., 2025. Electronic Properties of Carbon-Based Superatomic Structures. *Advanced Functional Materials*, p.e08106.
10. Li, J., Yin, D. and Qin, Y., 2023. Carbon materials: structures, properties, synthesis and applications. *Manufacturing Review*, *10*, p.13.
11. Yang, G., Li, L., Lee, W.B. and Ng, M.C., 2018. Structure of graphene and its disorders: a review. *Science and technology of advanced materials*, *19*(1), pp.613-648.
12. Rano, N.A. and Martsinovich, N., 2025. Stability of sp3 carbons in hydrogenated graphene quantum dots and their electronic and optical

properties studied using density functional theory. *The Journal of Physical Chemistry A*, *129*(17), pp.3790-3806.

13. Zhang, H., Yang, Y., Ren, D., Wang, L. and He, X., 2021. Graphite as anode materials: Fundamental mechanism, recent progress and advances. *Energy Storage Materials*, *36*, pp.147-170.
14. Zhao, W., Zhao, C., Wu, H., Li, L. and Zhang, C., 2024. Progress, challenge and perspective of graphite-based anode materials for lithium batteries: A review. *Journal of Energy Storage*, *81*, p.110409.
15. Liu, Y., Shi, H. and Wu, Z.S., 2023. Recent status, key strategies and challenging perspectives of fast-charging graphite anodes for lithium-ion batteries. *Energy & Environmental Science*, *16*(11), pp.4834-4871.
16. Bar-Tow, D., Peled, E. and Burstein, L., 1999. A study of highly oriented pyrolytic graphite as a model for the graphite anode in Li-Ion batteries. *Journal of the Electrochemical Society*, *146*(3), p.824.
17. Zhu, H., Russell, J.A., Fang, Z., Barnes, P., Li, L., Efaw, C., Muenzer, A., May, J., Hamal, K., Cheng, I.F. and Davis, P.H., 2021. A Comparison of Solid Electrolyte Interphase Formation and Evolution on Highly Oriented Pyrolytic and Disordered Graphite Negative Electrodes in Lithium-Ion Batteries. *Small*, *17*(52), p.2105292.
18. Asenbauer, J., Eisenmann, T., Kuenzel, M., Kazzazi, A., Chen, Z. and Bresser, D., 2020. The success story of graphite as a lithium-ion anode material–fundamentals, remaining challenges, and recent developments including silicon (oxide) composites. *Sustainable Energy & Fuels*, *4*(11), pp.5387-5416.
19. Velicky, M., Toth, P.S., Woods, C.R., Novoselov, K.S. and Dryfe, R.A., 2019. Electrochemistry of the basal plane versus edge plane of graphite revisited. *The Journal of Physical Chemistry C*, *123*(18), pp.11677-11685.
20. Terrones, M., Botello-Méndez, A.R., Campos-Delgado, J., López-Urías, F., Vega-Cantú, Y.I., Rodríguez-Macías, F.J., Elías, A.L., Muñoz-Sandoval, E., Cano-Márquez, A.G., Charlier, J.C. and Terrones, H., 2010. Graphene and graphite nanoribbons: Morphology, properties, synthesis, defects and applications. *Nano today*, *5*(4), pp.351-372.

21. Yang, G., Li, L., Lee, W.B. and Ng, M.C., 2018. Structure of graphene and its disorders: a review. *Science and technology of advanced materials*, *19*(1), pp.613-648.

22. Splendiani, A., Sun, L., Zhang, Y., Li, T., Kim, J., Chim, C.Y., Galli, G. and Wang, F., 2010. Emerging photoluminescence in monolayer MoS2. *Nano letters*, *10*(4), pp.1271-1275.

23. Lin, Y., Ling, X., Yu, L., Huang, S., Hsu, A.L., Lee, Y.H., Kong, J., Dresselhaus, M.S. and Palacios, T., 2014. Dielectric screening of excitons and trions in single-layer MoS2. *Nano letters*, *14*(10), pp.5569-5576.

24. Britnell, L., Ribeiro, R.M., Eckmann, A., Jalil, R., Belle, B.D., Mishchenko, A., Kim, Y.J., Gorbachev, R.V., Georgiou, T., Morozov, S.V. and Grigorenko, A.N., 2013. Strong light-matter interactions in heterostructures of atomically thin films. *Science*, *340*(6138), pp.1311-1314.

25. Geim, A.K. and Grigorieva, I.V., 2013. Van der Waals heterostructures. *Nature*, *499*(7459), pp.419-425.

26. Zou, Y., Ma, Q.S., Zhang, Z., Pu, R., Zhang, W., Suo, P., Sun, K., Chen, J., Li, D., Ma, H. and Lin, X., 2022. Observation of ultrafast interfacial exciton formation and relaxation in graphene/MoS2 heterostructure. *The Journal of Physical Chemistry Letters*, *13*(23), pp.5123-5130.

27. Phuc, H.V., Hieu, N.N., Hoi, B.D., Phuong, L.T. and Nguyen, C.V., 2018. First principle study on the electronic properties and Schottky contact of graphene adsorbed on MoS2 monolayer under applied out-plane strain. *Surface Science*, *668*, pp.23-28.

28. Zhou, K.G., Withers, F., Cao, Y., Hu, S., Yu, G. and Casiraghi, C., 2014. Raman modes of MoS2 used as fingerprint of van der Waals interactions in 2-D crystal-based heterostructures. *ACS nano*, *8*(10), pp.9914-9924.

29. Luo, D., Tang, J., Shen, X., Ji, F., Yang, J., Weathersby, S., Kozina, M.E., Chen, Z., Xiao, J., Ye, Y. and Cao, T., 2021. Twist-angle-dependent ultrafast charge transfer in MoS2-graphene van der Waals heterostructures. *Nano Letters*, *21*(19), pp.8051-8057.

30. Shih, C.J., Wang, Q.H., Son, Y., Jin, Z., Blankschtein, D. and Strano, M.S., 2014. Tuning on–off current ratio and field-effect mobility in a MoS2–graphene heterostructure via Schottky barrier modulation. *ACS nano*, *8*(6), pp.5790-5798.

31. Wang, C., Chen, Y., Ma, Q., Suo, P., Sun, K., Cheng, Y., Lin, X., Liu, W. and Ma, G., 2025. Observation of transient trion induced by ultrafast charge transfer in graphene/MoS2 heterostructure. *Applied Physics Letters*, *126*(4).

32. Facure, M.H., Schneider, R., Mercante, L.A. and Correa, D.S., 2020. A review on graphene quantum dots and their nanocomposites: from laboratory synthesis towards agricultural and environmental applications. *Environmental Science: Nano*, *7*(12), pp.3710-3734.

33. Suvarnaphaet, P. and Pechprasarn, S., 2017. Graphene-based materials for biosensors: a review. *Sensors*, *17*(10), p.2161.

34. Uran, S., Alhani, A. and Silva, C., 2017. Study of ultraviolet-visible light absorbance of exfoliated graphite forms. *AIP Advances*, *7*(3).

35. Ning, H., Farha, F., Ullah, A. and Mao, L., 2020. Physical unclonable function: Architectures, applications and challenges for dependable security. *IET Circuits, Devices & Systems*, *14*(4), pp.407-424.

36. Kumar, S.S., Guajardo, J., Maes, R., Schrijen, G.J. and Tuyls, P., 2008, June. The butterfly PUF protecting IP on every FPGA. In *2008 IEEE International Workshop on Hardware-Oriented Security and Trust* (pp. 67-70). IEEE.

37. Guajardo, J., Kumar, S.S., Schrijen, G.J. and Tuyls, P., 2007, September. FPGA intrinsic PUFs and their use for IP protection. In *International workshop on cryptographic hardware and embedded systems* (pp. 63-80). Berlin, Heidelberg: Springer Berlin Heidelberg.

38. Pappu R, Recht B, Taylor J, Gershenfeld N. Physical one-way functions. Science 2002;297(5589):2026–2030.

39. Chen, F., Li, Q., Li, M., Huang, F., Zhang, H., Kang, J. and Wang, P., 2021. Unclonable fluorescence behaviors of perovskite quantum dots/chaotic metasurfaces hybrid nanostructures for versatile security primitive. *Chemical Engineering Journal*, *411*, p.128350.

40. Suh, G.E. and Devadas, S., 2007, June. Physical unclonable functions for device authentication and secret key generation. In *Proceedings of the 44th annual design automation conference* (pp. 9-14).

41. Gassend, B., Clarke, D., Van Dijk, M. and Devadas, S., 2002, November. Silicon physical random functions. In *Proceedings of the 9th ACM Conference on Computer and Communications Security* (pp. 148-160).

42. Guajardo, J., Kumar, S.S., Schrijen, G.J. and Tuyls, P., 2007. International workshop on cryptographic hardware and embedded systems.

43. Škorić, B., Maubach, S., Kevenaar, T. and Tuyls, P., 2006. Information-theoretic analysis of capacitive physical unclonable functions. *Journal of Applied physics*, *100*(2).

44. Lusher, A.L., Tirelli, V., O'Connor, I. and Officer, R., 2015. Microplastics in Arctic polar waters: the first reported values of particles in surface and sub-surface samples. *Scientific reports*, *5*(1), p.14947.

45. Klausen, M., Zhang, J. and Stevens, M.M., 2025. Designing Physical Unclonable Functions From Optically Active Materials. *Advanced Materials*, p.2502059.

46. Herder, C., Yu, M.D., Koushanfar, F. and Devadas, S., 2014. Physical unclonable functions and applications: A tutorial. *Proceedings of the IEEE*, *102*(8), pp.1126-1141.

47. Rührmair, U., Sehnke, F., Sölter, J., Dror, G., Devadas, S. and Schmidhuber, J., 2010, October. Modeling attacks on physical unclonable functions. In *Proceedings of the 17th ACM conference on Computer and communications security* (pp. 237-249).

48. Maes, R., 2013. Physically unclonable functions: Concept and constructions. In *Physically unclonable functions: constructions, Properties and applications* (pp. 11-48). Berlin, Heidelberg: Springer Berlin Heidelberg.

49. Fong, M.J., 2022. *Novel Physical Security Devices Exploiting the Optical Properties of Low-Dimensional Materials*. Lancaster University (United Kingdom).

50. Bera, D., Qian, L., Tseng, T.K. and Holloway, P.H., 2010. Quantum dots and their multimodal applications: a review. *Materials*, *3*(4), pp.2260-2345.

51. Klimov, V.I., 2007. Spectral and dynamical properties of multiexcitons in semiconductor nanocrystals. *Annu. Rev. Phys. Chem.*, *58*(1), pp.635-673.

52. Gan, Z., Xu, H. and Hao, Y., 2016. Mechanism for excitation-dependent photoluminescence from graphene quantum dots and other graphene oxide derivates: consensus, debates and challenges. *Nanoscale*, *8*(15), pp.7794-7807.

53. Van Dam, B., Nie, H., Ju, B., Marino, E., Paulusse, J.M., Schall, P., Li, M. and Dohnalová, K., 2017. Excitation-dependent photoluminescence from single-carbon dots. *Small*, *13*(48), p.1702098.

54. Pan, D., Zhang, J., Li, Z. and Wu, M., 2010. Hydrothermal route for cutting graphene sheets into blue-luminescent graphene quantum dots. *Advanced materials*, *22*(6), pp.734-738.

55. Folorunso, O., Olukanmi, P.O. and Shongwe, T., 2023. Progress towards sustainable energy storage: A concise review. *Engineering Reports*, *5*(11), p.e12731.

56. Xiao, P., Yun, X., Chen, Y., Guo, X., Gao, P., Zhou, G. and Zheng, C., 2023. Insights into the solvation chemistry in liquid electrolytes for lithium-based rechargeable batteries. *Chemical Society Reviews*, *52*(15), pp.5255-5316.

57. Kim, T., Song, W., Son, D.Y., Ono, L.K. and Qi, Y., 2019. Lithium-ion batteries: outlook on present, future, and hybridized technologies. *Journal of materials chemistry A*, *7*(7), pp.2942-2964.

58. Verma, P., Maire, P. and Novák, P., 2010. A review of the features and analyses of the solid electrolyte interphase in Li-ion batteries. *Electrochimica Acta*, *55*(22), pp.6332-6341.

59. Winter, M., Barnett, B. and Xu, K., 2018. Before Li ion batteries. *Chemical reviews*, *118*(23), pp.11433-11456.

60. Wieboldt, D., Ruff, I. and Hahn, M., 2015. Techniques for raman analysis of lithium-ion batteries. *Spectroscopy online. Special issues. Volume*, *30*.

61. Goodenough, J.B. and Kim, Y., 2010. Challenges for rechargeable Li batteries. *Chemistry of materials*, *22*(3), pp.587-603.

62. Cheng, H., Shapter, J.G., Li, Y. and Gao, G., 2021. Recent progress of advanced anode materials of lithium-ion batteries. *Journal of Energy Chemistry*, *57*, pp.451-468.

63. Velicky, M., Toth, P.S., Woods, C.R., Novoselov, K.S. and Dryfe, R.A., 2019. Electrochemistry of the basal plane versus edge plane of graphite revisited. *The Journal of Physical Chemistry C*, *123*(18), pp.11677-11685.

64. Agubra, V.A. and Fergus, J.W., 2014. The formation and stability of the solid electrolyte interface on the graphite anode. *Journal of Power Sources*, *268*, pp.153-162.

65. Tan, S., Ji, Y.J., Zhang, Z.R. and Yang, Y., 2014. Recent progress in research on high-voltage electrolytes for lithium-ion batteries. *ChemPhysChem*, *15*(10), pp.1956-1969.
66. Le, J.B. and Cheng, J., 2021. Modeling electrified metal/water interfaces from ab initio molecular dynamics: Structure and Helmholtz capacitance. *Current Opinion in Electrochemistry*, *27*, p.100693.
67. Lu, D., Li, R., Rahman, M.M., Yu, P., Lv, L., Yang, S., Huang, Y., Sun, C., Zhang, S., Zhang, H. and Zhang, J., 2024. Ligand-channel-enabled ultrafast Li-ion conduction. *Nature*, *627*(8002), pp.101-107.
68. Kilian, H., Pothmann, T., Lorenz, M., Middendorf, M., Seus, S., Schönhoff, M. and Roling, B., 2025. Quantification of vehicular versus uncorrelated Li+–solvent transport in highly concentrated electrolytes via solvent-related Onsager coefficients. *Physical Chemistry Chemical Physics*, *27*(3), pp.1593-1603.
69. Hirasawa, M., Orita, A., Mimuro, T. and Kondo, S.I., 2024. Unlocking the use of LiCl as an inexpensive salt for lithium-ion batteries with a novel anion receptor. *Materials*, *17*(13), p.3244.
70. Dokko, K., Watanabe, D., Ugata, Y., Thomas, M.L., Tsuzuki, S., Shinoda, W., Hashimoto, K., Ueno, K., Umebayashi, Y. and Watanabe, M., 2018. Direct evidence for Li ion hopping conduction in highly concentrated sulfolane-based liquid electrolytes. *The Journal of Physical Chemistry B*, *122*(47), pp.10736-10745.
71. von Cresce, A. and Xu, K., 2011. Preferential solvation of Li+ directs formation of interphase on graphitic anode. *Electrochemical and Solid-State Letters*, *14*(10), p.A154.
72. Sodeyama, K., Yamada, Y., Aikawa, K., Yamada, A. and Tateyama, Y., 2014. Sacrificial anion reduction mechanism for electrochemical stability improvement in highly concentrated Li-salt electrolyte. *The Journal of Physical Chemistry C*, *118*(26), pp.14091-14097.
73. Wu, Q. and Qi, Y., 2025. Revealing heterogeneous electric double layer (EDL) structures of localized high-concentration electrolytes (LHCEs) and their impact on solid–electrolyte interphase (SEI) formation in lithium batteries. *Energy & Environmental Science*, *18*(6), pp.3036-3046.

74. Hu, A., Li, F., Chen, W., Lei, T., Li, Y., Fan, Y., He, M., Wang, F., Zhou, M., Hu, Y. and Yan, Y., 2022. Ion transport kinetics in low-temperature lithium metal batteries. *Advanced Energy Materials*, *12*(42), p.2202432.
75. Wang, F. and Cheng, J., 2022. Unraveling the origin of reductive stability of super-concentrated electrolytes from first principles and unsupervised machine learning. *Chemical Science*, *13*(39), pp.11570-11576.
76. Yamada, Y., Furukawa, K., Sodeyama, K., Kikuchi, K., Yaegashi, M., Tateyama, Y. and Yamada, A., 2014. Unusual stability of acetonitrile-based superconcentrated electrolytes for fast-charging lithium-ion batteries. *Journal of the American Chemical Society*, *136*(13), pp.5039-5046.
77. Liu, M.L., Chen, B.B., Li, C.M. and Huang, C.Z., 2019. Carbon dots: synthesis, formation mechanism, fluorescence origin and sensing applications. *Green chemistry*, *21*(3), pp.449-471.
78. Hu, X., Li, Y., Xu, Y., Gan, Z., Zou, X., Shi, J., Huang, X., Li, Z. and Li, Y., 2021. Green one-step synthesis of carbon quantum dots from orange peel for fluorescent detection of Escherichia coli in milk. *Food Chemistry*, *339*, p.127775.
79. Surendran, P., Lakshmanan, A., Priya, S.S., Balakrishnan, K., Rameshkumar, P., Kannan, K., Geetha, P., Hegde, T.A. and Vinitha, G., 2020. Bioinspired fluorescence carbon quantum dots extracted from natural honey: efficient material for photonic and antibacterial applications. *Nano-Structures & Nano-Objects*, *24*, p.100589.
80. Ye, W., Yang, S., Jin, R., Liang, D., Ren, Z. and Lin, R., 2025. The reutilization of oolong tea waste: Synthesis of carbon dots and antibacterial mechanism against Staphylococcus aureus. *Food Bioscience*, *65*, p.106037.
81. Xie, Y., Cheng, D., Liu, X. and Han, A., 2019. Green hydrothermal synthesis of N-doped carbon dots from biomass highland barley for the detection of Hg2+. *Sensors*, *19*(14), p.3169.
82. Yong, C., Lei, Y., Du, J., Liu, Y., Li, Y., Ye, F., Xu, L., Ni, G. and Zhang, S., 2025. Regulation mechanisms of tea residue-based carbon dots in water-induced full-color emission and applications of visual ratio water sensors in organic solvents and WLEDs. *Analytica Chimica Acta*, *1345*, p.343763.

83. Chen, D.R. and Pui, D.Y., 1997. Experimental investigation of scaling laws for electrospraying: dielectric constant effect. *Aerosol science and technology*, *27*(3), pp.367-380.

84. Basak, S., Chen, D.R. and Biswas, P., 2007. Electrospray of ionic precursor solutions to synthesize iron oxide nanoparticles: Modified scaling law. *Chemical engineering science*, *62*(4), pp.1263-1268.

85. Wang, Z., Jia, H., Zheng, X., Yang, R., Wang, Z., Ye, G.J., Chen, X.H., Shan, J. and Feng, P.X.L., 2015. Black phosphorus nanoelectromechanical resonators vibrating at very high frequencies. *Nanoscale*, *7*(3), pp.877-884.

86. Gao, E., Lin, S.Z., Qin, Z., Buehler, M.J., Feng, X.Q. and Xu, Z., 2018. Mechanical exfoliation of two-dimensional materials. *Journal of the Mechanics and Physics of Solids*, *115*, pp.248-262.

87. Sinclair, R.C., Suter, J.L. and Coveney, P.V., 2019. Micromechanical exfoliation of graphene on the atomistic scale. *Physical Chemistry Chemical Physics*, *21*(10), pp.5716-5722.

88. Jayasena, B. and Melkote, S.N., 2015. An investigation of PDMS stamp assisted mechanical exfoliation of large area graphene. *Procedia Manufacturing*, *1*, pp.840-853.

89. Frisenda, R., Navarro-Moratalla, E., Gant, P., De Lara, D.P., Jarillo-Herrero, P., Gorbachev, R.V. and Castellanos-Gomez, A., 2018. Recent progress in the assembly of nanodevices and van der Waals heterostructures by deterministic placement of 2D materials. *Chemical Society Reviews*, *47*(1), pp.53-68.

90. Pizzocchero, F., Gammelgaard, L., Jessen, B.S., Caridad, J.M., Wang, L., Hone, J., Bøggild, P. and Booth, T.J., 2016. The hot pick-up technique for batch assembly of van der Waals heterostructures. *Nature communications*, *7*(1), p.11894.

91. Huang, Z. and Shahrjerdi, D., 2024. Advances in Engineering Toolkits for Construction of Ultralow Disordered Van der Waals Heterostructures. *Advanced Functional Materials*, *34*(29), p.2314439.

92. Fan, S., Vu, Q.A., Tran, M.D., Adhikari, S. and Lee, Y.H., 2020. Transfer assembly for two-dimensional van der Waals heterostructures. *2D Materials*, *7*(2), p.022005.

93. Castellanos-Gomez, A., Buscema, M., Molenaar, R., Singh, V., Janssen, L., Van Der Zant, H.S. and Steele, G.A., 2014. Deterministic transfer of two-

dimensional materials by all-dry viscoelastic stamping. *2D Materials*, *1*(1), p.011002.

94. Jain, A., Bharadwaj, P., Heeg, S., Parzefall, M., Taniguchi, T., Watanabe, K. and Novotny, L., 2018. Minimizing residues and strain in 2D materials transferred from PDMS. *Nanotechnology*, *29*(26), p.265203.

95. Dresselhaus, M.S. and Dresselhaus, G., 1981. Intercalation compounds of graphite. *Advances in Physics*, *30*(2), pp.139-326.

96. Pierson, H.O., 2012. *Handbook of carbon, graphite, diamonds and fullerenes: processing, properties and applications*. William Andrew.

97. Peng, Z., Yang, R., Kim, M.A., Li, L. and Liu, H., 2017. Influence of O 2, H 2 O and airborne hydrocarbons on the properties of selected 2D materials. *RSC advances*, *7*(43), pp.27048-27057.

98. Ni, Z.H., Wang, H.M., Kasim, J., Fan, H.M., Yu, T., Wu, Y.H., Feng, Y.P. and Shen, Z.X., 2007. Graphene thickness determination using reflection and contrast spectroscopy. *Nano letters*, *7*(9), pp.2758-2763.

99. Bing D, Wang Y, Bai J, Du R, Wu G, Liu L. Optical contrast for identifying the thickness of two-dimensional materials. Optics Communications 2018; 406:128–138.

100. Li, H., Wu, J., Huang, X., Lu, G., Yang, J., Lu, X., Xiong, Q. and Zhang, H., 2013. Rapid and reliable thickness identification of two-dimensional nanosheets using optical microscopy. *ACS nano*, *7*(11), pp.10344-10353.

101. Gomes, A.J., Lunardi, C.N., Rocha, F.S. and Patience, G.S., 2019. Experimental methods in chemical engineering: Fluorescence emission spectroscopy. *The Canadian Journal of Chemical Engineering*, *97*(8), pp.2168-2175.

102. Li, H., Kang, Z., Liu, Y. and Lee, S.T., 2012. Carbon nanodots: synthesis, properties and applications. *Journal of materials chemistry*, *22*(46), pp.24230-24253.

103. Zhu, S., Song, Y., Zhao, X., Shao, J., Zhang, J. and Yang, B., 2015. The photoluminescence mechanism in carbon dots (graphene quantum dots, carbon nanodots, and polymer dots): current state and future perspective. *Nano research*, *8*(2), pp.355-381.

104. Sun, Y.P., Zhou, B., Lin, Y., Wang, W., Fernando, K.S., Pathak, P., Meziani, M.J., Harruff, B.A., Wang, X., Wang, H. and Luo, P.G., 2006. Quantum-sized

carbon dots for bright and colorful photoluminescence. *Journal of the American Chemical Society*, *128*(24), pp.7756-7757.

105. Klausen, M., Zhang, J. and Stevens, M.M., 2025. Designing Physical Unclonable Functions From Optically Active Materials. *Advanced Materials*, p.2502059.

106. Pan, L., Wei, Y., Wang, J. and Ma, X., 2026. Architected Nanomaterials Powering Optical Physical Unclonable Functions. *Laser & Photonics Reviews*, p.e01958.

107. Lin, X., Shi, D., Yi, G. and Yu, D., 2024. Structural color-based physical unclonable function. *Responsive Materials*, *2*(1), p.e20230031.

108. Liu, Y., Han, F., Li, F., Zhao, Y., Chen, M., Xu, Z., Zheng, X., Hu, H., Yao, J., Guo, T. and Lin, W., 2019. Inkjet-printed unclonable quantum dot fluorescent anti-counterfeiting labels with artificial intelligence authentication. *Nature communications*, *10*(1), p.2409.

109. Ali SR, Kershaw SV, Faisal MM, Halak B, Abdelazim NM. Illuminating Advances in Materials: Optical Physical Unclonable Functions for Security Applications. Advanced Optical Materials 2025;13.

110. Hardman, R., 2005. A toxicologic review of quantum dots: toxicity depends on physicochemical and environmental factors. *Environmental health perspectives*, *114*(2), p.165.

111. Aftab, S., Ali, Z., Hussain, M.I., Assiri, M.A., Rubab, N., Ozel, F. and Akman, E., 2025. Perovskite Quantum Dots: Fabrication, Degradation, and Enhanced Performance Across Solar Cells, Optoelectronics, and Quantum Technologies. *Carbon Energy*, p.e70018.

112. Suvarnaphaet, P. and Pechprasarn, S., 2017. Graphene-based materials for biosensors: a review. Sensors, 17(10), p.2161.

113. Bressi, V., Ferlazzo, A., Iannazzo, D. and Espro, C., 2021. Graphene quantum dots by eco-friendly green synthesis for electrochemical sensing: Recent advances and future perspectives. *Nanomaterials*, *11*(5), p.1120.

114. Li, L.L., Ji, J., Fei, R., Wang, C.Z., Lu, Q., Zhang, J.R., Jiang, L.P. and Zhu, J.J., 2012. A facile microwave avenue to electro chemiluminescent two-colour graphene quantum dots. *Advanced Functional Materials*, *22*(14), pp.2971-2979.

115. Tetsuka, H., Asahi, R., Nagoya, A., Okamoto, K., Tajima, I., Ohta, R. and Okamoto, A., 2012. Optically tunable amino-functionalized graphene quantum dots. *Advanced Materials (Deerfield Beach, Fla.)*, *24*(39), pp.5333-5338.
116. Zhao, J., Zheng, Y., Pang, Y., Chen, J., Zhang, Z., Xi, F. and Chen, P., 2020. Graphene quantum dots as full-color and stimulus responsive fluorescence ink for information encryption. *Journal of Colloid and Interface Science*, *579*, pp.307-314.
117. Kalytchuk, S., Wang, Y., Poláková, K. and Zboril, R., 2018. Carbon dot fluorescence-lifetime-encoded anti-counterfeiting. *ACS applied materials & interfaces*, *10*(35), pp.29902-29908.
118. Li, C., Jiao, F., Dong, L., Hu, J., Ma, X., Lou, Q., Chen, X., Xu, W., Zhu, Y. and Zhu, J., 2025. Time-Division Multiplexing Physical Unclonable Functions Based on Multicolor Phosphorescent Carbon Dots. *Advanced Materials*, p.2502522.
119. Wang, B., Yu, J., Sui, L., Zhu, S., Tang, Z., Yang, B. and Lu, S., 2021. Rational design of multi-color-emissive carbon dots in a single reaction system by hydrothermal. *Advanced science*, *8*(1), p.2001453.
120. Carpio, A.R.E., Juan-Corpuz, L.M.D. and Corpuz, R.D., 2025. Next-generation anti-counterfeit security using carbon nanodots: Tunable luminescence and sustainable ink design—A review. *Journal of the Chinese Chemical Society*.
121. Abbas, A., Tabish, T.A., Bull, S.J., Lim, T.M. and Phan, A.N., 2020. High yield synthesis of graphene quantum dots from biomass waste as a highly selective probe for Fe3+ sensing. *Scientific reports*, *10*(1), p.21262.
122. Inayat, A., Albalawi, K., Rehman, A.U., Saad, A.Y., Saleh, E.A.M., Alamri, M.A., El-Zahhar, A.A., Haider, A. and Abbas, S.M., 2023. Tunable synthesis of carbon quantum dots from the biomass of spent tea leaves as supercapacitor electrode. *Materials Today Communications*, *34*, p.105479.
123. Facure, M.H., Schneider, R., Mercante, L.A. and Correa, D.S., 2020. A review on graphene quantum dots and their nanocomposites: from laboratory synthesis towards agricultural and environmental applications. *Environmental Science: Nano*, *7*(12), pp.3710-3734.
124. Bao, L., Liu, C., Zhang, Z.L. and Pang, D.W., 2015. Photoluminescence-tunable carbon nanodots: surface-state energy-gap tuning. *Advanced Materials*, *27*(10), pp.1663-1667.

125. Iravani, S. and Varma, R.S., 2020. Green synthesis, biomedical and biotechnological applications of carbon and graphene quantum dots. A review. *Environmental chemistry letters*, *18*(3), pp.703-727.

126. Kang, X., Jiang, K., Ge, S., Wei, K., Zhou, Y., Xu, B.B., Wang, K. and Zhang, X., 2025. Frontier in Advanced Luminescent Biomass Nanocomposites for Surface Anticounterfeiting. *ACS nano*, *19*(12), pp.11547-11575.

127. Sun, W., Bai, L., Chi, M., Xu, X., Chen, Z. and Yu, K., 2023. Study on the evolution pattern of the aromatics of lignin during hydrothermal carbonization. *Energies*, *16*(3), p.1089.

128. Gao, S., Zhang, P., Xu, L., Lian, H. and Xu, C., 2025. Hydrothermal formation mechanism of lignocellulose-derived carbon dots: From sawdust to carbon nanomaterials with blue fluorescence. *Bioresource Technology*, *429*, p.132493.

129. Liu, M., 2020. Optical properties of carbon dots: a review. *Nanoarchitectonics*, pp.1-12.

130. Huang, X., Ye, W., Zhuang, J., Hu, C., Dong, H., Lei, B. and Liu, Y., 2024. π-Conjugated structure enhances the UV absorption performance of carbon dots and application in the design of light-colored sunglasses. *ACS sustainable chemistry & engineering*, *12*(28), pp.10399-10410.

131. Song, P., Zhang, L., Long, H., Meng, M., Liu, T., Yin, Y. and Xi, R., 2017. A multianalyte fluorescent carbon dots sensing system constructed based on specific recognition of Fe (III) ions. *RSC advances*, *7*(46), pp.28637-28646.

132. Wang, L., Li, W., Wu, B., Li, Z., Wang, S., Liu, Y., Pan, D. and Wu, M., 2016. Facile synthesis of fluorescent graphene quantum dots from coffee grounds for bioimaging and sensing. *Chemical Engineering Journal*, *300*, pp.75-82.

133. Shi, L., Zhao, B., Li, X., Zhang, G., Zhang, Y., Dong, C. and Shuang, S., 2017. Green-fluorescent nitrogen-doped carbon nanodots for biological imaging and paper-based sensing. *Analytical Methods*, *9*(14), pp.2197-2204.

134. Li, H., Kang, Z., Liu, Y. and Lee, S.T., 2012. Carbon nanodots: synthesis, properties and applications. *Journal of materials chemistry*, *22*(46), pp.24230-24253.

135. He, C., Xu, P., Zhang, X. and Long, W., 2022. The synthetic strategies, photoluminescence mechanisms and promising applications of carbon dots: Current state and future perspective. *Carbon*, *186*, pp.91-127.

136. Tuinstra, F. and Koenig, J.L., 1970. Raman spectrum of graphite. *The Journal of chemical physics*, *53*(3), pp.1126-1130.

137. Ferrari, A.C. and Robertson, J., 2000. Interpretation of Raman spectra of disordered and amorphous carbon. *Physical review B*, *61*(20), p.14095.

138. Ferrari, A.C. and Basko, D.M., 2013. Raman spectroscopy as a versatile tool for studying the properties of graphene. *Nature nanotechnology*, *8*(4), pp.235-246.

139. Hola, K., Zhang, Y., Wang, Y., Giannelis, E.P., Zboril, R. and Rogach, A.L., 2014. Carbon dots—Emerging light emitters for bioimaging, cancer therapy and optoelectronics. *Nano Today*, *9*(5), pp.590-603.

140. Hasan, M.T., Gonzalez-Rodriguez, R., Ryan, C., Pota, K., Green, K., Coffer, J.L. and Naumov, A.V., 2019. Nitrogen-doped graphene quantum dots: Optical properties modification and photovoltaic applications. *Nano Research*, *12*(5), pp.1041-1047.

141. Lim, S.Y., Shen, W. and Gao, Z., 2015. Carbon quantum dots and their applications. *Chemical Society Reviews*, *44*(1), pp.362-381.

142. Sun, Y.P., Zhou, B., Lin, Y., Wang, W., Fernando, K.S., Pathak, P., Meziani, M.J., Harruff, B.A., Wang, X., Wang, H. and Luo, P.G., 2006. Quantum-sized carbon dots for bright and colorful photoluminescence. *Journal of the American Chemical Society*, *128*(24), pp.7756-7757.

143. Kaur, M., Kaur, M. and Sharma, V.K., 2018. Nitrogen-doped graphene and graphene quantum dots: A review onsynthesis and applications in energy, sensors and environment. *Advances in colloid and interface science*, *259*, pp.44-64.

144. Cervetti, C., Rettori, A., Pini, M.G., Cornia, A., Repollés, A., Luis, F., Dressel, M., Rauschenbach, S., Kern, K., Burghard, M. and Bogani, L., 2016. The classical and quantum dynamics of molecular spins on graphene. *Nature materials*, *15*(2), pp.164-168.

145. Boukellal, Y., Ducourtieux, S. and Poyet, B., 2013. Improvement of the LNE's metrological Atomic Force Microscope (mAFM) performance: Design of new mAFM head dedicated for nanometrology applications. In *16th International Congress of Metrology* (p. 06008). EDP Sciences.

146. Kiss, L.B., Söderlund, J., Niklasson, G.A. and Granqvist, C.G., 1999. The real origin of lognormal size distributions of nanoparticles in vapor growth processes. *Nanostructured Materials*, *12*(1-4), pp.327-332.

147. THECHARMSOFS, O., BILITY—NORMAL, V.R.R.B., LOG, O. and AT, T., 2001. L og-no rmal Distributions across the Sciences: Keys and Clues. *BioScience*, *51*(5).

148. Novoselov, K.S., Geim, A.K., Morozov, S.V., Jiang, D.E., Zhang, Y., Dubonos, S.V., Grigorieva, I.V. and Firsov, A.A., 2004. Electric field effect in atomically thin carbon films. *science*, *306*(5696), pp.666-669.

149. Nanda, S.S., Kim, M.J., Yeom, K.S., An, S.S.A., Ju, H. and Yi, D.K., 2016. Raman spectrum of graphene with its versatile future perspectives. *TrAC Trends in Analytical Chemistry*, *80*, pp.125-131.

150. Nemes-Incze, P., Osváth, Z., Kamarás, K. and Biró, L.P., 2008. Anomalies in thickness measurements of graphene and few layer graphite crystals by tapping mode atomic force microscopy. *Carbon*, *46*(11), pp.1435-1442.

151. Jin, S.H., Kim, D.H., Jun, G.H., Hong, S.H. and Jeon, S., 2013. Tuning the photoluminescence of graphene quantum dots through the charge transfer effect of functional groups. *ACS nano*, *7*(2), pp.1239-1245.

152. Sun, J., He, Y. and Wang, L., 2017. Enzyme-free fluorescence sensing of catechins in green tea using bifunctional graphene quantum dots. *Analytical Methods*, *9*(23), pp.3525-3530.

153. Abbas, A., Rubab, S., Rehman, A., Irfan, S., Sharif, H.M.A., Liang, Q. and Tabish, T.A., 2023. One-step green synthesis of biomass-derived graphene quantum dots as a highly selective optical sensing probe. *Materials Today Chemistry*, *30*, p.101555.

154. Gedda, G., Lee, C.Y., Lin, Y.C. and Wu, H.F., 2016. Green synthesis of carbon dots from prawn shells for highly selective and sensitive detection of copper ions. *Sensors and Actuators B: Chemical*, *224*, pp.396-403.

155. Shi, L., Zhao, B., Li, X., Zhang, G., Zhang, Y., Dong, C. and Shuang, S., 2017. Green-fluorescent nitrogen-doped carbon nanodots for biological imaging and paper-based sensing. *Analytical Methods*, *9*(14), pp.2197-2204.

156. Hola, K., Zhang, Y., Wang, Y., Giannelis, E.P., Zboril, R. and Rogach, A.L., 2014. Carbon dots—Emerging light emitters for bioimaging, cancer therapy and optoelectronics. *Nano Today*, *9*(5), pp.590-603.

157. Gaurav, A., Jain, A. and Tripathi, S.K., 2022. Review on fluorescent carbon/graphene quantum dots: promising material for energy storage and next-generation light-emitting diodes. *Materials*, *15*(22), p.7888.

158. Yang, A., Su, Y., Zhang, Z., Wang, H., Qi, C., Ru, S. and Wang, J., 2022. Preparation of graphene quantum dots by visible-fenton reaction and ultrasensitive label-free immunosensor for detecting lipovitellin of paralichthys olivaceus. *Biosensors*, *12*(4), p.246.

159. Sharma, A., Gadly, T., Gupta, A., Ballal, A., Ghosh, S.K. and Kumbhakar, M., 2016. Origin of excitation dependent fluorescence in carbon nanodots. *The journal of physical chemistry letters*, *7*(18), pp.3695-3702.

160. Sciortino, A., Cannizzo, A. and Messina, F., 2018. Carbon nanodots: a review—from the current understanding of the fundamental photophysics to the full control of the optical response. *C*, *4*(4), p.67.

161. Sun, S., Zhang, L., Jiang, K., Wu, A. and Lin, H., 2016. Toward high-efficient red emissive carbon dots: facile preparation, unique properties, and applications as multifunctional theranostic agents. *Chemistry of Materials*, *28*(23), pp.8659-8668.

162. Zhang, B., Wang, B., Ushakova, E.V., He, B., Xing, G., Tang, Z., Rogach, A.L. and Qu, S., 2023. Assignment of core and surface states in multicolor-emissive carbon dots. *Small*, *19*(31), p.2204158.

163. Alafeef, M., Srivastava, I., Aditya, T. and Pan, D., 2024. Carbon dots: from synthesis to unraveling the fluorescence mechanism. *Small*, *20*(4), p.2303937.

164. Zheng, W.X., Li, T.X., Xie, Y.H., Lv, Y.D., Xie, D.L. and Wu, F., 2025. Preparation of multi-colored carbon dots via pH-controlled degradation of wheat bran/o-phenylenediamine for Fe 3+ ion detection. *RSC advances*, *15*(15), pp.12028-12041.

165. Tepliakov, N.V., Kundelev, E.V., Khavlyuk, P.D., Xiong, Y., Leonov, M.Y., Zhu, W., Baranov, A.V., Fedorov, A.V., Rogach, A.L. and Rukhlenko, I.D., 2019. sp2–sp3-Hybridized atomic domains determine optical features of carbon dots. *ACS nano*, *13*(9), pp.10737-10744.

166. Mei, Q., Liu, B., Han, G., Liu, R., Han, M.Y. and Zhang, Z., 2019. Graphene oxide: from tunable structures to diverse luminescence behaviors. *Advanced science*, *6*(14), p.1900855.

167. Ding, H., Li, X.H., Chen, X.B., Wei, J.S., Li, X.B. and Xiong, H.M., 2020. Surface states of carbon dots and their influences on luminescence. *Journal of Applied Physics*, *127*(23).

168. Zhao, B., Ma, H., Zheng, M., Xu, K., Zou, C., Qu, S. and Tan, Z.A., 2022. Narrow-bandwidth emissive carbon dots: A rising star in the fluorescent material family. *Carbon Energy*, *4*(1), pp.88-114.

169. Van Dam, B., Nie, H., Ju, B., Marino, E., Paulusse, J.M., Schall, P., Li, M. and Dohnalová, K., 2017. Excitation-dependent photoluminescence from single-carbon dots. *Small*, *13*(48), p.1702098.

170. Li, D., Ushakova, E.V., Rogach, A.L. and Qu, S., 2021. Optical properties of carbon dots in the deep-red to near-infrared region are attractive for biomedical applications. *Small*, *17*(43), p.2102325.

171. Li, X., Rui, M., Song, J., Shen, Z. and Zeng, H., 2015. Carbon and graphene quantum dots for optoelectronic and energy devices: a review. *Advanced Functional Materials*, *25*(31), pp.4929-4947.

172. Li, H., Kang, Z., Liu, Y. and Lee, S.T., 2012. Carbon nanodots: synthesis, properties and applications. *Journal of materials chemistry*, *22*(46), pp.24230-24253.

173. Yogesh, G.K., Shuaib, E.P. and Sastikumar, D., 2017. Photoluminescence properties of carbon nanoparticles synthesized from activated carbon powder (4% ash) by laser ablation in solution. *Materials Research Bulletin*, *91*, pp.220-226.

174. Mann-Andrews, E., McGrath, T., Halliday, B. and Young, R.J., 2025. A guide for assessing optically imaged physically unclonable functions for authentication. *Applied Physics Reviews*, *12*(2).

175. Tillich, J.P. and Zemor, G., 2009. Proceedings of the IEEE International Symposium on Information Theory (ISIT).

176. Meijs, Z.C., Yun, H.S., Fandre, P., Park, G., Yoon, D.K. and Isa, L., 2023. Pixelated physical unclonable functions through capillarity-assisted particle assembly. *ACS Applied Materials & Interfaces*, *15*(45), pp.53053-53061.

177. Liu, Y., Han, F., Li, F., Zhao, Y., Chen, M., Xu, Z., Zheng, X., Hu, H., Yao, J., Guo, T. and Lin, W., 2019. Inkjet-printed unclonable quantum dot fluorescent

anti-counterfeiting labels with artificial intelligence authentication. *Nature communications*, *10*(1), p.2409.

178. Wang, H., Ai, L., Song, H., Song, Z., Yong, X., Qu, S. and Lu, S., 2023. Innovations in the solid-state fluorescence of carbon dots: strategies, optical manipulations, and applications. *Advanced Functional Materials*, *33*(41), p.2303756.
179. Kaniyankandy, S., Rawalekar, S. and Ghosh, H.N., 2012. Ultrafast charge transfer dynamics in photoexcited CdTe quantum dot decorated on graphene. *The Journal of Physical Chemistry C*, *116*(30), pp.16271-16275.
180. Mandal, T., Mishra, S.R. and Singh, V., 2023. Comprehensive advances in the synthesis, fluorescence mechanism and multifunctional applications of red-emitting carbon nanomaterials. *Nanoscale Advances*, *5*(21), pp.5717-5765.
181. Shang, J., Ma, L., Li, J., Ai, W., Yu, T. and Gurzadyan, G.G., 2012. The origin of fluorescence from graphene oxide. *Scientific reports*, *2*(1), p.792.
182. Sk, M.A., Ananthanarayanan, A., Huang, L., Lim, K.H. and Chen, P., 2014. Revealing the tunable photoluminescence properties of graphene quantum dots. *Journal of Materials Chemistry C*, *2*(34), pp.6954-6960.
183. Deegan, R.D., Bakajin, O., Dupont, T.F., Huber, G., Nagel, S.R. and Witten, T.A., 1997. Capillary flow as the cause of ring stains from dried liquid drops. *Nature*, *389*(6653), pp.827-829.
184. Peng, T., Thorn, K., Schroeder, T., Wang, L., Theis, F.J., Marr, C. and Navab, N., 2017. A BaSiC tool for background and shading correction of optical microscopy images. *Nature communications*, *8*(1), p.14836.
185. Gonzalez RC. Digital image processing.: Pearson education india; 2009.
186. Woebbecke, D.M., Meyer, G.E., Bargen, K.V. and Mortensen, D.A., 1994. Color indices for weed identification under various soil, residue, and lighting conditions.
187. Otsu, N., 1975. A threshold selection method from gray-level histograms. *Automatica*, *11*(285-296), pp.23-27.
188. Jafari Mamaghani, M., Andersson, M. and Krieger, P., 2010. Spatial point pattern analysis of neurons using Ripley's K-function in 3D. *Frontiers in neuroinformatics*, *4*, p.1285.
189. Peiss, C.N., 1989. Evaporation of small water drops maintained at constant volume. *Journal of applied physics*, *65*(12), pp.5235-5237.

190. Shakoor, M.H. and Boostani, R., 2018. Radial mean local binary pattern for noisy texture classification. *Multimedia Tools and Applications*, *77*(16), pp.21481-21508.

191. Li, Q., Chen, F., Kang, J., Wang, P., Su, J., Huang, F., Li, M. and Zhang, J., 2022. Intrinsic random optical features of the electronic packages as physical unclonable functions for Internet of Things security. *Advanced Photonics Research*, *3*(6), p.2100207.

192. Kwak, J.K., Moon, C., Yu, H.B., Kim, S. and Kim, D.H., 2026. All-Optical Reconfigurable Physical Unclonable Function for Sustainable Security. *Advanced Materials*, p.e21712.

193. Rhodes, D., Chae, S.H., Ribeiro-Palau, R. and Hone, J., 2019. Disorder in van der Waals heterostructures of 2D materials. *Nature materials*, *18*(6), pp.541-549.

194. Fang, H., Tosun, M., Seol, G., Chang, T.C., Takei, K., Guo, J. and Javey, A., 2013. Degenerate n-doping of few-layer transition metal dichalcogenides by potassium. *Nano letters*, *13*(5), pp.1991-1995.

195. Liu, Y., Weiss, N.O., Duan, X., Cheng, H.C., Huang, Y. and Duan, X., 2016. Van der Waals heterostructures and devices. *Nature Reviews Materials*, *1*(9), pp.1-17.

196. Yu, W.J., Liu, Y., Zhou, H., Yin, A., Li, Z., Huang, Y. and Duan, X., 2013. Highly efficient gate-tunable photocurrent generation in vertical heterostructures of layered materials. *Nature nanotechnology*, *8*(12), pp.952-958.

197. Cao, Y., Robson, A.J., Alharbi, A., Roberts, J., Woodhead, C.S., Noori, Y.J., Bernardo-Gavito, R., Shahrjerdi, D., Roedig, U., Fal’ko, V.I. and Young, R.J., 2017. Optical identification using imperfections in 2D materials. *2D Materials*, *4*(4), p.045021.

198. Ren, Y., Sun, C.H., De Silva, M., Pan, H., Nie, X., Hamdan, E., Zhou, Z., Cetin, A.E. and Chen, P.Y., 2025. Reconfigurable Electromagnetically Unclonable Functions Based on Graphene Radio-Frequency Modulators. *ACS nano*, *20*(1), pp.421-431.

199. Ali, S.R., Kershaw, S.V., Faisal, M.M., Halak, B. and Abdelazim, N.M., 2025. Illuminating advances in materials: optical physical unclonable functions for security applications. *Advanced Optical Materials*, *13*(29), p.e01564.

200. Alharbi, A., Armstrong, D., Alharbi, S. and Shahrjerdi, D., 2017. Physically unclonable cryptographic primitives by chemical vapor deposition of layered MoS2. *ACS nano*, *11*(12), pp.12772-12779.

201. Lee, S., Pekdemir, S., Kayaci, N., Kalay, M., Onses, M.S. and Ye, J., 2023. Graphene-based physically unclonable functions with dual source of randomness. *ACS applied materials & interfaces*, *15*(28), pp.33878-33889.

202. Feng, X., Tao, H., Yang, S., Liu, C., Wei, C., Wang, Y., Zhao, H., Yao, S. and Cheng, Z., 2025. Recent Advances of Plasma Technology Applications in 2D Materials and Electronics. *Advanced Materials Technologies*, p.2402207.

203. Duan, J., Li, G., Xiong, Y., Zhu, X., Chen, Y., Liu, W., Xu, X., Shum, P.P., Hao, Q. and Wang, J., 2025. Scalable plasmonic physical unclonable functions empowered by a multi-dimensional expanding strategy. *Advanced Photonics Nexus*, *4*(1), pp.016003-016003.

204. Goorden, S.A., Horstmann, M.A.R.C.E.L.L., Mosk, A.P., Škorić, B.O.R.I.S. and Pinkse, P.W., Quantum-secure authentication of a physical unclonable key: supplementary material. *Quantum*, *9*(10).

205. Škorić, B., 2012. Quantum readout of physical unclonable functions. *International Journal of Quantum Information*, *10*(01), p.1250001.

206. Abdelazim, N.M., Fong, M.J., McGrath, T., Woodhead, C.S., Al-Saymari, F., Bagci, I.E., Jones, A.T., Wang, X. and Young, R.J., 2021. Hotspot generation for unique identification with nanomaterials. *Scientific Reports*, *11*(1), p.1528.

207. Roddaro, S., Pingue, P., Piazza, V., Pellegrini, V. and Beltram, F., 2007. The optical visibility of graphene: interference colors of ultrathin graphite on SiO2. *Nano letters*, *7*(9), pp.2707-2710.

208. Lee, C., Yan, H., Brus, L.E., Heinz, T.F., Hone, J. and Ryu, S., 2010. Anomalous lattice vibrations of single-and few-layer MoS2. *ACS nano*, *4*(5), pp.2695-2700.

209. Carvalho, B.R., Wang, Y., Mignuzzi, S., Roy, D., Terrones, M., Fantini, C., Crespi, V.H., Malard, L.M. and Pimenta, M.A., 2017. Intervalley scattering by acoustic phonons in two-dimensional MoS2 revealed by double-resonance Raman spectroscopy. *Nature communications*, *8*(1), p.14670.

210. Li, S.L., Miyazaki, H., Song, H., Kuramochi, H., Nakaharai, S. and Tsukagoshi, K., 2012. Quantitative Raman spectrum and reliable thickness identification for atomic layers on insulating substrates. *ACS nano*, *6*(8), pp.7381-7388.

211. Zhang, X., Han, W.P., Wu, J.B., Milana, S., Lu, Y., Li, Q.Q., Ferrari, A.C. and Tan, P.H., 2013. Raman spectroscopy of shear and layer breathing modes in multilayer MoS 2. *Physical Review B—Condensed Matter and Materials Physics*, *87*(11), p.115413.

212. Li, H., Zhang, Q., Yap, C.C.R., Tay, B.K., Edwin, T.H.T., Olivier, A. and Baillargeat, D., 2012. From bulk to monolayer MoS2: evolution of Raman scattering. *Advanced Functional Materials*, *22*(7), pp.1385-1390.

213. Yin, Z., Li, H., Li, H., Jiang, L., Shi, Y., Sun, Y., Lu, G., Zhang, Q., Chen, X. and Zhang, H., 2012. Single-layer MoS2 phototransistors. *ACS nano*, *6*(1), pp.74-80.

214. Ferrari, A.C., Meyer, J.C., Scardaci, V., Casiraghi, C., Lazzeri, M., Mauri, F., Piscanec, S., Jiang, D., Novoselov, K.S., Roth, S. and Geim, A.K., 2006. Raman spectrum of graphene and graphene layers. *Physical review letters*, *97*(18), p.187401.

215. Malard, L.M., Pimenta, M.A., Dresselhaus, G. and Dresselhaus, M.S., 2009. Raman spectroscopy in graphene. *Physics reports*, *473*(5-6), pp.51-87.

216. Ferrari, A.C. and Basko, D.M., 2013. Raman spectroscopy as a versatile tool for studying the properties of graphene. *Nature nanotechnology*, *8*(4), pp.235-246.

217. Das, A., Pisana, S., Chakraborty, B., Piscanec, S., Saha, S.K., Waghmare, U.V., Novoselov, K.S., Krishnamurthy, H.R., Geim, A.K., Ferrari, A.C. and Sood, A.K., 2008. Monitoring dopants by Raman scattering in an electrochemically top-gated graphene transistor. *Nature nanotechnology*, *3*(4), pp.210-215.

218. Gupta, S., Johnston, A. and Khondaker, S., 2022. Optoelectronic Properties of MoS 2/Graphene Heterostructures Prepared by Dry Transfer for Light-Induced Energy Applications. *Journal of Electronic Materials*, *51*(8).

219. Zhou KG, Withers F, Cao Y, Hu S, Yu G, Casiraghi C. Raman modes of MoS2 used as fingerprint of van der Waals interactions in 2-D crystal-based heterostructures. ACS nano 2014;8(10):9914–9924.

220. Cao, Y., Wang, Z., Bian, Q., Cheng, Z., Shao, Z., Zhang, Z., Sun, H., Zhang, X., Li, S., Gedeon, H. and Liu, L., 2019. Phonon modes and photonic excitation transitions of MoS2 induced by top-deposited graphene revealed by Raman spectroscopy and photoluminescence. *Applied Physics Letters*, *114*(13).

221. Yang, M., Wang, L., Hu, G., Chen, X., Gong, P.L., Cong, X., Liu, Y., Yang, Y., Li, X., Zhao, X. and Liu, X., 2021. Optical identification of interlayer coupling of graphene/MoS2 van der Waals heterostructures. *Nano Research*, *14*(7), pp.2241-2246.

222. Wang, Z., Chen, Q. and Wang, J., 2015. Electronic structure of twisted bilayers of graphene/MoS2 and MoS2/MoS2. *The Journal of Physical Chemistry C*, *119*(9), pp.4752-4758.

223. Rao, R., Islam, A.E., Singh, S., Berry, R., Kawakami, R.K., Maruyama, B. and Katoch, J., 2019. Spectroscopic evaluation of charge-transfer doping and strain in graphene/MoS 2 heterostructures. *Physical Review B*, *99*(19), p.195401.

224. Fang, Q., Li, M., Zhao, X., Yuan, L., Wang, B., Xia, C. and Ma, F., 2022. van der Waals graphene/MoS 2 heterostructures: tuning the electronic properties and Schottky barrier by applying a biaxial strain. *Materials Advances*, *3*(1), pp.624-631.

225. Yang, M., Wang, L., Hu, G., Chen, X., Gong, P.L., Cong, X., Liu, Y., Yang, Y., Li, X., Zhao, X. and Liu, X., 2021. Optical identification of interlayer coupling of graphene/MoS2 van der Waals heterostructures. *Nano Research*, *14*(7), pp.2241-2246

226. Gupta, S., Johnston, A. and Khondaker, S., 2022. Optoelectronic Properties of MoS 2/Graphene Heterostructures Prepared by Dry Transfer for Light-Induced Energy Applications. *Journal of Electronic Materials*, *51*(8).

227. Han, T., Liu, H., Wang, S., Chen, S., Yang, K. and Li, Z., 2021. Synthesis and Spectral Characteristics Investigation of the 2D-2D vdWs Heterostructure Materials. *International Journal of Molecular Sciences*, *22*(3), p.1246.

228. Mak, K.F., He, K., Lee, C., Lee, G.H., Hone, J., Heinz, T.F. and Shan, J., 2013. Tightly bound trions in monolayer MoS2. *Nature materials*, *12*(3), pp.207-211.

229. Zhumagulov, Y.V., Vagov, A., Gulevich, D.R., Faria Junior, P.E. and Perebeinos, V., 2020. Trion induced photoluminescence of a doped MoS2 monolayer. *The Journal of Chemical Physics*, *153*(4).

230. Fang, H., Battaglia, C., Carraro, C., Nemsak, S., Ozdol, B., Kang, J.S., Bechtel, H.A., Desai, S.B., Kronast, F., Unal, A.A. and Conti, G., 2014. Strong interlayer coupling in van der Waals heterostructures built from single-layer chalcogenides. *Proceedings of the National Academy of Sciences*, *111*(17), pp.6198-6202.

231. Golovynskyi, S., Datsenko, O.I., Dong, D., Lin, Y., Irfan, I., Li, B., Lin, D. and Qu, J., 2021. Trion binding energy variation on photoluminescence excitation energy and power during direct to indirect bandgap crossover in monolayer and few-layer MoS2. *The Journal of Physical Chemistry C*, *125*(32), pp.17806-17819.

232. Ross, J.S., Wu, S., Yu, H., Ghimire, N.J., Jones, A.M., Aivazian, G., Yan, J., Mandrus, D.G., Xiao, D., Yao, W. and Xu, X., 2013. Electrical control of neutral and charged excitons in a monolayer semiconductor. *Nature communications*, *4*(1), p.1474.

233. Mouri, S., Miyauchi, Y. and Matsuda, K., 2013. Tunable photoluminescence of monolayer MoS2 via chemical doping. *Nano letters*, *13*(12), pp.5944-5948.

234. Raja, A., Chaves, A., Yu, J., Arefe, G., Hill, H.M., Rigosi, A.F., Berkelbach, T.C., Nagler, P., Schüller, C., Korn, T. and Nuckolls, C., 2017. Coulomb engineering of the bandgap and excitons in two-dimensional materials. *Nature communications*, *8*(1), p.15251.

235. Han, T., Liu, H., Chen, S., Wang, S. and Yang, K., 2021. Construction and electrical performance improvement of MoS2 FET with graphene/metal contact. *Optical Materials Express*, *11*(9), pp.3099-3110.

236. Liu, Y., Shen, T., Linghu, S., Zhu, R. and Gu, F., 2022. Electrostatic control of photoluminescence from A and B excitons in monolayer molybdenum disulfide. *Nanoscale Advances*, *4*(11), pp.2484-2493.

237. Newaz, A.K.M., Prasai, D., Ziegler, J.I., Caudel, D., Robinson, S., Haglund Jr, R.F. and Bolotin, K.I., 2013. Electrical control of optical properties of monolayer MoS2. *Solid State Communications*, *155*, pp.49-52.

238. Han, T., Liu, H., Chen, S., Wang, S. and Yang, K., 2021. Construction and electrical performance improvement of MoS2 FET with graphene/metal contact. *Optical Materials Express*, *11*(9), pp.3099-3110.

239. Ghatak, S., Pal, A.N. and Ghosh, A., 2011. Nature of electronic states in atomically thin MoS2 field-effect transistors. *ACS nano*, *5*(10), pp.7707-7712.

240. Mouri, S., Miyauchi, Y. and Matsuda, K., 2013. Tunable photoluminescence of monolayer MoS2 via chemical doping. *Nano letters*, *13*(12), pp.5944-5948.

241. Borys, N.J., Barnard, E.S., Gao, S., Yao, K., Bao, W., Buyanin, A., Zhang, Y., Tongay, S., Ko, C., Suh, J. and Weber-Bargioni, A., 2017. Anomalous above-

gap photoexcitations and optical signatures of localized charge puddles in monolayer molybdenum disulfide. *ACS nano*, *11*(2), pp.2115-2123.

242. Yu, W.J., Liu, Y., Zhou, H., Yin, A., Li, Z., Huang, Y. and Duan, X., 2013. Highly efficient gate-tunable photocurrent generation in vertical heterostructures of layered materials. *Nature nanotechnology*, *8*(12), pp.952-958.

243. O'donnell, K.P. and Chen, X., 1991. Temperature dependence of semiconductor band gaps. *Applied physics letters*, *58*(25), pp.2924-2926.

244. McCreary, K.M., Hanbicki, A.T., Sivaram, S.V. and Jonker, B.T., 2018. A-and B-exciton photoluminescence intensity ratio as a measure of sample quality for transition metal dichalcogenide monolayers. *Apl Materials*, *6*(11).

245. Christopher, J.W., Goldberg, B.B. and Swan, A.K., 2017. Long tailed trions in monolayer MoS2: Temperature dependent asymmetry and resulting red shift of trion photoluminescence spectra. *Scientific reports*, *7*(1), p.14062.

246. Korn, T., Heydrich, S., Hirmer, M., Schmutzler, J. and Schüller, C., 2011. Low temperature photocarrier dynamics in monolayer MoS2. *Applied Physics Letters*, *99*(10).

247. Koirala, S., Mouri, S., Miyauchi, Y. and Matsuda, K., 2016. Homogeneous linewidth broadening and exciton dephasing mechanism in MoT e 2. *Physical Review B*, *93*(7), p.075411.

248. Korn, T., Heydrich, S., Hirmer, M., Schmutzler, J. and Schüller, C., 2011. Low temperature photocarrier dynamics in monolayer MoS2. *Applied Physics Letters*, *99*(10).

249. Raja, A., Chaves, A., Yu, J., Arefe, G., Hill, H.M., Rigosi, A.F., Berkelbach, T.C., Nagler, P., Schüller, C., Korn, T. and Nuckolls, C., 2017. Coulomb engineering of the bandgap and excitons in two-dimensional materials. *Nature communications*, *8*(1), p.15251.

250. Cadiz, F., Courtade, E., Robert, C., Wang, G., Shen, Y., Cai, H., Taniguchi, T., Watanabe, K., Carrere, H., Lagarde, D. and Manca, M., 2017. Excitonic linewidth approaching the homogeneous limit in MoS 2-based van der Waals heterostructures. *Physical Review X*, *7*(2), p.021026.

251. Onga, M., Zhang, Y., Ideue, T. and Iwasa, Y., 2017. Exciton Hall effect in monolayer MoS2. *Nature materials*, *16*(12), pp.1193-1197.

252. Li, H. and Zhang, X.H., 2020. Temperature-dependent photoluminescence and time-resolved photoluminescence study of monolayer molybdenum disulfide. *Optical Materials*, *107*, p.110150.

253. Garcia-Basabe, Y., Rocha, A.R., Vicentin, F.C., Villegas, C.E., Nascimento, R., Romani, E.C., De Oliveira, E.C., Fechine, G.J., Li, S., Eda, G. and Larrude, D.G., 2017. Ultrafast charge transfer dynamics pathways in two-dimensional MoS 2–graphene heterostructures: a core-hole clock approach. *Physical Chemistry Chemical Physics*, *19*(44), pp.29954-29962.

254. Robledo, A.K.R., Salazar, M.F., Martinez, B.A.M., Torres-Rosales, A.A., Lara-Alfaro, H.F., Del Pozo-Zamudio, O., Cerda-Mendez, E.A., Jimenez-Sandoval, S. and Bugallo, A.D.L., 2023. Interlayer charge transfer in supported and suspended MoS2/Graphene/MoS2 vertical heterostructures. *PLoS One*, *18*(7), p.e0283834.

255. Lin, Y., Ling, X., Yu, L., Huang, S., Hsu, A.L., Lee, Y.H., Kong, J., Dresselhaus, M.S. and Palacios, T., 2014. Dielectric screening of excitons and trions in single-layer MoS2. *Nano letters*, *14*(10), pp.5569-5576.

256. Drüppel, M., Deilmann, T., Krüger, P. and Rohlfing, M., 2017. Diversity of trion states and substrate effects in the optical properties of an MoS2 monolayer. *Nature communications*, *8*(1), p.2117.

257. Mouri, S., Miyauchi, Y. and Matsuda, K., 2013. Tunable photoluminescence of monolayer MoS2 via chemical doping. *Nano letters*, *13*(12), pp.5944-5948.

258. Tongay, S., Suh, J., Ataca, C., Fan, W., Luce, A., Kang, J.S., Liu, J., Ko, C., Raghunathanan, R., Zhou, J. and Ogletree, F., 2013. Defects activated photoluminescence in two-dimensional semiconductors: interplay between bound, charged and free excitons. *Scientific reports*, *3*(1), p.2657.

259. Pham, T., Ramnani, P., Villarreal, C.C., Lopez, J., Das, P., Lee, I., Neupane, M.R., Rheem, Y. and Mulchandani, A., 2019. MoS2-graphene heterostructures as efficient organic compounds sensing 2D materials. *Carbon*, *142*, pp.504-512.

260. Lin, W., Zhuang, P., Chou, H., Gu, Y., Roberts, R., Li, W., Banerjee, S.K., Cai, W. and Akinwande, D., 2019. Electron redistribution and energy transfer in graphene/MoS2 heterostructure. *Applied Physics Letters*, *114*(11).

261. Mangu, V.S., Zamiri, M., Brueck, S.R.J. and Cavallo, F., 2017. Strain engineering, efficient excitonic photoluminescence, and exciton funnelling in unmodified MoS 2 nanosheets. Nanoscale, 9(43), pp.16602-16606.

262. Ma, Y., Kalt, R.A. and Stemmer, A., 2022. Local strain and tunneling current modulate excitonic luminescence in MoS 2 monolayers. *RSC advances*, *12*(38), pp.24922-24929.

263. Lin, Y., Ling, X., Yu, L., Huang, S., Hsu, A.L., Lee, Y.H., Kong, J., Dresselhaus, M.S. and Palacios, T., 2014. Dielectric screening of excitons and trions in single-layer MoS2. *Nano letters*, *14*(10), pp.5569-5576.

264. Amsterdam, S.H., Stanev, T.K., Wang, L., Zhou, Q., Irgen-Gioro, S., Padgaonkar, S., Murthy, A.A., Sangwan, V.K., Dravid, V.P., Weiss, E.A. and Darancet, P., 2021. Mechanistic investigation of molybdenum disulfide defect photoluminescence quenching by adsorbed metallophthalocyanines. *Journal of the American Chemical Society*, *143*(41), pp.17153-17161.

265. Tsai, H.S., Huang, Y.H., Tsai, P.C., Chen, Y.J., Ahn, H., Lin, S.Y. and Lu, Y.J., 2020. Ultrafast exciton dynamics in scalable monolayer MoS2 synthesized by metal sulfurization. *ACS omega*, *5*(19), pp.10725-10730.

266. Steinhoff, A., Kim, J.H., Jahnke, F., Rosner, M., Kim, D.S., Lee, C., Han, G.H., Jeong, M.S., Wehling, T.O. and Gies, C., 2015. Efficient excitonic photoluminescence in direct and indirect band gap monolayer MoS2. *Nano letters*, *15*(10), pp.6841-6847.

267. Saito, K., Okada, M., Kitaura, R., Kishida, H. and Koyama, T., 2021. Femtosecond photoluminescence from monolayer MoS 2: Time-domain study on exciton diffusion. *Physical Review B*, *103*(20), p.L201401.

268. Alexeev, E.M., Catanzaro, A., Skrypka, O.V., Nayak, P.K., Ahn, S., Pak, S., Lee, J., Sohn, J.I., Novoselov, K.S., Shin, H.S. and Tartakovskii, A.I., 2017. Imaging of interlayer coupling in van der Waals heterostructures using a bright-field optical microscope. *Nano letters*, *17*(9), pp.5342-5349.

269. Luo, W., Song, R., Whetten, B.G., Huang, D., Cheng, X., Belyanin, A., Jiang, T. and Raschke, M.B., 2024. Nonlinear Nano-Imaging of Interlayer Coupling in 2D Graphene-Semiconductor Heterostructures. *Small*, *20*(24), p.2307345.

270. Du, K., Qiao, B., Ding, X., Huang, C. and Hu, H., 2025. Bubbles in 2D Materials: Formation Mechanisms, Impacts, and Removal Strategies for Next-Generation Electronic Devices. *Nanomaterials*, *15*(24), p.1888.

271. Ko, P.J., Abderrahmane, A., Thu, T.V., Ortega, D., Takamura, T. and Sandhu, A., 2015. Laser power dependent optical properties of mono-and few-layer MoS2. *Journal of nanoscience and nanotechnology*, *15*(9), pp.6843-6846

272. Nan, H., Wang, Z., Wang, W., Liang, Z., Lu, Y., Chen, Q., He, D., Tan, P., Miao, F., Wang, X. and Wang, J., 2014. Strong photoluminescence enhancement of MoS2 through defect engineering and oxygen bonding. *ACS nano*, *8*(6), pp.5738-5745.

273. Li, H. and Zhang, X.H., 2020. Temperature-dependent photoluminescence and time-resolved photoluminescence study of monolayer molybdenum disulfide. *Optical Materials*, *107*, p.110150.

274. Varshni, Y.P., 1967. Temperature dependence of the energy gap in semiconductors. *physica*, *34*(1), pp.149-154.

275. O'donnell, K.P. and Chen, X., 1991. Temperature dependence of semiconductor band gaps. *Applied physics letters*, *58*(25), pp.2924-2926.

276. Xu, Z., Liu, Z., Zhang, D., Zhong, Z. and Norris, T.B., 2021. Ultrafast dynamics of charge transfer in CVD grown MoS2–graphene heterostructure. *Applied Physics Letters*, *119*(9).

277. Garcia-Basabe, Y., Rocha, A.R., Vicentin, F.C., Villegas, C.E., Nascimento, R., Romani, E.C., De Oliveira, E.C., Fechine, G.J., Li, S., Eda, G. and Larrude, D.G., 2017. Ultrafast charge transfer dynamics pathways in two-dimensional MoS 2–graphene heterostructures: a core-hole clock approach. *Physical Chemistry Chemical Physics*, *19*(44), pp.29954-29962.

278. Hong, J., Hu, Z., Probert, M., Li, K., Lv, D., Yang, X., Gu, L., Mao, N., Feng, Q., Xie, L. and Zhang, J., 2015. Exploring atomic defects in molybdenum disulphide monolayers. *Nature communications*, *6*(1), p.6293.

279. Kim, Y.C., Ahn, Y.H., Lee, S. and Park, J.Y., 2020. Large-area growth of high-quality graphene/MoS2 vertical heterostructures by chemical vapor deposition with nucleation control. *Carbon*, *168*, pp.580-587.

280. Rademacher, N., Reato, E., Völkel, L., Grundmann, A., Heuken, M., Kalisch, H., Vescan, A., Daus, A. and Lemme, M.C., 2024. CVD graphene-MoS2 Van der Waals heterostructures on the millimeter-scale. *Micro and Nano Engineering*, *23*, p.100256.

281. Liu, Z., Amani, M., Najmaei, S., Xu, Q., Zou, X., Zhou, W., Yu, T., Qiu, C., Birdwell, A.G., Crowne, F.J. and Vajtai, R., 2014. Strain and structure

heterogeneity in MoS2 atomic layers grown by chemical vapour deposition. *Nature communications*, *5*(1), p.5246.

282. Xin, H., Zhang, J., Yang, C. and Chen, Y., 2022. Direct detection of inhomogeneity in CVD-grown 2D TMD materials via K-means clustering Raman analysis. *Nanomaterials*, *12*(3), p.414.
283. Seravalli, L. and Bosi, M., 2021. A review on chemical vapour deposition of two-dimensional MoS2 flakes. *Materials*, *14*(24), p.7590.
284. Ling, X., Lee, Y.H., Lin, Y., Fang, W., Yu, L., Dresselhaus, M.S. and Kong, J., 2014. Role of the seeding promoter in MoS2 growth by chemical vapor deposition. *Nano letters*, *14*(2), pp.464-472.
285. Sitek, J., Plocharski, J., Pasternak, I., Gertych, A.P., McAleese, C., Conran, B.R., Zdrojek, M. and Strupinski, W., 2020. Substrate-induced variances in morphological and structural properties of MoS2 grown by chemical vapor deposition on epitaxial graphene and SiO2. *ACS Applied Materials & Interfaces*, *12*(40), pp.45101-45110.
286. Peruzzo, A., McClean, J., Shadbolt, P., Yung, M.H., Zhou, X.Q., Love, P.J., Aspuru-Guzik, A. and O’brien, J.L., 2014. A variational eigenvalue solver on a photonic quantum processor. *Nature communications*, *5*(1), p.4213.
287. Kataria, S., Wagner, S., Cusati, T., Fortunelli, A., Iannaccone, G., Pandey, H., Fiori, G. and Lemme, M.C., 2017. Growth-induced strain in chemical vapor deposited monolayer MoS2: experimental and theoretical investigation. *Advanced Materials Interfaces*, *4*(17), p.1700031.
288. Islam, M.S., Za'abar, F.I., Doroody, C., Tiong, S.K., Zuhdi, A.W.M., Rahman, K.S., Feng, Z.J. and Amin, N., 2025. Thermal modulation of crystallinity and defect landscape in sputtered MoS2 thin films for optoelectronic applications. *Journal of Science: Advanced Materials and Devices*, p.101060
289. Miwa, J.A., Dendzik, M., Grønborg, S.S., Bianchi, M., Lauritsen, J.V., Hofmann, P. and Ulstrup, S., 2015. Van der Waals epitaxy of two-dimensional MoS2–graphene heterostructures in ultrahigh vacuum. *ACS nano*, *9*(6), pp.6502-6510.
290. Haigh, S.J., Gholinia, A., Jalil, R., Romani, S., Britnell, L., Elias, D.C., Novoselov, K.S., Ponomarenko, L.A., Geim, A.K. and Gorbachev, R., 2012. Cross-sectional imaging of individual layers and buried interfaces of graphene-based heterostructures and superlattices. *Nature materials*, *11*(9), pp.764-767.

291. Du, K., Qiao, B., Ding, X., Huang, C. and Hu, H., 2025. Bubbles in 2D Materials: Formation Mechanisms, Impacts, and Removal Strategies for Next-Generation Electronic Devices. *Nanomaterials*, *15*(24), p.1888.

292. Liang, S.J., Cheng, B., Cui, X. and Miao, F., 2020. Van der Waals heterostructures for high-performance device applications: challenges and opportunities. *Advanced Materials*, *32*(27), p.1903800.

293. Castellanos-Gomez, A., Roldán, R., Cappelluti, E., Buscema, M., Guinea, F., Van Der Zant, H.S. and Steele, G.A., 2013. Local strain engineering in atomically thin MoS2. *Nano letters*, *13*(11), pp.5361-5366.

294. Tyurnina, A.V., Bandurin, D.A., Khestanova, E., Kravets, V.G., Koperski, M., Guinea, F., Grigorenko, A.N., Geim, A.K. and Grigorieva, I.V., 2019. Strained bubbles in van der Waals heterostructures as local emitters of photoluminescence with adjustable wavelength. *ACS photonics*, *6*(2), pp.516-524.

295. Chen, P., Li, D., Li, Z., Xu, X., Wang, H., Zhou, X. and Zhai, T., 2023. Programmable physical unclonable functions using randomly anisotropic two-dimensional flakes. *ACS nano*, *17*(23), pp.23989-23997.

296. Wang, A., Kadam, S., Li, H., Shi, S. and Qi, Y., 2018. Review on modeling of the anode solid electrolyte interphase (SEI) for lithium-ion batteries. NPJ Computational materials, 4(1), p.15.

297. An, S.J., Li, J., Daniel, C., Mohanty, D., Nagpure, S. and Wood III, D.L., 2016. The state of understanding of the lithium-ion-battery graphite solid electrolyte interphase (SEI) and its relationship to formation cycling. *Carbon*, *105*, pp.52-76.

298. Andrenacci, N., Vitiello, F., Boccaletti, C. and Vellucci, F., 2025. Powering the Future Smart Mobility: A European Perspective on Battery Storage. *Batteries*, *11*(5), p.185.

299. Iermakova, D.I., Dugas, R., Palacín, M.R. and Ponrouch, A., 2015. On the comparative stability of Li and Na metal anode interfaces in conventional alkyl carbonate electrolytes. *Journal of The Electrochemical Society*, *162*(13), p.A7060.

300. Megahed, S., Barnett, B.M. and Xie, L. eds., 1995. Proceedings of the Symposium on Rechargeable Lithium and Lithium-ion Batteries. The Electrochemical Society.

301. Winter, M., Besenhard, J.O., Spahr, M.E. and Novak, P., 1998. Insertion electrode materials for rechargeable lithium batteries. *Advanced materials*, *10*(10), pp.725-763.

302. Ein-Eli, Y. and Koch, V.R., 1997. Chemical oxidation: a route to enhanced capacity in Li-ion graphite anodes. *Journal of the Electrochemical Society*, *144*(9), p.2968

303. Bhattacharya, S., Riahi, A.R. and Alpas, A.T., 2014. Electrochemical cycling behaviour of lithium carbonate (Li2CO3) pre-treated graphite anodes–SEI formation and graphite damage mechanisms. *Carbon*, *77*, pp.99-112.

304. Buqa, H., Golob, P., Winter, M. and Besenhard, J.O., 2001. Modified carbons for improved anodes in lithium-ion cells. *Journal of power sources*, *97*, pp.122-125.

305. Pan, H., Chen, Y., Pang, W., Sun, H., Li, J., Lin, Y., Kolosov, O. and Huang, Z., 2021. Complementary sample preparation strategies (PVD/BEXP) combining with multifunctional SPM for the characterizations of battery interfacial properties. *MethodsX*, *8*, p.101250.

306. Xie, W., Weng, L.T., Ng, K.M., Chan, C.K. and Chan, C.M., 2015. Clean graphene surface through high temperature annealing. *Carbon*, *94*, pp.740-748.

307. Rousseau, B., Estrade-Szwarckopf, H., Thomann, A.L. and Brault, P., 2003. Stable C-atom displacements on HOPG surface under plasma low-energy argon-ion bombardment. *Applied Physics A*, *77*(3), pp.591-597.

308. Hu, J., Ji, Y., Zheng, G., Huang, W., Lin, Y., Yang, L. and Pan, F., 2022. Influence of electrolyte structural evolution on battery applications: cationic aggregation from dilute to high concentration. *Aggregate*, *3*(1), p.e153.

309. Efaw, C.M., Wu, Q., Gao, N., Zhang, Y., Zhu, H., Gering, K., Hurley, M.F., Xiong, H., Hu, E., Cao, X. and Xu, W., 2023. Localized high-concentration electrolytes get more localized through micelle-like structures. *Nature materials*, *22*(12), pp.1531-1539.

310. Kleijn, D., Winfree, R., Bartomeus, I., Carvalheiro, L.G., Henry, M., Isaacs, R., Klein, A.M., Kremen, C., M'gonigle, L.K., Rader, R. and Ricketts, T.H., 2015. Delivery of crop pollination services is an insufficient argument for wild pollinator conservation. *Nature communications*, *6*(1), p.7414.

311. Wu, J., Gao, Z., Wang, Y., Yang, X., Liu, Q., Zhou, D., Wang, X., Kang, F. and Li, B., 2022. Electrostatic interaction tailored anion-rich solvation sheath stabilizing high-voltage lithium metal batteries. *Nano-Micro Letters*, *14*(1), p.147.

312. Faheem, A.B., Pham, T.D. and Lee, K.K., 2024. Solvation structures in weakly solvating solvents lead to hybrid vehicular/structural ion transport. *Journal of Molecular Liquids*, *415*, p.126344.

313. Yao, Y.X., Chen, X., Yan, C., Zhang, X.Q., Cai, W.L., Huang, J.Q. and Zhang, Q., 2021. Regulating interfacial chemistry in lithium-ion batteries by a weakly solvating electrolyte. *Angewandte Chemie International Edition*, *60*(8), pp.4090-4097.

314. Zhao, W., Zhao, C., Wu, H., Li, L. and Zhang, C., 2024. Progress, challenge and perspective of graphite-based anode materials for lithium batteries: A review. *Journal of Energy Storage*, *81*, p.110409.

315. Leung, K., 2015. Predicting the voltage dependence of interfacial electrochemical processes at lithium-intercalated graphite edge planes. *Physical Chemistry Chemical Physics*, *17*(3), pp.1637-1643.

316. Wang, Y., Alsmeyer, D.C. and McCreery, R.L., 1990. Raman spectroscopy of carbon materials: structural basis of observed spectra. *Chemistry of Materials*, *2*(5), pp.557-563.

317. Ott, A.K. and Ferrari, A.C., 2024. Raman spectroscopy of graphene and related materials. *Encyclopedia of Condensed Matter Physics*, *2*, pp.233-247.

318. Ferrari, A.C., 2007. Raman spectroscopy of graphene and graphite: Disorder, electron–phonon coupling, doping and nonadiabatic effects. *Solid state communications*, *143*(1-2), pp.47-57.

319. Sole, C., Drewett, N.E. and Hardwick, L.J., 2014. In situ Raman study of lithium-ion intercalation into microcrystalline graphite. *Faraday discussions*, *172*, pp.223-237.

320. Hardwick, L.J., Buqa, H. and Novák, P., 2006. Graphite surface disorder detection using in situ Raman microscopy. *Solid State Ionics*, *177*(26-32), pp.2801-2806.

321. Cabo-Fernandez, L., Neale, A.R., Braga, F., Sazanovich, I.V., Kostecki, R. and Hardwick, L.J., 2019. Kerr gated Raman spectroscopy of LiPF 6 salt and LiPF

6-based organic carbonate electrolyte for Li-ion batteries. *Physical Chemistry Chemical Physics*, *21*(43), pp.23833-23842.

322. Hardwick, L.J., Buqa, H. and Novák, P., 2006. Graphite surface disorder detection using in situ Raman microscopy. *Solid State Ionics*, *177*(26-32), pp.2801-2806.

323. Li, N. and Su, D., 2019. In-situ structural characterizations of electrochemical intercalation of graphite compounds. *Carbon Energy*, *1*(2), pp.200-218.

324. Chen Y, Wu W, Gonzalez-Munoz S, Forcieri L, Wells C, Jarvis SP, et al. Nanoarchitecture factors of solid electrolyte interphase formation via 3D nano-rheology microscopy and surface force-distance spectroscopy. Nature communications 2023;14(1).

325. Shi, Q., Dokko, K. and Scherson, D.A., 2004. In situ Raman microscopy of a single graphite microflake electrode in a Li+-containing electrolyte. *The Journal of Physical Chemistry B*, *108*(15), pp.4789-4793.

326. Nie, M., Chalasani, D., Abraham, D.P., Chen, Y., Bose, A. and Lucht, B.L., 2013. Lithium-ion battery graphite solid electrolyte interphase revealed by microscopy and spectroscopy. *The Journal of Physical Chemistry C*, *117*(3), pp.1257-1267.

327. Kong, F., Kostecki, R., Nadeau, G., Song, X., Zaghib, K., Kinoshita, K. and McLarnon, F., 2001. In situ studies of SEI formation. *Journal of power sources*, *97*, pp.58-66.

328. Cabañero, M.A., Hagen, M. and Quiroga-González, E., 2021. In-operando Raman study of lithium plating on graphite electrodes of lithium-ion batteries. *Electrochimica acta*, *374*, p.137487.

329. Aurbach, D., Ein-Eli, Y., Chusid, O., Carmeli, Y., Babai, M. and Yamin, H., 1994. The correlation between the surface chemistry and the performance of Li-carbon intercalation anodes for rechargeable 'Rocking-Chair'type batteries. Journal of The Electrochemical Society, 141(3), p.603.

330. Aurbach, D., Ein-Eli, Y., Markovsky, B., Zaban, A., Luski, S., Carmeli, Y. and Yamin, H., 1995. The study of electrolyte solutions based on ethylene and diethyl carbonates for rechargeable Li batteries: II. Graphite electrodes. *Journal of The Electrochemical Society*, *142*(9), p.2882.

331. Chusid, O.Y., Ely, E.E., Aurbach, D., Babai, M. and Carmeli, Y., 1993. Electrochemical and spectroscopic studies of carbon electrodes in lithium battery electrolyte systems. *Journal of power sources*, *43*(1-3), pp.47-64.

332. Yang, C.R., Wang, Y.Y. and Wan, C.C., 1998. Composition analysis of the passive film on the carbon electrode of a lithium-ion battery with an EC-based electrolyte. *Journal of power sources*, *72*(1), pp.66-70.

333. Martín-Yerga, D., Kang, M. & Unwin, P. R. Scanning electrochemical cell microscopy in a glovebox: structure-activity correlations in the early stages of solid-electrolyte interphase formation on graphite. ChemElectroChem 8, 4240–4251 (2021).

334. Abe, T., Fukuda, H., Iriyama, Y. and Ogumi, Z., 2004. Solvated Li-ion transfer at interface between graphite and electrolyte. *Journal of the Electrochemical Society*, *151*(8), p.A1120.

335. von Wald Cresce, A., Borodin, O. and Xu, K., 2012. Correlating Li+ solvation sheath structure with interphasial chemistry on graphite. *The Journal of Physical Chemistry C*, *116*(50), pp.26111-26117.

336. Nachaki, E.O. and Kuroda, D.G., 2024. Lithium-ion Speciation in Cyclic Solvents: Impact of Anion Charge Delocalization and Solvent Polarizability. *The Journal of Physical Chemistry B*, *128*(14), pp.3408-3415.

337. Chen, J., Lu, H., Kong, X., Liu, J., Liu, J., Yang, J., Nuli, Y. and Wang, J., 2024. Interphase engineering via solvent molecule chemistry for stable lithium metal batteries. *Angewandte Chemie International Edition*, *63*(23), p.e202317923.

338. Smiatek, J., Heuer, A. and Winter, M., 2018. Properties of ion complexes and their impact on charge transport in organic solvent-based electrolyte solutions for lithium batteries: insights from a theoretical perspective. *Batteries*, *4*(4), p.62.

339. Szczęsna-Chrzan, A., Vogler, M., Yan, P., Żukowska, G.Z., Wölke, C., Ostrowska, A., Szymańska, S., Marcinek, M., Winter, M., Cekic-Laskovic, I. and Wieczorek, W., 2023. Ionic conductivity, viscosity, and self-diffusion coefficients of novel imidazole salts for lithium-ion battery electrolytes. *Journal of Materials Chemistry A*, *11*(25), pp.13483-13492.

340. Chen, X., Li, Z., Zhao, H., Li, J., Li, W., Han, C., Zhang, Y., Lu, L., Li, J. and Qiu, X., 2024. Dominant solvent-separated ion pairs in electrolytes enable

superhigh conductivity for fast-charging and low-temperature lithium-ion batteries. *ACS nano*, *18*(11), pp.8350-8359.

341. Yang, H. and Wu, N., 2022. Ionic conductivity and ion transport mechanisms of solid-state lithium-ion battery electrolytes: A review. *Energy Science & Engineering*, *10*(5), pp.1643-1671.
342. Berhaut, C.L., Lemordant, D., Porion, P., Timperman, L., Schmidt, G. and Anouti, M., 2019. Ionic association analysis of LiTDI, LiFSI and LiPF 6 in EC/DMC for better Li-ion battery performances. RSC advances, 9(8), pp.4599-4608.
343. Borodin, O., Self, J., Persson, K.A., Wang, C. and Xu, K., 2020. Uncharted waters: super-concentrated electrolytes. *Joule*, *4*(1), pp.69-100.
344. Wang, A., Kadam, S., Li, H., Shi, S. and Qi, Y., 2018. Review on modelling of the anode solid electrolyte interphase (SEI) for lithium-ion batteries. *NPJ Computational materials*, *4*(1), p.15.
345. Perez-Beltran, S., Kuai, D. and Balbuena, P.B., 2024. Sei formation and lithium-ion electrodeposition dynamics in lithium metal batteries via first-principles kinetic monte carlo modelling. *ACS Energy Letters*, *9*(11), pp.5268-5278.
346. Han, M., Zhu, C., Ma, T., Pan, Z., Tao, Z. and Chen, J., 2018. In situ atomic force microscopy study of nano–micro sodium deposition in ester-based electrolytes. *Chemical Communications*, *54*(19), pp.2381-2384.
347. Berhaut, C.L., Lemordant, D., Porion, P., Timperman, L., Schmidt, G. and Anouti, M., 2019. Ionic association analysis of LiTDI, LiFSI and LiPF 6 in EC/DMC for better Li-ion battery performances. *RSC advances*, *9*(8), pp.4599-4608.
348. Morita M, Asai Y, Yoshimoto N, Ishikawa M. A Raman spectroscopic study of organic electrolyte solutions based on binary solvent systems of ethylene carbonate with low viscosity solvents which dissolve different lithium salts. Journal of the Chemical Society 1998;94(23):3451–3456.
349. Chen, X., Yao, N., Zeng, B.S. and Zhang, Q., 2021. Ion–solvent chemistry in lithium battery electrolytes: From mono-solvent to multi-solvent complexes. *Fundamental Research*, *1*(4), pp.393-398.
350. Chen, X. and Zhang, Q., 2020. Atomic insights into the fundamental interactions in lithium battery electrolytes. *Accounts of Chemical Research*, *53*(9), pp.1992-2002.

351. Li L, Zhou S, Han H, Li H, Nie J, Armand M, et al. Transport and Electrochemical Properties and Spectral Features of Non-Aqueous Electrolytes Containing LiFSI in Linear Carbonate Solvents. Journal of The Electrochemical Society 2011;158(2).

352. Xiao, P., Yun, X., Chen, Y., Guo, X., Gao, P., Zhou, G. and Zheng, C., 2023. Insights into the solvation chemistry in liquid electrolytes for lithium-based rechargeable batteries. *Chemical Society Reviews*, *52*(15), pp.5255-5316.

353. Shi, P., Zheng, H., Liang, X., Sun, Y., Cheng, S., Chen, C. and Xiang, H., 2018. A highly concentrated phosphate-based electrolyte for high-safety rechargeable lithium batteries. *Chemical communications*, *54*(35), pp.4453-4456.

354. Kimura, K., Motomatsu, J. and Tominaga, Y., 2016. Correlation between solvation structure and ion-conductive behavior of concentrated poly (ethylene carbonate)-based electrolytes. *The Journal of Physical Chemistry C*, *120*(23), pp.12385-12391.

355. Li, L., Zhou, S., Han, H., Li, H., Nie, J., Armand, M., Zhou, Z. and Huang, X., 2011. Transport and electrochemical properties and spectral features of non-aqueous electrolytes containing LiFSI in linear carbonate solvents. *Journal of The Electrochemical Society*, *158*(2), pp. A74-A82.

356. Chu, Y., Shen, Y., Guo, F., Zhao, X., Dong, Q., Zhang, Q., Li, W., Chen, H., Luo, Z. and Chen, L., 2020. Advanced characterizations of solid electrolyte interphases in lithium-ion batteries. *Electrochemical energy reviews*, *3*(1), pp.187-219.

357. Yamada, Y. and Yamada, A., 2015. Super concentrated electrolytes for lithium batteries. Journal of The Electrochemical Society, 162(14), p.A2406.

358. Suo, L., Borodin, O., Gao, T., Olguin, M., Ho, J., Fan, X., Luo, C., Wang, C. and Xu, K., 2015. “Water-in-salt” electrolyte enables high-voltage aqueous lithium-ion chemistries. *Science*, *350*(6263), pp.938-943.

359. Obrovac, M.N. and Chevrier, V.L., 2014. Alloy negative electrodes for Li-ion batteries. *Chemical reviews*, *114*(23), pp.11444-11502.

360. Hebert, A. and McCalla, E., 2021. The role of metal substitutions in the development of Li batteries, part I: cathodes. *Materials Advances*, *2*(11), pp.3474-3518.

361. Liu, X., Zhang, J., Yun, X., Li, J., Yu, H., Peng, L., Xi, Z., Wang, R., Yang, L., Xie, W. and Chen, J., 2024. Anchored weakly-solvated electrolytes for high-voltage and low-temperature lithium-ion batteries. *Angewandte Chemie International Edition*, *63*(36), p.e202406596.

362. Xu, Z.L., Yoon, G., Park, K.Y., Park, H., Tamwattana, O., Joo Kim, S., Seong, W.M. and Kang, K., 2019. Tailoring sodium intercalation in graphite for high energy and power sodium ion batteries. *Nature communications*, *10*(1), p.2598.

363. Tsuchiya, T., Takayanagi, M., Mitsuishi, K., Imura, M., Ueda, S., Koide, Y., Higuchi, T. and Terabe, K., 2021. The electric double layer effect and its strong suppression at Li+ solid electrolyte/hydrogenated diamond interfaces. *Communications Chemistry*, *4*(1), p.117.

364. Li, P., Jiao, Y., Huang, J. and Chen, S., 2023. Electric double layer effects in electrocatalysis: insights from ab initio simulation and hierarchical continuum modeling. *JACS Au*, *3*(10), pp.2640-2659.

365. Gebbie, M.A., Liu, B., Guo, W., Anderson, S.R. and Johnstone, S.G., 2023. Linking electric double layer formation to electrocatalytic activity. *ACS Catalysis*, *13*(24), pp.16222-16239.

366. Feng, G., Huang, J., Sumpter, B.G., Meunier, V. and Qiao, R., 2010. Structure and dynamics of electrical double layers in organic electrolytes. *Physical Chemistry Chemical Physics*, *12*(20), pp.5468-5479.

367. Kim, Y., Kim, K.J., Kim, S.H. and Choi, J., 2024. Unveiling Ion Dynamics in the Electric-Double Layer Under Piezoionic Actuation of Chemo-Mechanical Energy Harvesters. *Advanced Energy Materials*, *14*(44), p.2402216.

368. Piernas-Muñoz, M.J., Tornheim, A., Trask, S., Zhang, Z. and Bloom, I., 2021. Surface-enhanced Raman spectroscopy (SERS): a powerful technique to study the SEI layer in batteries. *Chemical Communications*, *57*(18), pp.2253-2256.

369. Mozhzhukhina N, Gasteiger HA, Roosen J. Direct operando observation of double layer charging and early solid electrolyte interphase formation in lithium-ion battery electrolytes using surface-enhanced Raman spectroscopy. Journal of Physical Chemistry Letters 2020;11(16):6773–6779.

370. Gu, Y., You, E.M., Lin, J.D., Wang, J.H., Luo, S.H., Zhou, R.Y., Zhang, C.J., Yao, J.L., Li, H.Y., Li, G. and Wang, W.W., 2023. Resolving nanostructure and chemistry of solid-electrolyte interphase on lithium anodes by depth-sensitive

plasmon-enhanced Raman spectroscopy. *Nature Communications*, *14*(1), p.3536.

371. Galloway, T.A., Cabo-Fernandez, L., Aldous, I.M., Braga, F. and Hardwick, L.J., 2017. Shell isolated nanoparticles for enhanced Raman spectroscopy studies in lithium–oxygen cells. *Faraday Discussions*, *205*, pp.469-490.

372. Nanda, J., Yang, G., Hou, T., Voylov, D.N., Li, X., Ruther, R.E., Naguib, M., Persson, K., Veith, G.M. and Sokolov, A.P., 2019. Unraveling the nanoscale heterogeneity of solid electrolyte interphase using tip-enhanced Raman spectroscopy. *Joule*, *3*(8), pp.2001-2019.

373. Stephan, A.K., 2019. Completing the picture of the solid electrolyte interphase. *Joule*, *3*(8), pp.1812-1814.

374. Niciński, K., Krajczewski, J., Kudelski, A., Witkowska, E., Trzcińska-Danielewicz, J., Girstun, A. and Kamińska, A., 2019. Detection of circulating tumor cells in blood by shell-isolated nanoparticle–enhanced Raman spectroscopy (SHINERS) in microfluidic device. *Scientific reports*, *9*(1), p.9267.

375. Zhang, L.; Chen, Y., Electrolyte solvation structure as a stabilization mechanism for electrodes. Energy Materials 2021, 1 (1), 100004.

376. Lei, S.; Zeng, Z.; Liu, M.; Zhang, H.; Cheng, S.; Xie, J., Balanced solvation/de-solvation of electrolyte facilitates Li-ion intercalation for fast charging and low-temperature Li-ion batteries. Nano Energy 2022, 98, 107265.

377. Uchida, S.; Ishikawa, M., Lithium bis(fluorosulfonyl)imide based low ethylene carbonate content electrolyte with unusual solvation state. Journal of Power Sources 2017, 359, 480-486.

378. Yao, Y. X.; Chen, X.; Yan, C.; Zhang, X. Q.; Cai, W. L.; Huang, J. Q.; Zhang, Q., Regulating Interfacial Chemistry in Lithium-Ion Batteries by a Weakly Solvating Electrolyte. Angewandte Chemie 2021,60 (8), 4090-4097.

379. Ding, J. F.; Xu, R.; Yao, N.; Chen, X.; Xiao, Y.; Yao, Y. X.; Yan, C.; Xie, J.; Huang, J. Q., Non-Solvating and Low-Dielectricity Cosolvent for Anion-Derived Solid Electrolyte Interphases in Lithium Metal Batteries. Angewandte Chemie International Edition 2021

380. Borowski, P.; Gac, W.; Pulay, P.; Woliński, K., The vibrational spectrum of 1,4-dioxane in aqueous solution – theory and experiment. New Journal of Chemistry 2016, 40 (9), 7663-7670.

381. Yamada, Y. et al. Hydrate-melt electrolytes for high-energy-density aqueous batteries. Nature Energy https://doi.org/10.1038/nenergy.2016.129 (2016).

382. Suo, L., Hu, Y. S., Li, H., Armand, M. & Chen, L. A new class of solvent-in-salt electrolyte for high-energy rechargeable metallic lithium batteries. Nat. Commun. 4, 1481 (2013).

383. Suo, L. et al. Water-in-salt electrolyte enables high-voltage aqueous lithium-ion chemistries. Science 350, 938–943 (2015).